University of Liège
Faculty of Applied Sciences
Aerospace and Mechanical Engineering Department

Multiple outputs operational modal identification of time-varying systems

Thesis submitted in fulfillment of the requirements for the degree of
Doctor in Engineering Sciences

by

BERTHA Mathieu, Ir.

Supervisor: Prof. Jean-Claude GOLINVAL

November 2017

University of Liège
Faculty of Applied Sciences
Aerospace and Mechanical Engineering Department

Multiple outputs operational modal identification of time-varying systems

Thesis submitted in fulfillment of the requirements for the degree of
Doctor in Engineering Sciences

by

BERTHA Mathieu, Ir.

Supervisor: Prof. Jean-Claude GOLINVAL

November 2017

Members of the Examination Committee

Prof. Grigorios DIMITRIADIS (President of the Committee)
University of Liège (Liège, Belgium)
gdimitriadis@uliege.be

Prof. Jean-Claude GOLINVAL (Advisor)
University of Liège (Liège, Belgium)
JC.Golinval@uliege.be

Prof. Olivier BRÜLS
University of Liège (Liège, Belgium)
O.Bruls@uliege.be

Prof. Vincent DENOËL
University of Liège (Liège, Belgium)
V.Denoel@uliege.be

Prof. Spilios D. FASSOIS
University of Patras (Patras, Greece)
fassois@mech.upatras.gr

Prof. Luigi GARIBALDI
Politecnico di Torino (Torino, Italy)
luigi.garibaldi@polito.it

Maître de Conférence Pierre Argoul
University of Paris-Est (Marne-la-Vallée, France)
pierre.argoul@lami.enpc.fr

"Around here, however, we don't look backwards for very long. We ***keep moving forward****, opening up new doors and doing new things, because we're curious... and curiosity keeps leading us down new paths."*

Walt Disney

Abstract

The present doctoral thesis addresses the problem of modal identification of time-varying dynamical systems. The methodologies proposed in this work cover parametric and nonparametric approaches and are able to deal with output-only and multiple degrees-of-freedom measurements. The nonparametric approach is based on source decomposition methods and the use of the Hilbert transform in order to get the varying frequencies and mode shapes. Concerning the parametric methods, both autoregressive moving-average (uni- and multivariate) and state-space models are considered. The way to introduce the time variation in the models is performed by the basis functions approach which projects the parameters on a preselected basis of functions.

Each of the proposed methods are presented before being experimentally tested on a laboratory time-varying structure. The structure is pretty simple and is commonly found in research works in the domain. It is composed of a supported beam on which a mass is moving. The mass is chosen sufficiently heavy to have a significant influence on the dynamics of the primary system. The structure is randomly excited by a shaker and several sensors record the response of the structure during the traveling of the moving mass.

Résumé

Le sujet de cette thèse porte sur l'identification modale de systèmes temps-variant. Les méthodes proposées dans ce travail couvrent à la fois des approches paramétriques et non paramétriques et sont capables de traiter des problèmes dans des conditions opérationnelles avec plusieurs canaux de mesures. L'approche non paramétrique est basée sur les méthodes de séparation de sources pour le traitement des multiples mesures ainsi que sur la transformée de Hilbert pour l'obtention des fréquences et modes propres instantanés. Pour les méthodes paramétriques, deux classes de modèles sont utilisées : des modèles autorégressifs et moyenne mobile (à la fois dans des modélisations scalaires et vectorielles) ainsi que des modèles d'état. Le traitement de la variation temporelle des systèmes étudiés se fait par l'approche des fonctions de base. Ces variations sont représentées par projection sur une base de fonctions préalablement choisie.

Chacune des méthodes proposées est en premier lieu présentée en détail avant d'être testée dans des conditions expérimentales sur une structure temps variante en laboratoire. La structure étudiée dans le cadre de cette thèse est assez simple et est basée sur de multiples exemples utilisés par d'autres chercheurs travaillant sur la même problématique. La structure utilisée comprend une poutre suspendue par deux ressorts à ses extrémités sur laquelle se déplace une masse. Le rapport des masses entre la masse mobile et la poutre est choisi suffisamment important pour que la masse mobile ait un impact visible sur les propriétés dynamiques du système. Le système entier est alors excité par une force aléatoire transmise par un pot vibrant et des accéléromètres enregistrent la réponse du système en différents endroits pendant le déplacement de la masse sur la poutre.

Acknowledgements

My first thanks go to the department of Aerospace and Mechanical Engineering of the University of Liège and to my supervisor, Professor Jean-Claude Golinval, that gave me the opportunity to fulfill the present doctoral research. Besides the scientific research, I also learned a lot with the teaching assistant tasks I was in charge of. The latter brought me soft skills and lessons I will keep in mind for the future.

I would then like to thank the other members of my thesis committee, Professors Gaëtan Kerschen, Grigorios Dimitriadis and Olivier Brüls for their follow-up throughout this work and advice.

I also wish to express my gratitude to all the members of the jury for the attention they will bring to this work.

Je terminerais en remerciant tous mes proches, famille et amis, mais également Pierre Grégoire et Aïcha Boutara. Merci pour votre support constant tout au long de la réalisation de ce travail, mais aussi pour votre soutient lors des derniers moments plus difficiles.

Contents

Introduction

In many fields of engineering, from civil to aerospace structures, modal analysis has always played a major role. Its main goal is to provide a good understanding about the dynamics of the structure of interest. The purpose of the analysis is to obtain a good model able to represent the structure. The needs of such accurate models is of prior interest for several reasons. One of the most common application is the validation or update of numerical models, such as finite elements ones, used for subsequent analyses without to resort to experimental tests on prototypes. Identifying an experimental model may also serve as a part of a larger numerical one in a substructuring approach when the modeling of the piece under study is not an easy task. Another field of application is the health monitoring of structures. Any change in the dynamics information of a structure extracted from experimental data can indicate the appearance of a damage on a structure or a malfunction of a machine.

Performing a modal analysis may be done in many ways, depending on the needs of the test engineer or simply on the testing possibilities. The first major distinction that can be observed is between Experimental Modal Analysis (EMA) and Operational Modal Analysis (OMA). The former one is generally performed in laboratories and all the testing conditions, including the applied force, are well controlled. Conversely, the analysis if often performed in an OMA way when testing the structure in a lab can not be done or when a lot of excitation sources are impossible to measure. One speak about output-only identification. This is generally the case for large civil engineering structures (buildings, bridges, and so on). Other subdifferentiation are more related to the type and amount of available data. Indeed, the modal identification methods work either with time or frequency data. Further, they are also differentiated between Single Degree of Freedom (SDOF) or Multiple Degree of Freedom (MDOF) methods. MDOF methods are generally preferred when the mode shapes of the structure are required in the identification. Finally, a last distinction in the type of methods is between parametric and nonparametric representations.

Besides the all the latter types of modal analysis methods, the system to be identified may also itself impose some constraints. Modal identification methods are now

mature with respect to their application in the field of Linear Time Invariant (LTI) systems. Those systems are characterized by a fixed frequency content. Nowadays, new challenges target the identification of systems expressing a nonlinear behavior [1, 2] or a time dependency of their modal parameters [3]. A nice graphical representation of the actual state-of-the-art of modal identification for MDOF systems is presented by Garibaldi in [4] and shown in Figure 1.

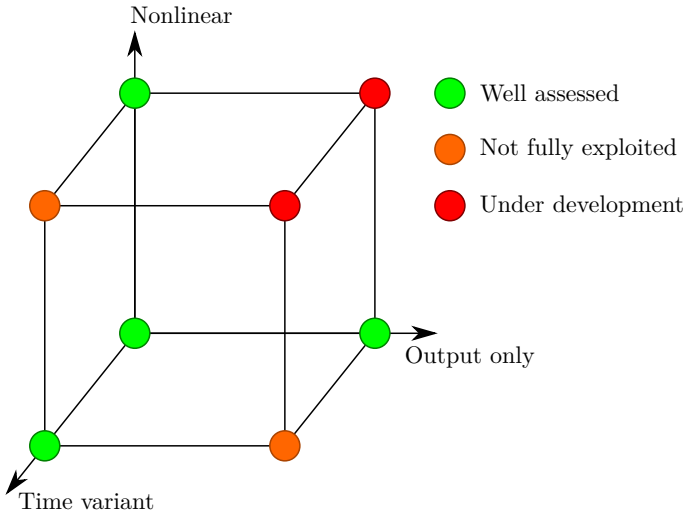

Figure 1: Basic illustration of the state-of-the-art of modal identification [4].

The goal of this thesis is to bring some new content in the field of MDOF output-only identification of time-varying systems. Indeed, only few methods in the literature are concerned by MDOF measurements and even fewer pay attention to the varying mode shapes. Further, in many applications employing time-varying structures, the applied excitation is rarely known.

Time-varying structures

In real life structures, many parameters may bring a sufficient modification of their structural properties which can have a non negligible effect on their modal properties. As an example, in civil engineering structures, the traffic or the passing of a train on a bridge affects the mass repartition of the whole structure which affects the dynamics of the brige [5, 6]. On a smaller scale, the crowd on a footpath acts in a similar way. Structures with changing configuration such as robots, cranes or even wind turbines also show dependencies in time of their modal properties with respect to their instantaneous configuration or operational conditions. The wind turbine case may also fall in a subclass of time-varying problems if the angular position of the rotor is the parameter that has the highest impact on the dynamics of the blades. The system then becomes periodically-varying [7]. In the aerospace industry, the decrease in the mass of embedded fuel may also be considered. In airplanes, this decrease rate may be small but this is not the case for rockets or launchers for example [8, 9]. Another aspect related to launch vehicle is the rapid change of temperature in some parts of the structure, such as the nozzle, that may also encounter variations in their properties [10].

Outline of the dissertation

As stated above, this thesis aims to bring new methodologies for the analysis of time-varying systems. This means that the proposed methods should be able to track the varying modal properties of such systems. The attention is put on MDOF systems and especially on the ability to extract the varying mode shapes as it is not so covered in the literature. All the proposed methods remain in the time domain.

The following of the thesis is subdivided in four main chapters. The three first ones described methodologies and their test on a laboratory varying structure. The last one is a test of the application of the methods on more complex cases and the use of the obtained varying mode shapes for monitoring purposes. Each of the three first chapters cover different methods based on nonparametric, semi-parametric and fully parametric identifications, respectively.

Chapter 1 first analyses time-varying systems by the application of the Hilbert transform. The proposed method is totally nonparametric. The Hilbert transform is a useful tool for the extraction of instantaneous properties of signals. Thanks to this ability, it is tempting to incorporate it in a method dedicated to the identification of varying modal properties. The use of the Hilbert transform in structural dynamics is generally applied to nonlinear vibrations applications. The second point of this chapter is the consideration of multiple measurement channels conversely to the majority of researches that only consider a single signal at a time. The experimental laboratory structure is also presented here.

Chapter 2 continues the whole identification by mixing a part of parametric identification of the varying poles followed by the same nonparametric identification of the mode shapes as in Chapter 1. This way to proceed improves the identification capabilities of the method. The parametric part is composed with a scalar parametric model with a constraint linking all the measurement channels in order to treat multiple measurements.

Chapter 3 provides two fully multivariate parametric models for the identification of varying mechanical systems. The multivariate way to model the identification problem directly consider multiple measurements and the mode shapes are direct parts of the results.

Chapter 4 applies the methods of Chapter 3 on the same experimental problem but in extended conditions (more channels, larger frequency band). The aim of this chapter is first to test the capabilities of the proposed methods. Other objectives are the application of the identification process for monitoring purposes and the treatment of additional measured information about the system besides the response channels.

Finally, a conclusion ends the thesis by recalling all the major comments and results covered in the whole work.

1 Non-parametric approach

This chapter is dedicated to the modal identification of time-varying vibrating structures through a non-parametric approach. First, some classical non-parametric methods are remind before we present a novel original method to deal with the identification of time-varying dynamical systems.

1.1 Nonstationarity in signal processing and instantaneous frequency calculation

In many applications, the main assumption behind common signal processing and system identification techniques is that the system response is stationary. The stationarity is a key assumption required for many of the most commonly used tools in system identification, including the Fourier Transform (FT), the Correlation Function (CF) or the Power Spectral Density (PSD). These tools, for example, are the most encountered in many system identification methods, being in time or frequency domain.

Stationarity is lost when the system exhibits some time-dependent characteristics. When dealing with the experimental identification of such time-varying systems, the loss of stationarity is the main complication we first have to face. To account for time variations, traditional signal processing and identification methods evolved, leading to the introduction of Time-Frequency Representation (TFR) to capture the evolution in time of the phase, amplitude and frequency content of a signal.

Many different time-frequency representations exist to model the varying frequency content of nonstationary signals and we will focus here on how they can identify a varying resonance frequency of a dynamical system. The simplest method is the Short-Time Fourier Transform (STFT), also known as the Windowed Fourier Transform, which assumes that the processed signal can be considered as stationary in a short time window sliding along the time axis. The classical FT is applied without any modification and represents the frequency content of the signal at the time set by the location of the active window. Note that the STFT is only an estimate of the varying

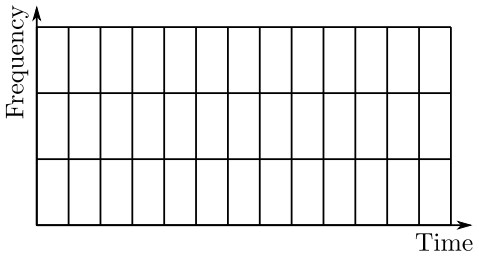

(a) STFT with high time resolution.

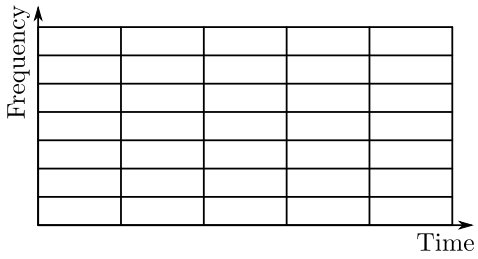

(b) STFT with high frequency resolution.

Figure 1.1: Illustration of the trade-off between time and frequency resolution in the STFT.

frequency content of the signal because it leads to different results depending on the choice in length and type of the applied moving window.

Due to the FT properties there is a trade-off between time resolution and frequency resolution. If we want to gain in frequency resolution, the sliding window has to be enlarged, which decreases the time resolution. Conversely, an increase in time resolution implies shorter windows and a lower frequency resolution. This is related to the uncertainty principle stating that it is not possible to refine the time and frequency resolutions simultaneously. The STFT time-frequency resolution is ruled by the relation $\Delta f.\Delta t = \text{Constant} \geq 1/(4\pi)$. Figure 1.1 represents two cases of STFT in which the time (1.1(a)) or the frequency (1.1(b)) resolution is preferred.

The STFT is computed as follows:

$$S_{STFT}(t,\, \omega) = \int_{-\infty}^{\infty} f(\tau)\, w(\tau - t)\, e^{-i\,\omega\,\tau} \mathrm{d}\tau \tag{1.1}$$

where w is the time window function. Taking the squared complex norm of the STFT leads to the so-called spectrogram of the signal.

Another useful tool to represent the time-varying frequency content of a signal is the Wavelet Transform (WT). The idea of the WT was first introduced by Harr in 1910 [11]. He showed that it is possible to represent any continuous function $f(x)$ in the support $[0, 1]$ by a series of orthogonal piecewise constant functions now known as the Haar wavelets. Each of the successive Haar functions is built based on a reference function that is scaled and shifted, as illustrated in Figure 1.2. The wavelet transforms used in modern signal processing are based on the same principle. Starting from a first function, called the mother wavelet, a series of other functions, the daughter wavelets, are built by scaling and shifting to fill a function basis of the desired dimension. In this way, each wavelet is located in frequency (through its scaling) and time (through its shifting) domains. The Continous Wavelet Transform is computed as

$$S_{CWT}(a,\, b) = \frac{1}{\sqrt{|a|}} \int_{-\infty}^{\infty} f(x)\, \psi\left(\frac{x-b}{a}\right) \mathrm{d}x \tag{1.2}$$

where ψ is the mother wavelet and a and b the scaling and shifting factors, respectively. A very common function used to represent the time-frequency content of a signal is

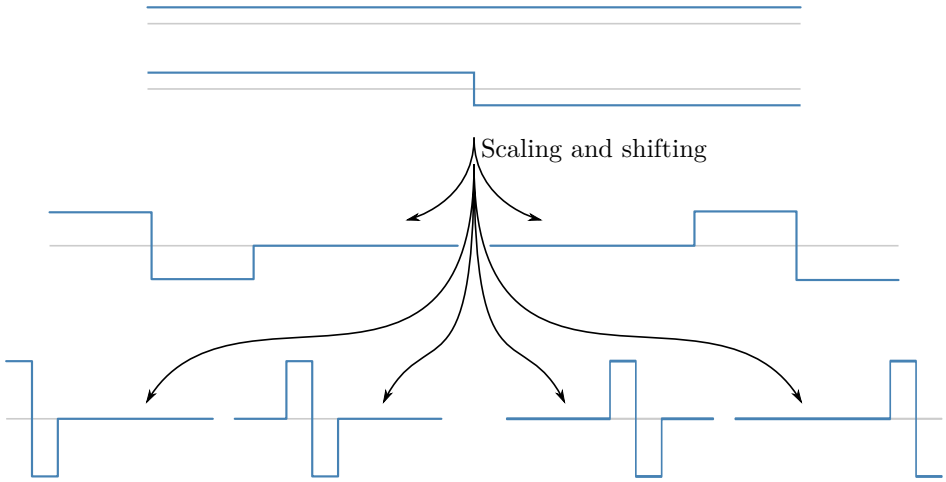

Figure 1.2: Illustration of the Haar wavelet functions.

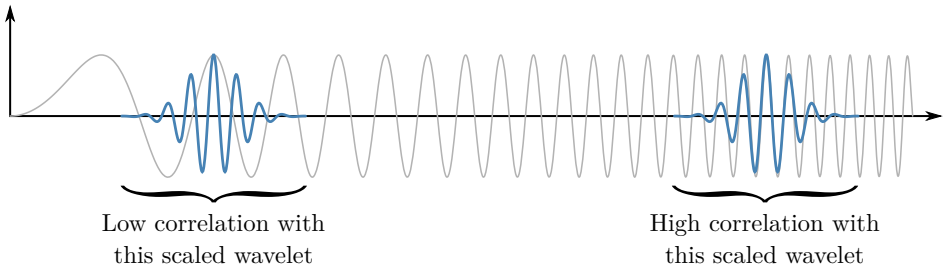

Figure 1.3: Illustration of the wavelet transform.

the Morlet wavelet. The Morlet wavelet is the product of a complex exponential and a Gaussian window. The time and frequency content of the Morlet wavelet then depends on the shifting and scaling of the Gaussian envelope and on the pulsation of the complex exponential. This is illustrated in Figure 1.3. The squared complex norm of the WT is named the scalogram and is similar to the spectrogram. Note that conversely to the STFT, the wavelet spectrum does not have the same time-frequency resolution in the whole domain, as illustrated in Figure 1.4.

The Wigner-Ville distribution is another method able to represent the time-frequency content of a signal. Originally, it was first developed in the field of quantum mechanics by Wigner [12] and then applied in signal processing by Ville [13]. The definition of the Wigner-Ville spectrum is

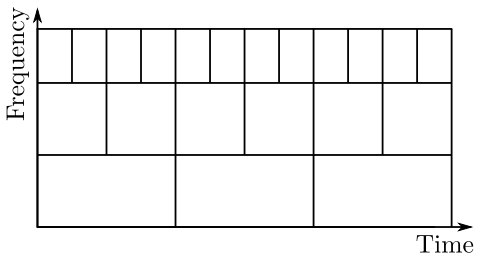

Figure 1.4: Illustration of the wavelet transform.

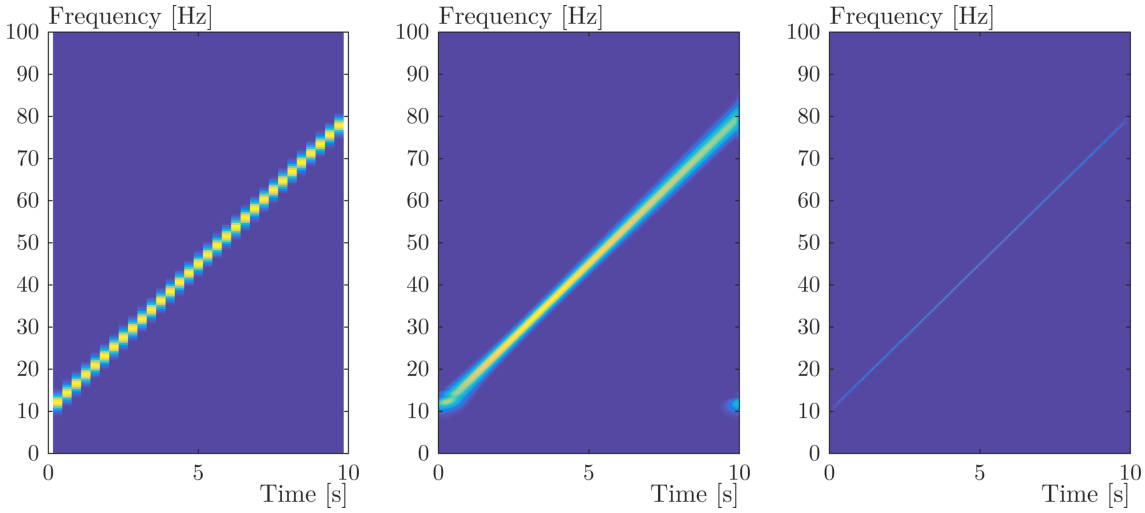

(a) Spectrogram with the STFT. (b) Scalogram with the WT. (c) Wigner-Ville distribution.

Figure 1.5: Illustration of different time-frequency representations.

$$S_{WVD}(t,\,\omega) = \int_{-\infty}^{+\infty} z\left(t + \frac{\tau}{2}\right) \bar{z}\left(t - \frac{\tau}{2}\right) e^{-i\omega\tau} \mathrm{d}\tau \tag{1.3}$$

where z is the complex analytic form of the real-valued signal x and $\bar{\blacksquare}$ denotes the complex conjugated value. The analytic signal (AS) will be described hereafter together with the Hilbert Transform (HT).

The Wigner-Ville distribution has some advantages compared to the previously cited time-frequency representations, but also suffers from some drawbacks. Regarding Equation (1.3), it appears as the Fourier transform of the local autocorrelation function with a lag τ. This is equivalent to the power spectral density at time t. The Wigner-Ville distribution is a part of a greater family of time-frequency distributions, the Cohen's class, that differ through the introduction of a multiplicative kernel in (1.3) [14].

A comparison between these methods for the representation of a simple chirp signal of unit amplitude is illustrated in Figure 1.5. It can be observed that the spectrogram and scalogram add some spread around the linear increasing frequency, conversely to the WVD which precisely locates the chirp signal in the time-frequency domain.

However, if the WVD perfectly works for a single component, things become worse if the signal possesses multiple frequency components. For example, adding a second component with a fixed frequency at 50 Hz and a constant amplitude of 0.5, the WVD shows some artifacts polluting the time-frequency spectrum. This is inherent to the computation of the WVD, which is a quadratic transform. This makes appear these artefacts as the product of the cross terms between all the components of the signal in the WVD computation. As shown in Figure 1.6, the auto-terms (from the sub components) are well represented in Figure 1.6(c) but are polluted by the cross-terms of the two components. This does not appear with the STFT or the WT as shown in Figures 1.6(a) and 1.6(b).

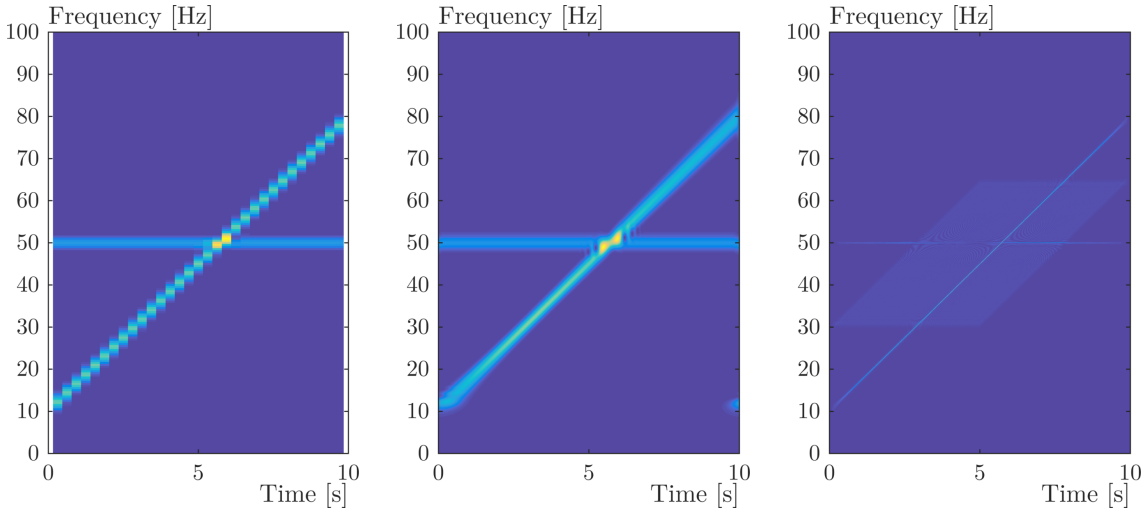

(a) Spectrogram with the STFT.

(b) Scalogram with the WT.

(c) Wigner-Ville distribution.

Figure 1.6: Illustration of different time-frequency representations for a multicomponent signal.

These families of time-frequency representations are useful to represent the frequency content of non-stationary signals. Throughout the present manuscript, many time-frequency plots are displayed but they are only used for illustration purposes and not for identification.

The next method presented here is based directly on the Hilbert transform and the Analytic Signal. In 1946 [15], Gabor wanted to bring useful tools coming from quantum mechanics to the field of signal processing. The majority of them are based on complex representations, while usually recorded signals are real-valued. Gabor's goal was to expand real-valued signals in the complex space, such as the well-know Euler's formula that links real-valued sine and cosine functions to a complex exponential representation. Let us also mention another contribution by Ville in 1948 about the analytic signal which is less known due to the fact it is written in French [13]. Starting from a real-valued signal $x(t)$, the idea is to create a complex signal by adding a signal in quadrature with respect to $x(t)$ multiplied by the complex unit such that

$$z(t) = x(t) + i\tilde{x}(t) \tag{1.4}$$

in which $z(t)$ is the complex analytic signal and $\tilde{x}(t)$ is the quadrature signal. It remains now to build the signal in quadrature and the HT is a good candidate method to build the quadrature signal $\tilde{x}(t)$. The HT $\mathcal{H}$ is a special linear transformation that has the particularity, to remain in the same domain as the one of the original signal. It also means that the output of the Hilbert transform applied to a real signal is also a real signal. Mathematically, the Hilbert transform of a signal $x(t)$ is obtained by the convolution product with a function $h(t)$ equal to

$$h(t) = \frac{1}{\pi\, t}. \tag{1.5}$$

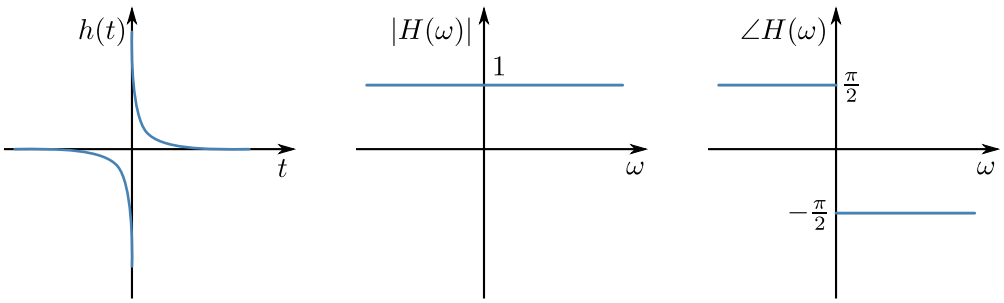

Figure 1.7: Illustration of $h(t)$ and its Fourier transform.

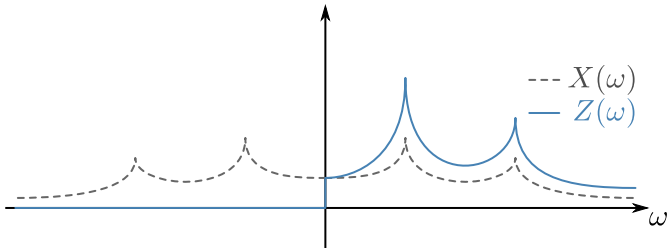

Figure 1.8: Specra of a signal and its correspondent analytic signal.

Because the convolution product $x(t) * h(t)$ is an improper integral due to the singularity of $h(t)$ at $t = 0$, the Hilbert transform is calculated using the Cauchy principal value of the integral. The integration is done up to an ϵ value close to the singularity and the limit for $\epsilon \to 0$ is calculated.

$$\begin{aligned} \tilde{x}(t) = \mathcal{H}(x(t)) &= \text{p.v.} \int_{-\infty}^{+\infty} x(t)\, h(t-\tau)\, \mathrm{d}\tau \\ &= \frac{1}{\pi} \text{p.v.} \int_{-\infty}^{+\infty} \frac{x(t)}{t-\tau}\, \mathrm{d}\tau \\ &= \frac{1}{\pi} \lim_{\epsilon \to 0} \left[\int_{-\infty}^{t-\epsilon} \frac{x(t)}{t-\tau}\, \mathrm{d}\tau + \int_{t+\epsilon}^{+\infty} \frac{x(t)}{t-\tau}\, \mathrm{d}\tau \right]. \end{aligned} \tag{1.6}$$

It results after the transformation that $\tilde{x}(t)$ is a signal with a phase shift of $+$ and $-\frac{\pi}{2}$ with respect to the original $x(t)$ for its negative and positive frequencies, respectively. The amplitude remains unchanged along the frequency axis. Figure 1.7 represents the HT both in the time and frequency domains. It is interesting to note some properties of the Hilbert transform. The spectral representation of the analytic signal is somehow particular. A consequence of the multiplication between the complex unit and the phase shifts of the Hilbert transform is that the negative frequency content of the Fourier transform of the analytic signal vanishes. Further, the components on the positive frequency part are doubled compared to the Fourier spectrum of the initial signal $x(t)$. Note that this property enables another way of computing of the analytic signal. It is indeed that property that the `hilbert()` Matlab function uses for the computation of the whole analytic signal (not only its Hilbert transform as its name could suggest). The fact that the amplitude of the positive frequencies is doubled ensures the conservation of the energy of the signal. Figure 1.8 illustrates the one-sided feature of the spectrum of the analytic signal.

Aside from the convolution product (1.6) and its spectral characteristics (Figure 1.8), the Hilbert transform also possesses the following features:

Inverse Hilbert transform. We saw that the Hilbert transform shifts the signal with a phase lag of $\frac{\pi}{2}$. Then, applying twice the transform on a signal results in a phase opposition:

$$\mathcal{H}\left[\mathcal{H}\left[x(t)\right]\right] = -x(t).$$

The inverse transform is then easily obtained by:

$$\mathcal{H}^{-1} = -\mathcal{H}. \tag{1.7}$$

Differentiation. Being a linear operator, the Hilbert transform commutes with the derivative operator. This implies that the Hilbert transform of the derivative of a signal is equal to the derivative of its Hilbert transform:

$$\mathcal{H}\left[\frac{\mathrm{d}x(t)}{\mathrm{d}t}\right] = \frac{\mathrm{d}}{\mathrm{d}t}\mathcal{H}\left[x(t)\right]. \tag{1.8}$$

More generally, if we consider higher-order derivatives, it follows that:

$$\mathcal{H}\left[\frac{\mathrm{d}^k\, x(t)}{\mathrm{d}t^k}\right] = \frac{\mathrm{d}^k}{\mathrm{d}t^k}\,\mathcal{H}\left[x(t)\right]. \tag{1.9}$$

This property will be helpful when dealing with dynamical systems ruled by second-order equations of motion.

The Bedrosian product theorem. This theorem was demonstrated by Bedrosian in [16] and concerns the transformation of a product of functions. It states that if $f(t)$ and $g(t)$ are two functions characterized by a low and a high (but non overlapping) spectrum respectively, the low frequency signal can be pulled out from the transformation such that:

$$\mathcal{H}\left[f(t)\,g(t)\right] = f(t)\,\mathcal{H}\left[g(t)\right]. \tag{1.10}$$

The complex analytic signal now gains in interpretation if we write it in polar coordinates. Its modulus corresponds to the instantaneous amplitude $a(t)$, and its argument to the phase angle $\phi(t)$, such that

$$\begin{aligned} z(t) &= x(t) + i\,\tilde{x}(t) \\ &= a(t)\,e^{i\,\phi(t)}. \end{aligned} \tag{1.11}$$

According to this form, the signal can be represented as a rotating phasor in the complex plane and it is possible to define its instantaneous amplitude as its complex modulus, and its instantaneous frequency as the time derivative of its instantaneous phase angle [13]:

$$a(t) = |z(t)| \tag{1.12}$$

$$\omega(t) = \dot{\phi}(t) \tag{1.13}$$

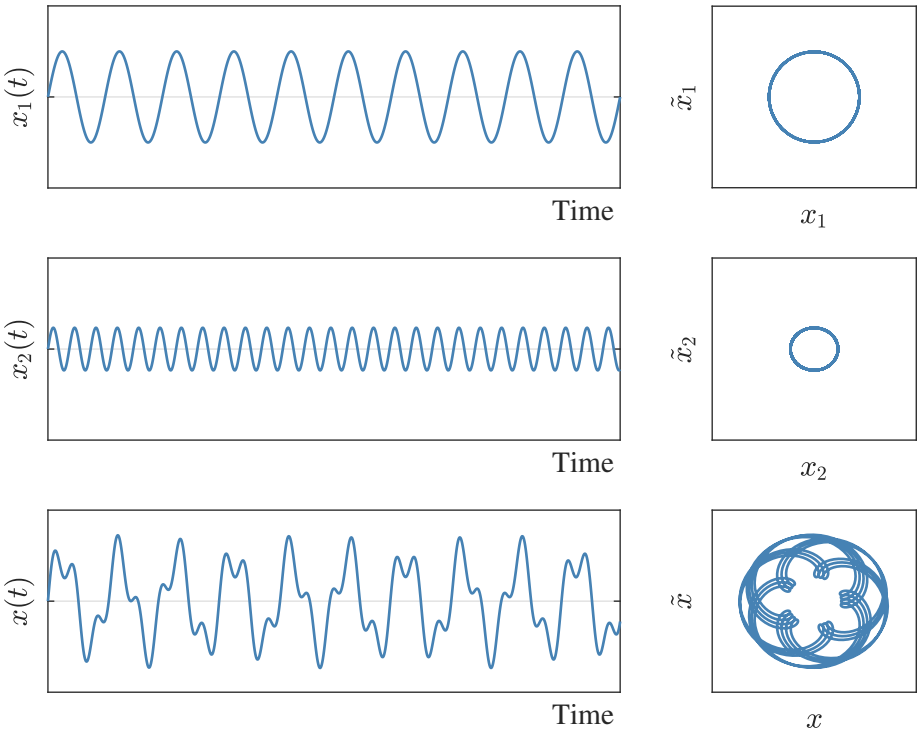

Figure 1.9: Signal composed of two different monocomponents.

Note also that from (1.11), the instantaneous frequency may alternatively be computed as:

$$\omega(t) = \frac{x(t)\,\dot{\tilde{x}}(t) - \dot{x}(t)\,\tilde{x}(t)}{a^2(t)} \tag{1.14}$$

$$= \mathrm{Im}\left[\frac{\dot{z}(t)}{z(t)}\right] \tag{1.15}$$

It is now possible to draw the amplitude with respect to time and frequency. Such a plot is called the Hilbert spectrum.

The definitions of $a(t)$ and $\omega(t)$ are pretty straightforward in the simple case of a simple oscillation signal with amplitude and/or frequency modulation, but what happens if the signal is composed of two or several components, each one with its own amplitude and frequency? Let us consider now an example with a compound signal $x(t)$ with two components: one of high amplitude and low frequency $x_1(t)$, and one of low amplitude and high frequency $x_2(t)$, as illustrated in Figure 1.9. The time signals are illustrated on the left side of the figure and the polar representation of their respective analytic signals on the right side. Note that for the sake of simplicity, the signal and its two components are taken stationary, but the following explanations remain valid for time-varying amplitudes and frequencies.

This simple example directly highlights that the definition of the instantaneous frequency when more than one component are present in the signal may loose its physical meaning. One may observe in Figure 1.10 that the instantaneous frequency of the composed signal does not correspond to any of the initial frequencies ω_1 or ω_2

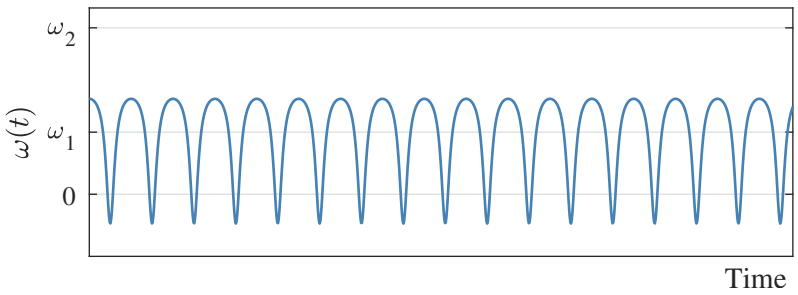

Figure 1.10: Instantaneous frequency calculated as the time derivative of the phase angle.

or a combination of them. Further, one may also see that the instantaneous frequency may be negative at some instants. These negative frequencies occur when the phasor representing the complex analytic signal rotates clockwise as shown in the last polar plot in Figure 1.9, the phasor drawing the small inside loops.

The fact that the instantaneous frequency looses its physical meaning when several oscillating components are present in the signal is an issue for the analysis of structural vibrations. Indeed, vibration data will usually contain more than one component. The use of the instantaneous frequency for modal analysis of time-varying systems will then need a preprocessing of the data to isolate each of the components before computing their own instantaneous frequency. This justifies the application of signal decomposition techniques, explained in the next section.

1.2 Signal decomposition methods

1.2.1 The Empirical Mode Decomposition (EMD) method and the Hilbert-Huang Transform (HHT)

As previously pointed out, the estimation of instantaneous frequencies is only valid for monocomponent signals. Some techniques were then developed to overcome this limitation. In 1998, Huang *et al.* [17] addressed that problem and developed the Empirical Mode Decomposition (EMD) method which is now commonly used in various fields of engineering, from mechanical monitoring [18] to the analysis of brain signals in bio-engineering [19]. The EMD method is data-driven and completely adaptive. It is able to decompose any nonlinear or nonstationary signal into a sum of basic monocomponents called Intrinsic Mode Functions (IMF). These mono-components are better suited for the application of the Hilbert transform and valuable information, such as the instantaneous frequency and amplitude, can be extracted. The whole process, *i.e.* EMD followed by the spectral analysis with the application of the Hilbert transform on each IMF, is named the Hilbert-Huang Transform (HHT).

The EMD method is based on a sifting process of the signal by an iterative extraction of each of its IMF component. According to Huang, an extracted component is

an IMF if it meets two conditions:

- when counting the number of extrema and zero-crossing of an IMF candidate, their difference must be at most equal to one. This simple condition will ensure that the candidate is a monocomponent.
- the mean value between the upper and lower envelopes of the IMF candidate must be zero. This condition preserves the IMF candidate to be asymmetric, which could deteriorate the further computation of its instantaneous frequency by the Hilbert transform.

The whole sifting process works as follows:

1. All the local maxima of the signal are located.
2. An empirical upper envelope is built by the cubic spline interpolation of all the maxima.
3. The same operation is performed to construct the lower envelope using the same approach with the local minima.
4. With the upper and lower envelopes, a mean envelope is calculated and subtracted from the signal. The mean envelope represents a slow oscillation signal.
5. Operation from 1. to 4. are repeated until the remaining signal corresponds to the definition of an IMF. Once it is the case the IMF, corresponding to the fastest oscillating component, is subtracted from the signal and the sifting process continues for the extraction of the other IMFs.

The process is illustrated in Figure 1.11. The minima and maxima are located and represented on the two-component signal by upper and lower triangles, respectively. The upper and lower envelopes constructed by spline interpolations are represented by the dashed red lines and the mean envelope by a solid black line.

1.2.2 The Hilbert Vibration Decomposition (HVD) Method

More recently, Feldman developed an alternative method to EMD to perform signal decomposition [20, 21]. His method, named Hilbert Vibration Decomposition (HVD), is designed to achieve the same goal: decompose nonlinear and/or nonstationary time series into its intrinsic monocomponents. However, the way to process the decomposition is quite different from the EMD method. The HVD method directly focuses on the analytic form of a given signal and especially on its frequency variation.

To illustrate the method, let us take again the two-component signal used to illustrate the EMD method in Figure 1.9. We have:

$$x(t) = x_1(t) + x_2(t) \tag{1.16}$$

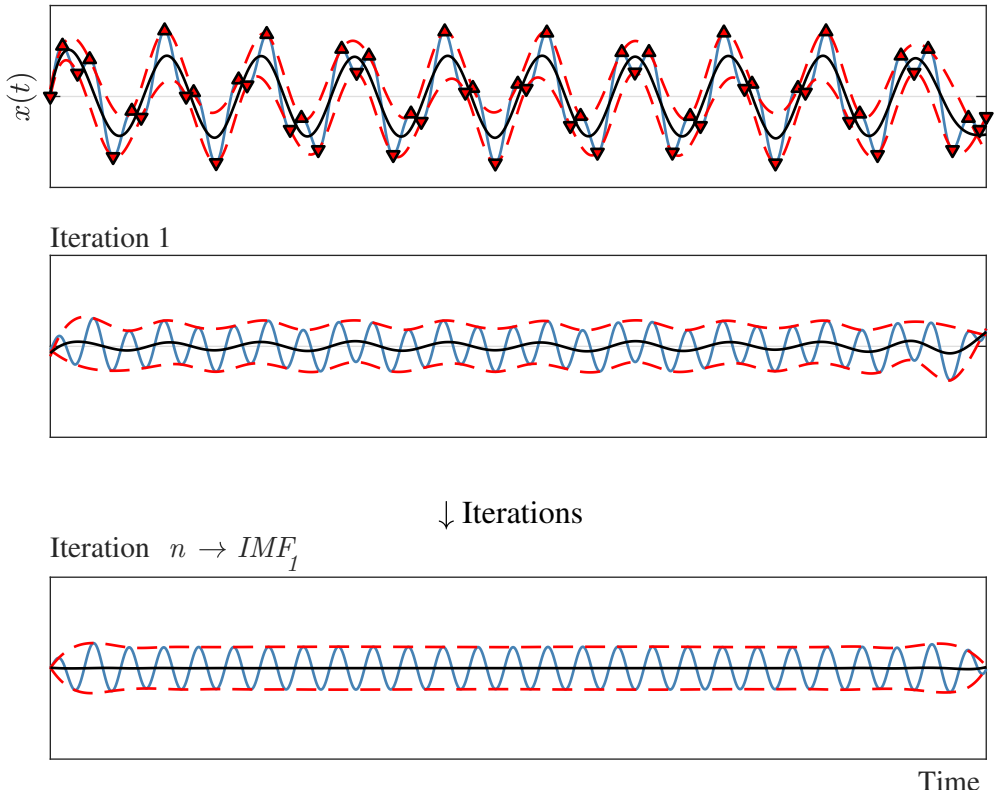

Figure 1.11: Illustration of the slow oscillation removal from the initial signal until only the fast oscillation component remains.

with $x_1(t)$ and $x_2(t)$ being the two components of the signal $x(t)$. Each of these components is defined by its amplitude and frequency $a_1(t)$, $\omega_1(t)$ and $a_2(t)$, $\omega_2(t)$, respectively. In the present case, we have $a_1(t) > a_2(t)$ and $\omega_2(t) > \omega_1(t)$. Remember that the amplitude and frequency of each monocomponent are kept constant for the illustrative example.

Let us compute the analytic signal corresponding to (1.16):

$$z(t) = z_1(t) + z_2(t). \tag{1.17}$$

The latter complex analytic signal writes in terms of amplitudes and complex exponentials:

$$\begin{aligned} z(t) &= z_1(t) + z_2(t) && (1.18)\\ &= a_1\, e^{i\phi_1(t)} + a_2\, e^{i\phi_2(t)} && (1.19)\\ &= a_1\, e^{i\omega_1 t} + a_2\, e^{i\omega_2 t} && (1.20) \end{aligned}$$

by expressing the instantaneous phase angle $\phi(t)$ by the time integration of the corresponding frequency ω. Computing the instantaneous amplitude and frequency of this

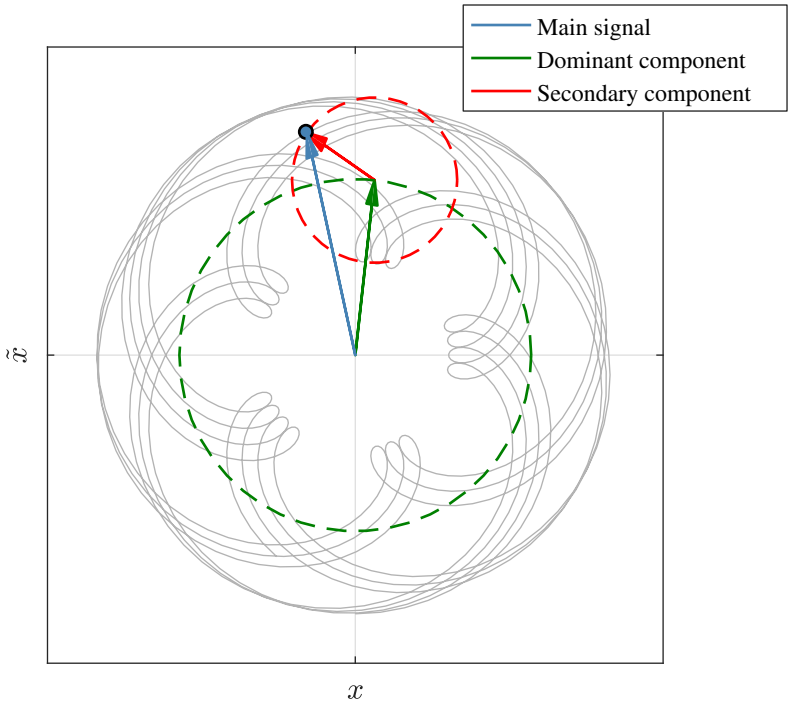

Figure 1.12: Trajectory in the phase plane (real versus imaginary part) of the analytic signal with two components. The gray track represents the trajectory of the combined signal and the green and red vectors represent the phasors of the two monocomponent signals.

compound signal gives:

$$a(t) = \left[a_1^2 + a_2^2 + a_1 a_2 e^{i(\phi_1(t)-\phi_2(t))} + a_1 a_2 e^{i(\phi_2(t)-\phi_1(t))}\right]^{\frac{1}{2}} \quad (1.21)$$

$$= \left[a_1^2 + a_2^2 + 2\, a_1 a_2 \cos\left(\phi_2(t) - \phi_1(t)\right)\right]^{\frac{1}{2}} \quad (1.22)$$

$$= \left[a_1^2 + a_2^2 + 2\, a_1 a_2 \cos\left((\omega_2 - \omega_1)t\right)\right]^{\frac{1}{2}} \quad (1.23)$$

$$\omega(t) = \omega_1 + \frac{(\omega_2 - \omega_1)\left[a_2^2 + a_1 a_2 \cos\left((\omega_2 - \omega_1)t\right)\right]}{a^2(t)} \quad (1.24)$$

Note that (1.23) corresponds to the modulated amplitude in the beating phenomenon when a signal is composed of a couple of component with close frequencies. One may also remark that the instantaneous frequency (1.24) is dominated by the frequency of the largest component, ω_1, and also features a variation due to the second term in (1.24) which depends on the difference between ω_1 and ω_2. Graphically, Figure 1.12 represents this signal in the complex plane, where the larger amplitude of the first component is clearly visible. The second component adds only smaller oscillations around the main trajectory. This behaviour was previously illustrated in Figure 1.10.

It can be shown that if the instantaneous frequency (1.24) is averaged over a well-chosen time window T, the second oscillating term of the instantaneous frequency

vanishes [21]:

$$\int_0^T \frac{(\omega_2 - \omega_1)\left[a_2^2 + a_1 a_2 \cos\left((\omega_2 - \omega_1)t\right)\right]}{a^2(t)} \mathrm{d}t = 0 \tag{1.25}$$

for

$$T = \frac{2\pi}{\omega_2 - \omega_1}.$$

From that observation, the averaging of the instantaneous frequency is a way to recover the frequency of the dominant component of the signal:

$$\int_0^T \omega(t)\mathrm{d}t = \omega_1 + 0. \tag{1.26}$$

This observation is also valid for monocomponents with varying amplitudes and frequencies, but provided that the time averaging on a period T is replaced by a low-pass filtering of the instantaneous frequency with an appropriate cutoff frequency. The identification of the instantaneous frequency of the largest component is a key step in Feldman's algorithm and is used for the subsequent operation, namely the extraction of the dominant component from the compound signal. This extraction in the HVD method is performed by a synchronous demodulation of the signal based on the identified varying frequency in order to obtain its corresponding envelope. In practice, if a signal is a mixture of several components such as :

$$\begin{aligned} x(t) &= \sum_l x_l(t) && (1.27)\\ &= \sum_l a_l(t) \cos\left(\int \omega_l(t)\mathrm{d}t + \phi_l\right) && (1.28) \end{aligned}$$

the aim of the synchronous detection is to recover the envelope $a_r(t)$ corresponding to the r^{th} component with a reference frequency $\omega_r(t)$. In the case of the HVD method, the reference frequency used for the demodulation of the frequency of the dominant component previously identified. To recover the amplitude $a_r(t)$, the signal is multiplied by two reference signals, in quadrature, and oscillating at the reference frequency. The two signal $\cos\left(\int \omega_r(t)\mathrm{d}t\right)$ and $\sin\left(\int \omega_r(t)\mathrm{d}t\right)$ may be used for that purpose. We have, for the component l:

$$\begin{aligned} x_l^{\cos}(t) &= a_l(t)\, \cos\left(\int \omega_l(t)\mathrm{d}t + \phi_l\right) \cos\left(\int \omega_r(t)\mathrm{d}t\right) && (1.29)\\ &= \frac{a_l(t)}{2}\left[\cos\left(\int \omega_l(t) - \omega_r(t)\mathrm{d}t + \phi_l\right)\right. \\ &\quad \left. + \cos\left(\int \omega_l(t) + \omega_r(t)\mathrm{d}t + \phi_l\right)\right] && (1.30) \end{aligned}$$

Similarly, we have

$$\begin{aligned} x_l^{\sin}(t) &= a_l(t)\, \cos\left(\int \omega_l(t)\mathrm{d}t + \phi_l\right) \sin\left(\int \omega_r(t)\mathrm{d}t\right) && (1.31)\\ &= \frac{a_l(t)}{2}\left[-\sin\left(\int \omega_l(t) - \omega_r(t)\mathrm{d}t + \phi_l\right)\right. \\ &\quad \left. + \sin\left(\int \omega_l(t) + \omega_r(t)\mathrm{d}t + \phi_l\right)\right] && (1.32) \end{aligned}$$

In the case where the component l equals the reference frequency ω_r, we have

$$x_{l=r}^{\cos}(t) = \frac{a_{l=r}(t)}{2}\left[\cos\left(\phi_{l=r}\right) + \cos\left(\int \omega_{l=r}(t) + \omega_r(t)\mathrm{d}t + \phi_{l=r}\right)\right] \quad (1.33)$$

$$x_{l=r}^{\sin}(t) = \frac{a_{l=r}(t)}{2}\left[-\sin\left(\phi_{l=r}\right) + \sin\left(\int \omega_{l=r}(t) + \omega_r(t)\mathrm{d}t + \phi_{l=r}\right)\right] \quad (1.34)$$

By an averaging operation (or equivalently lowpass filtering) on the two latter signals, the slow envelope corresponding to the reference frequency can be isolated:

$$\langle x_{l=r}^{\cos}(t)\rangle = \begin{cases} \dfrac{a_{l=r}(t)}{2}\cos\left(\phi_{l=r}\right) & \text{if } \omega_l(t) = \omega_r(t) \\ 0 & \text{if } \omega_l(t) \neq \omega_r(t) \end{cases} \quad (1.35)$$

$$\left\langle x_{l=r}^{\sin}(t)\right\rangle = \begin{cases} -\dfrac{a_{l=r}(t)}{2}\sin\left(\phi_{l=r}\right) & \text{if } \omega_l(t) = \omega_r(t) \\ 0 & \text{if } \omega_l(t) \neq \omega_r(t) \end{cases} \quad (1.36)$$

The amplitude and phase of the r^{th} component can finally be calculated as

$$a_{l=r}(t) = 2\sqrt{\langle x_{l=r}^{\cos}(t)\rangle^2 + \langle x_{l=r}^{\sin}(t)\rangle^2} \quad (1.37)$$

$$\phi_{l=r} = -\arctan\frac{\langle x_{l=r}^{\sin}(t)\rangle}{\langle x_{l=r}^{\cos}(t)\rangle} \quad (1.38)$$

The r^{th} component can now be fully computed and extracted from the initial signal following the same sifting process as in the EMD method. The process is iterated on the residual for the extraction of the next dominant component until no more oscillating component can be extracted from the signal.

1.2.3 Comparison between the EMD and HVD methods

In Sections 1.2.1 and 1.2.2, the processes of the EMD and HVD methods are explained to decompose a multicomponent signal in a sum of monocomponent ones. Even if they are similar (non-parametric, adaptive, iterative sifting), the result of the decomposition is not the same. First, it was shown that, from its construction, the EMD method decomposes a signal starting by its highest instantaneous frequency by the successive subtraction of the slow mean envelope. Conversely, the HVD method first extracts the component having the highest amplitude which drives the mean motion of the analytic signal in the complex plane. Both methods can be subject to some mode-mixing in the decomposition, meaning that each of the decomposed component, always being a monocomponent, could switch between different time scales. Let us mention some attempts to overcome this limitation such as the noise-assisted Ensemble Empirical Mode Decomposition (EEMD) method [22]. To summarize the main idea underlying this method, the decomposition is performed several times on a signal to which some noise is added. The envelopes are then computed as the average of all the computed envelopes. This is justified by the fact that the average of all the noise contributions

should be zero if a sufficient number of realizations is performed. The signal to added noise ratio has to be properly chosen to avoid the mode mixing.

In [23, 21], Feldman proposes an analysis and comparison of both the EMD and HVD methods. He first developed his analysis by classifying nonstationary signals into 3 different types.

Type I: This represents the simplest case. All the monocomponents of the signal are well separated (there is no crossing in amplitude and/or frequency) and smooth (their instantaneous characteristics vary slowly).

Type II: This is an intermediate case. The monocomponents remain well separated but can encounter fast variations of their envelope or instantaneous frequency.

Type III: This is the most complicated case. The monocomponents may have their envelopes or instantaneous frequency that cross each other.

Clearly, for type III signals, both methods fail because they will follow a dominant feature: the instantaneous frequency for the EMD method, and the instantaneous amplitude for the HVD method. In this case, the decomposition is not unique. Boashash suggests that the choice of the trajectory to follow depends on the application [24]. For types II and III, Feldman also recommends that a combination of the two methods can be used.

Figure 1.13 represents in a block diagram the two previous algorithms.

Feldman highlighted two other properties for which the HVD lightly outperforms the EMD method. He shows that HVD has a better frequency resolution than EMD. This means that HVD is able to separate components with closer frequencies than EMD. In the EMD method, the ability to separate two components essentially depends on their amplitude and frequency ratios. Conversely, in the HVD method, it is the cutoff frequency of the lowpass filter that defines the frequency resolution of the decomposition. Figure 1.14 shows the decomposition capabilities of the two methods [25]. He also estimates the number of oscillating components that could be extracted from a signal with the two methods. This number depends on their amplitude and frequency ratios but Feldman's conclusion is that the HVD method is able to extract a few more components than the EMD method. But in any case, this number of extractable components is rather limited.

1.3 Applications in mechanical vibration analysis

The previously introduced methods have been applied for the study of nonstationary time series, mainly in the field of nonlinear vibration identification, which increasingly has gained interest over the years. A non exhaustive review of their application is given in what follows. The Gabor transform, which is a particular STFT using a Gaussian

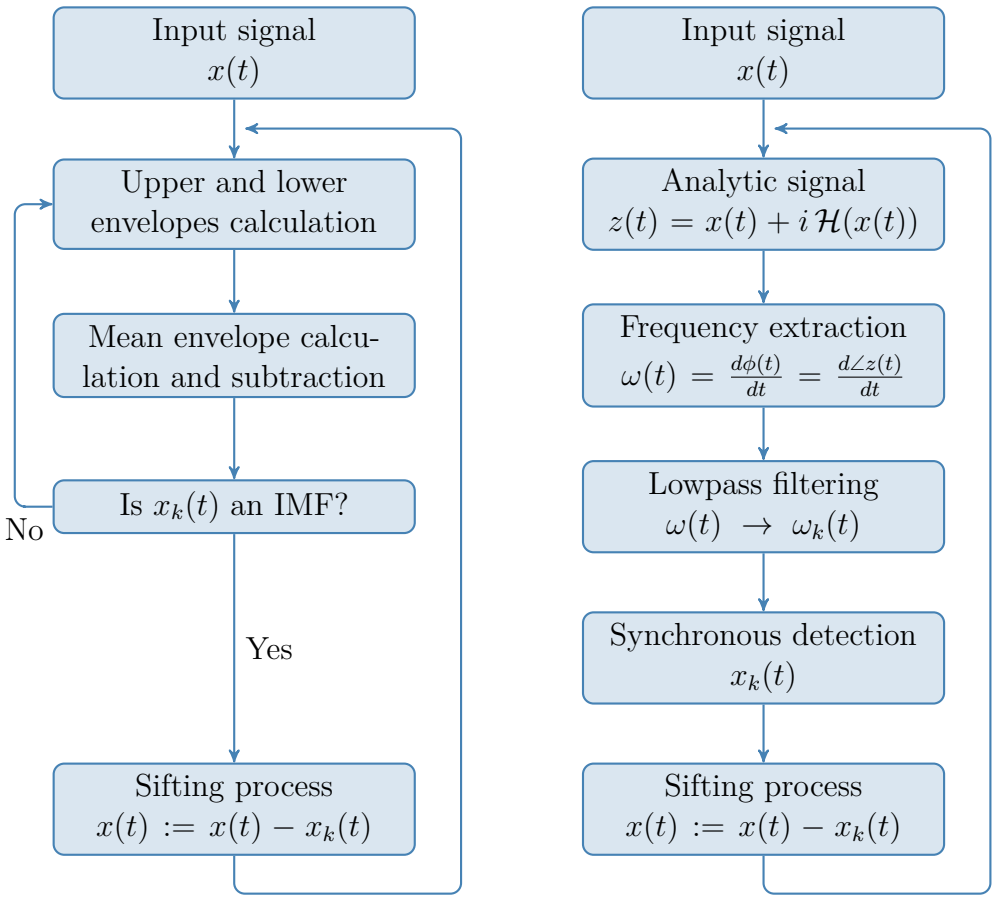

Figure 1.13: Comparative block diagram representations of the EMD (left) and HVD (right) methods.

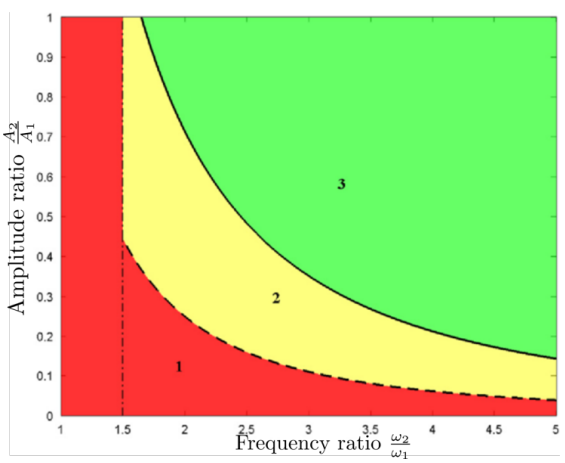

(a) EMD method. 1: Impossible decomposition. 2: Decomposition with several iterations. 3: Decomposition in one iteration.

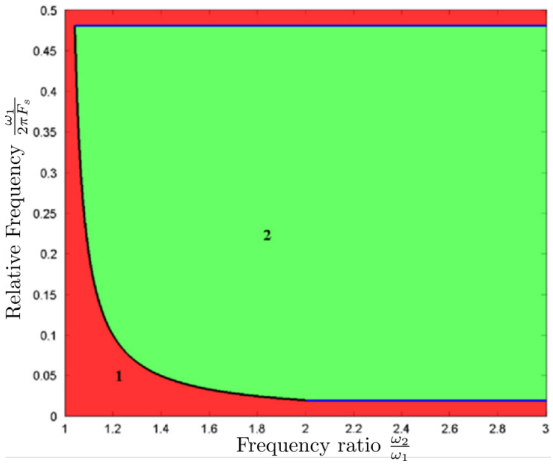

(b) HVD method. 1: Impossible decomposition. 2: Possible decomposition.

Figure 1.14: Illustration of the frequency resolution of both EMD and HVD methods [25].

window in (1.1), together with the HT were used in [26]. The Gabor transform is used first to separate quasi-harmonic component for a further analysis by the Hilbert transform to compute damping and restoring forces curves. The WT is also widely used in this topic. In [27], Staszewski used the WT to extract the instantaneous frequencies and amplitudes from impulse responses of single- and multi-degree-of-freedom systems. The amplitude-frequency relation estimates the backbone of the nonlinear mode which draws the locus of the nonlinear resonance peaks. Argoul and Le also used the WT for the study of the transient response of a nonlinear beam in [28]. The EMD, and more generally the complete HHT method, has also been used to consider the nonstationarity, such as the amplitude-dependent resonance frequency, of nonlinear vibration responses. In [29] and [30], Kerschen *et al.* and Vakakis *et al.* used the HHT method for the identification of the slow-flow dynamics of nonlinear systems. The HVD method is also used by Feldman in nonlinear identification. In [31, 32, 21], two methods named FREEVIB and FORCEVIB were developped for the nonparametric identification of nonlinear systems based on the Hilbert transform. As their names suggest, they work with free and forced responses and are able to draw the backbones and stiffness and damping curves. A comparison of STFT and WVD is also present in [33]. In [21], the FREEVIB and FORCEVIB methods were illustrated on various numerical problems but were also tested on an experimental structure [34, 21]. However, because the two latter methods require the knowledge of displacements, velocities and accelerations, the author warned the user of these techniques about the quality of his measurements to not drastically increase the inherent noise present in the experimental measurements by numerical derivative/integration.

In [35, 36], Staszewski explores the concept of time-varying FRFs through the use of the wavelet transform for time-varying systems. The concept is a generalization of the classical FRF (ratio between spectra) in which the wavelet transforms of the input and output data are used instead of the classical Fourier spectra to keep the time variation into account.

1.4 How to manage multiple output responses?

In most of the research works dealing with the analysis of time-varying systems, often only SDOF systems are considered or, if MDOF systems are studied, identification is performed on a single channel at a time. Further, the varying mode shapes are generally ignored in the studies. However, let us cite [37] in which Dziedziech *et al.* compute the mode shapes by the amplitude and phase on a series of wavelet-based time-varying FRFs. The first contribution of the present thesis is to go further in the analysis of time-varying system with nonparametric methods. The objective is to be able to deal with several measurement channels monitoring a time-varying system having multiple modes excited in the considered frequency band. As seen earlier, many of the previously mentioned methods deal with single channel measurements. In the case of a multichannel setup, one could apply these methods to all channels separately, but nothing ensures that the results will be close from one to another. Because of the spatial distribution of the experimental setup, all the channels are not submitted to the

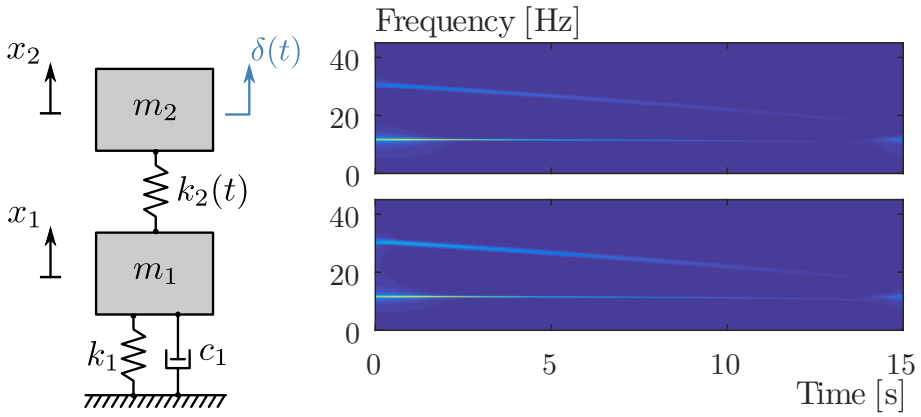

Figure 1.15: Simple 2 DOFs system submitted to an impulse.

same amplitude of vibration and it is also mode-dependent. A sensor close to a nodal point of a mode will not efficiently record its response because of its low amplitude at its location. Trying to identify this mode using only this channel would not be a good choice.

Further, we have also seen that the EMD and HVD methods are proned to mode mixing if the instantaneous frequencies or amplitudes of the constitutive monocomponents cross. For illustrative purpose, let us consider the simple 2 DoF system given in Figure 1.15. The system simply varies through its stiffness $k_2(t)$ that decreases linearly with time. The properties of the system are listed hereafter and the time-frequency free response of each DOF is shown on the right side of Figrure 1.15:

- $m_1 = 3$ kg;
- $m_2 = 1$ kg;
- $k_1 = 20000$ N/m;
- $k_2 = 25000 \searrow 5000$ N/m (linear decrease over the time span);
- $c_1 = 3$ Ns/m.

The system in its initial configuration has resonance frequencies of 10.9 and 29.9 Hz and damping ratios of 0.48 and 0.09 % for each of its modes, respectively. The system is submitted to a unit impulse at DoF x_2 and the response of the whole system is simulated during 15 seconds. A classical Newmark integration scheme is used for the time integration in which the stiffness matrix is updated at each time step to take into account the dependence of k_2 on time.

Applying the standard HVD method to the two channels separately leads to some undesirable behavior. On both channels, the first mode is the best excited and responds with the highest amplitude. But because of the difference in damping ratio, the amplitude of the first mode decreases faster and the response of the second mode becomes dominant at some time instants. Each time an intrinsic component becomes

dominant in the signal, the method targets it and a mode switching phenomenon occurs during the extraction process. Moreover, as it can be seen in Figure 1.16, the mode switching does not occur at the same time on each measurement channel, which makes the correction of these switches more difficult. When the frequency curve jumps from one mode to the other, the corresponding demodulated component also follows the jump.

In Figure 1.17, the extraction of each monocomponent with its instantaneous frequency and amplitude enable us to draw the Hilbert spectra of the responses. The figure well illustrates that the crossings occur at equivalent amplitudes between components.

This undesirable behavior is the first issue tackled in this work. The following sections present a method able to manage several sensor measurements and produce a single set of identified parameters. The idea is to upgrade the HVD algorithm by a preprossessing step based on Blind Source Separation (BSS) techniques.

1.4.1 Blind source separation techniques

In signal processing, source separation methods are used to recover initial signals, the *sources*, from a set of recorded signals assumed to be mixtures of the initial sources. They are usually nonparametric methods. A large variety of methods exists trying to separate them as much as possible based on decorrelation or independence. One can cite, among others, the Principal Component Analysis (PCA) (also known as Proper Orthogonal Decomposition (POD) or Karhunen-Loève transform (KLT)), the Smooth Orthogonal Decomposition (SOD), the Independent Component Analysis (ICA) and the Second-Order Blind Source Identification (SOBI). Some of these techniques have been already used in the field of structural dynamics. For example, the POD method was studied in [38] by Kerschen or in [39] by Han with an interest in the relation between the proper orthogonal modes and the mode shapes of the system. In a similar way, Chelidze applied the SOD to dynamical systems for modal analysis purposes [40]. The ICA and SOBI methods were also employed in modal analysis by Poncelet [41, 42] with a validation with the Stochastic Subspace Identification (SSI) method. The main properties of the latter blind source identification methods are recalled hereafter.

The principle of blind source separation methods is to assume that the recorded signals are composed of a mixture of original source signals. A mathematical description of this mixture is as:

$$\boldsymbol{x}(t) = \boldsymbol{A}\,\boldsymbol{s}(t) \tag{1.39}$$

where $\boldsymbol{A}$ is the $p \times q$ mixing matrix and $\boldsymbol{s}(t)$ the q-variate source signals. One will assume in a first time that the $\boldsymbol{A}$ matrix is square ($p = q$). Equation (1.39) recalls the well-known principle of modal expansion in modal analysis theory in which the mixing matrix would represent the mode shape matrix and the sources the normal coordinates. All the BSS methods differ in the way to compute the latter mixing matrix, which also impacts the properties owned by the computed sources. Note two indeterminations in the methods. Looking to Equation (1.39), it is straightforward that the scaling of the

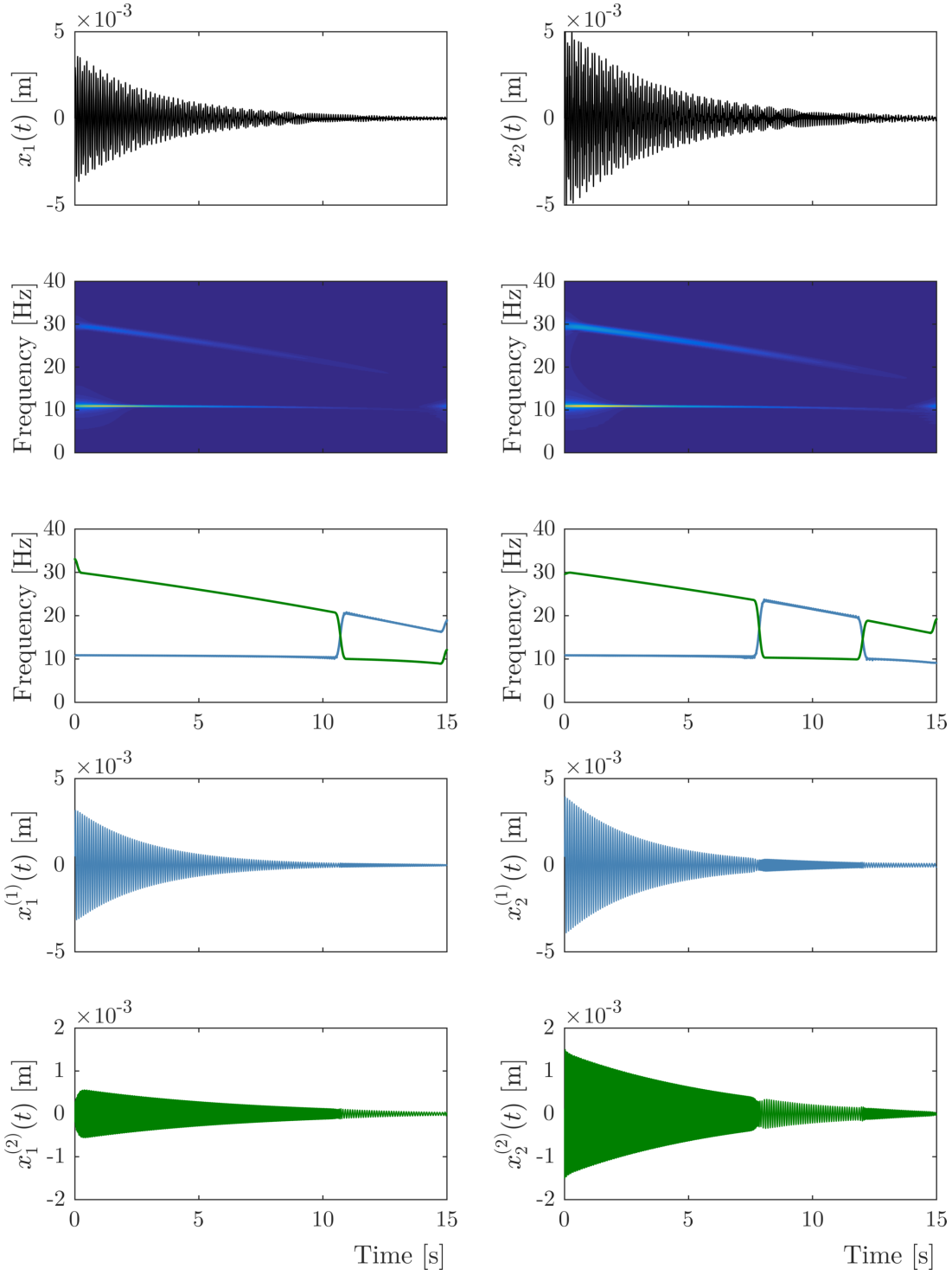

Figure 1.16: Time responses and extracted instantaneous frequencies and components. First row: time response of each DoF. Second row: Wavelet plots of each response. Third row: identified instantaneous frequencies for each DoF by the HVD method. Fourth and fifth rows : monocomponents corresponding to the each identified instantaneous frequencies.

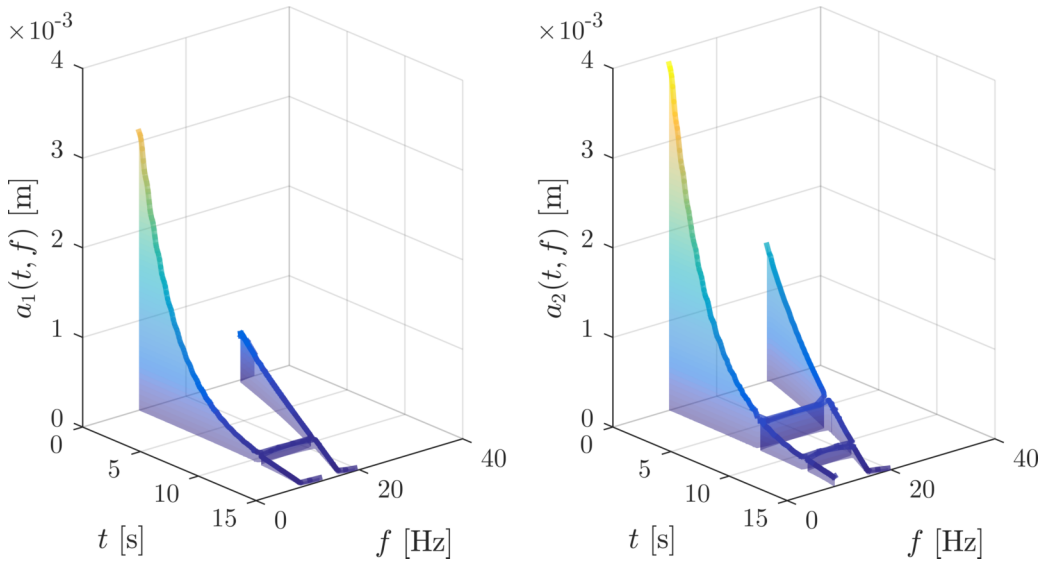

Figure 1.17: Hilbert spectra of each components after the decomposition by the HVD method.

modes in the mixing matrix and the sources is unknown because both $\boldsymbol{A}$ and $\boldsymbol{s}(t)$ are to be determined. Scaling a mode by a factor α and a source by a factor $1/\alpha$ gives the same result. Second, the decomposition is also not sensitive to the permutation of the modes and sources in the decomposition (permutation of the columns in $\boldsymbol{A}$ and rows in $\boldsymbol{s}(t)$. We will later see that those indeterminations do not have importance in the way the sources will be used. More details about blind source separation methods are given in Appendix A.

Of course, all the these source separation methods are based on the assumption that the mixing matrix in Equation (1.39) is independent of time. In case of time-varying systems this property is not met anymore but the targeted goal here is not to perform a perfect nonstationary source separation but an approximated one in which each source is dominated by the response of one mode and completed by lower amplitude subcomponents from the other modes. Such kind of signals (dominant component plus other dominated components) are well convenient for the identification of instantaneous frequency using the HVD method. Moreover, each source gathers information from all the measurement channels. This is also useful in the case when a mode is absent or weakly present in one measurement channel, as it could be the case if the sensor is located close to a node of vibration. Performing the identification on this single channel would miss that mode.

As an illustrative example, let us take again the 2-DoF system of Figure 1.15. By applying source separation to the two responses, the separated sources meet the conditions for a good instantaneous frequency estimation by the HVD method. Even the simple PCA method gives here sources continuously dominated by a single mode and the mode mixing previously observed is not present anymore. Figure 1.18 represents the decomposition with the BSS preprocessing. On the left column of Figure 1.18, the first source $s_1(t)$ from the PCA decomposition is dominated by the lower frequency mode. The extraction of its frequency is then performed and the corresponding com-

ponent is extracted from the two channels. The same operation is performed on the source $s_2(t)$ dominated by the second mode and here again, the second component is properly extracted. As previously, the Hilbert spectra can be represented for the two channels without the mode mixing. This is shown in Figure 1.19, to be compared with Figure 1.17.

This illustrative example shows how the BSS preprocessing works on a simple example. In more complicated problems, the philosophy remains the same but the BSS is applied at each iteration step of the HVD algorithm, after each component extraction. This facilitates the extraction of all the modes if their number is higher than the number of measurement channels.

1.4.2 Additional improvements to the HVD work flow

Besides the previously described preprocessing step based on blind source separation, two other improvements are brought to the initial algorithm. First, because the goal of the research is to deal with experimental data, the pollution of the experimental measurements by noise is unavoidable. In the original HVD algorithm (Figure 1.13), the phase of the analytic signal is extracted, derived to get the instantaneous frequency and then lowpass filtered to extract the instantaneous frequency of the dominant component. The later instantaneous frequency is finally integrated in the step of synchronous detection (Equations (1.35) and (1.36)). This is not a problem when dealing with numerical data but in the presence of noise, this causes noise amplification. Feldman warn the users of its FREEVIB and FORCEVIB methods about the measurment noise because these methods also require first and second derivative of the response signals [21]. It is decided here to only work with the phase signal. Looking back to Figure 1.12, the phase angle of the analysis signal is dominated by the phase angle of the dominant component (green arrow). The other subcomponent(s) of lower amplitude add(s) some oscillations around the dominant phase angle. This is also shown in Figure 1.20. Following the same idea as for the instantaneous frequency, lowpass filtering the phase angle makes vanish the oscillations due to the subcomponents and retains only the main trend corresponding to the dominant component. Besides the lowpass filtering procedure one also may use methods specifically designed in that way. In the econometric field, the problem of separating cycle oscillations from a global trend is a pretty common task. Two techniques are implemented here for this purpose: the Hodrick-Prescott filter (HPF) and the Singular Spectrum Analysis (SSA).

The Hodrick-Prescott filter: The HPF was proposed by Hodrick and Prescott in [43] for the analysis of economics time series. The basic assumption behind this filter is that a given signal, here the phase $\phi(t)$, is made up of a global trend, $\tau(t)$, some oscillating component, the cycle $c(t)$ and some noise $n(t)$:

$$\phi(t) = \tau(t) + c(t) + n(t) \tag{1.40}$$

This behavior of signal is exactly what we are faced if looking the the growing phase of a multicomponent signal, it is why it can be a substitute to the simple

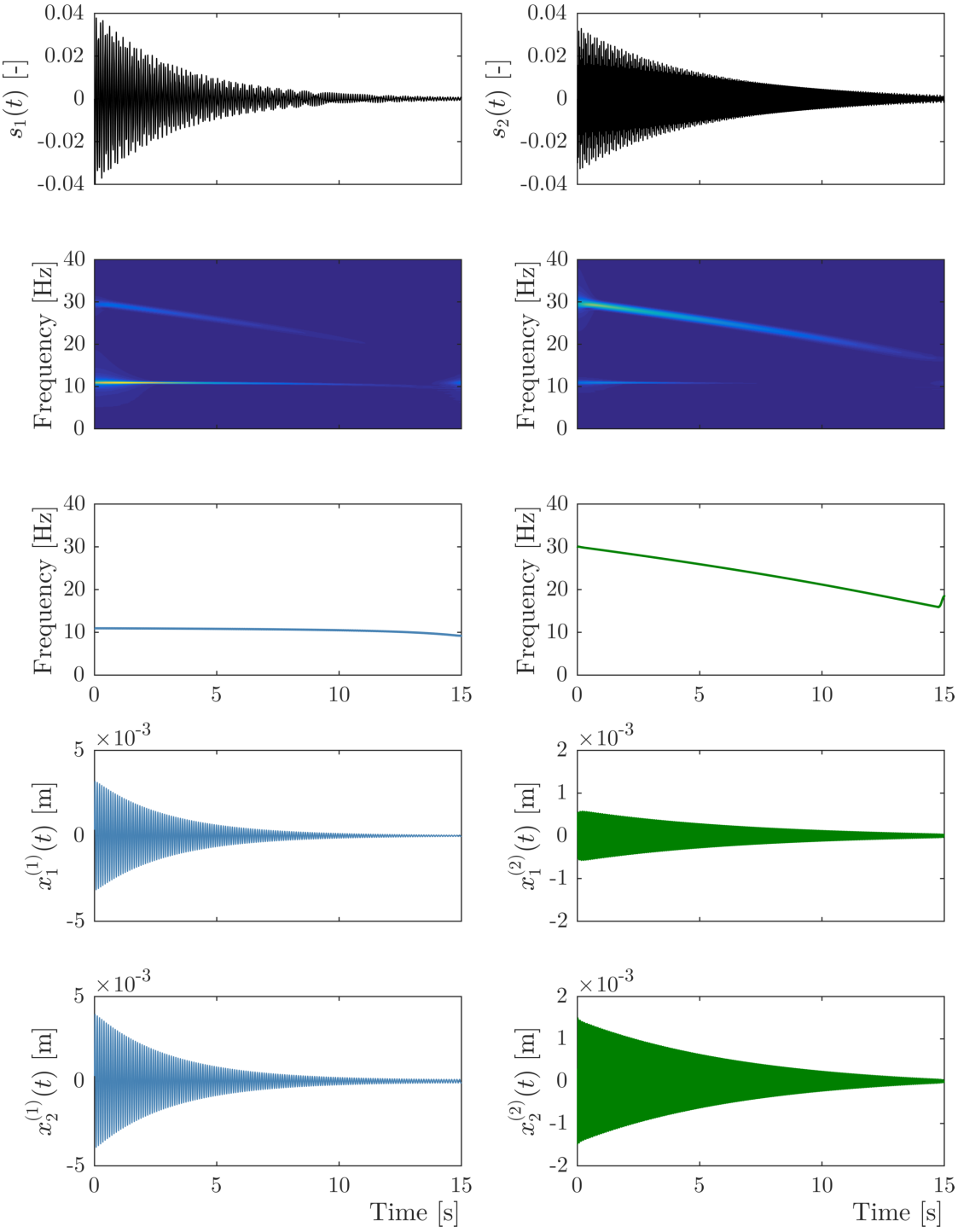

Figure 1.18: Application of the PCA blind source decomposition and extraction of the instantaneous frequency of their dominant component. First row: time evolution of each source. Second row: Wavelet plots of each source. Third row: identified instantaneous frequency of the dominant component. Fourth and fifth rows : monocomponents corresponding to the identified instantaneous frequencies in each channel.

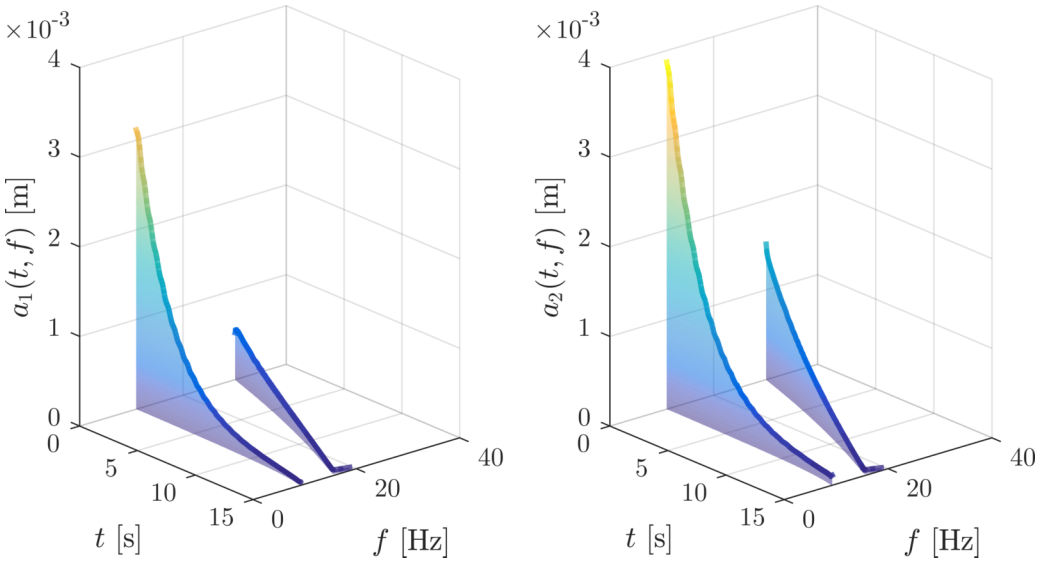

Figure 1.19: Hilbert spectra of each components after the decomposition by the HVD method preceeded by the source decomposition.

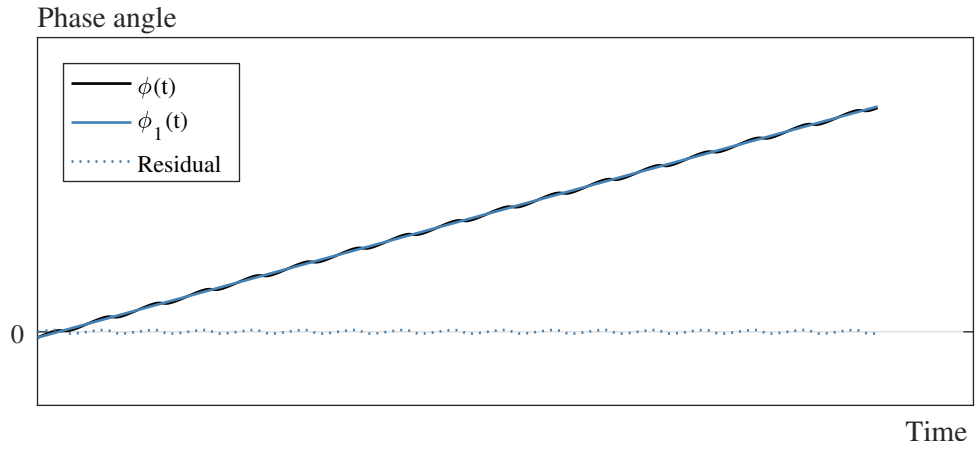

Figure 1.20: The phase angle of a multicomponent analytic signal dominated by the phase of the dominant component.

lowpass filter. In the Hodrick-Prescott method, the trend, $\tau(t)$, is found by solving an optimization problem :

$$\min_{\tau} \left[\sum_{t=1}^{T} \left(\phi(t) - \tau(t)\right)^2 + \lambda \sum_{t=2}^{T-1} \left[(\tau(t+1) - \tau(t)) - (\tau(t) - \tau(t-1)) \right]^2 \right]. \quad (1.41)$$

The first term penalizes strong deviations from the trend and the second penalizes fast variations of the trend. Indeed, the second term represents the square of the discrete second derivative of the trend. Finally, the smoothing parameter λ tunes the smoothness of the trend and replaces the cut-off frequency of the lowpass filter. The larger the λ value, the smoother the trend. The limit case is $\lambda \to \infty$ which gives as solution the least square linear fit of the curve.

The Singular Spectrum Analysis (SSA): The SSA method is another nonparametric decomposition method able to decompose a signal between a global trend, oscillating components and structureless components. It is used here in the same goal as the HP filter to extract the trend of the phase signal as the phase of the dominant component plus oscillating components. It was initially used by Broomhead and King for the analysis of nonlinear physical systems [44] but is also widely used in economics for its separation capabilities. The algorithm of the method is based on four steps: embedding delayed data in a trajectory matrix, the decomposition of the trajectory matrix, a grouping step and the reconstruction of the desired part of the signal. Let us illustrate the method on the phase signal represented in Figure 1.20:

1. First, the phase data $\phi(t)$ are embedded in a so called trajectory matrix by choosing a window length L and considering time lagged parts of the signal:

$$\boldsymbol{T} = \begin{bmatrix} \phi(1) & \phi(2) & \phi(3) & \cdots & \phi(L) \\ \phi(2) & \phi(3) & \phi(4) & \cdots & \phi(L+1) \\ \phi(3) & \phi(4) & \phi(5) & \cdots & \phi(L+2) \\ \vdots & \vdots & \vdots & \ddots & \vdots \\ \phi(N-L) & \phi(N-L+1) & \phi(N-L+2) & \cdots & \phi(N) \end{bmatrix} \quad (1.42)$$

2. The decomposition step is performed by a SVD decomposition of the trajectory matrix $\boldsymbol{T}$ in the same way as the PCA method for source separation:

$$\boldsymbol{T} = \boldsymbol{U}\,\boldsymbol{\Sigma}\,\boldsymbol{V}^T. \quad (1.43)$$

3. The grouping procedure gather a subset of $n < L$ decomposed singular values and left and right vectors as

$$\boldsymbol{T}_{gp} = \boldsymbol{T}_1 + \boldsymbol{T}_2 + \cdots + \boldsymbol{T}_n \quad (1.44)$$

in which each $\boldsymbol{T}_i$ is a rank one matrix of the same size as the trajectory matrix and is computed with the i^{th} singular triplet

$$\boldsymbol{T}_i = \boldsymbol{u}_i\,\sigma_i\,\boldsymbol{v}_i^T. \quad (1.45)$$

4. The final reconstruction step is to recover a signal from the grouped matrix $\boldsymbol{T}_{gp}$. This is done by a diagonal averaging the recombined trajectory matrix. Looking to the Hankel form of (1.42), the reconstructed signal is obtained computing the average value on each ascending diagonal of $\boldsymbol{T}_{gp}$.

Note also that in the decomposition, the oscillating components are represented by pairs of equal magnitude singular values. It is then also possible to use the SSA method in the source decomposition preprocessing part. A special utility is in the case where only one channel of measurements is provided. The SSA method then acts as a single channel source decomposition method and can also prevent mode mixing into the following HVD processing.

The second improvement concerns the extraction of the monocomponents based on their instantaneous frequency. In the previously described HVD algorithm, the extraction of each component is performed through synchronous detection. We choose here to perform the extraction with another method, the Vold-Kalman Filter (VKF). The VKF was initially presented in [45] by Vold and Leuridan for order tracking purposes in rotating devices. The goal of the method is to extract components based on prior knowledge. For example, in order tracking applications, the input information is the rotation speed, in rounds per minute (RPM), that can be measured using a tachometer. It is essentially a bandpass filter able to extract a component with a varying frequency. Further, it is also able to extract multiple components at once if several inputs are provided. In order tracking, it is possible to extract the main component at the rotation speed but also its harmonics (higher orders) which are of great importance too. This property is interesting in our case. In the proposed modified version of the HVD method, the monocomponents are jointly extracted at each iteration based on all the previously identified instantaneous frequencies. This is a great advantage in the case of the extraction of closely spaced or, event worst, crossing frequencies.

The Vold-Kalman filter is made up with a couple of equations, namely the *data equation* and the *structural equation*. Firstly, the data equation models the signal similarly to what is obtained by the Hilbert transform. Indeed, the signal $x(t)$ is assumed to be composed of a sum of oscillating phasors modulated by a time-varying complex amplitude:

$$x(t) = \sum_k a_k(t)\, e^{i\,\phi_k(t)} + n(t) \tag{1.46}$$

The aim of the method is to recover the complex amplitude of each component based on their phase information. Secondly, the structural equation brings some structure in the identification process by imposing a smoothness constraint. This is done through the minimization of the rate of variation of the extracted amplitudes. The result of the extraction is the solution that minimizes quantities from the data and structural equations:

$$x(t) - \sum_k a_k(t)\, e^{i\,\phi_k(t)} = \varepsilon(t) \tag{1.47}$$

$$\nabla^p a_k(t) = \varepsilon_k(t) \tag{1.48}$$

The first equation obviously minimizes the distance between the actual signal and its reconstruction by the sum of all the extracted components. In the second equation, the ∇^p operator represents the difference operator of order p such as

$$\begin{aligned}
\nabla^1 a_k(t) &= a_k(t) - a_k(t+1) && (1.49)\\
\nabla^2 a_k(t) &= a_k(t) - 2a_k(t+1) + a_k(t+2) && (1.50)\\
\nabla^3 a_k(t) &= a_k(t) - 3a_k(t+1) + 3a_k(t+2) - a_k(t+3) && (1.51)\\
&\vdots
\end{aligned}$$

for the operators up to the third order. The practical implementation details of the VKF algorithm can be found in [46] or [47] for example, together with the introduction of a regularizing parameter. The latter regularizing parameter, that can also be time-dependent, is closely related the the -3dB bandwidth around the provided time-varying frequency of the component to extract. Note that because of the introduction of complex numbers in Equation (1.46), the obtained amplitudes $a_k(t)$ are in fact the complex envelope of each component $x_k(t)$. Because the recorded signals are real-valued ones, the k^{th} component $x_k(t)$ is simply obtained as the real part of $a_k(t)e^{i\phi_k(t)}$.

The first benefit of the combined extraction of the monocomponents is illustrated in Figure 1.21. The illustrative signal is the same as the one previously used in Figure 1.6, *i.e.* a combination of a sine sweep and a constant frequency component. In Figure 1.21(a), each component is extracted separately based on the knowledge of its (time-dependent) frequency. In the vicinity of the crossing between the two frequencies, the two components interfere and their instantaneous amplitudes are not accurate. Conversely, if the two components are jointly extracted, the separation can be done properly and the extracted amplitudes are good as illustrated in Figure 1.21(b).

The second advantage of the extracted amplitudes with the VKF algorithm is that they are complex-valued envelopes. This means that they have a real amplitude and a phase shift with respect to the complex exponential used for the extraction in Equation (1.46). This valuable couple of information, amplitude and phase, can be used for the approximation of the varying mode shapes of the system by combining all the complex envelopes extracted from all the measurement channels based on the same instantaneous frequency information. The similarity with the modal expansion of linear systems is evident and the complex envelopes obtained in that way may be assimilated to "time-varying unscaled mode-shapes":

$$\begin{array}{rcccc}
\text{Vold-Kalman filter:} & \boldsymbol{x}(t) = \sum_k & \boldsymbol{a_k}(t) & e^{i\,\phi_k(t)} \\
 & & \updownarrow & \updownarrow \\
\text{Modal expansion:} & \boldsymbol{x}(t) = \sum_k & \boldsymbol{v_k}(t) & \eta_k(t)
\end{array} \qquad (1.52)$$

in which $\eta_k(t)$ is the modal coordinate of the k^{th} mode in the modal expansion.

Strictly speaking, it would be better not to speak of mode shapes but rather to "modal deflection shapes" by analogy with the concept of Operational Deflection Shapes (ODS) [48]. The mode shapes of a structure are only defined in the case of linearity and time-invariant assumptions and are the spatial solution of the differential

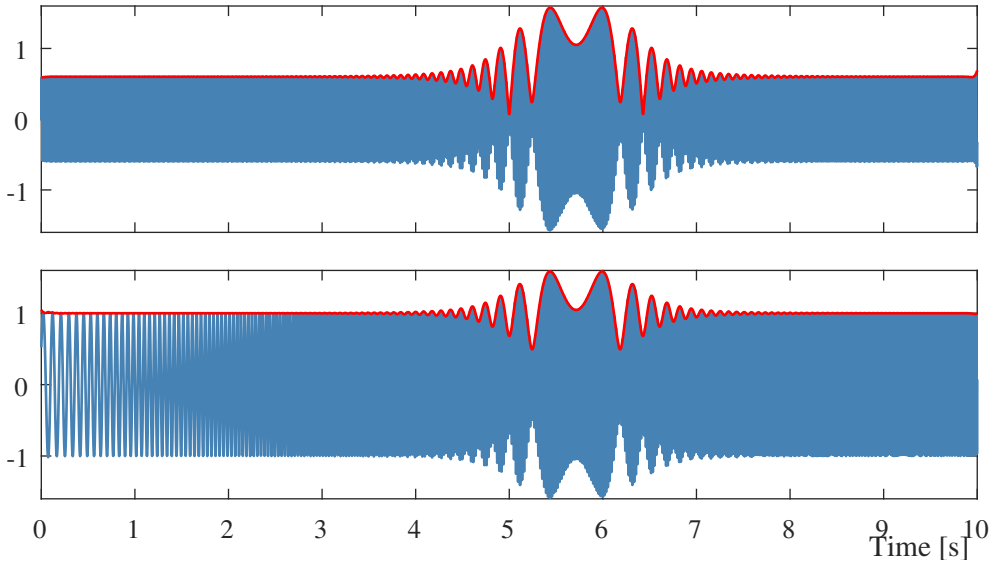

(a) Separated extraction of the components with respect to each instantaneous frequency.

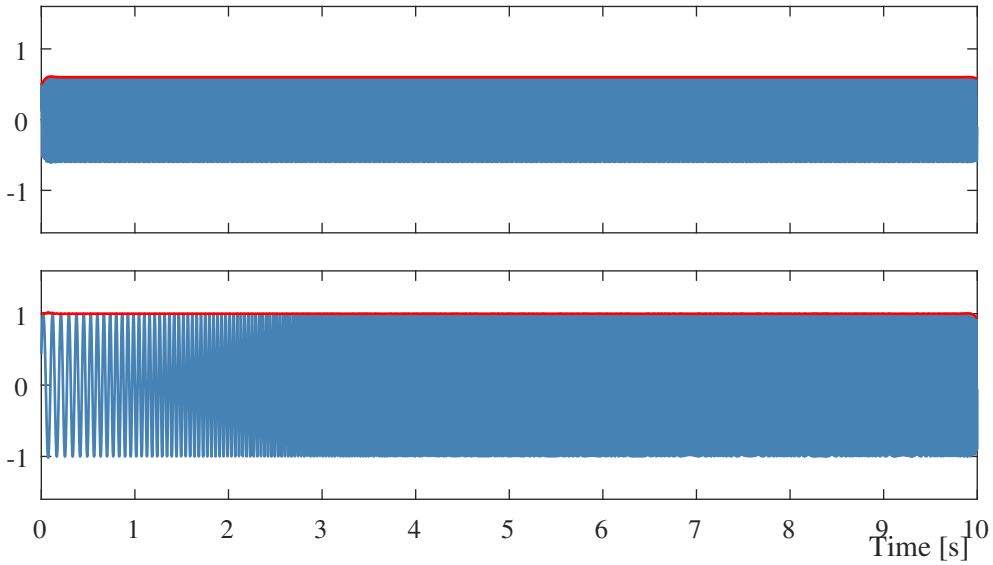

(b) Combined extraction of the components with respect to each instantaneous frequency.

Figure 1.21: Comparison between separated and combined extraction of components. The combined extraction is not perturbed by the interaction between the two components in the vicinity of the crossing of their frequency.

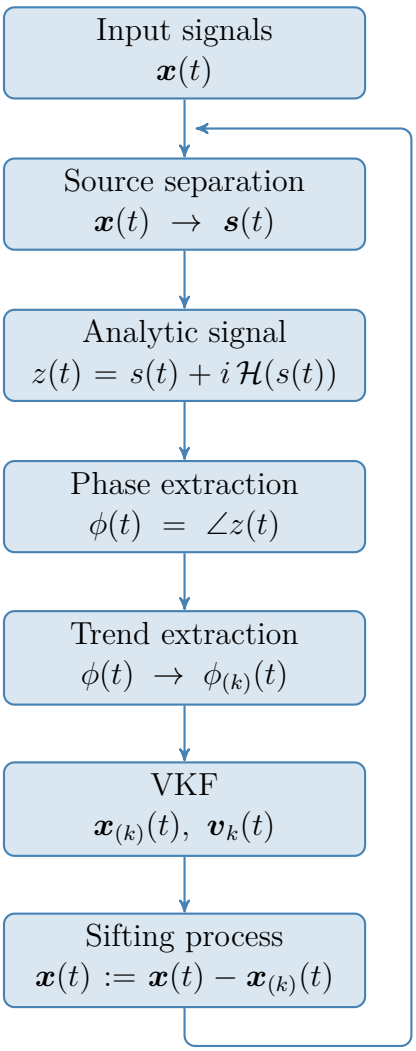

Figure 1.22: Flowchart of the modified HVD method.

motion equation. Conversely, the ODS can be computed in non stationary conditions. By definition, they represent the spatial deformation of the structure under some loading in contrast to the mode shapes that are inherent properties of the structure. If the ODS is computed at (or very close to) a resonance frequency, the ODS is highly dominated by the corresponding mode shape and it is a good approximation of it [48, 49].

The new modified algorithm of the HVD method is represented in the flowchart shown in Figure 1.22.

1.5 Application to a laboratory test structure

In order to test the performance of the presented method, it is tested on experimental measurements from the laboratory structure. The experimental setup studied in this work is a mass-varying system shown in Figure 1.23. It is made up of a doubly supported beam on which a mass is moving, just like a bridge with a varying traffic

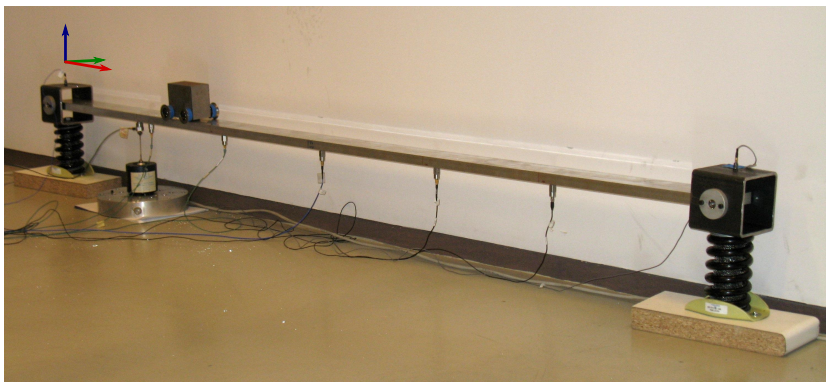

Figure 1.23: Picture of the experimental time-varying laboratory structure.

load [50, 5]. The beam is a 2.1-meter long aluminum beam weighting approximately 9 kilograms. The moving mass is a 3.5-kilograms block of steel mounted on small wheels. The ratio between the masses of the two parts is high enough (38.6%) to observe a significant change in the dynamic properties of the system depending on the position of the mass. The whole system is supported by springs in order to put the excitation and monitoring system.

1.5.1 Time invariant identification of the beam subsystem

To start the identification of the system, the supporting beam is first tested in linear time invariant conditions. This preliminary identification is performed to get a reference solution.

In this identification, we focus on the first five bending modes of the beam. To this purpose the structure is instrumented with seven accelerometers located on the neutral axis of the beam. A shaker is also mounted beneath the structure in order to excite it with a random force. The random excitation is chosen to have all the modes continuously excited during the measurement. The measurement sensors are located at coordinate $x = \{0, 0.4, 0.7, 1.05, 1.4, 1.7, 2.1\}$ m, the reference frame being located at the left hand side of the beam. The shaker is located under the second position, at 0.4 m. The excitation and the structural responses are measured using a *LMS SCADAS Mobile* [51] data aquisition system and all the signal processing and the identification are performed in the LMS Test.Lab software [52]. The modal identification is performed using the *PolyMAX* frequency domain method [53]. The result is summarized in the stabilization diagram of Figure 1.24. The five first modes are given in Table 1.1 with their frequency, damping ratio and mode shape.

1.5.2 Identification of the system with the moving mass

In this section, the dynamics of the beam loaded by the traveling mass is examined. To this end, the mass is slowly pulled by hand with a string attached to it. It moves along the beam while the latter is excited by a random force. In order to have a first idea of

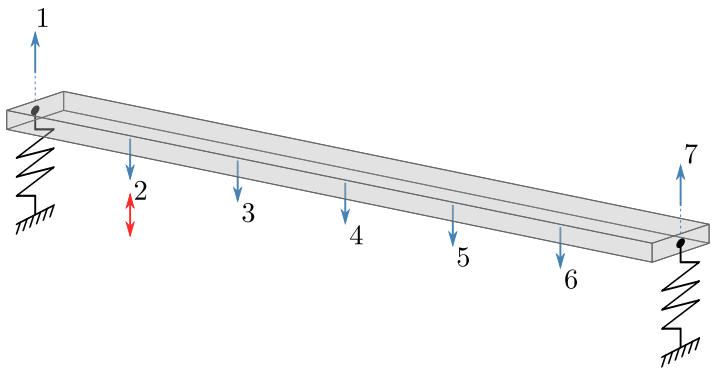

Figure 1.24: Scheme of the excitation-measurement setup.

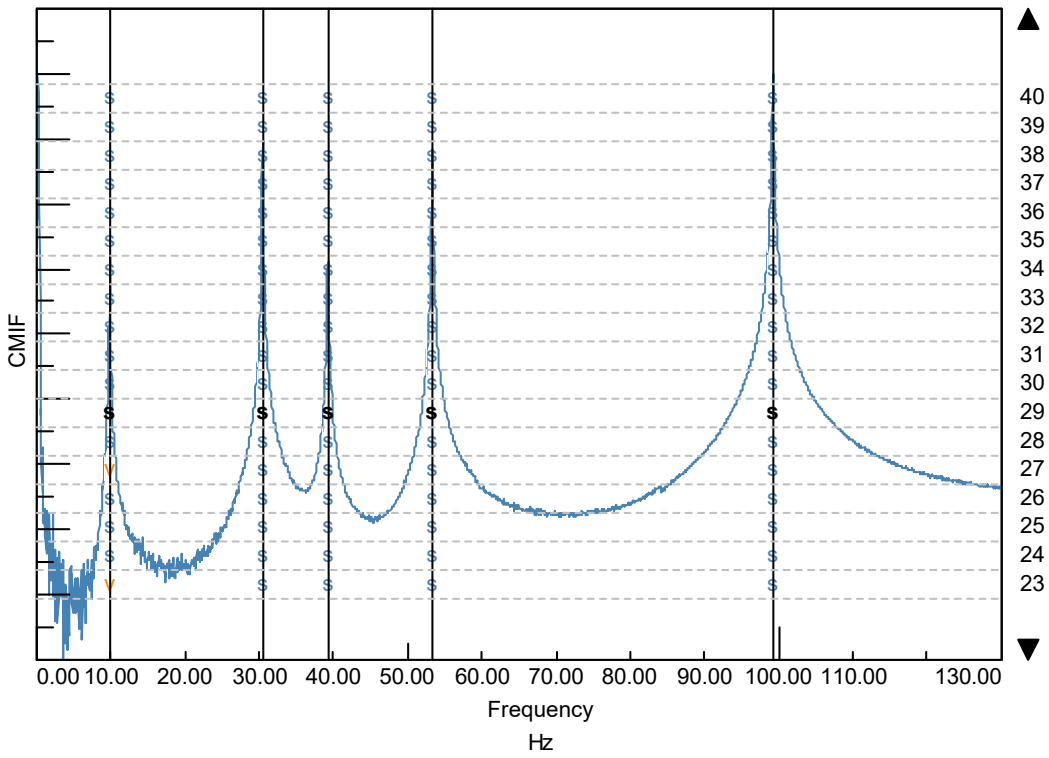

Figure 1.25: Stabilization diagram obtained using the PolyMAX identification on the reference beam.

Mode #	Frequency f_r [Hz]	Damping ratio ζ_r [%]	Mode shape
1	9.80	0.22	
2	30.43	0.10	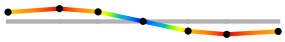
3	39.23	0.20	
4	53.32	0.08	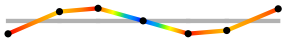
5	99.22	0.07	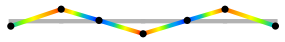

Table 1.1: Modal parameters of the reference structure.

the time-varying dynamics of the system, the wavelet spectra of the second sensor (at 0.4 m) is given in Figure 1.26.

In Figure 1.26, several properties can be observed. First, it appears that the first mode (close to 10 Hz) is not significantly excited in the response. The modes that are most excited are the second, forth and fifth modes due to the location of the shaker. Second, the frequency variation due to the motion of the mass is clearly visible. It appears as variations with top values very close to the natural frequencies of the unloaded beam. In the measurement process, the mass was pulled at an approximately constant speed so that the time axis can be broadly assimilated to the longitudinal axis of the beam. For each mode in Figure 1.26 the frequency oscillates between minimum and maximum values and if we compare with the mode-shapes shown in Table 1.1, we can easily see that the time instants at which the frequency comes back to the natural frequency of the unloaded beam correspond to the time instants when the mass is located to a node of vibration of the structure. In that configuration, the mass does not participate anymore to the mode so that it has the same properties as the initial one. On the contrary, when the mass is located at an anti-node of vibration, its participation to the system inertia forces is maximum and the frequency decay is maximum. The last thing that can be observed is that the higher the frequency is, the more important the perturbation due to the mass is.

Extraction of instantaneous frequencies and components

The modified version of the HVD method presented earlier is then applied on all the measurement data to perform the identification.The first step is to apply the source separation technique (the SOBI method is considered here) on all the channels. In Section A, it was highlighted that the separation of the sources with the SOBI method (as for the ICA method) owns an indeterminacy about the extraction order of the mode-source pairs. Due to this indeterminacy, a choice has to be done at each iteration of the method to select the source to consider. The choice we do here is based on the analysis

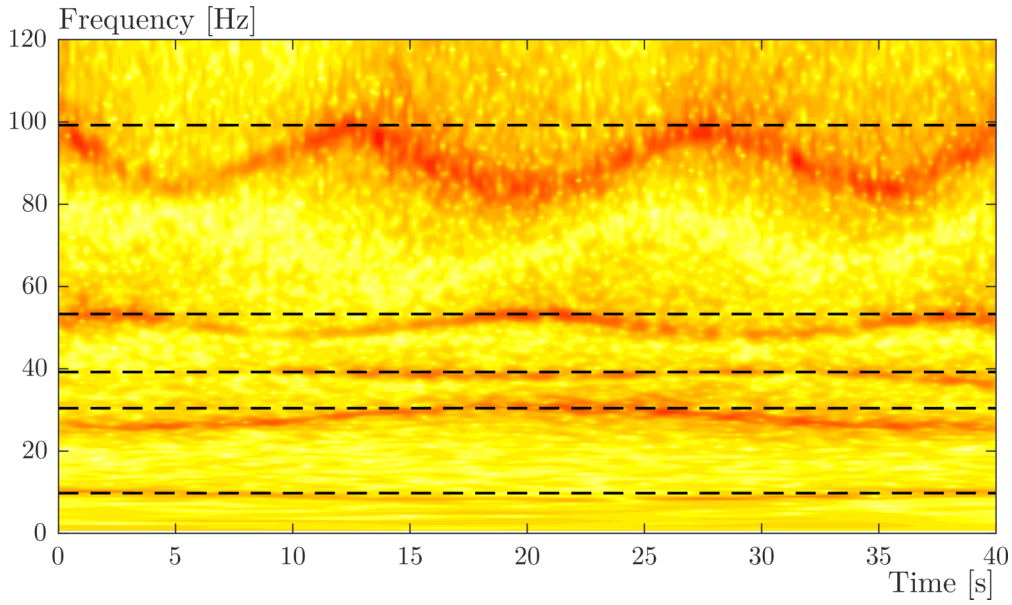

Figure 1.26: Wavelet spectra of the response of the second sensor. The dashed lines represent the natural frequencies without considering the additional mass (Table 1.1).

of the amplitude of each source (through the Hilbert transform) and more precisely, their rate of variation. The selected source is the one with the lowest average rate of variation of its amplitude. This selection is motivated by the fact that a signal owning several components has an amplitude with more variations than a monocomponent signal. Further, even between monocomponents choosing the signal with the lowest rate of variation of its amplitude reduces the risk to violate the Bedrosian theorem and thus the risk of polluting the instantaneous frequency by too fast variations of the amplitude of the signal.

In this experiment, the first selected source is illustrated in Figure 1.27. In this source, the fifth mode is dominant but some traces of the other modes are also visible because of the static behavior of the separation method. However, this kind of behavior is well convenient for the calculation of its instantaneous frequency with the HVD method.

Once the instantaneous frequency of the fifth mode is identified, the Vold-Kalman filter is used to perform the extractions of its monocomponent in each measurement channel. The residual after its extraction on the second channel is illustrated in Figure 1.28 which has to be compared with Figure 1.26. The algorithm is repeated for the extraction of the next modes based on the successively sifted signals.

After three more iteration steps, the modes from two to five are extracted from the response of all accelerometers. The first mode encounters some difficulties to be directly identified by the proposed method. The reason is that this mode is not enough excited to be well extracted by the method. The amplitude of its response on the measurement channel is similar to the amplitude of some remaining parts of the residual, especially at higher frequencies. This can be viewed in Figure 1.30 by comparing the color map at low and high frequencies.

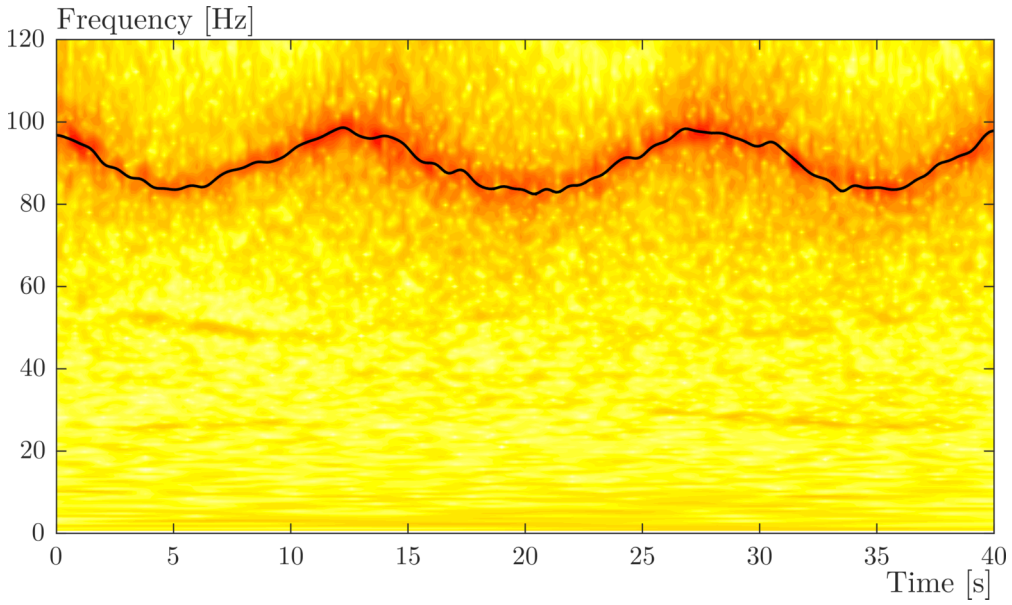

Figure 1.27: Wavelet spectra of the first selected source computed by the SOBI method. The dark line corresponds to the computed instantaneous frequency of its dominant component.

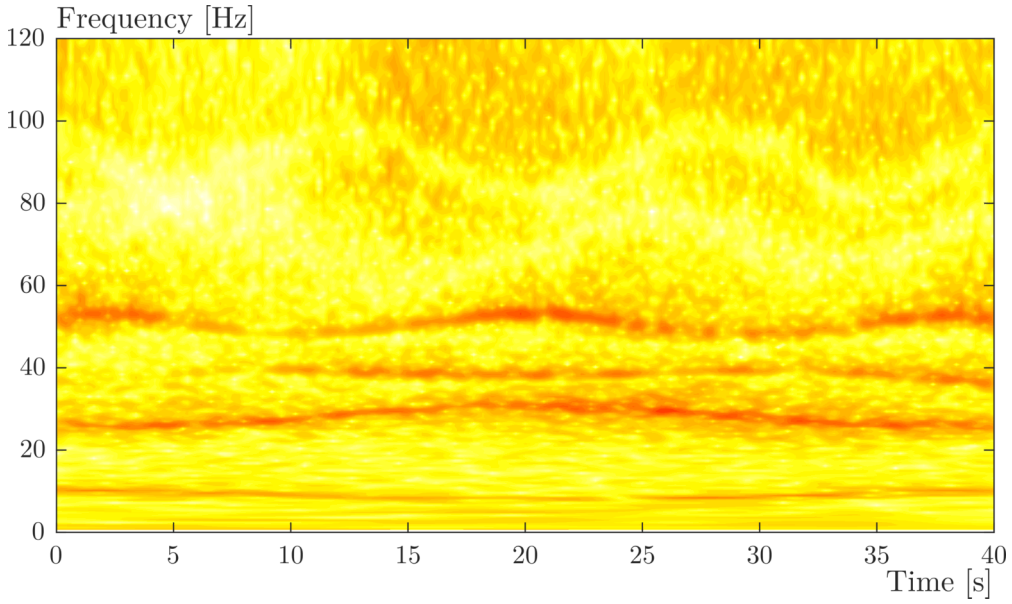

Figure 1.28: Residual after the first extraction of the fifth time-varying mode on the second sensor measurement.

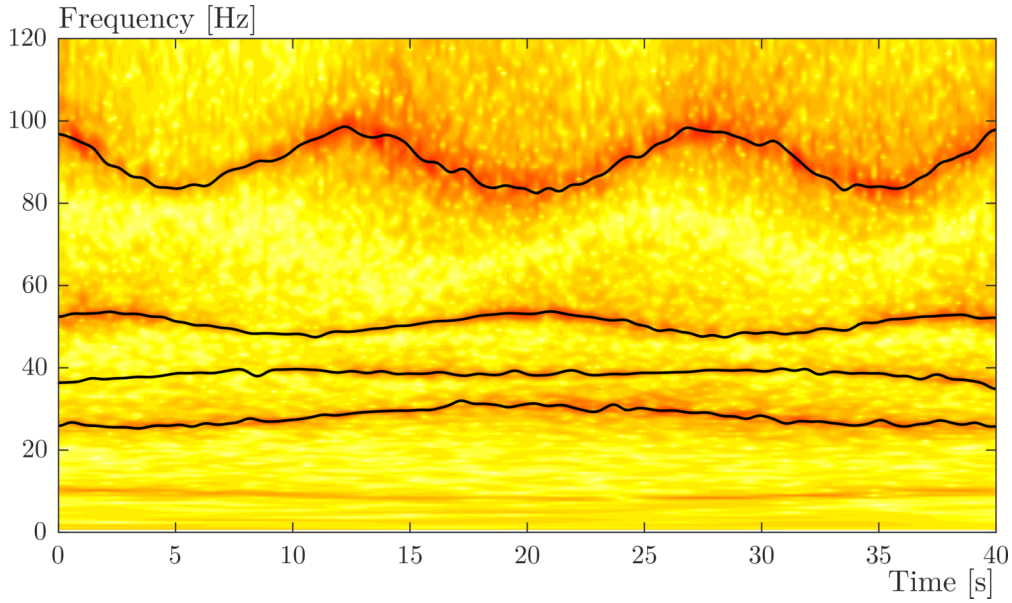

Figure 1.29: Instantaneous frequencies identified by the method after four iterations. The lowest frequency mode has a comparable amplitude with the remaining noise at higher frequencies.

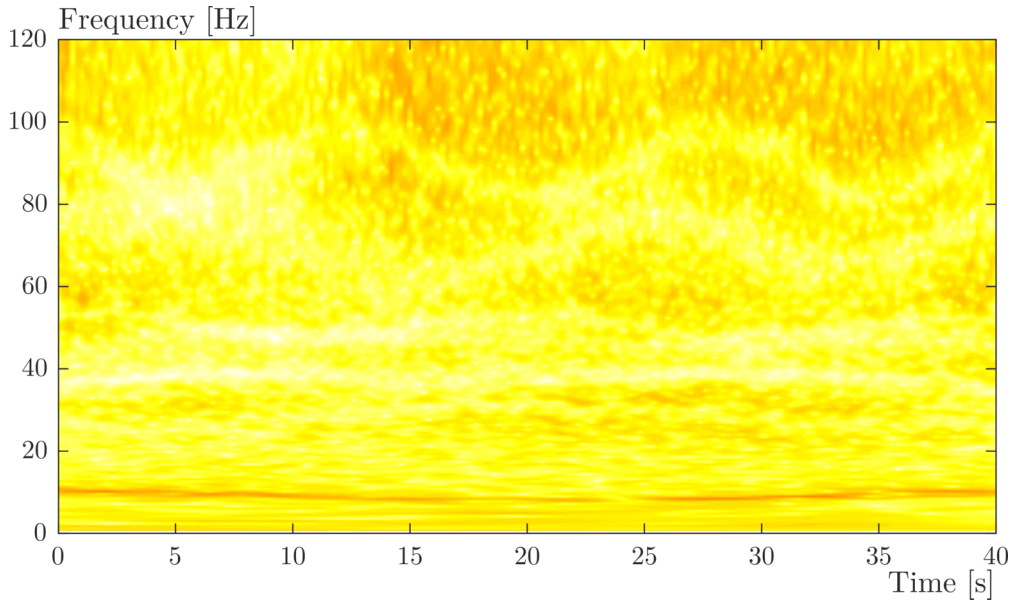

Figure 1.30: Residual after the extraction of the extraction of four identified modes.

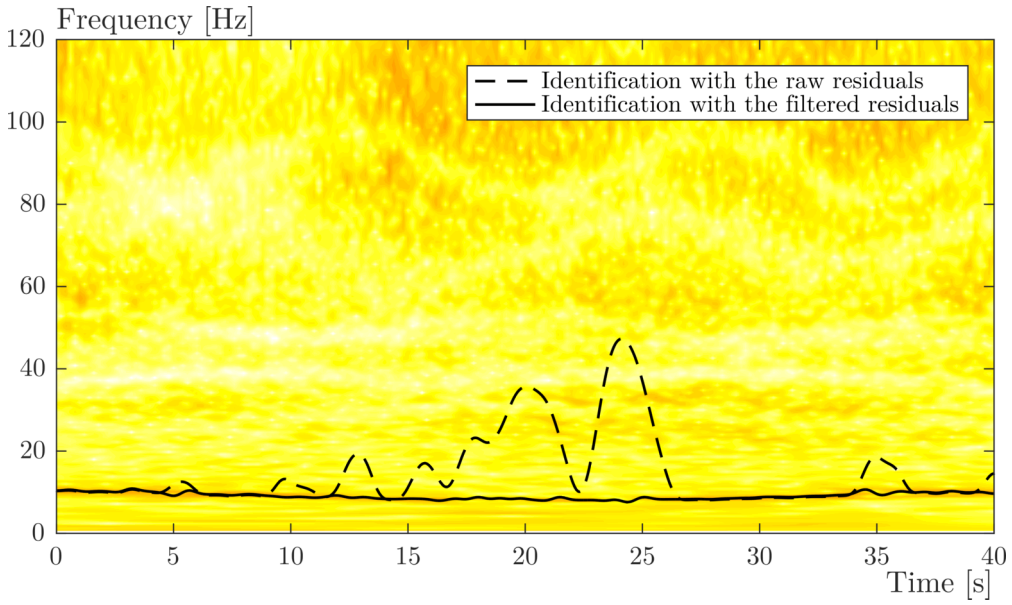

Figure 1.31: Identification of the lowest time-varying frequency by processing raw or filtered residual. The the wavelet decomposition of the raw residual is used as background support.

In order to complete the identification of the time-varying vibration modes, some signal processing is required to be able to catch the first mode. Such an operation is performed using a Butterworth low pass filter with a cutting frequency placed at 20 Hz. Processing these filtered residuals as new input in the modified HVD method renders possible the extraction of the first mode. This is shown in Figure 1.31 together with its identification without the filtering operation to illustrate the failure of the direct identification on the raw residual.

The identified instantaneous frequencies of the system are shown in Figure 1.32 with the wavelet spectra of the channel 2 as background support and the final residual of this channel is shown in Figure 1.33.

Correlation of instantaneous modal deformations

As described in Section 1.4.2, the Vold-Kalman filter is able to calculate the complex amplitude corresponding to a phase signal. With equation (1.52), we have seen than the complex amplitudes can be considered as modal deflection shapes similar to time-varying mode shapes.

In the case of linear time-varying systems, the natural frequency and mode-shapes associated to a specific complex amplitude and phase signal vary with time. To have an idea of the correlation between the reference mode-shapes (those calculated on the LTI unloaded beam) and the identified time-varying mode shapes (taking into account the moving mass), the Modal Assurance Criterion (MAC) is used instantaneously. It means that, at each time instant, the MAC matrix is computed between the reference modes and the time-varying mode shapes. Because of the additional time variable, the

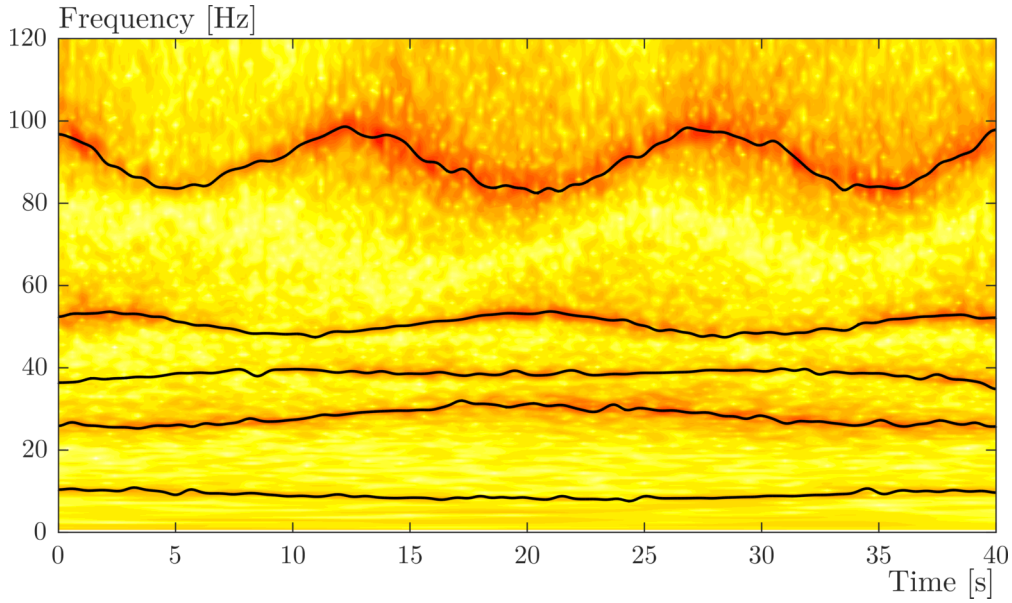

Figure 1.32: Final set of instantaneous freuquencies. All the modes are identified in the frequency band.

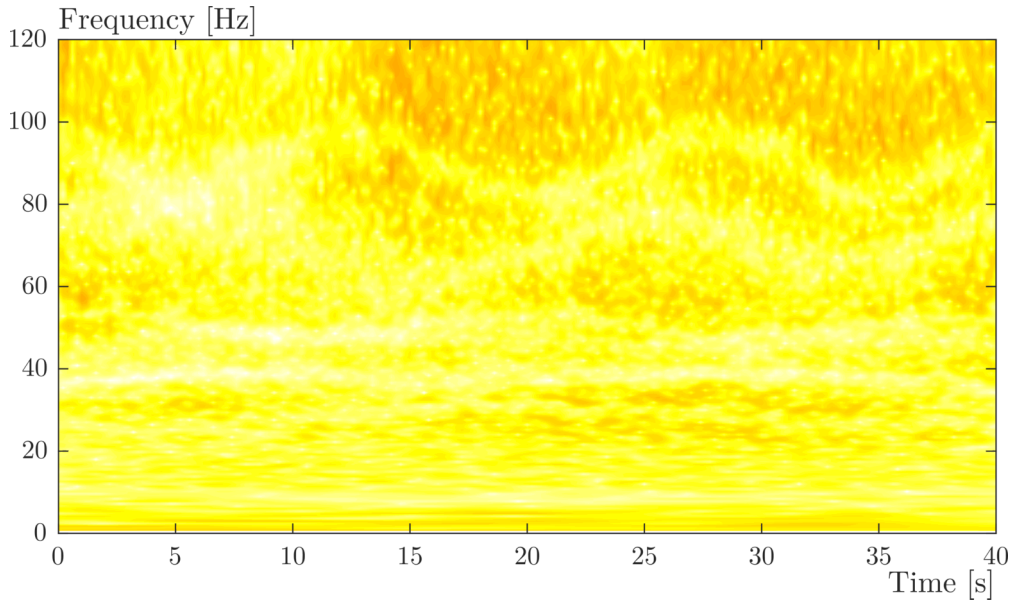

Figure 1.33: Residual signal in the second channel after the extraction of each mono-component related to the identified instantaneous frequencies.

MAC layout has to be modified for graphical representation. To do so, at each time instant, the calculated MAC matrix is reshaped in a column vector. Then all the MAC vectors corresponding to one time instant are concatenated in a global time-varying MAC (TV-MAC) matrix as illustrated in Figure 1.34. Whereas in LTI modal analysis a unitary diagonal corresponds to perfect matching, here a perfect matching will be given by unitary rows facing the right couples of similar modes.

On that TV-MAC matrix, some characteristics of the system may be seen. First, the global shape of the matrix shows that the time-varying mode-shapes remain more or less well correlated with their respective reference mode-shape. Second, looking to one specific correlated row, some small drops of correlation appear periodically, especially on the highest frequency modes. These drops are due to mode shape distortions caused by the presence of the moving mass. This is exactly the same phenomenon as explained in Section 1.5.2 where the instantaneous frequencies are compared to the natural frequencies of the time invariant subsystem (Figure 1.26). To have a better view of the modal correlation, the correlation values of each pair of correlated modes are plotted in Figure 1.35 where the cross correlations are omitted. This figure clearly shows the time instants when the moving mass crosses the vibration nodes of each mode. Similarly to the resonance frequencies, the modal correlation comes very close to the unit correlation when the mass does not perturb a mode.

Finally, one can note that the correlation curves are not very smooth and that occasional large drops may occur. This is a consequence of the way the varying mode shapes are calculated. Because they are approximated by the modal deflection shapes, themselves extracted as the complex amplitude of each modal component, their accuracy highly depends on the instantaneous modal amplitudes. At low instantaneous amplitudes, a small error may cause large discrepancies in the deformation shape.

To illustrate the influence of the moving mass on the varying mode shapes, let us take for example the fifth identified mode and let us consider the particular time instants from 0 to 40 s by steps of 5 s. Its evolution at these time instants is illustrated in Figure 1.36.

Looking to that few discrete snapshots of the deformation, the influence of the moving mass is visible and it is also possible to imagine its motion. The additional inertia added in the structure influence the deflection shape by locally decreasing its amplitude at its instantaneous position with respect to the amplitude of the other parts of the structure. The effect is the most visible when the mass is located to the antinodes of the vibration mode, where the maximum decreases in amplitudes are observed compared to the amplitude of the other antinodes.

1.6 Concluding remarks

In this chapter, the identification of time-varying dynamical systems was addressed by the mean of non-parametric methods. Based on the existing Hilbert Vibration De-

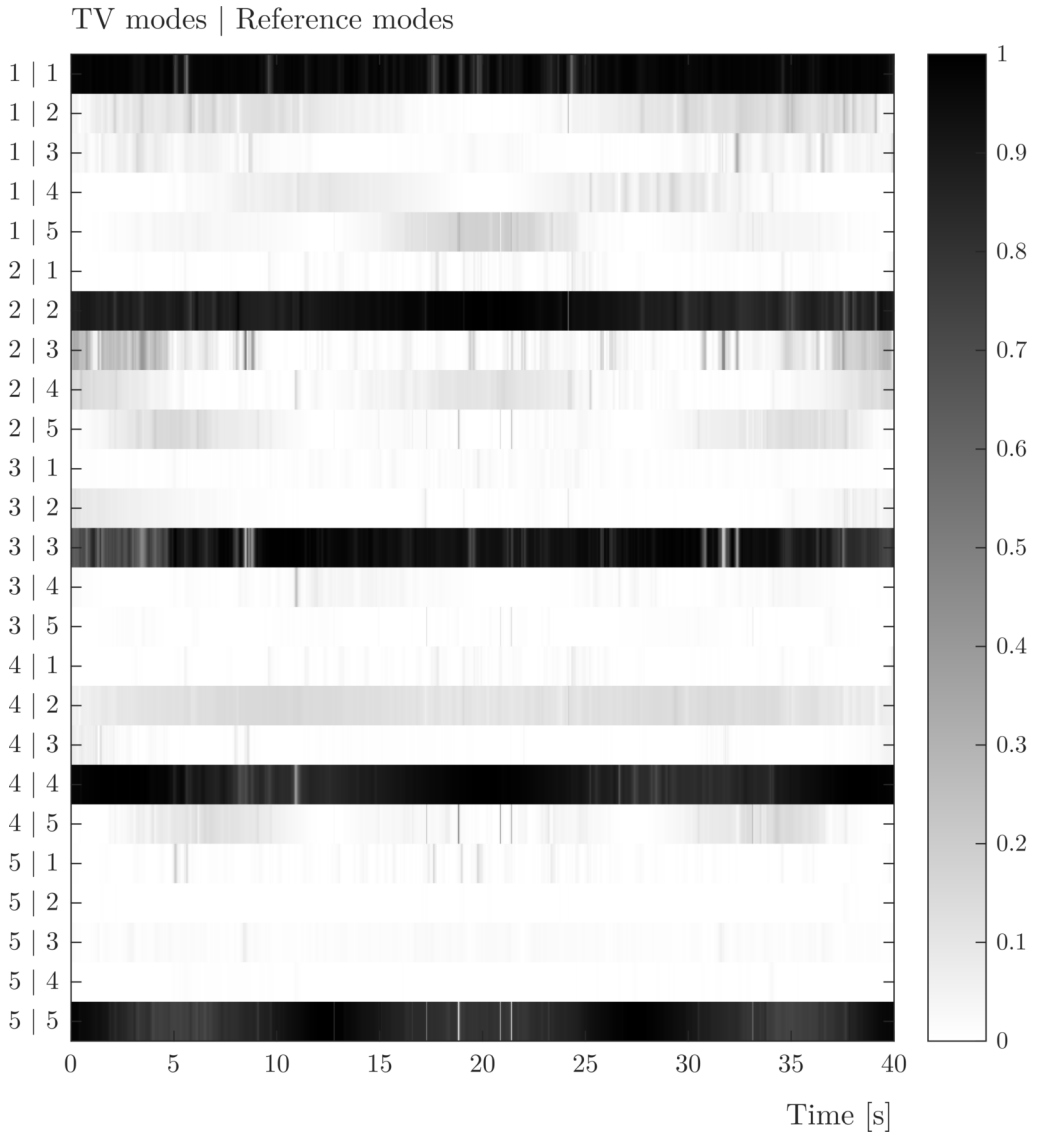

Figure 1.34: Time-varying modal assurance criterion (TV-MAC). The y-axis label indicates the couples of modes which are compared and the time dependency appears along the x-axis.

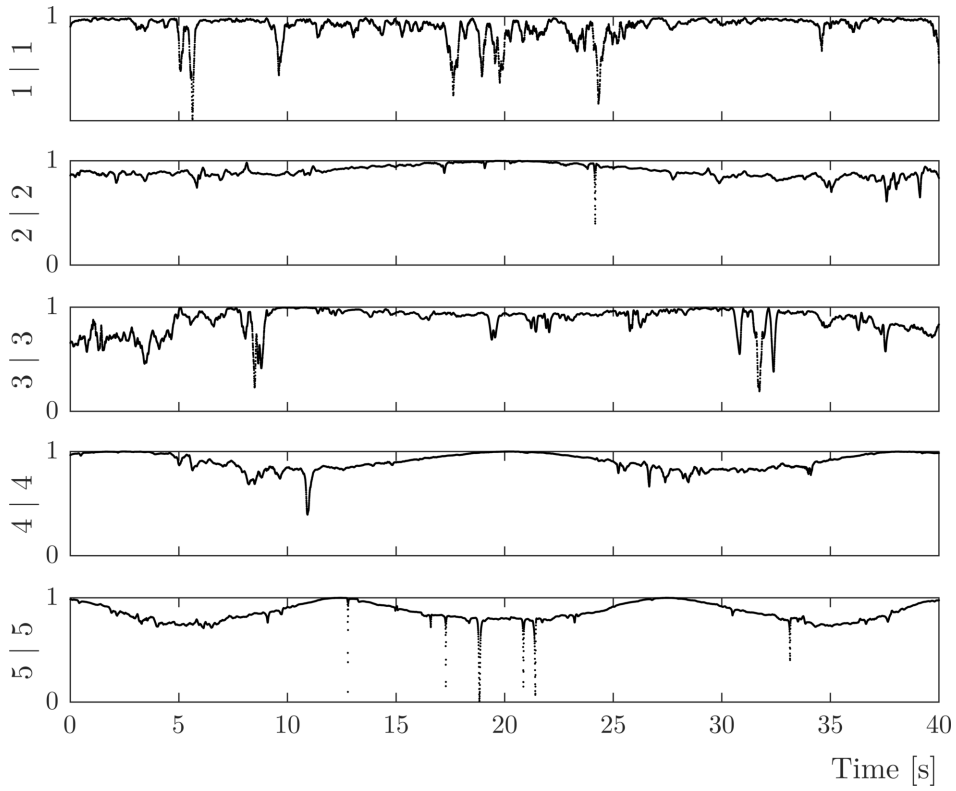

Figure 1.35: TV-MAC for each couple of correlated modes.

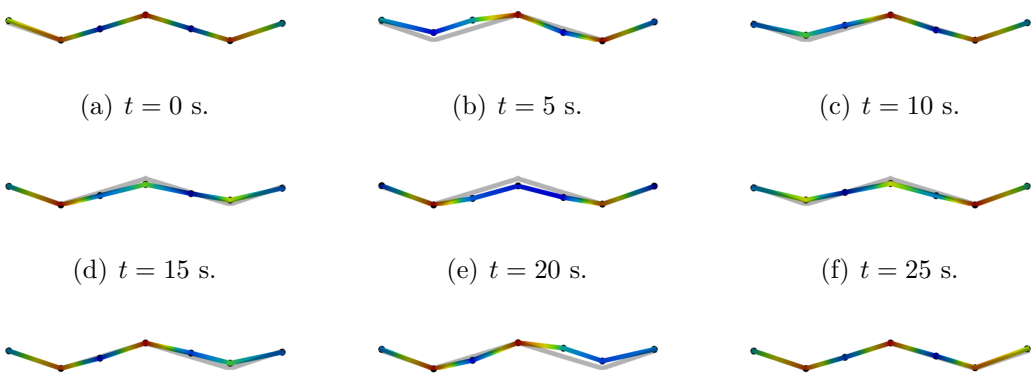

(a) $t = 0$ s. (b) $t = 5$ s. (c) $t = 10$ s.

(d) $t = 15$ s. (e) $t = 20$ s. (f) $t = 25$ s.

(g) $t = 30$ s. (h) $t = 35$ s. (i) $t = 40$ s.

Figure 1.36: Fifth time-varying mode shape at equally spaced time spots. The starting position of the mass is on the left hand side of the beam and travels to the right. The background grey shape represents the mode shape of the LTI structure.

composition method usually used with single measurement as input, the method was extended in order to manage multiple simultaneous measurements of the response of the system. The introduction of blind source separation methods as preprocessing for the decomposition shown several advantages. First, it gathers all the information of the measurement sensors in the sources. Next, even if the source separation methods considered here are static decomposition methods, the extracted sources are well convenient for the decomposition by the HVD method i.e. that one mode dominates the signal and the other components can be eliminated.

The proposed method was successfully applied on the laboratory structure but some weaknesses remain. The first one is related to the measurement noise that should not be excessive. Even if we minimize the use of discrete derivation of the experimental data, the treatment of more noisy data could be difficult. Second, all the modes of the structure have to be sufficiently excited by the external loading. In the proposed experiment, we saw that the first mode was difficult to track because of its weaker presence in the signal around the center of the time span. We had to apply a lowpass filter on the residual after the extraction of the four higher frequency modes in order to properly extract it. This additional signal processing step may introduce some complexity for an easy use of the method.

Based on the identified time-varying instantaneous frequencies, we saw that the extraction of their relative monocomponent was successfully performed by the Vold-Kalman filter. The advantages of the latter filter, such as the combined extraction of components (especially useful for close and crossing frequencies) and their complex envelope were presented. The complex envelopes of the components corresponding to the varying resonance frequencies of the system were finally used as approximates of the time-varying mode shapes in a pretty good way. The only lack of accuracy occur at low amplitude of the modal responses.

The identified weak point of the proposed method is the identification of the instantaneous frequencies. A defect in their identification may cause the failure of the whole identification algorithm because of the risk of deteriorating all the signal by a bad component extraction in the sifting process. It is why this crucial step is considered in the next chapter of the thesis by introducing parametric identification for the instantaneous frequencies.

2

Semi-parametric approach. Scalar parametric modeling.

The aim of this chapter is to improve the time-varying identification scheme of dynamical structures presented earlier. In the preceding chapter, it is shown that a key point of the method, the identification of instantaneous frequencies, may be prone to failure. Such a failure may cause the whole process to miss the extraction of the current but also the future components due to the iterative sifting. In order to make the whole method more robust, it is chosen to rely on parametric estimates of the time-varying frequencies instead of the iterative process of the HVD algorithm. Figure 2.1 graphically represents the scheme of the new method. The step of the estimation of the frequencies by smoothing and differentiating the phase is replaced by a parametric estimation step. The extraction of the modal deflection shapes is kept unchanged but is based on the newly estimated frequencies.

Parametric methods are first presented and the way they are used for the identification of the instantaneous frequencies follows. The method is then tested on the same data as in the preceding chapter and the results obtained by both approaches are finally compared.

2.1 Parametric modeling of processes

2.1.1 Modeling and estimation in the stationary case

Modeling the system

In parametric identification methods, a model represented by a set of parameters is assumed to be representative of the system under study. The goal is then to identify all its constitutive parameters based on the available recorded data. Proceeding in that way brings some advantages compared to non-parametric methods such as the Fourier-based ones used for spectral estimation. First, provided that the model structure to

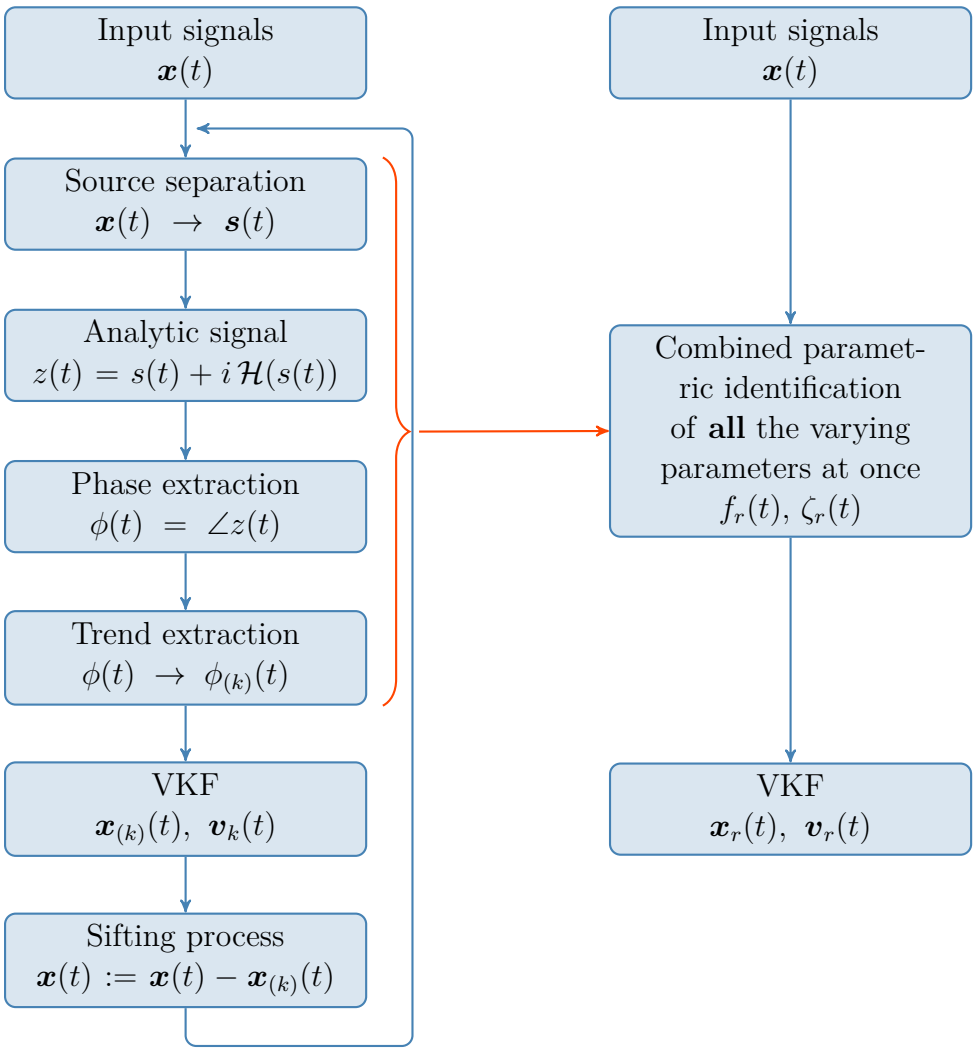

Figure 2.1: Graphical representation of the methodology for the identification of time-varying systems.

represent the system is good (this is a strong requirement) the parametric representation of the system is well suited because it is closer to its underlying physical laws, being in mechanical, electrical or from any other engineering applications. Such representations are also of higher quality (precision, resolution) than non-parametric ones and are also more parsimonious, a small number of parameters describes the whole system [54]. However, as stated above, this is true if the chosen model structure is adequate to represent the actual system. Violating this assumption may lead to completely wrong or non physical estimates of the model parameters.

Most of accurate modal analysis methods are based on parametric methods. Non-parametric methods are rather used to have a fast rough idea of the dynamics of the structure. Natural frequencies may be obtained by picking the peaks on Fourier-based spectra and the damping ratio's may computed with simple methods such as the peak-picking or circle-fitting methods [48] which are geometrical interpretations of the FRF data.

The parametric approaches work differently. They superimpose a mathematical

model on measured experimental data and the goal is to tune the internal parameters of the model to best fit the data. This may be performed in various ways and using different quantities (in time or frequency domain, using impulse or random responses). For example, the Least Square Complex Exponential (LSCE) methods [48] models the impulse response of a system of a priori chosen order. The impulse response of the structure is measured by impacting the structure with an impact hammer and the method identifies the parameters of a series of exponential functions [48]. The frequency domain counterpart of the latter method is the (poly-reference) Least Squares Complex Frequency domain estimator (also known under its commercial name PolyMAX [55, 56]) which fits a parametric model of the FRFs of the system in the frequency domain. Some other methods model the system in a state-space form and may be used in a variety of conditions (forced response, operational analysis, in time or frequency domains, etc...). The Stochastic Subspace Identification (SSI) method [57] is largely used in modal analysis too. Finally, one may also rely on the family of *polynomial models* owning the well known general ARMAX models (AutoRegressive Moving-Average with eXogenous input) to model the input-output relationship of a system. It is a very convenient approach in the present application in time-varying systems.

The ARMAX model is written in a general way as follows between the input u of the system and its output, the observed measurements, y:

$$\begin{aligned} y[t] + a_1 y[t-1] + \cdots + a_{n_a} y[t-n_a] &= e[t] + b_1 e[t-1] + \cdots + b_{n_b} e[t-n_a] \\ &+ c_1 u[t-1] + \cdots + c_{n_c} u[t-n_c] \end{aligned} \tag{2.1}$$

The autoregressive (AR) part is consituted with the lagged data from the output response. The signal e represents the *innovation sequence*. The innovation constitutes the part of the observed output which cannot be predicted with the past data [58] and is assumed to be a zero-mean normally-distributed random sequence. The part of the model dealing with the innovation sequence represents the moving-average (MA) part. It is modeled in the same way as the AR part i.e. that means by a combination of time lagged values of the innovation sequence. The exogenous part is treated similarly if the input of the system is known.

Introducing the lag operator q such as $q\,y[t] = y[t+1]$ and $q^{-1}\,y[t] = y[t-1]$, the previous ARMAX model in (2.1) can be shortly written as

$$A(q,\boldsymbol{\theta})\,y[t] = B(q,\boldsymbol{\theta})\,e[t] + C(q,\boldsymbol{\theta})\,u[t] \tag{2.2}$$

with $A(q,\boldsymbol{\theta})$; , $B(q,\boldsymbol{\theta})$ and $C(q,\boldsymbol{\theta})$ being polynomials in the q^{-1} operator and the vector of parameters $\boldsymbol{\theta}$ gathering all the a, b and c parameters:

$$\begin{aligned} A(q,\boldsymbol{\theta}) &= 1 + a_1 q^{-1} + a_2 q^{-2} + \cdots + a_{n_a} q^{-n_a} \\ B(q,\boldsymbol{\theta}) &= 1 + b_1 q^{-1} + b_2 q^{-2} + \cdots + b_{n_b} q^{-n_b} \\ C(q,\boldsymbol{\theta}) &= c_1 q^{-1} + c_2 q^{-2} + \cdots + c_{n_c} q^{-n_c} \end{aligned} \tag{2.3}$$

Taking the z-transform of Equation (2.2) and isolating the output response term, it comes:

$$Y[z] = \frac{B(z,\boldsymbol{\theta})}{A(z,\boldsymbol{\theta})}\,E[z] + \frac{C(z,\boldsymbol{\theta})}{A(z,\boldsymbol{\theta})}\,U[z]. \tag{2.4}$$

The polynomial ratio's

$$H(z,\boldsymbol{\theta}) = \frac{B(z,\boldsymbol{\theta})}{A(z,\boldsymbol{\theta})} \qquad \text{and} \qquad G(z,\boldsymbol{\theta}) = \frac{C(z,\boldsymbol{\theta})}{A(z,\boldsymbol{\theta})} \tag{2.5}$$

represent the parametric innovation and system discrete transfer functions, respectively. The goal of parametric identification is to find suitable parameters able to represent at best the true transfer function which is representative of the system. The quantities of first interest are the parameters designing the polynomial $A(z,\boldsymbol{\theta})$. Being at the denominator of $H(z,\boldsymbol{\theta})$ and $G(z,\boldsymbol{\theta})$, its roots represent the poles of the system. The resonance frequencies and damping ratio's can directly be extracted from the pole's value.

It is possible to represent the model in a convenient way as a relationship between the vector of parameters $\boldsymbol{\theta}$ and a regression vector $\boldsymbol{\phi}$ that contains all the lagged values of y, u and e:

$$\begin{aligned} y[t] &= \boldsymbol{\phi}^T[t]\,\boldsymbol{\theta} + e[t] && (2.6)\\ &= \hat{y}[t,\boldsymbol{\theta}] + e[t] && (2.7) \end{aligned}$$

in which $\hat{y}[t,\boldsymbol{\theta}]$ represents the output estimate (the *predictor*) based on the model parameters.

The ARMAX model (2.1) is quite general but some other common sub models are largely used depending on the system assumptions or available data. Considering a representation with only a single polynomial in (2.1) leads to three simple models:

The finite Impulse Response (FIR) filters: By only considering the regression of the available input, a simple filter is obtained as a model for the output. In such a model the output response is simply a linear combination of the past data of the input signal:

$$y[t] = c_1 u[t-1] + \cdots + c_{n_c} u[t-n_c] + e[t] \tag{2.8}$$

In the shorthand notation (2.7), the $\boldsymbol{\phi}$ and $\boldsymbol{\theta}$ vectors are equal to

$$\begin{aligned} \boldsymbol{\phi}_{FIR} &= \left[u[t-1],\, u[t-2],\, \cdots,\, u[t-n_c]\right]^T, \\ \boldsymbol{\theta}_{FIR} &= \left[c_1,\, c_2,\, \cdots,\, c_{n_c}\right]^T, \end{aligned} \tag{2.9}$$

respectively.

The autoregressive (AR) and moving-average (MA) models: Similarly to the FIR filter, the AR and MA models are built up with a regressive sequence of the past output data and the innovation sequence, respectively:

$$\begin{aligned} \boldsymbol{\phi}_{AR} &= \left[-y[t-1],\, -y[t-2],\, \cdots,\, -y[t-n_a]\right]^T, \\ \boldsymbol{\theta}_{AR} &= \left[a_1,\, a_2,\, \cdots,\, a_{n_a}\right]^T, \end{aligned} \tag{2.10}$$

and

$$\begin{aligned} \boldsymbol{\phi}_{MA} &= \left[e[t-1],\, e[t-2],\, \cdots,\, e[t-n_b]\right]^T, \\ \boldsymbol{\theta}_{MA} &= \left[b_1,\, b_2,\, \cdots,\, b_{n_b}\right]^T, \end{aligned} \tag{2.11}$$

Considering a pair of polynomials, two usual models are largely used:

The autoregressive model with exogenous input (ARX): In this model, only the known output and input data are considered in the regression vector:

$$\begin{aligned} \boldsymbol{\phi}_{ARX} &= [-y[t-1],\, -y[t-2],\, \cdots,\, -y[t-n_a] \,|\, u[t-1],\, u[t-2],\, \cdots,\, u[t-n_c]]^T, \\ \boldsymbol{\theta}_{ARX} &= [a_1,\, a_2,\, \cdots,\, a_{n_a} \,|\, c_1,\, c_2,\, \cdots,\, c_{n_c}]^T, \end{aligned} \tag{2.12}$$

The autoregressive moving-average (ARMA) model: In this model, the parameters and lagged values of the output data and innovation sequences populate the regression and parameters vectors:

$$\begin{aligned} \boldsymbol{\phi}_{ARMA} &= [-y[t-1],\, -y[t-2],\, \cdots,\, -y[t-n_a] \,|\, e[t-1],\, e[t-2],\, \cdots,\, e[t-n_b]]^T, \\ \boldsymbol{\theta}_{ARMA} &= [a_1,\, a_2,\, \cdots,\, a_{n_a} \,|\, b_1,\, b_2,\, \cdots,\, c_{n_b}]^T, \end{aligned} \tag{2.13}$$

The previous models represent commonly used models but note that the family of polynomial models is far larger. For example, looking at (2.5), it can be seen that G and H share the same denominator. This constraint could be relaxed by choosing different polynomials for the two transfer functions. By adding more and more complexity in the modeling of the system based on the input, output data and the innovation, there are up to 32 possible model combinations [58].

Identification of the model parameters

Once a model type is chosen for the identification, it remains to proceed to the identification of its constitutive parameters. The *Prediction Error Method* (*PEM*) is a common way to obtain good estimates of the model parameters. The method is based on the minimization of a function error between the model and the actual recorded data [58]. Defining the prediction error $e[t, \boldsymbol{\theta}]$ as the difference between the output data and the predictor

$$e[t, \boldsymbol{\theta}] = y[t] - \hat{y}[t, \boldsymbol{\theta}], \tag{2.14}$$

the prediction error method computes a scalar valued function of this prediction error which is minimal for the optimum set of model parameters. This cost function $V(\boldsymbol{\theta})$ is typically defined as

$$V(\boldsymbol{\theta}) = \frac{1}{N} \sum_{t=1}^{N} \ell\left(e[t, \boldsymbol{\theta}]\right) \tag{2.15}$$

where ℓ represents a function of the prediction error. A standard choice for this function is the quadratic norm

$$\ell(e) = \frac{1}{2}\, e^2 \tag{2.16}$$

which is scalar-valued and positive. With this choice of function for the computation of the cost function (2.15), it comes

$$V(\boldsymbol{\theta}) = \frac{1}{2N}\sum_{t=1}^{N}\left(e[t,\boldsymbol{\theta}]\right)^2 \tag{2.17}$$

$$= \frac{1}{2N}\sum_{t=1}^{N}\left(y[t]-\hat{y}[t,\boldsymbol{\theta}]\right)^2 \tag{2.18}$$

$$= \frac{1}{2N}\sum_{t=1}^{N}\left(y[t]-\boldsymbol{\phi}^T[t]\,\boldsymbol{\theta}\right)^2 \tag{2.19}$$

Depending on the chosen model structure, different strategies are possible to solve the minimization problem. One first have to make a distinction between two categories of models depending of the presence of a moving-average part or not. If the model does not contain a MA, the prediction error in (2.14) is linear in the parameters of the model. The minimization of the cost function then consist in imposing its derivative with respect to the vector of parameters $\boldsymbol{\theta}$ to be zero. Considering the choice of the quadratic norm, the derivation of the cost function with respect to the vector of parameters gives:

$$\frac{\mathrm{d}V(\boldsymbol{\theta})}{\mathrm{d}\boldsymbol{\theta}} = \frac{1}{N}\sum_{t=1}^{N}\left(\boldsymbol{\phi}[t]y[t]-\boldsymbol{\phi}[t]\boldsymbol{\phi}^T[t]\,\boldsymbol{\theta}\right) = \mathbf{0}. \tag{2.20}$$

This relation provides a direct solution for the parameters $\boldsymbol{\theta}$ in an ordinary least squares sense:

$$\boldsymbol{\theta} = \left(\sum_{t=1}^{N}\boldsymbol{\phi}[t]\boldsymbol{\phi}^T[t]\right)^{-1}\left(\sum_{t=1}^{N}\boldsymbol{\phi}[t]y[t]\right). \tag{2.21}$$

When the model structure involves a moving-average part, the prediction error in (2.14) is not linear anymore in the $\boldsymbol{\theta}$ parameters because of the dependence of the regression vector $\boldsymbol{\phi}$ in the innovation sequence. Therefore, the minimization of the quadratic cost function cannot be solved in a least squares sense anymore. In such a case, a nonlinear optimization scheme has to be performed. Optimization schemes such as Gauss-Newton (GN) or Levenberg-Marquardt (LM) may be used for that purpose [59].

Once the model parameters are properly identified, the analysis of its transfer function provides useful information about the underlying system. In this study, we are concerned with output only modal identification. In such configuration, no known input is given to feed the estimation algorithm, only the recorded response signals are available. The possible types of models are then the AR, MA or ARMA models. In each of these models, the transfer function is defined in a different manner:

- The AR model provides a rational transfer function based only on a denominator

$$H_{AR}(z,\boldsymbol{\theta}) = \frac{1}{A(z,\boldsymbol{\theta})}. \tag{2.22}$$

It is then an all-pole model and is able to well describe the peaks of the transfer function.

- Conversely, the transfer function of a MA model consists in a polynomial

$$H_{MA}(z, \boldsymbol{\theta}) = B(z, \boldsymbol{\theta}). \tag{2.23}$$

It is then an all-zero transfer function and it is able to well describe valleys.

- The ARMA transfer function is more complete as it is described by a ratio of polynomials

$$H_{ARMA}(z, \boldsymbol{\theta}) = \frac{B(z, \boldsymbol{\theta})}{A(z, \boldsymbol{\theta})}. \tag{2.24}$$

In such a way, it is able to well model the peaks and valleys of the transfer functions. It is a pole-zero modeling of the transfer function.

2.1.2 Modeling of time-dependent processes

Once the system to study exhibits a dependency with respect to time, the modeling strategy implied in order to identify its properties has to handle this time variation and time-varying models have to be chosen. Besides a direct application on time-varying systems, time-varying models are also used for the identification of other systems such as time invariant systems with unequal sampling rate or for the identification of nonlinear systems linearized around a certain trajectory [58]. Their identification is performed by letting the model parameters vary with time and tracking this variation. In this way, the parametric model equation (2.6) now shows a time dependency in its vector of parameters and becomes

$$y[t] = \boldsymbol{\phi}^T[t]\, \boldsymbol{\theta}[t] + e[t]. \tag{2.25}$$

With such a time-dependent vector of parameters, it is still possible to form ratio's between polynomials to compute the transfer function of the system depending on the chosen model. For example, considering an ARMA model such as in Equation (2.24) with time dependent parameters, leads to

$$\begin{aligned} H_{ARMA}(z, \boldsymbol{\theta}[t]) &= \frac{B(z, \boldsymbol{\theta}[t])}{A(z, \boldsymbol{\theta}[t])} \\ &= \frac{1 + b_1[t]z + b_2[t]z^{-2} + \cdots + b_{n_b}[t]z^{-n_b}}{1 + a_1[t]z + a_2[t]z^{-2} + \cdots + a_{n_a}[t]z^{-n_a}}. \end{aligned} \tag{2.26}$$

Such a straightforward introduction of the time-dependent parameters in the computation of the transfer function may seem a naive way to proceed but it can lead to good approximate of the real time-dependent transfer function of the underlying time-varying system. Spectra of transfer functions constructed as in Equation (2.26) are reffered to *frozen-time spectra* or *frozen-time transfer functions*. In [60], Zadeh demonstrates the applicability of the frozen models for the study of time-varying systems. His developments are performed for continuous time parameters but the result

is valid for discrete time models from sampled data. He shows that for a time-varying system described by differential polynomials

$$A(p,\,t)\,y(t) = B(p,\,t)\,e(t) \tag{2.27}$$

with

$$\begin{aligned} A(p,\,t) &= 1 + a_1(t)\,p + a_2(t)\,p^{^2} + \cdots + a_{n_a}(t)\,p^{n_a} && (2.28)\\ B(p,\,t) &= 1 + b_1(t)\,p + b_2(t)\,p^{^2} + \cdots + b_{n_b}(t)\,p^{n_b}, && (2.29) \end{aligned}$$

p being the differential operator $p^n = \mathrm{d}^n/\mathrm{d}t^n$, its time-varying transfer function $H(i\omega,\,t)$ in the frequency domain is the solution of the following differential equation

$$\left[\frac{1}{n_a!A(i\omega,\,t)}\frac{\partial^{n_a}A(i\omega,\,t)}{\partial(i\omega)^{n_a}}\right]\frac{\mathrm{d}^{n_a}H(i\omega,\,t)}{\mathrm{d}t^{n_a}} + \cdots + \left[\frac{1}{A(i\omega,\,t)}\frac{\partial A(i\omega,\,t)}{\partial(i\omega)}\right]\frac{\mathrm{d}H(i\omega,\,t)}{\mathrm{d}t} + H(i\omega,\,t) = \frac{B(i\omega,\,t)}{A(i\omega,\,t)}. \tag{2.30}$$

In the latter equation, it can be seen that the first n_a terms exhibit a time derivative of the transfer function. In the case of slowly varying systems, these terms become negligible as the rate of variation of $H(i\omega,\,t)$ decreases and it comes for such systems that the transfer function may be approximate by its frozen transfer function

$$H(i\omega,\,t) = \frac{1 + b_1(t)\,(i\omega) + b_2(t)\,(i\omega)^2 + \cdots + b_{n_b}(t)\,(i\omega)^{n_b}}{1 + a_1(t)\,(i\omega) + a_2(t)\,(i\omega)^2 + \cdots + a_{n_a}(t)\,(i\omega)^{n_a}}. \tag{2.31}$$

For a time-varying system, the poles and zeros are not a simple extension of the ones in time invariant condition but by computing the roots of both the denominator and numerator of the frozen transfer function for any time instant t, one can compute their frozen-time equivalent. From the frozen-poles, the frozen- frequencies and damping ratio's are finally obtained.

2.2 Estimation of the model parameters

Once a model type is chosen, it remains to proceed to the identification of its parameters in the vector $\boldsymbol{\theta}[t]$ in (2.25). Several methods exist to perform this task. In applications implying time-varying processes, Niedźwiecky [61] provides a series of different possible methods for the identification of the time-dependent parameters. Some of them are presented hereafter.

2.2.1 Short-time stationarity and process segmentation

As previously described in Section 1.1 in which the short-time Fourier transform and the spectrogram are presented, the assumption of local stationarity may be considered

in parametric estimation for slowly-varying processes. The assumption is exactly the same here, stating that on short time windows the system does not encounter important modifications. In such a way, any identification procedure for the identification of time-invariant processes can be applied on a short time window about the whole time axis to follow the whole variation of the system properties. Of course, the same trade-off between accuracy and tracking rate abilities is also present in the case of parametric identification. A system with a slow nonstationarity can be identified by considering large time windows with a lot of data points and conversely, a system with a higher variation rate enforced the use of shorter windows, which can impact the identification accuracy.

2.2.2 Recursive weighted least-squares

Another strategy employed to perform the identification of processes is to rely on recursive estimation algorithm. Often, their use is required in on-line applications for which the estimation is updated with each new measurements. Recursive estimation is widely used in a variety of engineering fields such as control, telecommunications, or for health monitoring purposes [58]. In the latter case, the properties of the system are monitored to seek for sufficient variations that could indicate the occurrence of a default or damage in the system. It is this ability to track variations that brings some attractiveness to this type of methods. In the recursive Weighted Least Squares (WLS) method, a decreasing exponential weighting function is introduced in the algorithm in order to bring higher importance to the measurements newly acquired and to forget the older ones. The algorithm may be summarized as follows [58, 61]:

$$\boldsymbol{\theta}[t] = \boldsymbol{\theta}[t-1] + \boldsymbol{L}[t]\, e\left[t, \boldsymbol{\theta}[t-1]\right] \tag{2.32}$$

$$e[t, \boldsymbol{\theta}] = y[t] - \boldsymbol{\phi}^T[t]\boldsymbol{\theta}[t-1] \tag{2.33}$$

$$\boldsymbol{L}[t] = \frac{\boldsymbol{P}[t-1]\boldsymbol{\phi}[t]}{\lambda + \boldsymbol{\phi}^T[t]\boldsymbol{P}[t-1]\boldsymbol{\phi}[t]} \tag{2.34}$$

$$\boldsymbol{P}[t] = \frac{1}{\lambda}\left[\boldsymbol{P}[t-1] - \frac{\boldsymbol{P}[t-1]\boldsymbol{\phi}[t]\boldsymbol{\phi}^T[t]\boldsymbol{P}[t-1]}{\lambda + \boldsymbol{\phi}^T[t]\boldsymbol{P}[t-1]\boldsymbol{\phi}[t]}\right] \tag{2.35}$$

In the latter equations, the forgetting factor of the method is represented by the λ parameter. $\boldsymbol{L}$ and $\boldsymbol{P}$ matrices represent the gain and the covariance matrices, respectively. Another similar approach is to estimate the vector of the model parameters as the state vector of state-space model by the Kalman filter algorithm.

Generally, recursive methods well behave when the rate of variation of the parameters is low.

2.2.3 The basis function approach

In the above recursive methods, no structure is assumed for the evolution of the model parameters. The present basis function approach is rather different. It assumes that the model parameters can be represented with a basis of a priori chosen functions. Mathematically, it comes that each of the model parameters can be expressed in a deterministic way as

$$\theta_i[t] = \sum_{j=1}^{k} \theta_{ij} f_j[t]. \tag{2.36}$$

In the latter equation, the new parameters θ_{ij} are the projection coefficients of the time evolution of the i^{th} model parameter on the j^{th} basis function. Such a parameterization provides several advantages. First, it drastically decreases the number of parameters implied in the model estimation, which improves the parsimonious feature of the method. Second, the rate of variation of the parameters is not limited anymore to slow variations required by the short-time or recursive methods. The rate of variation of the parameters in the basis function approach is driven by the choice of the functions in the basis. If the model parameters encounter fast variations, choosing a basis of functions able to represent the same rate of variation will be suitable for their identification. Finally, a modeling of the parameters following Equation (2.36) transforms the time-varying identification problem into a time-invariant one because the new model parameters θ_{ij} do not depend on t anymore.

The application of the basis functions approach for the study of time-varying processes goes back to the 1970's. In [62], Liporace uses a polynomial basis to model the time variation of its parameters to model a nonstationary speech signal. Later and always in speech analysis, Hall *et al.* model the speech with all poles filters (AR models) using both powers of time and Fourier functions as a basis to catch the time variation of the parameters [63]. In the 1980's, Grenier applied the basis function approach for the identification of ARMA models [64, 65, 66]. In the latter references, he uses Legendre polynomials and Fourier functions but also suggests the use of discrete prolate spheroidal wave functions. Many other function bases are possible (Chebyshev polynomials, splines, etc.) and they are not necessary required to be orthogonal even if the orthogonality may improve the conditioning of some estimation problems. If additional information about the process is available, it is also possible to create a suitable basis based on this knowledge. For example if a system is periodically-varying a Fourier series tuned on its fundamental period and an increasing number of harmonics is a good candidate for the tracking of the variation of its parameters.

In what follows, the basis function approach is considered, mainly for its parsimonious and accurate characteristics.

2.3 Application in time-varying modal analysis and consideration of multiple measurements channels.

In the field of the identification of mechanical systems with time-varying properties, Petsounis and Fassois [67] and Poulimenos and Fassois [50] applied the method of the basis functions (also named functional series) approach for their identification with varying ARMA models. Spiridonakos *et al.* [68] provide surveys about the identification of time-varying ARMA models with several approaches, included the recursive and basis functions ones. Spiridonakos and Fassois also provide a survey specifically focused on the basis functions approach [69]. In the latter references, even if the response of the structure is recorded at multiple locations, only a single sensor is chosen for the identification of the time-varying behavior of the system.

The objective of this section is to perform the identification of time-varying mechanical systems using simultaneous multiple measurements. Scalar valued models are considered first and the next chapter will cope with vector model parameterizations.

2.3.1 Model parameters estimation considering multiple measurements channels

If more than one sensor monitor the structure, it is interesting to take advantage of the information from multiple channels. In practice, parametric identification of the frozen-poles is performed on each channel with scalar models but a constraint is introduced in order to couple all the channels. To deal with output only identification, the used type of model is chosen to be a time-varying ARMA model. For each measurement channel $x_o[t]$ the following time-varying model is adopted:

$$x_o[t]+a_1^o[t]\,x_o[t-1]+\cdots+a_{n_a}^o[t]\,x_o[t-n_a]=e_o[t]+b_1^o[t]\,e_o[t-1]+\cdots+b_{n_b}^o[t]\,e_o[t-n_b] \quad (2.37)$$

with the assumption of the basis functions concerning the time evolution of the model parameters:

$$\left\{\begin{array}{lcl} a_i^o[t] & = & \sum_k a_{i,k}^o\, f_k[t] \\ b_j^o[t] & = & \sum_l\ b_{j,l}^o\, f_l[t] \end{array}\right. . \quad (2.38)$$

The constraint introduced in order to link the parameter identification in each channel is to consider the physical interpretation between the model parameters and the structure and the measurement process. Indeed, the information about the dynamics of the structure under study is located in the autoregressive part of the parametric model. The moving-average part in all the channels, however, may not be linked because they are related to their measurement location and the noise present in each channel separately. A simple interpretation of that relationship can be understood by looking to a set of frequency response functions of a LTI system. The peaks of the FRFs are all located at the same resonance frequencies whatever the FRF is considered. The

resonance peaks are related to the poles (roots of the AR polynomial) and are *global quantities*. However, the valleys are different in each FRF. They are related to the zeros of the transfer functions (roots of the MA polynomial). They are *local quantities*. In order to introduce this property in the parametric identification, the simple constraint to take into account is to enforce the AR polynomial to be the same in each channel such as $a_i^o[t] = a_i[t]$:

$$x_o[t]+a_1[t]\,x_o[t-1]+\cdots+a_{n_a}[t]\,x_o[t-n_a] = e_o[t]+b_1^o[t]\,e_o[t-1]+\cdots+b_{n_b}^o[t]\,e_o[t-n_b]. \quad (2.39)$$

With the latter equation, the estimation model is then a set of n_o equations, one for each output measurement channel and the coupling between all the equations is provided by the equality constraint of the autoregressive part:

$$\begin{aligned}
x_1[t] + a_1[t]\,x_1[t-1] + \cdots + a_{n_a}[t]\,x_1[t-n_a] &= e_1[t] + \cdots + b_{n_b}^1[t]\,e_1[t-n_b] \\
x_2[t] + a_1[t]\,x_2[t-1] + \cdots + a_{n_a}[t]\,x_2[t-n_a] &= e_2[t] + \cdots + b_{n_b}^2[t]\,e_2[t-n_b] \\
&\vdots \\
\underbrace{x_{n_o}[t] + a_1[t]\,x_{n_o}[t-1] + \cdots + a_{n_a}[t]\,x_{n_o}[t-n_a]}_{\text{Common AR modeling}} &= \underbrace{e_{n_o}[t] + \cdots + b_{n_b}^{n_o}[t]\,e_{n_o}[t-n_b]}_{\text{Individual MA modeling}}
\end{aligned}$$

This property of a common autoregressive part of the model leads to a common denominator modeling of the parametric transfer functions related to all the measurement channels. This way to model the system is the way followed by the frequency domain PolyMax methods in LTI modal analysis. Note also that this common denominator approach is also used by Zhou *et al.* [70] for the modeling of time-varying systems based on time-varying PSD in the time-frequency domain.

In order to perform the identification of the model parameters, the prediction method is employed to minimize the sum of squared errors (SSE) for all the measurement channels. To this end, the estimate of each signal based on the model parameters is defined as follows:

$$\begin{aligned}
\hat{x}^o[t,\boldsymbol{\theta}] &= -\sum_i \sum_k a_{i,k}\, f_k[t]\, x^o[t-i] + \sum_j \sum_l b_{i,k}^o\, f_l[t]\, e^o[t-j] \\
&= -\begin{bmatrix}\boldsymbol{\phi}^o[t]^T & \boldsymbol{\psi}^o[t]^T\end{bmatrix} \begin{bmatrix}\boldsymbol{a} \\ \boldsymbol{b}^o\end{bmatrix} \qquad (2.40)
\end{aligned}$$

in which the extended regressions vectors for the o^{th} channel are computed by the kronecker products between the signal and the innovation sequence with the functions from the selected basis:

$$\boldsymbol{\phi}^o[t]^T = \begin{bmatrix} f_1[t]x^o[t-1] & f_2[t]x^o[t-1] & \cdots & f_k[t]x^o[t-n_a]\end{bmatrix}, \quad (2.41)$$

$$\boldsymbol{\psi}^o[t]^T = -\begin{bmatrix} f_1[t]e^o[t-1] & f_2[t]e^o[t-1] & \cdots & f_k[t]e^o[t-n_b]\end{bmatrix}. \quad (2.42)$$

The vectors of parameters $\boldsymbol{a}$ and $\boldsymbol{b}^o$ gather the $a_{i,k}$ and $b_{i,k}^o$ parameters, respectively:

$$\boldsymbol{a} = \begin{bmatrix} a_{1,1} & a_{1,2} & \cdots & a_{p,r_A}\end{bmatrix}^T, \quad (2.43)$$

$$\boldsymbol{b}^o = \begin{bmatrix} b_{1,1}^o & b_{1,2}^o & \cdots & b_{q,r_B}^o\end{bmatrix}^T. \quad (2.44)$$

From the estimate in (2.40), the prediction error for the o^{th} channel is simply calculated as the difference between the o^{th} measurement and its predictor:

$$\begin{aligned} e^o[t,\boldsymbol{\theta}] &= x^o[t] - \hat{x}^o[t,\boldsymbol{\theta}] \\ &= x^o[t] + \sum_i \sum_k a_{i,k}\, f_k[t]\, x^o[t-i] - \sum_j \sum_l b^o_{i,k}\, f_l[t]\, e^o[t-j] \\ &= x^o[t] + \begin{bmatrix} \boldsymbol{\phi}^o[t]^T & \boldsymbol{\psi}^o[t]^T \end{bmatrix} \begin{bmatrix} \boldsymbol{a} \\ \boldsymbol{b}^o \end{bmatrix}. \end{aligned} \tag{2.45}$$

The minimization of the SSE has to take all the channels into account in a least squares sense. To this end, the squared errors are summed over all the time samples but also over all the channels:

$$V(\boldsymbol{\theta}) = \sum_o \frac{1}{2N} \sum_t e^o[t,\boldsymbol{\theta}]^2 \tag{2.46}$$

with N the number of data points in each channel and $\boldsymbol{\theta}$ the vector of all the parameters of the model:

$$\boldsymbol{\theta} = \begin{bmatrix} \boldsymbol{a} \\ \boldsymbol{b}^1 \\ \boldsymbol{b}^2 \\ \vdots \\ \boldsymbol{b}^{no} \end{bmatrix}. \tag{2.47}$$

As pointed out earlier in Section 2.1.1, because of the presence of the residual sequence in the moving-average part of the model, the minimization of (2.46) cannot exactly be solved using an ordinary linear least squares. It is however the case for pure AR or ARX models, even in time-varying conditions if the basis functions approach is employed. Two methods are used in order to solve that problem: the *Two Stages Least Squares (2SLS)* and the family of nonlinear optimization schemes.

The Two Stages Least Squares method [58]

The main idea of the 2SLS method is to replace the solving of a nonlinear problem by a sequence of linear subproblems. In the present case, the ARMA model is estimated in two steps using only ordinary linear least squares.

Step 1: The first stage of the method relies on the property that an ARMA (or even a MA) model can be expressed as an AR model of infinite order. The first stage is then to identify an AR model "equivalent" to the ARMA model by increasing its order. As shown earlier, this high-order AR model, AR_{ho}, may be identified by the least squares method because of the linearity of its prediction error in the model parameters.

Step 2: The second step is based on the result of the first one. Once the AR_{ho} model is identified, its corresponding residual may be computed. The past values of the estimate of the residual sequence is then used as an exogenous input for an ARX model. It was also shown that ARX models may be solved using ordinary least squares because their external input is known. The coefficient of the eXogenous part are then estimates of the MA coefficients.

The second step of the algorithm can be repeated in order to iteratively update the prediction error used as input for the next iteration. The advantage of this method is its rather fast computation time. The drawback is that it is a rather rough estimation method and there is no guarantee that the next estimate decreases the sum of squared errors. In other words, the convergence is not ensured.

The processing of the 2SLS method is as follows for our combined modeling. Combining Equations (2.45) and (2.46), it comes:

$$\begin{aligned} V(\boldsymbol{\theta}) &= \sum_o \frac{1}{2N} \sum_t e^o[t,\boldsymbol{\theta}]^2 \\ &= \sum_o \frac{1}{2N} \sum_t \left(x^o[t] + \begin{bmatrix} \boldsymbol{\phi}^o[t]^T \boldsymbol{\psi}^o[t]^T \end{bmatrix} \begin{bmatrix} \boldsymbol{a} \\ \boldsymbol{b}^o \end{bmatrix} \right)^2 \\ &= \sum_o \frac{1}{2N} \sum_t \Big(x^o[t]^2 \\ &\quad + x^o[t] \begin{bmatrix} \boldsymbol{\phi}^o[t]^T & \boldsymbol{\psi}^o[t]^T \end{bmatrix} \begin{bmatrix} \boldsymbol{a} \\ \boldsymbol{b}^o \end{bmatrix} \\ &\quad + x^o[t] \begin{bmatrix} \boldsymbol{a}^T & \boldsymbol{b}^{oT} \end{bmatrix} \begin{bmatrix} \boldsymbol{\phi}^o[t] \\ \boldsymbol{\psi}^o[t] \end{bmatrix} \\ &\quad + \begin{bmatrix} \boldsymbol{a}^T & \boldsymbol{b}^{oT} \end{bmatrix} \begin{bmatrix} \boldsymbol{\phi}^o[t] \\ \boldsymbol{\psi}^o[t] \end{bmatrix} \begin{bmatrix} \boldsymbol{\phi}^o[t]^T & \boldsymbol{\psi}^o[t]^T \end{bmatrix} \begin{bmatrix} \boldsymbol{a} \\ \boldsymbol{b}^o \end{bmatrix} \Big) \end{aligned} \tag{2.48}$$

In order to shorten the notations, lets introduce the following products:

$$\boldsymbol{R}_o = \sum_t \boldsymbol{\phi}^o[t] \boldsymbol{\phi}^o[t]^T, \tag{2.49}$$

$$\boldsymbol{S}_o = \sum_t \boldsymbol{\phi}^o[t] \boldsymbol{\psi}^o[t]^T, \tag{2.50}$$

$$\boldsymbol{T}_o = \sum_t \boldsymbol{\psi}^o[t] \boldsymbol{\psi}^o[t]^T, \tag{2.51}$$

$$\boldsymbol{X}_o = \sum_t x^o[t] \boldsymbol{\phi}^o[t]^T, \tag{2.52}$$

$$\boldsymbol{Y}_o = \sum_t x^o[t] \boldsymbol{\psi}^o[t]^T. \tag{2.53}$$

With the latter notations, (2.48) becomes

$$V(\boldsymbol{\theta}) = \sum_o \frac{1}{2N} \Bigg(\sum_t x^o[t]^2 + \boldsymbol{X}_o \boldsymbol{a} + \boldsymbol{Y}_o \boldsymbol{b}^o + \boldsymbol{a}^T \boldsymbol{X}_o^T + \boldsymbol{b}^{oT} \boldsymbol{Y}_o^T + \boldsymbol{a}^T \boldsymbol{R}_o \boldsymbol{a} + \boldsymbol{a}^T \boldsymbol{S}_o \boldsymbol{b}^o + \boldsymbol{b}^{oT} \boldsymbol{S}_o^T \boldsymbol{a} + \boldsymbol{b}^{oT} \boldsymbol{T}_o \boldsymbol{b}^o \Bigg) \tag{2.54}$$

The cost function $V(\boldsymbol{\theta})$ for the whole set of parameters in $\boldsymbol{\theta}$ is minimized by taking its derivative with respect to each of the $\boldsymbol{a}$ and all $\boldsymbol{b}_o$ vectors and put them to zero. From (2.54), the gradient of $V(\boldsymbol{\theta})$ can be computed with respect to the vectors of parameters $\boldsymbol{a}$ and each $\boldsymbol{b}_o$:

$$\frac{\partial V(\boldsymbol{\theta})}{\partial \boldsymbol{a}^T} = \sum_o \boldsymbol{X}_o^T + \boldsymbol{R}_o \boldsymbol{a} + \boldsymbol{S}_o \boldsymbol{b}^o = \boldsymbol{0} \tag{2.55}$$

$$\frac{\partial V(\boldsymbol{\theta})}{\partial \boldsymbol{b}^{oT}} = \boldsymbol{Y}_o^T + \boldsymbol{S}_o^T \boldsymbol{a} + \boldsymbol{T}_o \boldsymbol{b}^o = \boldsymbol{0} \tag{2.56}$$

Now, stacking Equation (2.55) and Equations (2.56) for each n_o outputs in a matrix form gives

$$\frac{\partial V(\boldsymbol{\theta})}{\partial \boldsymbol{\theta}} = \underbrace{\begin{bmatrix} \sum_o \boldsymbol{X}_o^T \\ \boldsymbol{Y}_1^T \\ \boldsymbol{Y}_2^T \\ \vdots \\ \boldsymbol{Y}_{no}^T \end{bmatrix}}_{\boldsymbol{g}} + \underbrace{\begin{bmatrix} \sum_o \boldsymbol{R}_o & \boldsymbol{S}_1 & \boldsymbol{S}_2 & \cdots & \boldsymbol{S}_{no} \\ \boldsymbol{S}_1^T & \boldsymbol{T}_1 & & & \\ \boldsymbol{S}_2^T & & \boldsymbol{T}_2 & & \\ \vdots & & & \ddots & \\ \boldsymbol{S}_{no}^T & & & & \boldsymbol{T}_{no} \end{bmatrix}}_{\boldsymbol{H}} \underbrace{\begin{bmatrix} \boldsymbol{a} \\ \boldsymbol{b}^1 \\ \boldsymbol{b}^2 \\ \vdots \\ \boldsymbol{b}^{no} \end{bmatrix}}_{\boldsymbol{\theta}} = \boldsymbol{0} \tag{2.57}$$

which can be easily solved by

$$\boldsymbol{\theta} = -\boldsymbol{H}^{-1} \boldsymbol{g}. \tag{2.58}$$

Nonlinear optimization

Various fields of engineering make use of nonlinear optimization including signal processing and system identification [58]. In the present context, the optimization is used to minimize an error function such as (2.15) in order to get the best fit between the chosen model and the observed data. As long as the minimization of the latter equation does not have a direct solution, iterative techniques are required. In such methods, the vector of parameters is iteratively updated to a new value leading to a decrease in the cost function

$$\boldsymbol{\theta}^{(k+1)} = \boldsymbol{\theta}^{(k)} + \alpha \, \boldsymbol{d} \tag{2.59}$$

where $\boldsymbol{\theta}^{(k+1)}$ and $\boldsymbol{\theta}^k$ are the values of to subsequent iterates. $\boldsymbol{d}$ represents the search direction to pass from one iterate to another and the α parameter tunes the step length. The complexity of the optimization algorithms is very scattered, from very simple to very costly in computation operations. They can be characterized by [58]:

- the knowledge of only the function's value,
- the knowledge of the function's value and its gradient,
- the knowledge of the function's value, its gradient and its Hessian matrix.

In the first case, the computations at each iteration are very simple but a lot of iterations are required and the convergence of the algorithm may be of poor quality in some cases. The second kind of methods use the gradient information to find the direction of the locally steepest way to decrease the cost function. A line search is then required to select the best length about that direction. The third kind is classified as the Newton method and is based on a Taylor approximation of the cost function at each iteration. This approximate draws the direction and the length of the step to the next one. In the vicinity of $\boldsymbol{\theta}^{(k)}$, a second order model of the cost function is built as

$$\mathcal{V}(\boldsymbol{\theta}) = V\left(\boldsymbol{\theta}^{(k)}\right) + \left(\boldsymbol{\theta} - \boldsymbol{\theta}^{(k)}\right)^T \left.\frac{\mathrm{d}V(\boldsymbol{\theta})}{\mathrm{d}\boldsymbol{\theta}}\right|_{\boldsymbol{\theta}=\boldsymbol{\theta}^{(k)}} + \frac{1}{2}\left(\boldsymbol{\theta} - \boldsymbol{\theta}^{(k)}\right)^T \left.\frac{\mathrm{d}^2V(\boldsymbol{\theta})}{\mathrm{d}\boldsymbol{\theta}^2}\right|_{\boldsymbol{\theta}=\boldsymbol{\theta}^{(k)}} \left(\boldsymbol{\theta} - \boldsymbol{\theta}^{(k)}\right) \tag{2.60}$$

The new value of the vector of parameters $\boldsymbol{\theta}$ is the one that minimizes the Taylor approximation $\mathcal{V}(\boldsymbol{\theta})$. This is computed by taking the derivative of $\mathcal{V}(\boldsymbol{\theta})$ with respect to $\boldsymbol{\theta}$ and putting it to zero:

$$\frac{\mathrm{d}\mathcal{V}(\boldsymbol{\theta})}{\mathrm{d}\boldsymbol{\theta}} = \left.\frac{\mathrm{d}V(\boldsymbol{\theta})}{\mathrm{d}\boldsymbol{\theta}}\right|_{\boldsymbol{\theta}=\boldsymbol{\theta}^{(k)}} + \left.\frac{\mathrm{d}^2V(\boldsymbol{\theta})}{\mathrm{d}\boldsymbol{\theta}^2}\right|_{\boldsymbol{\theta}=\boldsymbol{\theta}^{(k)}} \left(\boldsymbol{\theta}^{(k+1)} - \boldsymbol{\theta}^{(k)}\right) = \mathbf{0} \tag{2.61}$$

with the iteration step

$$\boldsymbol{d} = \boldsymbol{\theta}^{(k+1)} - \boldsymbol{\theta}^{(k)}. \tag{2.62}$$

At the iteration k, the step is then

$$\boldsymbol{d} = -\underbrace{\left(\left.\frac{\mathrm{d}^2V(\boldsymbol{\theta})}{\mathrm{d}\boldsymbol{\theta}^2}\right|_{\boldsymbol{\theta}=\boldsymbol{\theta}^{(k)}}\right)^{-1}}_{\boldsymbol{H}} \underbrace{\left.\frac{\mathrm{d}V(\boldsymbol{\theta})}{\mathrm{d}\boldsymbol{\theta}}\right|_{\boldsymbol{\theta}=\boldsymbol{\theta}^{(k)}}}_{\boldsymbol{g}} \tag{2.63}$$

in which $\boldsymbol{H}$ is the Hessian matrix of the cost function and $\boldsymbol{g}$ is its gradient.The Newton method is illustrated with a scalar parameter in Figure 2.2.

It remains to compute the derivatives of the cost function. In our case remember that we defined the cost function (2.46) as

$$\begin{aligned} V(\boldsymbol{\theta}) &= \sum_o \frac{1}{2N} \sum_t e^o[t,\boldsymbol{\theta}]^2 \\ &= \sum_o \frac{1}{2N} \sum_t \left(x^o[t] - \hat{x}^o[t,\boldsymbol{\theta}]\right)^2 \end{aligned}$$

The computation of the gradient and the Hessian of the cost function with respect to $\boldsymbol{\theta}$ is then obtained by differentiating our prediction errors $e^o[t,\boldsymbol{\theta}]$ with respect to $\boldsymbol{\theta}$:

$$\frac{\mathrm{d}V(\boldsymbol{\theta})}{\mathrm{d}\boldsymbol{\theta}} = \sum_o \frac{1}{N} \sum_t e^o[t,\boldsymbol{\theta}] \frac{\mathrm{d}e^o[t,\boldsymbol{\theta}]}{\mathrm{d}\boldsymbol{\theta}}, \tag{2.64}$$

$$\frac{\mathrm{d}^2V(\boldsymbol{\theta})}{\mathrm{d}\boldsymbol{\theta}^2} = \sum_o \frac{1}{N} \sum_t \left(\frac{\mathrm{d}e^o[t,\boldsymbol{\theta}]}{\mathrm{d}\boldsymbol{\theta}}\right) \left(\frac{\mathrm{d}e^o[t,\boldsymbol{\theta}]}{\mathrm{d}\boldsymbol{\theta}}\right)^T + \sum_o \frac{1}{N} \sum_t e^o[t,\boldsymbol{\theta}] \frac{\mathrm{d}^2e^o[t,\boldsymbol{\theta}]}{\mathrm{d}\boldsymbol{\theta}^2}. \tag{2.65}$$

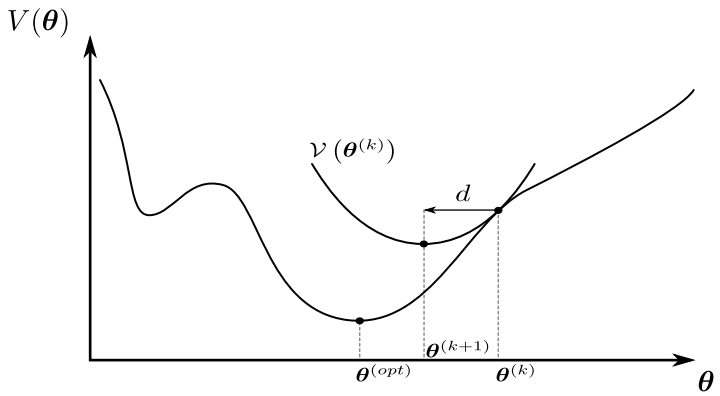

Figure 2.2: Illustration of the Newton approach. At iteration k, a quadratic model of the function is built based on the gradient and Hessian information. It is then minimized to give the next set of parameters.

In Equation (2.65), the second term is generally neglected and only an approximate of the Hessian matrix is computed. This is known as the quasi-Newton method. There are some reasons to neglect it. Close to the optimum, this part is negligible compared to the first term of (2.65). It also reduces the calculation cost, because of the complexity of the computation of the second derivatives. There is also another advantage to keep only the first term: the positive (semi)definiteness of the approximate of the Hessian matrix. This ensures that the iteration step of the algorithm always follows a descending direction in the cost function. This would not be the case if the Hessian would be negative definite due to the second term. A last potential risk subsists in the computation of the current step. When the approximate of the Hessian matrix has a rank deficiency, the computation of the iteration step (2.63) cannot be uniquely computed. In order to tackle this rank deficiency, Levenberg [71] and Marquardt [72] introduced in this operation a regularization parameter λ. This method is known as the *Levenberg-Marquardt* algorithm and is one of the widely used method to solve nonlinear problems:

$$\boldsymbol{d} = -\left(\boldsymbol{H} + \lambda\, \boldsymbol{I}\right)^{-1} \boldsymbol{g} \tag{2.66}$$

in which $\boldsymbol{I}$ is an identity matrix of adequate dimension. The regularization λ parameter drives the iterations of the method by increasing its value when the current iteration encounters some difficulties or by decreasing its value when the cost function is better suited for a quadratic approximation. When the λ parameter tends to zero or to the infinity, the method tends to the quasi-Newton or to the gradient descend with a decreased step length, respectively.

Another way to proceed to iteratively tune the iteration step is the trust region approach [73]. The idea is, as in the Newton method, to create a model of the cost function just as in Equation (2.60) and to minimize it with an additional constraint. This constraint is a limitation of the length of the iteration step as $||\boldsymbol{d}||_2 \leq \Delta$. The iteration is then solved by a constrained minimization of a quadratic problem:

$$\boldsymbol{d} = \arg\min_{\boldsymbol{d}} \mathcal{V}(\boldsymbol{\theta}) \quad \text{such that} \quad ||\boldsymbol{d}||_2 \leq \Delta. \tag{2.67}$$

It is now the Δ parameter that tunes the algorithm convergence of the method by increasing or decreasing its value. Note that the direction of the iteration step is not necessary aligned with the minimum of the quadratic model if the size of the trust-region is lower than the position of the minimum of the model because of the nonlinear norm constraint.

Either the Levenberg-Marquardt or the trust region approach make use of a quadratic model based on the gradient of the objective function. It is then advantageous if it can be computed analytically in order to avoid the use of finite differences to approximate it. The gradient computation (2.64) requires the computation of the derivative of the prediction errors with respect to the model parameters in the $\boldsymbol{\theta}$ vector. This is equivalent to perform the derivative of minus the corresponding predictors of the model:

$$\begin{aligned} \frac{\mathrm{d}\, e^o[t,\boldsymbol{\theta}]}{\mathrm{d}\boldsymbol{\theta}} &= \frac{\mathrm{d}\left(x^o[t] - \hat{x}^o[t,\boldsymbol{\theta}]\right)}{} \\ &= -\frac{\mathrm{d}\,\hat{x}^o[t,\boldsymbol{\theta}]}{\mathrm{d}\boldsymbol{\theta}}. \end{aligned} \tag{2.68}$$

Going back to the modeling with time dependent autoregressive and moving-average polynomials (such as in Equation (2.26)), one has the time-varying relation

$$A(z,\boldsymbol{\theta},\boldsymbol{f}[t])\, x^o[t] = C(z,\boldsymbol{\theta},\boldsymbol{f}[t])\, e^o[t] \tag{2.69}$$

with the time-varying polynomial $A(z,\boldsymbol{\theta},\boldsymbol{f}[t])$ and $C(z,\boldsymbol{\theta},\boldsymbol{f}[t])$ being constructed by the projection of the time invariant coefficient in $\boldsymbol{\theta}$ on their respective basis function in $\boldsymbol{f}[t]$. In [58], Ljung shows how to compute the gradient by filtering the recorded time data. When computing the gradient with respect to the parameter θ_i, two cases are possible. If θ_i belongs to the autoregressive part of the model, all the prediction errors have to be taken into account in the sum because the AR coefficients are constrained to be the same for all the channels. The predictor related to the model (2.69) is given by

$$C(z,\boldsymbol{\theta},\boldsymbol{f}[t])\,\hat{x}^o[t,\boldsymbol{\theta}] = \Big(C(z,\boldsymbol{\theta},\boldsymbol{f}[t]) - A(z,\boldsymbol{\theta},\boldsymbol{f}[t])\Big)\, x^o[t]. \tag{2.70}$$

The derivatives to be performed on the $\hat{x}^o[t,\boldsymbol{\theta}]$ predictor are those concerned by the o^{th} channel, that is the global $a_{i,k}$ autoregressive coefficients in $\boldsymbol{a}$ and the local (channel-dependent) $b^o_{i,k}$ moving average coefficients in $\boldsymbol{b}^o$. We then have the two following cases:

1. Differentiating Equation (2.70) with respect to the projection coefficients $a_{i,\,k}$ of the autoregressive part, one has:

$$C(z,\boldsymbol{\theta},\boldsymbol{f}[t])\,\frac{\mathrm{d}\,\hat{x}^o[t,\boldsymbol{\theta}]}{\mathrm{d}a_{i,k}} = \left(-z^{-i}\, f_k[t]\right)\, x^o[t] \tag{2.71}$$

This result gives:

$$\frac{\mathrm{d}\,\hat{x}^o[t,\boldsymbol{\theta}]}{\mathrm{d}a_{i,k}} = \left(\frac{-z^{-i}\, f_k[t]}{C(z,\boldsymbol{\theta},\boldsymbol{f}[t])}\right)\, x^o[t]. \tag{2.72}$$

2. Similarly, differentiating Equation (2.70) with respect to the projection coefficients $b^o_{i,\,k}$of the moving-average part, one has:

$$z^{-i}\, f_k[t]\, \hat{x}^o[t, \boldsymbol{\theta}] + C(z, \boldsymbol{\theta}, \boldsymbol{f}[t])\, \frac{\mathrm{d}\, \hat{x}^o[t, \boldsymbol{\theta}]}{\mathrm{d} b^o_{i,k}} = z^{-i}\, f_k[t]\, x^o[t]. \tag{2.73}$$

Passing the first term to the other side of the equation, one gets the derivative of the predictor with respect to the moving-average parameters:

$$\frac{\mathrm{d}\, \hat{x}^o[t, \boldsymbol{\theta}]}{\mathrm{d} b^o_{i,k}} = \frac{z^{-i}\, f_k[t]\, x^o[t] - z^{-i}\, f_k[t]\, \hat{x}^o[t, \boldsymbol{\theta}]}{C(z, \boldsymbol{\theta}, \boldsymbol{f}[t])}. \tag{2.74}$$

As it can be seen in Equations (2.72) and (2.74), both the derivatives of the predictor of the model are outputs of filters taking $x^o[t]$ and $x^o[t]$ and $\hat{x}^o[t, \boldsymbol{\theta}]$ as input signals, respectively.

Let us also remark that a large part of the computation may be avoided in the computation of the gradient. By keeping in mind our modeling of the system, the derivative of $V(\boldsymbol{\theta})$ with respect to a parameter θ_i in $\boldsymbol{\theta}$ belonging to one of the coefficients of the moving-average part of the r^{th} channel, only the r^{th} term in (2.64) is to be considered because of its local dependence.

2.3.2 Model structure selection

Up to now, we are able to identify a prescribed model to fit the data. But a question still remains unanswered: what model structure do we have to apply on the data? Parametric identification methods are very powerful and accurate tools but only under the assumption that the model used to fit the data is an adequate one. The choice of the model structure is thus of great importance. Otherwise, the use of a badly chosen model may lead to inaccurate and/or non physical results. In LTI modal analysis, usually one degree of freedom drives the complexity of the model structure: the order of the model which in general is a single parameter in the classical modal identification methods (LSCE, LSCF, SSI, etc...), or a couple of orders for the identification with ARMA models. In order to choose a good model, test engineers are familiar with the concept of stabilization diagram such as the one shown in Figure 1.25. The identification is performed with models of increasing complexity and the identified poles are stacked in a graph with a dedicated symbol giving an information about if they are close or not to their equivalent in neighboring models. In the present case, the quantity of tunable values driving the model structure (AR and MA orders, size of each basis of functions) makes it less practical. Further, the fact that the model properties are time-varying adds an additional dimension to take into account which renders the extension of the concept of stabilization diagram in the context of time-varying identification completely impractical. We then have to look for other alternatives to select a good model structure.

In order to perform a good selection, a series of models are put in competition and the best candidate is chosen based on some discriminating criterion. Of course, a

good candidate should be able to properly fit the input data, so the prediction errors it provides should be minimum. However, increasing the complexity of the model will tend to diminish the prediction error. Indeed, passing the optimal model structure, any additional increase in its complexity begins to "fit" the noise present in the data which are proper to the realization of the experiment and not to the actual system in itself. According to Ljung [58], the choice of a good model is a balance between the the ability to well describe the system and the parsimony of the model to not introduce unnecessary model parameters leading to an overfitting. To this goal, he advises the use of some criteria able to reproduce this balance. The three criteria he proposed are:

The Akaike's Final Prediction Error (FPE): Akaike first used this criteria in [74] as a merit function to discriminate several models in a trying set in order to get the one which is best suited to represent the system. Putting in competition a series of autoregressive models described by their respective order M, he defined the FPE criteria as

$$FPE = \frac{N+M+1}{N-M-1} R_M \tag{2.75}$$

in which R_M is the mean square of the residual sequence and $M+1$ being the number of parameters in each model of order M (the $+1$ is simply due to an additional constant term in addition to the M auto regressive parameters). In our case, for each model, the number of parameters for each model will depend on the autoregressive order, but also on the moving-average one and the dimensions of the function bases used to represent them. One will generally denotes by $d_{\mathcal{M}}$ the dimension of the vector of parameters of the model structure $\mathcal{M}$. According to this notation, the FPE criterion is computed as follows after our identification processes:

$$FPE = \frac{1+\frac{d_{\mathcal{M}}}{N}}{1-\frac{d_{\mathcal{M}}}{N}} V(\boldsymbol{\theta}^*_{\mathcal{M}}) \tag{2.76}$$

where $V(\boldsymbol{\theta}^*_{\mathcal{M}})$ is the value of the mean squares of the residuals which is minimized for the optimal set of parameter $\boldsymbol{\theta}^*_{\mathcal{M}}$. Looking at the two factors of Equation (2.76), one can observe that the first factor is an increasing function of the complexity of the model. It thus penalizes an overfitting of the model. The second is obviously a decreasing function as the model better fit the data. This expression then translates the trade-off between accuracy and parsimony in a mathematical way.

The Akaike's Information Criterion (AIC): Akaike defined the AIC criteria in an extension of the maximu-likelihood estimation procedure in [75]. The mathematical description of the criterion also computes a balance between the precision of the fitting of the model and its complexity. It is given as follows for the identification of models in the maximum-likelihood framework:

$$AIC = -2 \ln L\left(\boldsymbol{\theta}^*_{\mathcal{M}}\right) + 2\, d_{\mathcal{M}} \tag{2.77}$$

where $L\left(\boldsymbol{\theta}^*_{\mathcal{M}}\right)$ is the likelihood function of the model. The criterion can also be used in least-squares estimates under the assumption of Gaussian distribution of

the innovation sequence [58]. It is given by using the mean square errors criterion used in the optimization instead of the likelihood function:

$$AIC = \ln V(\boldsymbol{\theta}^*_{\mathcal{M}}) + \frac{2\, d_{\mathcal{M}}}{N}. \tag{2.78}$$

It is the latter equation that will be used in the following.

The Bayesian Information Criterion (BIC): This criterion was proposed by Rissanen in [76] under the name of Minimum Length Description (MLD) criterion. The BIC criterion can be written as follows (again with the assumption of Gaussian innovations):

$$BIC = \ln V(\boldsymbol{\theta}^*_{\mathcal{M}}) + d_{\mathcal{M}} \frac{\ln N}{N}. \tag{2.79}$$

The first term of both the AIC and BIC is similar, the difference comes from the penalization of the model complexity. It appears that the BIC criterion has a stronger penalization of the overparameterization than the AIC.

2.3.3 Physical poles selection

The stabilization diagram in LTI modal analysis helps to choose a good model order but is also useful for the discrimination between physical and spurious poles coming with the overparameterization of the problem. Ideally, in perfect conditions, a good model order in a modal analysis method should be equal to twice the number (because of the complex conjugated pairs) active modes in the recorded data set. But generally, restricting the model to this structure does not give satisfactory results and model structures with a higher complexity have to be considered.

Once a good model is selected, if its order enables it to identify more time-varying pole trajectories than the actual number of active modes in the system, one has to choose whose are physical and whose are spurious for the extraction of the modal deflection shapes. This discrimination between physical/spurious poles in time-varying conditions was tackled by Beex and Shan for the identification of frequency-modulated (FM) signal in noisy data with a time-varying AR modeling and the basis function approach [77]. The proposed idea is simple. Let's assume that our model is of order M, it is then able to identify M pole trajectories in time. Let's also assume that in this set, only p poles have a physical meaning ant the other $(M - p)$ poles are numerical ones, coming from the excess of parameters in the model. The idea in the selection process, is to look to the radius distribution of all the discrete poles trajectories. The discrimination is then performed by the property that the poles corresponding to FM component should travel on the unit circle. The unit radius is due to the constant amplitude of the FM components and their varying angle represents their variation in frequency. The trajectories associated to spurious poles are larger and sweep wider radius values. The radii of the poles being representative of their damping, values close to one correspond to lightly damped modes. This kind of discrimination based on low damping is also used by Reynders *et al.* as one (among various other) criteria in an attempt to automatize the pole selection in the stabilization diagram [78]. They

assume that a hard criteria that physical poles must meet is that their damping should be strictly positive and lower than a threshold value (that may depends on the problem to analyze). Such a criterion then makes sense in our case assuming that physical modes have low damping with respect to spurious ones even in the time-varying case. A remark may however be drawn here. Conversely to the LTI case, the varying pole trajectories have not to be considered lying strictly inside the unit circle in time-varying conditions [61]. They may not respect that constraint in some cases without affecting the stability of the time-varying system.

2.3.4 Time-varying modal analysis

We now apply the whole methodology described above on the same data as in Section 1.5 for the nonparametric identification. This will help us to compare the results obtained with both methods. The identification is performed as follows. First the system is roughly studied with the 2SLS method for a large variety of model structures because of its faster computation time. The discriminating criteria (FPE, AIC and BIC) are then computed on the large set of results in order to find good model candidates for a more detailed analysis. The latter one is performed using the iterative optimization scheme on the reduced set of model structures. Once the physical frozen-poles are precisely identified, the modal deflection shapes are extracted by the Vold-Kalman filter in a non parametric way, exactly as what was done in the previous chapter.

Rough analysis and model structure selection by the 2SLS method

In order to select one or few model structures for the subsequent more detailed analysis, a batch of 2SLS identifications of the system is performed on a set of model structures in which the "good" model is assumed to be present. First, a class of basis functions has to be chosen for the analysis. In the present case, a basis of increasing number of Chebyshev polynomials is chosen. Note that this choice is a bit arbitrary here. Indeed, the trajectory of a parameter can be approximated using different kind of functions with an equivalent precision. The difference is that the number of functions to consider may differ from a kind of basis to another. Without any particular physical information about how the system parameters vary (periodically varying, abrupt variations, ...) there is, a priori, no particular choice of functions that are better suited than others. Note also that, even if the trajectory of the resonance frequencies draws some kind of periodic motion, especially at higher frequencies, we have to keep in mind that these are the ARMA parameters that are modeled by the basis functions approach and not the poles. The latter one are computed as the roots of the AR polynomial and a direct intuition of how they relate one with each other is not trivial. This means that a Fourier series may of course be chosen as function basis, but nothing tells that it could be better than another without comparing the results.

The batch analysis on various model structures is performed as follows using a "for loop" notation:

for $n_a = 10$ to 30 by step of 2

for $n_b = n_a - 1$ to na

for $n_{f_a} = 5$ to 13

for $n_{f_b} = 1$ to n_{f_a}

Perform the identification with a model structure defined by the n_a, n_b, n_{f_a} and n_{f_b} parameters and compute the value of each of the FPE, AIC and BIC criteria.

end

end

end

end

The choice of starting the iterations of the AR order at ten is simply due to the presence of five modes in the frequency band. A lower value would be useless because all the modes could not be identified. For the same reason, the iterations are done by step of two in order to introduce an additional pair of poles at each iteration. The choice not to start the number of the basis functions for the AR part at one is simply due to the fact that the system configuration is actually varying with a certain complexity so a too low number of basis functions would obviously not be sufficient. It is arbitrary fixed to five in this case. If the following analysis of the discriminating criteria between models would not show a minimum, the upper and lower limit values for the size of the basis functions should be considered, as long as a possible increase of the maximum AR order. The considered MA orders do not start to 1 either. Indeed, in [79], Andersen *et al.* demonstrate the relationship between equivalent ARMA models in various cases, especially for the determination of the theoretical model orders to consider. They considered univariate modeling of SDOF systems, multivariate modeling of MDOF systems and univariate modeling of MDOF systems. This is the latter case that is of interest in this chapter because we deal with univariate models aiming to identify several excited modes in the data. The result is that, in theory, in order to identify a n-DOF system, an ARMA model of orders $(2n,\ 2n-1)$ should be considered. If some measurement noise is present in the data, an increase in the MA order should be considered and ARMA$(2n,\ 2n)$ model used for the identification.

The evolution of the FPE, AIC and BIC criteria is depicted in Figure 2.3. Looking to that figures, some comments may be drawn. The first one, is that there is no clear minimum for each criteria. At best, one cans select a set of model structures sharing close values of the criteria. Let us note that the values are not directly sorted by increasing complexity and that the values of each criterion evolves by following some kind of repeated patterns. Each of them indeed corresponds to either an $ARMA(2n,\ 2n-1)$ or $ARMA(2n,\ 2n)$ structure and the internal "sawtooth" evolution inside the patterns corresponds to the variation of the size of the functions bases for each of the AR and MA parts. It is also noticeable, as stated above, that the BIC criteria is more penalizing the model complexity than the FPE or BIC criteria whose follow a very similar

FPE / AIC						BIC					
Model index	$d_{\mathcal{M}}$	n_a	n_b	n_{f_a}	n_{f_b}	Model index	$d_{\mathcal{M}}$	n_a	n_b	n_{f_a}	n_{f_b}
1586	700	28	28	11	2	837	313	20	19	9	1
1597	728	28	28	12	2	846	333	20	19	10	1
1598	924	28	28	12	3	856	353	20	19	11	1
1609	756	28	28	13	2	867	373	20	19	12	1
1610	952	28	28	13	3	879	393	20	19	13	1
1667	736	30	29	11	2	918	320	20	20	9	1
1668	939	30	29	11	3	927	340	20	20	10	1
1678	766	30	29	12	2	937	360	20	20	11	1
1679	969	30	29	12	3	948	380	20	20	12	1
1690*	796	30	29	13	2	960	400	20	20	13	1
1691	999	30	29	13	3	999	345	22	21	9	1
1748	750	30	30	11	2	1008	367	22	21	10	1
1749	960	30	30	11	3	1018*	389	22	21	11	1
1759	780	30	30	12	2	1029	411	22	21	12	1
1760	990	30	30	12	3	1041	433	22	21	13	1
1771	810	30	30	13	2						
1772	1020	30	30	13	3						

Table 2.1: List of potential model structure candidates based on the FPE, AIC and BIC criteria. Chebyshev polynomials are used as basis functions. The models depicted with a $\star$ correspond to the global minimum in the criteria.

evolution. A first set of potential good candidates are chosen by taking the model candidates close to the neighborhood of the minimum values in each criterion. Those are shown in Figure 2.3 as blue circles and they are tabulated in Table 2.1. The chosen model candidates give here a first indication on the model structures to be used in the subsequent analysis.

Looking to Table 2.1, it seems that models with AR order equal to 20 to 22 and MA orders from 19 to 21 could be suitable for the identification according to the BIC criterion. AR and MA orders from 28 to 30 are them selected using the FPE and AIC criteria. It is clear that, for each criteria, the theoretical value for the model order is well overshot. This is due to two factors: the noise present in the experimental data, but the sampling frequency also brings an increase in the model orders. In [80, 81], Smail *et al.* study the influence of the noise and the sampling rate of the data on the selection of the best model order to consider. They show that a too high level of noise in the data requires higher order models to perform a good identification, but, more interestingly, they also show that the sampling rate of the data has also a great influence. Ideally, they advise to choose a sampling frequency from three to ten times the frequency of interest in the data [80]. Some difficulties may appear if several

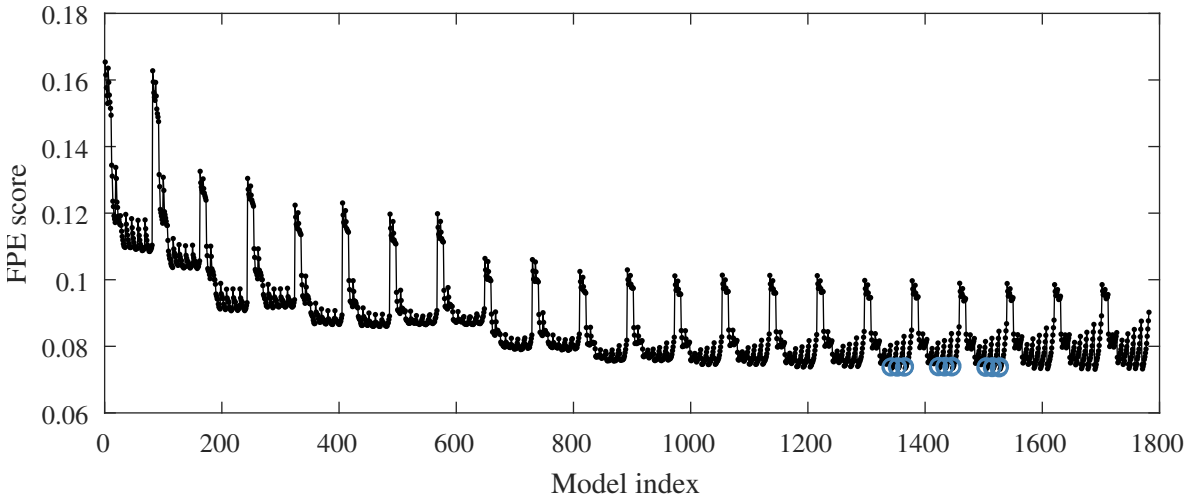

(a) FPE scores for the large batch od model candidates.

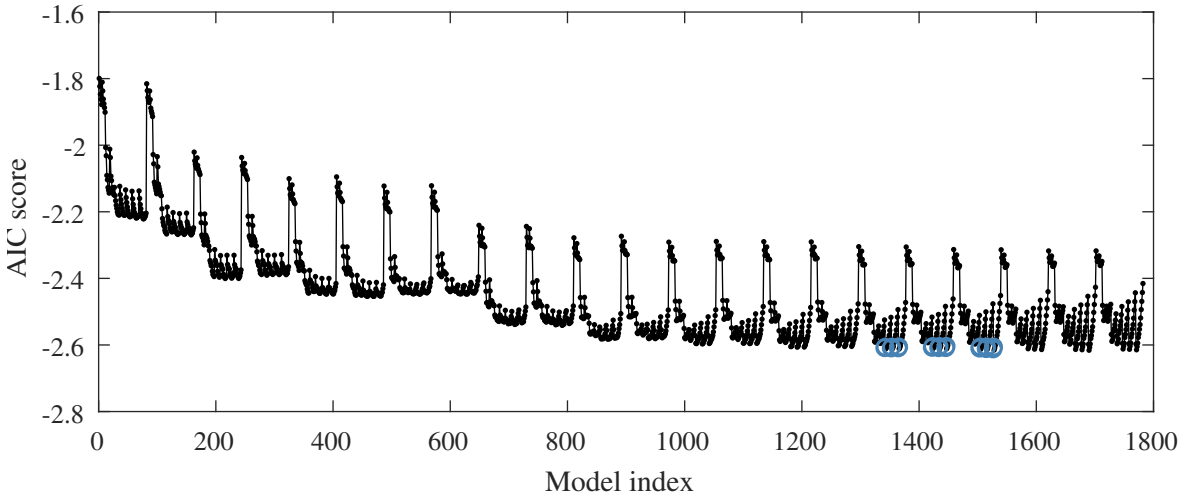

(b) AIC scores for the large batch od model candidates.

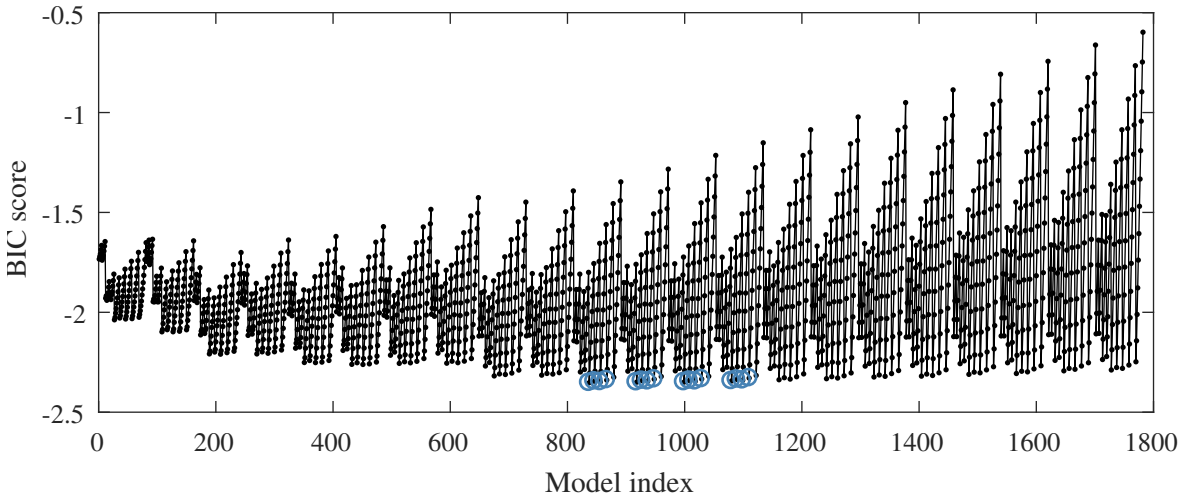

(c) BIC scores for the large batch od model candidates.

Figure 2.3: Good model structures candidates are selected based on the values of the FPE, AIC and BIC criterion. Chebyshev polynomials are used as basis functions.

frequencies (modes) are spread in a large frequency band. Of course, the sampling frequency has to be chosen in order to cope with the highest frequency we want to observe, but in that way, the higher the sampling frequency the lower the part of the period corresponding to low frequency is covered by the regression vector. The effect of high sampling frequencies is that the modes at higher frequencies are easily identified with the theoretical order in the model, but the modes at lower frequencies require an increase in the model order to be caught. This is even more true as the interval between the lowest and highest frequencies increases. Figure 2.4 illustrates the phenomenon.

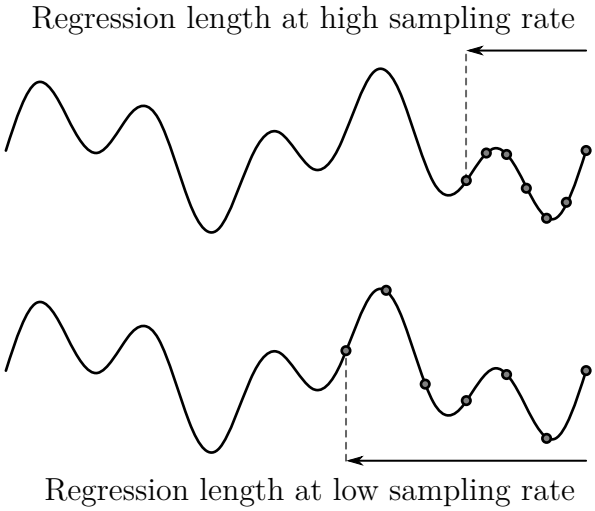

Figure 2.4: Comparison of the regression lengths for a fixed model order with low and high sampling frequency of the data.

Concerning the size of the functions bases, 9 to 13 functions seem to be good sizes for the AR part of the model, but quite surprisingly, only bases up to 3 Chebyshev polynomials seem to be sufficient to model the MA part. This is surprising because the MA part models the valleys in the spectrum and, at least in the wavelet spectrum corresponding to channel 2, there is a valley between the two last modes with a time-varying evolution comparable in complexity with the one of the higher frequency mode. We should then have a higher number of functions employed to model the MA part. The MA part of the model seems to be more discriminated than the AR one. It is suspected that this behavior could be due to the unequal importance of each model structure parameter on the complexity of the whole model. Indeed, because of the equality constraint of the AR parameters but not on the MA ones, one has:

- a unit increase in the AR order adds n_{f_a} new parameters to the model,
- a unit increase in the AR functions basis adds n_a new parameters to the model,
- a unit increase in the MA order adds $n_o \times n_{f_a}$ new parameters to the model,
- a unit increase in the MA functions basis adds $n_o \times n_a$ new parameters to the model,

where n_o is the number of output measurement channels. Because of this difference, the complexity of the MA part is more penalized as long as we have more than one measurement channel. A zoom on one pattern of the evolution of the BIC criterion is shown in Figure 2.5 where the drastic increase in the BIC value when additional basis functions are considered in the modeling of the MA part is clearly visible.

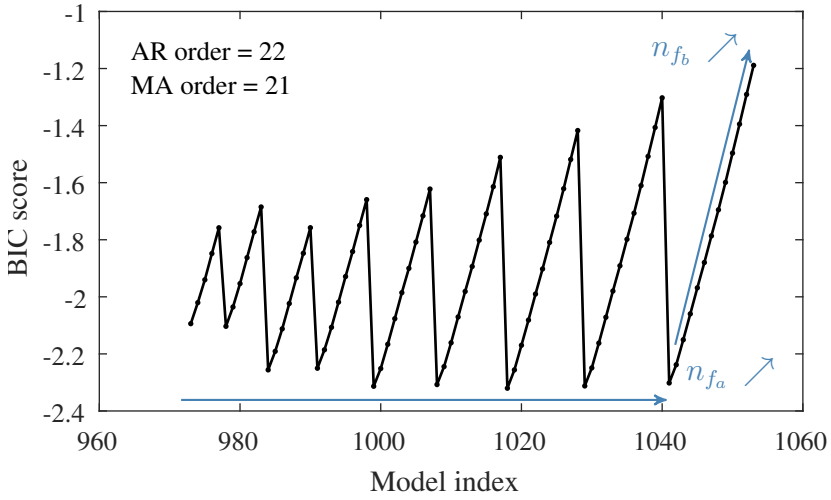

Figure 2.5: Zoom on the BIC criterion for the model structure with AR and MA orders fixed at 22 and 21, respectively. The variations of the BIC values are due to the increase in both n_{f_a} and n_{f_b}.

In order to find a better value for the MA modeling, an alternative criterion is used: the Residual Sum of Squares over the Signal Sum of Squares (RSS/SSS). This is simply the square of the residuals normalized by the signal amplitude. Conversely to the previous criteria, it does not penalize the overparameterization because each increment in the model complexity enables to decrease the residual sequence. In Figure 2.6, the RSS/SSS ratio is plotted four times, one with respect to a fixed value of each of the model structure parameter. Additionally, the median value of each column is plotted to better see the global decreasing trend. In Figure 2.6(a), the AR order of 22 as identified by the BIC criterion seems to be a good value, even if no clear gap is observed on the RSS/SSS value. In Figure 2.6(b) related to the MA order, the values of the criterion between couples $(2n,\ 2n-1)$ and $(2n,\ 2n)$ do not differ a lot. A MA order at 21 is then chosen. In Figures 2.6(c), the last noticeable gain in accuracy is obtained once at least 9 Chebyshev polynomials are contained in the basis, which is in accordance with the BIC criterion. Finally, no clear gap is visible in Figure 2.6(d) to identify a good size for the MA basis but adding more than 9 functions does not bring a great gain in accuracy. Further, with at least 9 functions one also may observe a large decrease in the dispersion of the RSS/SSS values, which can indicate it could be a good choice.

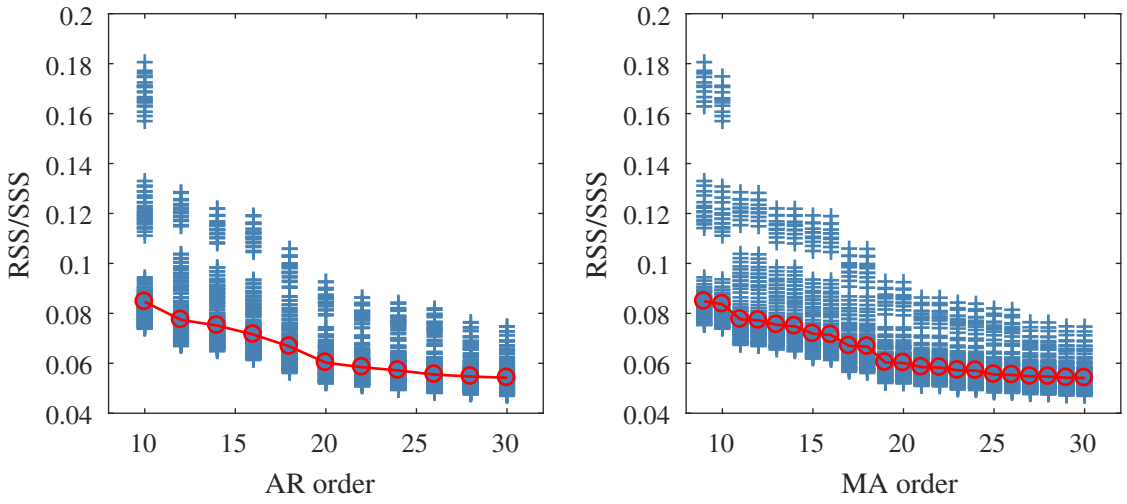

(a) RSS/SSS vs n_a.

(b) RSS/SSS vs n_b.

(c) RSS/SSS vs n_{f_a}.

(d) RSS/SSS vs n_{f_b}.

Figure 2.6: RSS/SSS values with respect to each of the model structure parameter.

Accurate identification by the optimization process

The chosen model structure candidate being fixed with the following parameters: $n_a = 22$, $n_b = 21$, $n_{f_a} = 9$ and $n_{f_b} = 9$, the estimation of the model parameters based on the nonlinear optimization process may be performed. The obtained results are illustrated in the following figures. First, Figure 2.7 shows the identified frozen frequencies of the system. It can be seen in Figure 2.7(a) that the procedure for the discrimination between physical and spurious poles gives good results by looking to the black (physical) and gray (spurious) poles and frequencies in both 2.7(a) and 2.7(b).

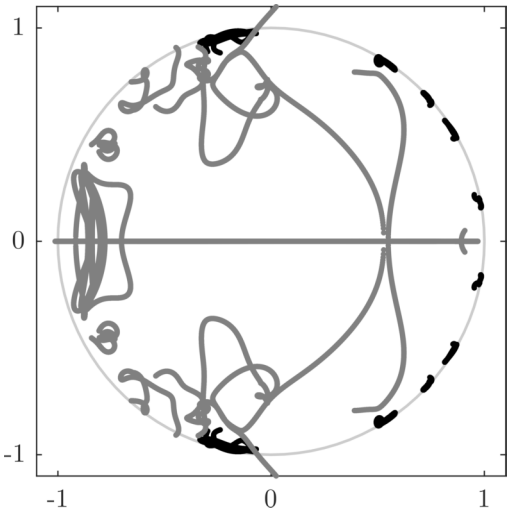

(a) Poles trajectories in the complex plane. Black: poles selected as physical, gray: poles selected as spurious.

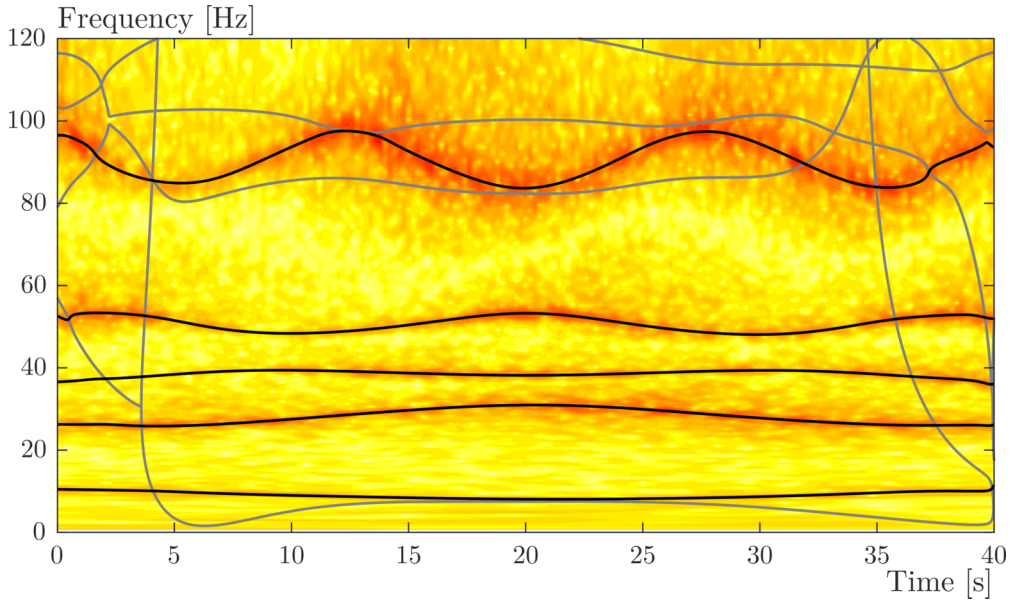

(b) Identified frequencies. Black: frozen frequencies associated to the physical poles, gray: frozen frequencies associated to the spurious ones.

Figure 2.7: Frozen-time frequencies identified through the time-varying parametric model.

Because the frozen poles are identified, besides the frequencies, the damping ratio's of the structure may also be obtained. Given a pole λ_r (in the continuous time domain and under general viscous damping assumption), its related frequency and damping ratio are given as follows [48]:

$$\lambda_r = -\zeta_r \omega_r - i\sqrt{1-\zeta_r^2} \tag{2.80}$$

$$\omega_r = |\lambda_r| \tag{2.81}$$

$$\zeta_r = -\frac{\mathrm{Re}\,(\lambda_r)}{\omega_r} \tag{2.82}$$

The damping ratios identified for the five modes are shown in Figure 2.8. It is more difficult to compare the damping with the previously obtained values in the LTI analysis. First, because the damping is generally the identified parameter with the lower accuracy, but also because the motion of the mass directly affects the value of the damping ratios. This phenomenon is shown by Ma *et al.* in [82] where they built a dynamical model of a similar beam with a moving mass problem. They show that, in addition to the position, the velocity and the acceleration of the moving mass impact the dynamics of the system. In their example, the velocity has an effect on both the damping and stiffness matrices but its effect is mainly visible on the damping of the system. The acceleration affects only the stiffness matrix.

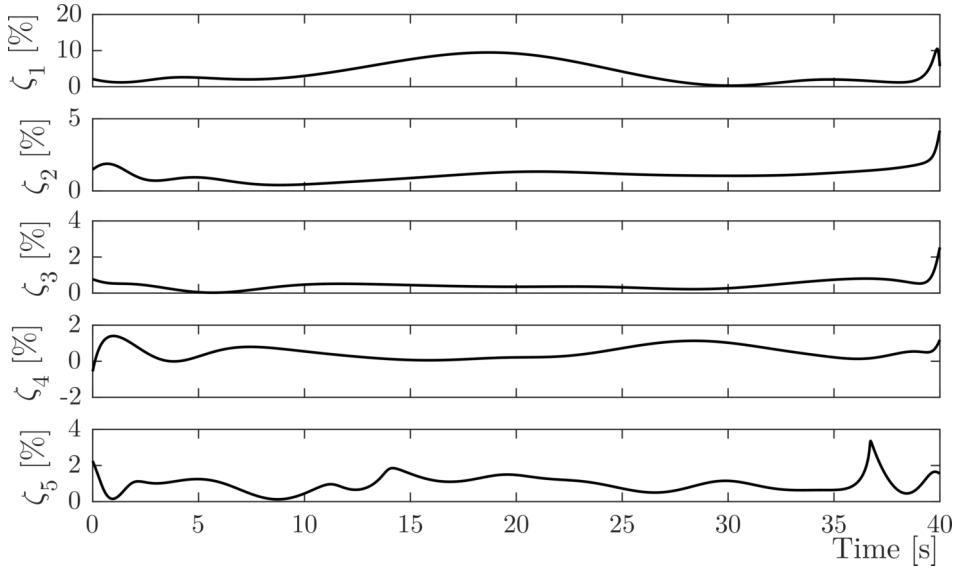

Figure 2.8: Time-varying evolution of the frozen damping ratio's of the structure corresponding to the identified frozen poles.

A word about model validation

When dealing with model based identification, the validation of the model is important. There are many ways to perform this task. However in the present case, the possibilities are limited for several reasons:

- The usual methods based on cross-validation are not adapted in our case. The method assumes that we can split all the data in two sets, one used for the identification and the other one used to validate the identified model. This method is not possible here because of the nonstationarity of the process which prevents such a decomposition neither by cutting a small part of the data, nor by reproducing the experiment because we deal with operational conditions.

- Another way to asses the quality of the model is to simulate the output response of the identified model with the input data and compare them with the measured ones. For the same reason as above, due to the absence of input data because of the operational condition, that is not possible either.

- Other strategies rely on the analysis of the residuals after the identification. But here again, some techniques as the whiteness test of the residual sequence are not possible due to the nonstationarity which can induce a time variation in its variance.

In time-varying condition, Poulimenos and Fassois [50] propose to use a simple test on the residual sequence in order to know if they are representative of a usual random sequence or not. Draper and Smith [83] explain this test which is simply based on the analysis of the signs in the residual sequence and how they are ordered without taking their amplitude into account. A statistical test is then performed in order to know if the sequence is usual for a zero-mean uncorrelated random sequence or not. The main idea is the following one. First, the sequence of residuals is analyzed in terms of number of occurrences of positive, n_1, and negative, n_2, residuals and of number of "runs", r (a run designating a sequence of residuals with the same sign). In the case of sufficient samples, an estimate of the mean value and variance of the discrete distribution of the number of runs in a random sequence may be computed based on the numbers n_1 and n_2 as follows:

$$\mu = \frac{2n_1n_2}{n_1+n_2} + 1 \tag{2.83}$$

$$\sigma^2 = \frac{2n_1n_2\left(2n_1n_2 - n_1 - n_2\right)}{(n-1+n_2)^2\left(n_1+n_2-1\right)} \tag{2.84}$$

If the number of samples is sufficiently large, the comparison can be performed based on a normal distribution. The comparison is split into a lower and an upper case depending if the actual number of runs is lower or higher than the estimated mean value in the same condition (same number of positive and negatives residuals). For each case, a unit normal random variables z_l or z_u is computed for the test with the normal distribution as follows:

$$z_l = \frac{r-\mu+1/2}{\sigma} \tag{2.85}$$

$$z_u = \frac{r-\mu-+1/2}{\sigma} \tag{2.86}$$

and the probability to have less or more runs based on the same number of positive and negative residuals is computed. If this probability is under a chosen threshold, the

Channel #	n_1	n_2	r	μ	
1	6442	6359	6374	6401.2	31.8 % probability to have a lower number of runs.
2	6405	6396	6317	6401.5	6.9 % probability to have a lower number of runs.
3	6339	6462	6376	6400.9	33.3 % probability to have a lower number of runs.
4	6424	6377	6322	6401.4	8.2 % probability to have a lower number of runs.
5	6387	6414	6376	6401.5	32.9 % probability to have a lower number of runs.
6	6405	6396	6390	6401.5	42.3 % probability to have a lower number of runs.
7	6410	6391	6433	6401.5	29.2 % probability to have a higher number of runs.

Table 2.2: Detailed results for the sign test in each channel.

residual sequence is considers as unusual for a random sequence, which may imply the invalidation of the model.

The statistical test may be illustrated as follows. Let the following sequence be the signs of the residuals obtained after the identification of the model:

$$(+)(--)(+++)(-)(++++)(--)$$

It is composed of 8 positive and 5 negative residuals ordered in 6 runs. It is easily understood this kind of arrangement is more usual for a random sequence than extreme ordering as

$$(+++)(-----)(+++++)$$

or

$$(+)(-)(++)(-)(+)(-)(++)(-)(+)(-)(+)$$

The two latter cases may indicate some correlation in the residual data meaning that the identification procedure missed something.

As a practical example, let us consider the residual of channel 2. In this sequence there is actually $n_1 = 6405$ residuals with a positive value and $n_2 = 6396$ residuals with a negative value in $r = 6317$ runs. At first sight, there is approximately the same number of positive and negative values as it is generally the case for a random sequence. Based on n_1 and n_2, the computed mean and standard deviation for the number of runs equal $\mu = 6401.5$ and $\sigma = 56.57$. r being lower than μ the lower tail test is applied. Computing z_l and comparing it to a normal distribution one gets a value of $z_l = -1.49$ which means that there is 6.9 % chance of occurrence to have a lower number of runs with a similar number of positive and negative residuals. This is a low probability but far to be negligible. With such a value we could validate the result of the identification.

The same operation is performed with the residual sequence of all the measurement channels to fully validate the combined identification. The position in the normal distribution of each sequence of residuals is shown in Figure 2.9. The detail of the sign tests in each channel is also tabulated in Table 2.2. As it can be observed in both Figure 2.9 and Table 2.2, the model validity can be accepted.

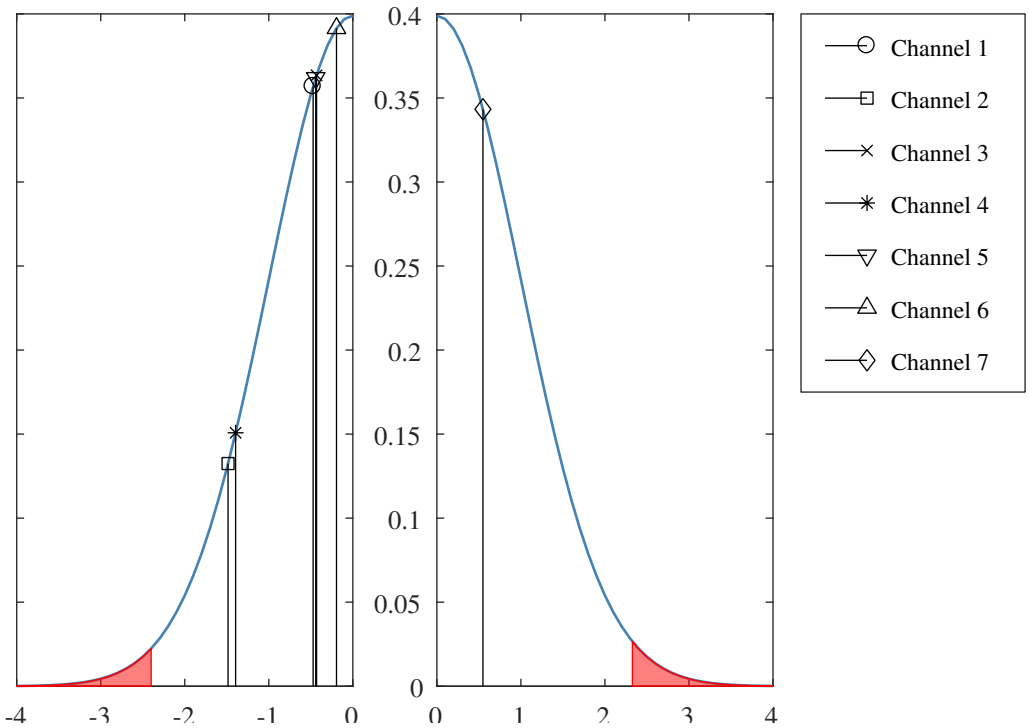

Figure 2.9: Sign test validation for the residual sequences in each measurement channel. The rejection criteria is fixed at 1% chance to have less or higher runs in each distribution tail.

Additionally to the sign test, the computation of the wavelet spectrum of the residual sequence may indicate if a remaining oscillatory component is still present or not. Figure 2.10 represents the time-frequency plot of the residual in the second channel. As it can be observed, no oscillatory component is visible, which is also a good clue for the validation of the model because it means that all the dynamics of the system is taken into account in the predictor of the model.

Comparison with the nonparametric approach

Let us now compare the results obtained by both the parametric time-varying ARMA model and the nonparametric method based on the Hilbert transform of the previous chapter with respect to the frequencies and modal deflection shapes. First, concerning the time-varying frequencies, Figure 2.11 plots the identified frequencies obtained by both methods on top of the wavelet spectrum of the second channel. It can be seen that the matching between the two set of frequencies is quite good. This comparison is important because this good agreement between the parametric frozen-time frequencies and the nonparametric instantaneous frequencies also increase the confidence in the assumption of slow variation enabling the use of the frozen-time approach.

Second, the two sets of time-varying modal deflection shapes are compared using the time-varying MAC criterion as in Section 1.5.2 but considering here that the two sets of modes are varying. The time-expanded MAC matrix is illustrated in Figure 2.12. As it can be shown, the paired modes show (quasi-)monochromic black rows,

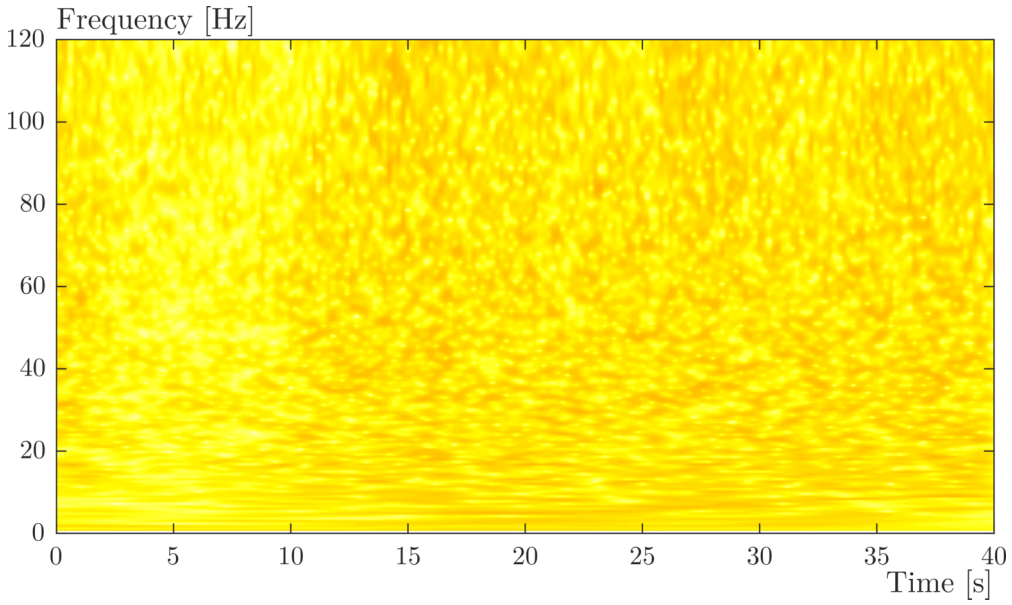

Figure 2.10: Time-frequency representation of the residual sequence of the second channel. Each active mode in the frequency band of interest is properly modeled and extracted from the measurement data.

which indicates a good matching between them all along the time axis. Second, the amount of cross correlation is also quite weak. To better evaluate the correlation between corresponding modes, the values of each correlated pair are also plotted in Figure 2.13. As expected by the shape of the full time-varying MAC matrix, the values of each correlated pair is most of the time equal to one. This is not surprising because the deflection shapes are extracted with the same Vold-Kalman filter based on quite similar reference frequencies. The few drops in correlation may also be explained as before as troubles in the extraction procedure when the instantaneous amplitude of the corresponding mode in the actual signal is close to zero.

The comparison between the data and the identified model may also be performed by looking to the time-varying power spectral densities calculated with both nonparametric methods, such as the wavelet transform (to form a scalogram) on the data or by synthetizing it with the model such as

$$S^o_{ARMA}[t,\,\omega] = \left| \frac{1 + \sum_k b^o_k[t]\, e^{-k\, i\omega T_s}}{1 + \sum_k a_k[t]\, e^{-k\, i\omega T_s}} \right| \sigma^2_{e^o}[t] \tag{2.87}$$

with the ratio of both the AR and MA polynomials modulated by the time-varying variance of the residual sequence of the current channel. The time-varying variance of the residual may be empirically calculated by sliding a time window on the data assuming a short-time stationarity of the variance over $2K+1$ time samples:

$$\sigma^2_{e^o}[t] = \frac{1}{2K+1} \sum_{\tau=t-K}^{t+K} e^{o2}[\tau, \boldsymbol{\theta}]. \tag{2.88}$$

The comparison is presented in Figure 2.14 with a common colorbar for both their amplitude.

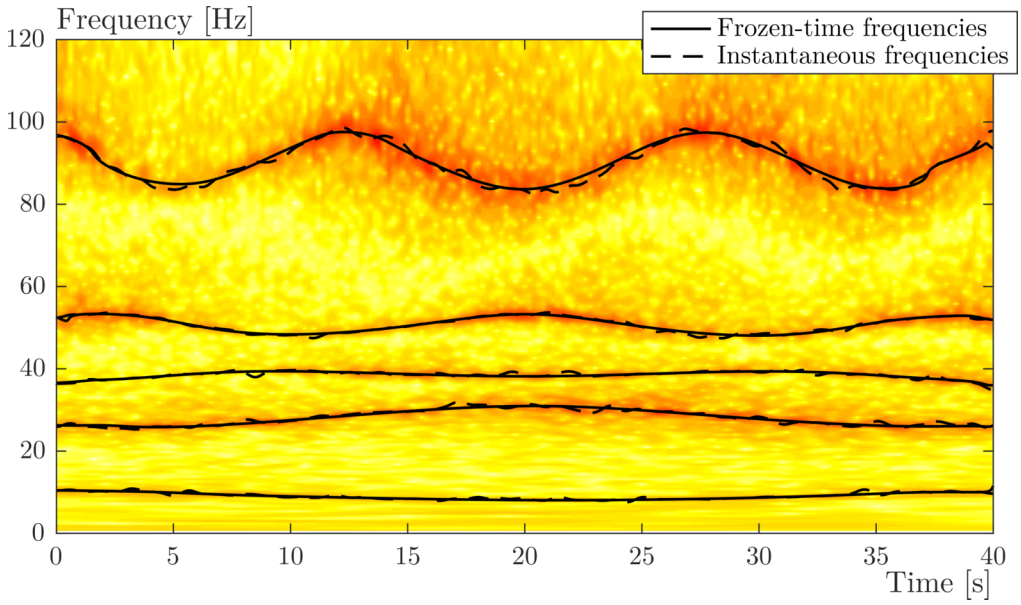

Figure 2.11: Comparison of obtained frequencies with both methods.

2.4 Concluding remarks

This chapter presented a way to parametrically model time-varying systems in view of modal identification. This step is used to straighten the step of the identification of time-varying frequencies with a model-based approach while the modal deflection shapes remain computed with the nonparmetric Vold-Kalman filter.

Based on existing work on the modeling of time-varying univariate ARMA models with the basis function approach, multiples measurement channels are here taken into account by a common modeling of the autoregressive part of each channel. The method is validated by comparison with the results computed with the nonparametric methods of the previous chapter. In this comparison, the difference between the nonparametric instantaneous frequencies and the frozen-time ones is compared. The good matching we obtain confirms that the assumption of slowly-varying rate of the system properties enabling the use of the frozen-time approach is valid.

Because we are dealing with noisy measurements and because several modes are spread in a large frequency band, it is also observed that the model structures enabling a good identification largely overparameterize the system compared to the theoretical orders for such a system. This overparameterization brings its part of spurious results that have to be eliminated. The very simple discrimination based on the difference in radii dispersion of the physical and spurious poles shows good performances for this task.

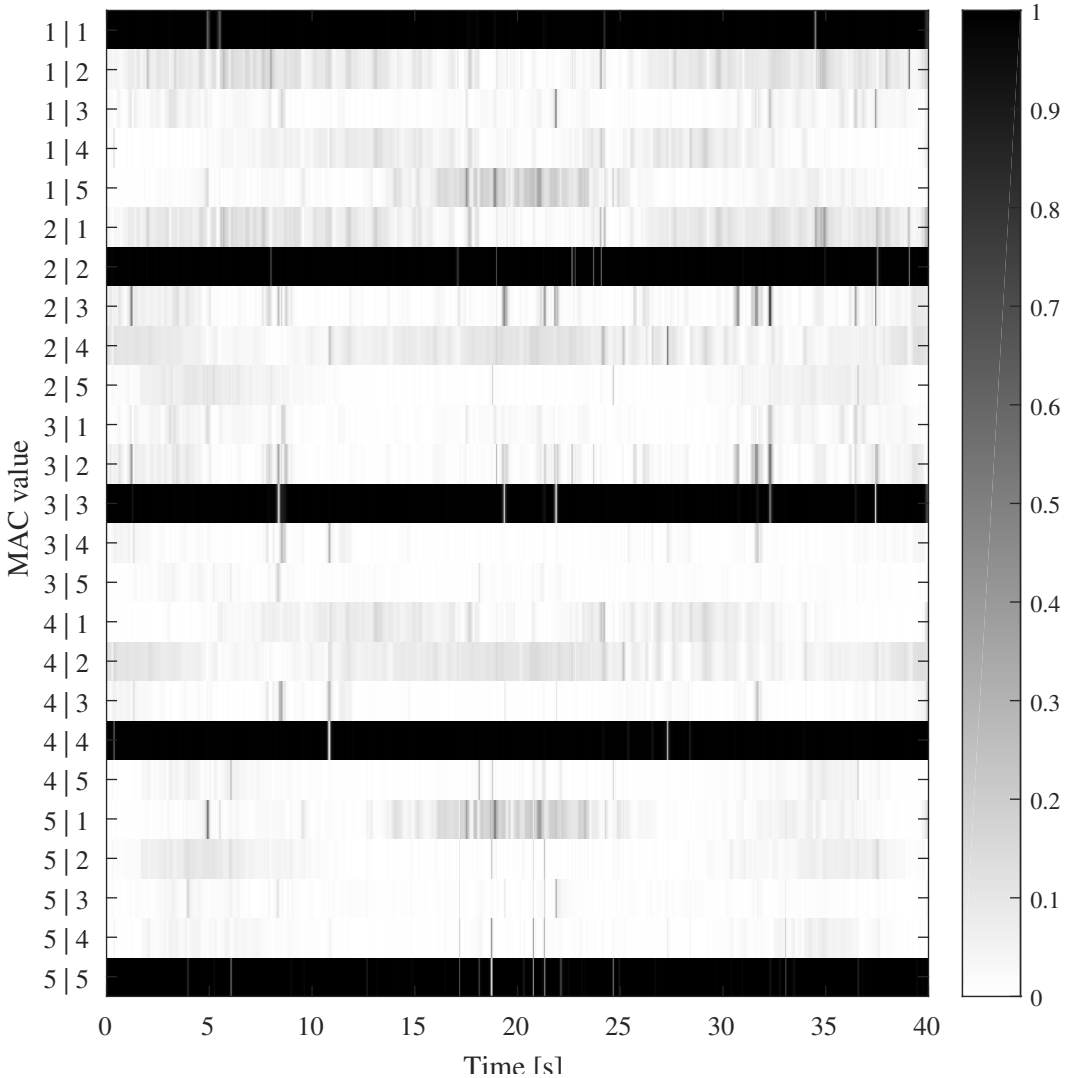

Figure 2.12: Time-varying modal correlation between the time-varying modes obtained with both methods.

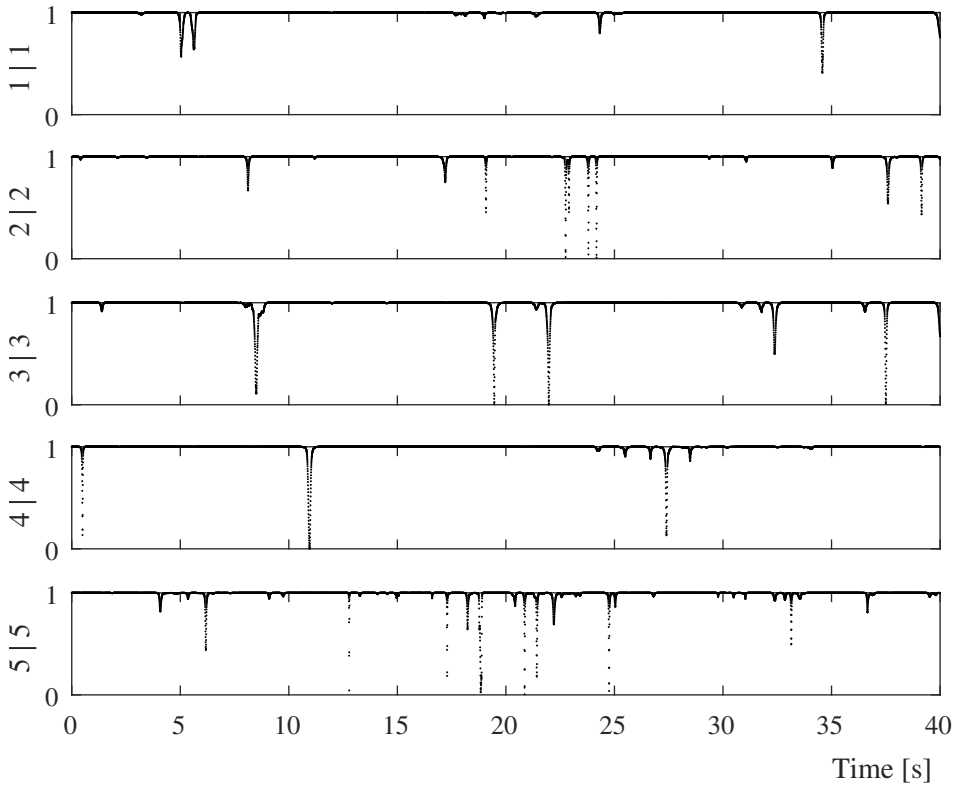

Figure 2.13: Pairwise correlation between corresponding modes.

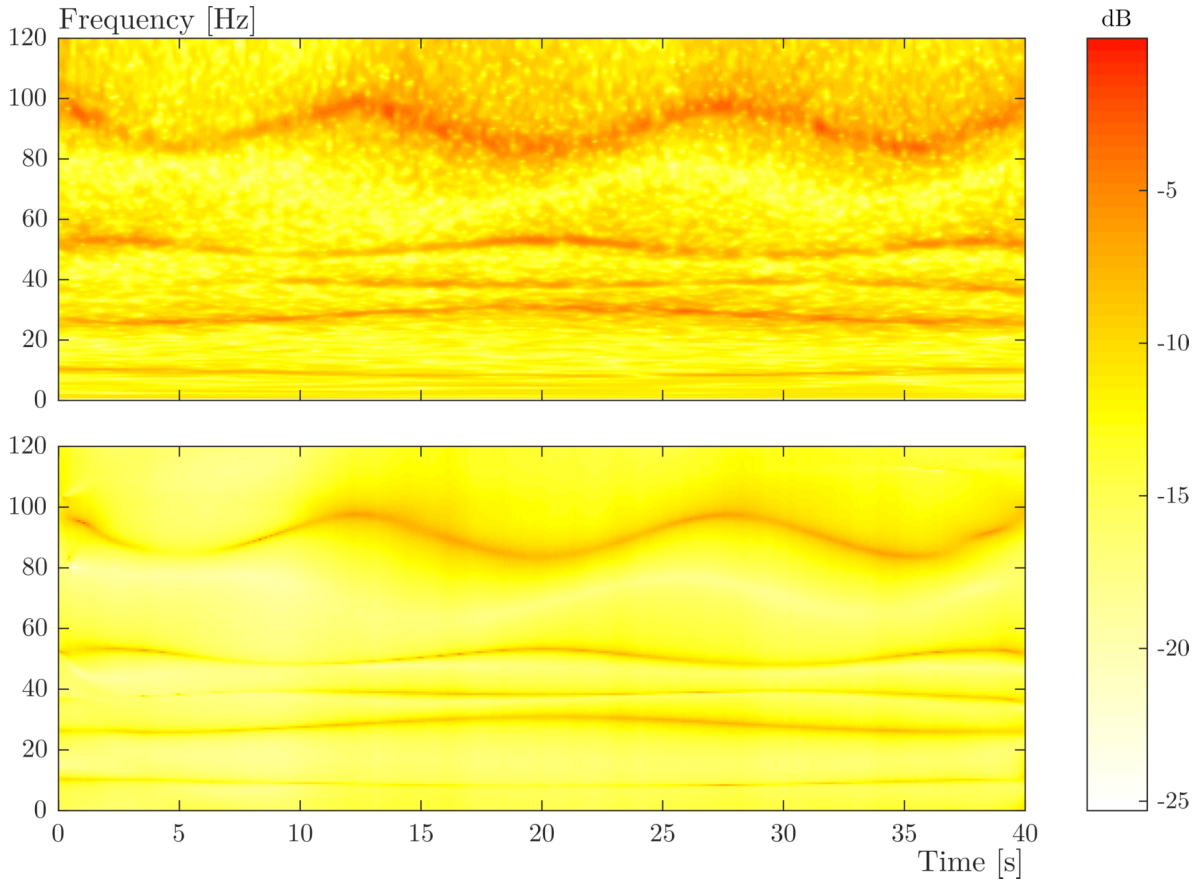

Figure 2.14: Comparison of the time-varying PSDs between nonparametric and model-based approaches. Top: scalogram with the wavelets spectrum, bottom: computed with (2.87).

3

Multivariate parametric modeling

This chapter is concerned by the multivariate modeling of time-varying systems for their identification. The multivariate modeling is a natural extension of the univariate one presented earlier when multiple records are available. The method presented in the previous chapter uses scalar models with a common autoregressive part in order to treat the multiple measurements available. In the multivariate case, vector models are used, meaning that the measured quantities are treated as vectors instead of scalars and the identification models are thus composed of matrix quantities. The goal of the identification is then to identify all the coefficients of the matrices of the model. The interesting aspect about considering multivariate models is that they give acces to the full set of modal parameters by providing the mode shapes in addition to the poles of the system. Scalar methods usually require an additional method to compute the mode shapes. In LTI modal analysis, the Least Squares Frequency Domain (LSFD) [84] method is often used to compute the mode shapes of the system based on a set of a priori estimated poles and a set of FRFs measurements. The scalar method proposed in the previous chapter works in the same way. The scalar ARMA model provides information about the time-varying poles and an additional method, the Vold-Kalman Filter, is used to compute the varying deflection shapes a posteriori.

The question to know if multivariate models have to be considered depends on the application and on the needs of the identification. If only the frequencies and/or the damping information are wanted, it may not be necessary to rely on multivariate identification schemes and scalar models may be sufficient. The multivariate modeling has several advantages with respect to the univariate one but it also brings some drawbacks. The mode shapes being a part of the model, they are directly identified without requiring the application of other methods for that purpose. This kind of modeling is also beneficial when there is a strong relationship between the different variables and multivariate models in modal analysis have better performance in the identification of closely spaced modes. The identification of local modes is also improved with respect to scalar models. Note that the local modes may also be observed with scalar models as in the previous chapter when multiple channels are considered with a linking constraint. If some sensors are placed in the local deflection areas of a local mode, such a model is also able to identify it.

The main drawback of multivariate models is the computational complexity due to the drastic increase of the number of model parameters. The higher complex structure of the model also reduced its parsimony which can make them more sensitive to initial guesses (in the optimization procedure) and may easily be prone to fall in local minima. The more complex structure also brings another drawback. Because of the higher number of parameters in the model, any overparameterization required for a good identification drastically adds more parameters to estimate. This is even more true as long as the number of measurements channels increases.

In time invariant modal analysis, several multivariate methods are available. The Ibrahim Time Domain (IDT) method [85] was proposed by Ibrahim and Mikulcik to treat multiple free vibration responses in order to identify a complete set of modal parameters. By complete, we understand here that the poles (frequencies and damping ratio's) can be identified but also the mode shapes. The algorithm models the free response data by the Prony method, assuming that the response can be modeled with a series of damped complex exponential waves. Two other usual ways to model MDOF linear systems are the multivariate autoregressive moving-average (often written ARMAV or VARMA depending on the author, the V standing for *"Vector"*) and the state-space models. In the identification of civil engineering structures, Andersen uses ARMAV models for modal analysis [86] and Bodeux and Golinval use them for damage detection purposes [87]. Fassois [88] and Florakis *et al.* [89] also present and compare multivariate ARMAX-based experimental modal analysis. The state-space way to model linear MDOF systems is also used for identification purposes and they may be solved by the prediction error method, recursive (such as the Kalman filter) or subspace techniques. The Eigensystem Realizaton Algorithm (ERA) proposed by Juang and Papa in [90] aims to identify the state transition matrix of a dynamic system based on its impulse response recorded in multiple channels. In case of operational conditions (assumed to be broad-band random), it is possible to feed the ERA method with auto- and cross-correlation functions of the measured structural response. In this procedure, it is possible to show that the correlation functions are also a sum of decaying sine waves owning the same modal properties of the system. This is the base of the NExT method (Natural Excitation Technique) [91]. Other state-space based methods which are currently very popular and powerful are the subspace identification methods. This familly of methods can identify deterministic, stochastic or mixed state-space systems [57] and are then very interesting in many applications and especially in stochastic operational conditions.

Dealing with time-varying identification some multivariate methods were also developed. Of course, in case of slowly varying systems, the classical modal analysis methods may be employed in a short-time stationary assumption. In this way, Marchesiello *et al.* applied the SSI method on a bridge-like structure on sliding short time windows in [5]. Similarly, Goursat *et al.* [92] apply a variant of this method (the Crystal Clear SSI method [93]) on flight data of the Ariane 5 launcher to track the variation of its modal properties due to its decrease in mass with time. The time-varying behavior of structures is also treated by several authors using ARMAV and state-space models. In [94], Spiridonakos and Fassois apply multivariate ARMA modeling estimated both by a recursive algorithm and by a two stages least squares functional series (basis

functions) approaches. They also compare their results with a short-time approach. The problem we address here is similar but we put more emphasis on the mode shapes estimates which are not considered in [94]. Concerning the identification based on state-space models, some attempts were also made to track the variations of the system's properties. Liu in [95, 96] and Liu and Deng in [97], propose to perform the identification of time-varying systems through the subspace identification state-space models in which the discrete state transition matrix is free to vary with time. An eigenvalue decomposition of this series of matrices results in what the author called the pseudo-modal parameters (pseudo-natural frequencies, -damping ratio's and -mode shapes). The method is experimentally tested in [97] on a set-up made of an axially cantilever beam. In this set-up, the time-varying boundary condition of the system brings the time-dependent characteristics of its modal properties. Another approach is also provided by Tasker *et al.* [98] for an online subspace identification. Their method implies an efficient update of the subspace as new data are available. The method is experimentally tested in [99] on a truss structure with a mass-loading/unloading as time-varying structural change.

In this chapter, two approaches are followed. First, a multivariate ARMA modeling of the time-varying system is used (Section 3.1). Second, a time-varying state-space model is used with the particularity that it is written in a modal form (Section 3.3). In each case, the time-variability of the parameters are modeled with the basis function approach just as in the preceding chapter. Both the methods are then applied on the same data set which was used earlier.

3.1 Multivariate ARMA model

In this section, the method of Auto-Regressive Moving Average in Vector form (ARMAV) is first recalled in the field of linear time invariant system identification. It leads to the determination of the modal properties in terms of poles (eigen frequencies ω_r and damping ratio's ζ_r) as well as mode shapes $\boldsymbol{v}_r$ of the structure. Next, the method is extended to the time-varying behavior using the previously presented basis function approach in a multivariate form. According to this multivariate modeling, the parameters to be estimated become matrices instead of scalar coefficients and each of their component is expressed in the basis of functions.

3.1.1 The ARMAV method for output-only modal identification

The ARMAV method is able to perform modal identification of a structure in operational conditions based only on response measurements. A required assumption is that the external excitation generating the response of the structure is an uncorrelated white noise. This method is commonly used in the field of structural dynamics. In structural identification, Piombo *et al.* [100] use ARMAV models for the identification

of modal parameters both numerically on a simulated problem and experimentally on a laboratory setup and on an actual bridge structure. Andersen in [86] provides a lot of details about the ARMAV modeling for modal identification in civil applications. His thesis provides all the details about the method, the way to perform the identification (multi stages least squares and nonlinear optimization) and to select an appropriate model structure and the extraction of the modal parameters. Bodeux and Golinval also use ARMAV models for structural health monitoring purposes (damage detection) [87, 101].

In what follows, let us denote by $\boldsymbol{y}[t]$ the $d \times 1$ multivariate responses measurement vector gathering the data of all the sensors spread on the structure. The ARMAV(n_a, n_b) model of the output signal writes:

$$\boldsymbol{y}[t] + \sum_{i=1}^{n_a} \boldsymbol{A}_i \, \boldsymbol{y}[t-i] = \boldsymbol{e}[t] + \sum_{j=1}^{n_b} \boldsymbol{B}_j \, \boldsymbol{e}[t-j], \tag{3.1}$$

where the innovation vector $\boldsymbol{e}[t]$ is a zero-mean uncorrelated white noise process. Similarly to the scalar model, the n_a $\boldsymbol{A}_i$ matrix coefficients represent the autoregressive part of the model that contains the dynamic information of the system. The other n_b $\boldsymbol{B}_j$ matrix coefficients constitute the moving average part of the model.

The relationship between an ARMAV model and a mechanical system is established in [79, 86] by the comparison between state-space representation of both the motion equations and the ARMAV model. Let us consider a mechanical system of order n for which the governing equation writes

$$\boldsymbol{M}\,\ddot{\boldsymbol{y}}(t) + \boldsymbol{C}\,\dot{\boldsymbol{y}}(t) + \boldsymbol{K}\,\boldsymbol{y}(t) = \boldsymbol{f}(t) \tag{3.2}$$

and suppose that all the n degrees of freedom are measured. Similarly to the univariate case, Andersen *et al.* show in [79] that an ARMAV(2,1) is a covariance equivalent model of the structure dynamics. However, in a general case, the number of measurement channels will not be strictly equal to the number of modes in the response of the structure. In such a case, assuming m signals are measured from the structure exhibiting n modes in the measured frequency range, an ARMAV model of autoregressive and moving average orders equal to $2n/m$ and $2n/m - 1$, respectively, should be considered. Providing of course that the n/m ratio is an integer. If this is not the case, its upper rounded value is chosen. As an example, in our practical application, having five excited modes under 120 Hz and recording the response of the structure with seven measurement channels, the theory says that an ARMAV(2,1) model is sufficient for the identification. Unfortunately, as previously encountered with the scalar model, when dealing with experimental data, a certain degree of overparameterization is required in order to get a good identification result.

3.1.2 Time-varying ARMAV model

Let us now consider the problem of time-varying mechanical systems where it is again assumed that the rate of variation of the system is slow with respect to the period of

vibration (i.e. the term $\dot{\boldsymbol{M}}(t)\,\dot{\boldsymbol{y}}(t)$ is negligible):

$$\boldsymbol{M}(t)\,\ddot{\boldsymbol{y}}(t) + \boldsymbol{C}(t)\,\dot{\boldsymbol{y}}(t) + \boldsymbol{K}(t)\,\boldsymbol{y}(t) = \boldsymbol{f}(t) \tag{3.3}$$

Regarding to the signal model (3.1), the time dependence have to be captured by the AR and MA coefficients. It follows that the ARMAV model in the framework of LTV systems is simply obtained by time-dependent matrices $\boldsymbol{A}_i[t]$ and $\boldsymbol{B}_j[t]$, i.e.:

$$\boldsymbol{y}[t] + \sum_{i=1}^{n_a} \boldsymbol{A}_i[t]\,\boldsymbol{y}[t-i] = \boldsymbol{e}[t] + \sum_{j=1}^{n_b} \boldsymbol{B}_j[t]\,\boldsymbol{e}[t-j]. \tag{3.4}$$

The coefficients to be estimated are now components of the time-varying $\boldsymbol{A}_i[t]$ and $\boldsymbol{B}_j[t]$ matrices. The same basis functions approach as in the previous chapter is used to project these matrices on a previously selected set of known time functions $f_k[t]$:

$$\boldsymbol{A}_i[t] = \sum_{k=1}^{n_{f_a}} \boldsymbol{A}_{i,k}\, f_k[t], \tag{3.5}$$

$$\boldsymbol{B}_j[t] = \sum_{k=1}^{n_{f_b}} \boldsymbol{B}_{j,k}\, f_k[t]. \tag{3.6}$$

in which n_{f_a} and n_{f_b} correspond to the number of basis functions in the AR and MA parts, respectively.

In this way, the identification problem becomes a time invariant problem when looking for the projection coefficients $\boldsymbol{A}_{i,k}$ and $\boldsymbol{B}_{j,k}$. Introducing (3.5) and (3.6) into (3.4) yields to

$$\boldsymbol{y}[t] + \sum_{i=1}^{n_a}\sum_{k=1}^{n_{f_a}} \boldsymbol{A}_{i,k}\, f_k[t]\,\boldsymbol{y}[t-i] = \boldsymbol{e}[t] + \sum_{j=1}^{n_b}\sum_{k=1}^{n_{f_b}} \boldsymbol{B}_{j,k}\, f_k[t]\,\boldsymbol{e}[t-j]. \tag{3.7}$$

The solving of the identification problem in the multivariate case is highly similar to the one with the scalar model. In this work, the prediction error method is used again for the identification. The latter is performed with the same two stages least squares and nonlinear optimization scheme adapted to the new multivariate model structure.

Two stages least squares identification

As previously said, the aim of the method is to identify the AR and MA projection coefficients. To do so, let us first gather all these coefficients in a single matrix $\boldsymbol{\Theta}$:

$$\boldsymbol{\Theta} = \left[\boldsymbol{A}_{1,1},\, \boldsymbol{A}_{1,2},\, \cdots,\, \boldsymbol{A}_{1,n_{f_a}},\, \boldsymbol{A}_{2,1},\, \cdots,\, \boldsymbol{A}_{n_a,n_{f_a}},\, \boldsymbol{B}_{1,1},\, \cdots,\, \boldsymbol{B}_{n_b,n_{f_b}}\right]. \tag{3.8}$$

In the same way, the product of the basis functions and the lagged values of the output and error term are also put in the following vector forms:

$$\boldsymbol{\phi}[t]^T = \left[f_1[t]\boldsymbol{y}[t-1]^T,\, f_2[t]\boldsymbol{y}[t-1]^T,\, \cdots,\, f_{n_{f_a}}[t]\boldsymbol{y}[t-p]^T\right] \tag{3.9}$$

$$\boldsymbol{\psi}[t]^T = \left[-f_1[t]\boldsymbol{e}[t-1]^T,\, -f_2[t]\boldsymbol{e}[t-1]^T,\, \cdots,\, -f_{n_{f_b}}[t]\boldsymbol{e}[t-q]^T\right] \tag{3.10}$$

The prediction error of the model can now be expressed by subtracting the estimate of the response $\hat{\boldsymbol{y}}[t, \boldsymbol{\Theta}]$ from the response signal itself $\boldsymbol{y}[t]$:

$$\boldsymbol{e}[t, \boldsymbol{\Theta}] = \boldsymbol{y}[t] - \hat{\boldsymbol{y}}[t, \boldsymbol{\Theta}] \tag{3.11}$$

where the estimate of the output signal is given by

$$\hat{\boldsymbol{y}}[t, \boldsymbol{\Theta}] = -\sum_{i=1}^{n_a} \sum_{k=1}^{n_{f_a}} \boldsymbol{A}_{i,k}\, f_k[t]\, \boldsymbol{y}[t-i] + \sum_{j=1}^{n_b} \sum_{k=1}^{n_{f_b}} \boldsymbol{B}_{j,k}\, f_k[t]\, \boldsymbol{e}[t-j]. \tag{3.12}$$

Using the notations (3.8), (3.9) and (3.10), the prediction error becomes

$$\boldsymbol{e}[t, \boldsymbol{\Theta}] = \boldsymbol{y}[t] + \boldsymbol{\Theta} \begin{bmatrix} \boldsymbol{\phi}[t] \\ \boldsymbol{\psi}[t] \end{bmatrix} \tag{3.13}$$

The matrix regression parameters of the system can be found by minimizing a positive scalar cost function of the modelling error with respect to the parameters. A commonly used cost function is the Sum of Squared Errors (SSE) defined as

$$V(\boldsymbol{\Theta}) = \frac{1}{2N} \sum_{t=1}^{N} \boldsymbol{e}[t, \boldsymbol{\Theta}]^T\, \boldsymbol{e}[t, \boldsymbol{\Theta}], \tag{3.14}$$

where N is the number of data samples. A good estimate of $\boldsymbol{\Theta}$ is given by the minimum of $V(\boldsymbol{\Theta})$, i.e.

$$\boldsymbol{\Theta} = \arg\min_{\boldsymbol{\Theta}} \frac{1}{2N} \sum_{t=1}^{N} \boldsymbol{e}[t, \boldsymbol{\Theta}]^T\, \boldsymbol{e}[t, \boldsymbol{\Theta}]. \tag{3.15}$$

The latter equation leads to a nonlinear optimization problem because $\boldsymbol{\psi}[t]$ depends on the error term (3.13) which itself depends on the $\boldsymbol{\Theta}$ parameter. To solve this problem, the Two Stage Least Squares (2SLS) method [58] presented in Section 2.3.1 of the preceding chapter is first used. In a first step, a high-order autoregressive model is used to fit the data which requires only a least square estimate as the nonlinearity is located in the MA part. Once this model is known, it is used to get an estimate of the innovation $\boldsymbol{e}[t,\, \boldsymbol{\Theta}_{\text{high order}}]$. In the second step, an ARMAV model is estimated by using the innovation as a known input in an ARX way. The process may then be iterated by updating the output estimate and the innovation.

Nonlinear minimization of the cost function.

In order to perform the minimization of the nonlinear cost function (3.15), with the Levenberg-Marquard or trust-region algorithms, we will have to compute its gradient with respect to the parameters of the multivariate model. To this goal, and for the computation of the predictors, the time-varying ARMAV is rewritten in an observer canonical state-space form (also known as the companion form of the model) as follows [58]:

$$\begin{aligned} \boldsymbol{x}[t+1] &= \boldsymbol{F}[t]\, \boldsymbol{x}[t] + \boldsymbol{K}[t]\, \boldsymbol{e}[t] \\ \boldsymbol{y}[t] &= \boldsymbol{C}\, \boldsymbol{x}[t] + \boldsymbol{e}[t] \end{aligned} \tag{3.16}$$

in which the matrices $\boldsymbol{F}$ and $\boldsymbol{K}$ are populated with the AR and MA matrices :

$$\boldsymbol{F}[t] = \begin{bmatrix} -\boldsymbol{A}_1[t] & \boldsymbol{I} & \boldsymbol{0} & \cdots & \boldsymbol{0} \\ -\boldsymbol{A}_2[t] & \boldsymbol{0} & \boldsymbol{I} & \cdots & \boldsymbol{0} \\ \vdots & \vdots & \vdots & \ddots & \vdots \\ -\boldsymbol{A}_{n_a-1}[t] & \vdots & \vdots & & \boldsymbol{I} \\ -\boldsymbol{A}_{n_a}[t] & \boldsymbol{0} & \boldsymbol{0} & \cdots & \boldsymbol{0} \end{bmatrix}, \tag{3.17}$$

$$\boldsymbol{K}[t] = \begin{bmatrix} \boldsymbol{B}_1[t] - \boldsymbol{A}_1[t] \\ \boldsymbol{B}_2[t] - \boldsymbol{A}_2[t] \\ \vdots \\ \boldsymbol{B}_n[t] - \boldsymbol{A}_n[t] \end{bmatrix}, \tag{3.18}$$

n being the maximum value of n_a and n_b and any $\boldsymbol{A}_i$ or $\boldsymbol{B}_i$ with an order higher than the model orders n_a and n_b, respectively, is put to zero. The output matrix $\boldsymbol{C}$ is equal to

$$\boldsymbol{C} = \begin{bmatrix} \boldsymbol{I} & \boldsymbol{0} & \boldsymbol{0} & \cdots & \boldsymbol{0} \end{bmatrix} \tag{3.19}$$

with $\boldsymbol{I}$ the identity matrix of appropriate dimension.

The same optimization scheme previously presented in Section 2.3.1 is adapted in the case of the multivariate identification model. A quadratic model of the cost function is built around the current set of parameters

$$\mathcal{V}(\boldsymbol{\theta}) = V\left(\boldsymbol{\theta}^{(k)}\right) + \left(\boldsymbol{\theta} - \boldsymbol{\theta}^{(k)}\right)^T \left.\frac{\mathrm{d}V(\boldsymbol{\theta})}{\mathrm{d}\boldsymbol{\theta}}\right|_{\boldsymbol{\theta}=\boldsymbol{\theta}^{(k)}} + \frac{1}{2}\left(\boldsymbol{\theta} - \boldsymbol{\theta}^{(k)}\right)^T \left.\frac{\mathrm{d}^2V(\boldsymbol{\theta})}{\mathrm{d}\boldsymbol{\theta}^2}\right|_{\boldsymbol{\theta}=\boldsymbol{\theta}^{(k)}} \left(\boldsymbol{\theta} - \boldsymbol{\theta}^{(k)}\right) \tag{3.20}$$

with

$$\frac{\mathrm{d}\mathcal{V}(\boldsymbol{\theta})}{\mathrm{d}\boldsymbol{\theta}} = \left.\frac{\mathrm{d}V(\boldsymbol{\theta})}{\mathrm{d}\boldsymbol{\theta}}\right|_{\boldsymbol{\theta}=\boldsymbol{\theta}^{(k)}} + \left.\frac{\mathrm{d}^2V(\boldsymbol{\theta})}{\mathrm{d}\boldsymbol{\theta}^2}\right|_{\boldsymbol{\theta}=\boldsymbol{\theta}^{(k)}} \left(\boldsymbol{\theta}^{(k+1)} - \boldsymbol{\theta}^{(k)}\right) = \boldsymbol{0} \tag{3.21}$$

and $\boldsymbol{\theta}$ being a vector stacking all the model coefficients in the matrix of parameters $\boldsymbol{\Theta}$. The iteration step is then given by

$$\left(\boldsymbol{\theta}^{(k+1)} - \boldsymbol{\theta}^{(k)}\right) = -\underbrace{\left(\left.\frac{\mathrm{d}^2V(\boldsymbol{\theta})}{\mathrm{d}\boldsymbol{\theta}^2}\right|_{\boldsymbol{\theta}=\boldsymbol{\theta}^{(k)}}\right)^{-1}}_{\boldsymbol{H}} \underbrace{\left.\frac{\mathrm{d}V(\boldsymbol{\theta})}{\mathrm{d}\boldsymbol{\theta}}\right|_{\boldsymbol{\theta}=\boldsymbol{\theta}^{(k)}}}_{\boldsymbol{g}} \tag{3.22}$$

As for the optimization performed in the previous chapter, one has to compute the gradient of the cost functions in order to iterate in the optimization scheme, again by neglecting the second order term in the Hessian matrix:

$$\frac{\mathrm{d}V(\boldsymbol{\theta})}{\mathrm{d}\boldsymbol{\theta}} = \frac{1}{N}\sum_t \frac{\mathrm{d}\boldsymbol{e}^T[t,\boldsymbol{\theta}]}{\mathrm{d}\boldsymbol{\theta}}\,\boldsymbol{e}[t,\boldsymbol{\theta}], \tag{3.23}$$

$$\frac{\mathrm{d}^2V(\boldsymbol{\theta})}{\mathrm{d}\boldsymbol{\theta}^2} = \frac{1}{N}\sum_t \left(\frac{\mathrm{d}\boldsymbol{e}^T[t,\boldsymbol{\theta}]}{\mathrm{d}\boldsymbol{\theta}}\right)\left(\frac{\mathrm{d}\boldsymbol{e}^T[t,\boldsymbol{\theta}]}{\mathrm{d}\boldsymbol{\theta}}\right)^T + \underbrace{\frac{1}{N}\sum_t \frac{\mathrm{d}^2}{\mathrm{d}\boldsymbol{\theta}^2}\left(\boldsymbol{e}[t,\boldsymbol{\theta}]^T\boldsymbol{e}[t,\boldsymbol{\theta}]\right)}_{\text{To be neglected}} \tag{3.24}$$

The derivative of the prediction error then needs to be computed, which is equivalent to minus the derivative of the predictor with respect to the same parameter:

$$\frac{\mathrm{d}\,\boldsymbol{e}^T[t,\boldsymbol{\theta}]}{\mathrm{d}\boldsymbol{\theta}} = \frac{\mathrm{d}\,\left(\boldsymbol{y}[t]-\boldsymbol{y}[t,\boldsymbol{\theta}]\right)^T}{\mathrm{d}\boldsymbol{\theta}} \tag{3.25}$$

$$= -\frac{\mathrm{d}\,\boldsymbol{y}[t,\boldsymbol{\theta}]^T}{\mathrm{d}\boldsymbol{\theta}} \tag{3.26}$$

Writing the state space equation in a predictor form, one has:

$$\begin{aligned} \hat{\boldsymbol{x}}[t+1] &= \Big[\boldsymbol{F}[t]-\boldsymbol{K}[t]\boldsymbol{C}\Big]\hat{\boldsymbol{x}}[t]+\boldsymbol{K}[t]\,\boldsymbol{y}[t] \\ \hat{\boldsymbol{y}}[t,\boldsymbol{\theta}] &= \boldsymbol{C}\,\boldsymbol{x}[t] \end{aligned} \tag{3.27}$$

which is helpful for the computation of all the derivatives of the predictor. Indeed, for each parameter θ_i in the identification model, one gets for its respective derivative of the predictor:

- if θ_i belongs to the autoregressive part:

$$\begin{aligned} \boldsymbol{z}[t+1] &= \frac{\mathrm{d}\,\boldsymbol{F}[t]}{\mathrm{d}\,\theta_i}\hat{\boldsymbol{x}}[t]-\frac{\mathrm{d}\,\boldsymbol{K}[t]}{\mathrm{d}\,\theta_i}\boldsymbol{C}\hat{\boldsymbol{x}}[t]+\Big[\boldsymbol{F}[t]-\boldsymbol{K}[t]\boldsymbol{C}\Big]\boldsymbol{z}[t]+\frac{\mathrm{d}\boldsymbol{K}[t]}{\mathrm{d}\,\theta_i}\,\boldsymbol{y}[t] \\ \frac{\mathrm{d}\,\hat{\boldsymbol{y}}[t,\boldsymbol{\theta}]}{\mathrm{d}\,\theta_i} &= \boldsymbol{C}\,\boldsymbol{z}[t] \end{aligned} \tag{3.28}$$

- if θ_i belongs to the moving-average part:

$$\begin{aligned} \boldsymbol{z}[t+1] &= -\frac{\mathrm{d}\,\boldsymbol{K}[t]}{\mathrm{d}\,\theta_i}\boldsymbol{C}\hat{\boldsymbol{x}}[t]+\Big[\boldsymbol{F}[t]-\boldsymbol{K}[t]\boldsymbol{C}\Big]\boldsymbol{z}[t]+\frac{\mathrm{d}\boldsymbol{K}[t]}{\mathrm{d}\,\theta_i}\,\boldsymbol{y}[t] \\ \frac{\mathrm{d}\,\hat{\boldsymbol{y}}[t,\boldsymbol{\theta}]}{\mathrm{d}\,\theta_i} &= \boldsymbol{C}\,\boldsymbol{z}[t] \end{aligned} \tag{3.29}$$

with $\boldsymbol{z}[t]$ being the derivative of $\hat{\boldsymbol{x}}[t]$ with respect to θ_i. The computation of the derivative may then be obtained by a state-space filter fed with the measured signal $\boldsymbol{y}[t]$ and the states sequence $\hat{\boldsymbol{x}}[t]$ at the current iteration step.

Note that the computation of the gradient and the approximate of the Hessian matrix is a computationally demanding task. When the number of model parameters, measurement channels and/or data samples is high, this step can be problematic on standard computers, mainly because of lack of memory. In order to cope with this issue, it is possible to perform the computation in several batches and iteratively update the gradient vector and the Hessian matrix. This method is explained in details in Appendix A.2.

3.1.3 Computation of the modal parameters

At the end of the optimization of the parameters of the model, it remains to compute the modal parameters of the system. This is done by a series of eigenvalue decomposition of the state transition matrix $\boldsymbol{F}[t]$ in (3.16)-(3.17) which corresponds to the

companion matrix of the autoregressive matrix polynomial. These decompositions are representative of the instantaneous dynamics of the system at time t following the same *frozen-time* approach. The obtained parameters are a first approximation of those of the actual time-varying system under the same assumption of a slowly-varying system. In [96], Liu gives the justification of the computation of its pseudo-modal parameters based on the decomposition of the instantaneous state transition matrix. Let's assume that $\boldsymbol{F}_c(t)$ is the state transition matrix of the time-varying system in the continuous-time domain. Its transformation to the discrete-time domain is given by

$$\begin{aligned} \boldsymbol{F}[t] &= \boldsymbol{I} + \boldsymbol{F}_c(t)\,\tau && (3.30)\\ &+ \frac{1}{2}\left[\boldsymbol{F}_c(t)^2 + \dot{\boldsymbol{F}}_c(t)\right]\tau^2 && (3.31)\\ &+ \frac{1}{3!}\left[\boldsymbol{F}_c(t)^3 + \boldsymbol{F}_c(t)\dot{\boldsymbol{F}}_c(t) + 2\dot{\boldsymbol{F}}_c(t) + \ddot{\boldsymbol{F}}_c(t)\right]\tau^3 && (3.32)\\ &+ \cdots && (3.33) \end{aligned}$$

in which τ is the sampling time. The true discrete state matrix is then dependent of the rate of variation of the dynamic system. However, if its rate of variation can be neglected, we recover the classical approximate of the matrix exponential form computed at the instantaneous configuration of the system:

$$\boldsymbol{F}[t] \approx \boldsymbol{I} + \boldsymbol{F}_c(t)\,\tau + \frac{1}{2}\,\boldsymbol{F}_c(t)^2\,\tau^2 + \frac{1}{3!}\,\boldsymbol{F}_c(t)^3\,\tau^3 + \cdots = \exp\left[\boldsymbol{F}_c(t)\,\tau\right]. \tag{3.34}$$

The successive eigenvalue decompositions of the $\boldsymbol{F}$ matrices lead to a series of eigenvalues μ_r which are the discrete-time frozen poles of the system and are related to the poles of the system λ_r by

$$\mu_r[t] = e^{\lambda_r[t]\,\tau}. \tag{3.35}$$

The d first components of the corresponding eigenvectors give the mode shapes of the system.

3.2 Experimental identification with the multivariate time-varying ARMA model

This section presents the application of the multivariate time-varying ARMAV modeling for the identification of the varying beam-mass structure. The procedure followed for the identification is similar to the one presented in the previous chapter, i.e. a first batch of fast identifications by the 2SLS method in order to identify good model candidates followed by the application of the nonlinear optimization method on a reduced set of candidates for better identification results.

3.2.1 Selection of the model structure with the 2SLS method

Just as in the scalar model, a large family of model structure candidates are tested in order to locate the best combination of AR and MA orders as well as the best

sizes of their basis of functions. To this goal, the autoregressive order is tested from order 2, which is the minimum value given by the theory, up to an overestimated order equal to 8. Concerning the size of the bases of functions, Chebychev polynomials up to the order 7 (8 functions in the basis) are considered. The evaluation of the model candidates is then performed based on the same citeria as in the previous chapter, i.e. the FPE, AIC and BIC criteria. The scores obtained by each criteria with respect to each model structure are given in Figure 3.1. The evolution of each criteria follows the same kind of behavior as what we obtained with the scalar model. The evolution of the scores follows a repetition of a pattern which corresponds to a couple of AR and MA orders. The internal variations inside a pattern are again due to the variation in the size of the bases of functions. First, concerning the AR and MA orders, model structures ARMAV(3,2) and ARMAV(3,3) seem to be good candidates. ARMAV(4,3) and ARMAV(4,4) structures may also be considered but at the price of a higher model complexity.

In order to refine the choice of the model structure, the RSS/SSS criteria is used as done in the previous chapter to clarify the selection of the model orders but also the size of the bases of functions. This criteria is plotted in Figure 3.2 with respect with each of the tunable parameters of the model structure. First, a confirmation about the model order may be obtained, the third order in each of the AR and MA parts brings a large decrease in the criterion. Any subsequent refinement of these parameters does not bring any significant improvement and the ARMA(3,3) family seems to be the best one at first sight. However, things are not so easy for the selection of the number of basis functions for each part of the model. Concerning the scalar model, a drop in median value and spread of the RSS/SSS score was observed and it indicated a good choice for the selections of the sizes of each basis of functions. Facing that difficulty in the selection of proper sizes for the bases, it is chosen to perform a second selection based on a reduced set of candidates identified this time with the nonlinear optimization approach.

3.2.2 Refined identification with the nonlinear optimization

Based on the information obtained with the 2SLS batch identification and the representation of their scores for each selection criteria, it is observed that the model orders (3,2), (3,3), (4,3) and (4,4) may be suitable candidates model structures. In order to select the proper size of each basis of functions, these only four couples of model orders are considered in a second run of identifications. The preselected number of functions to test are here chosen from 6 to 9 for the AR part. The number of functions to model the MA part of the model is iterated from 1 to the current number of functions used to represents the AR part. This selection process is obviously far slower that the previous one based on the 2SLS estimation but we hope that it could bring better information regarding the structure selection purpose.

Once all the calculations are performed, the new scores obtained by each model candidate are saved and plotted in Figure 3.3. Once again, The FPE and AIC criteria bring similar results and the BIC criterion is more strict than the other two. Among

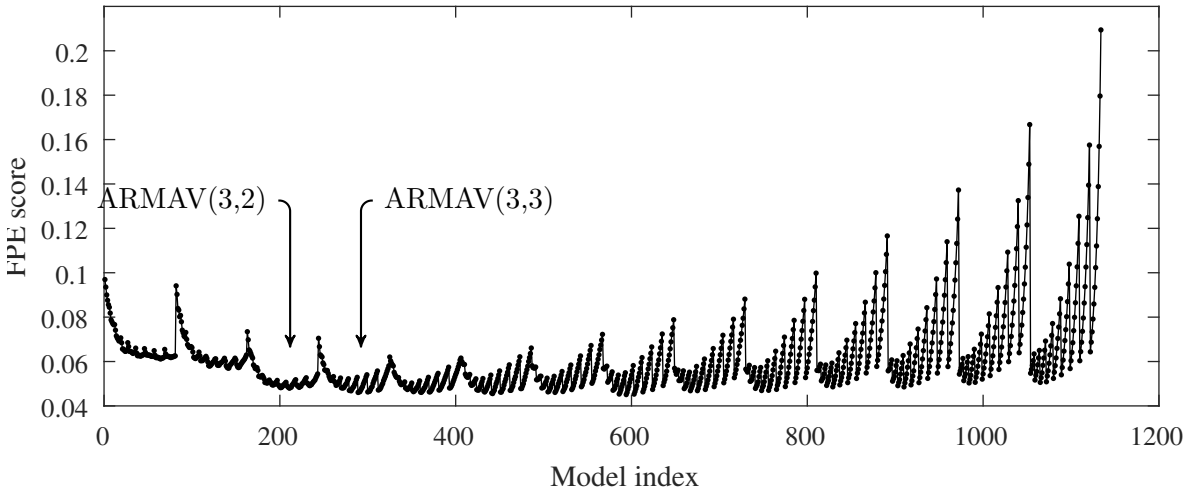

(a) FPE scores for the large batch of model candidates.

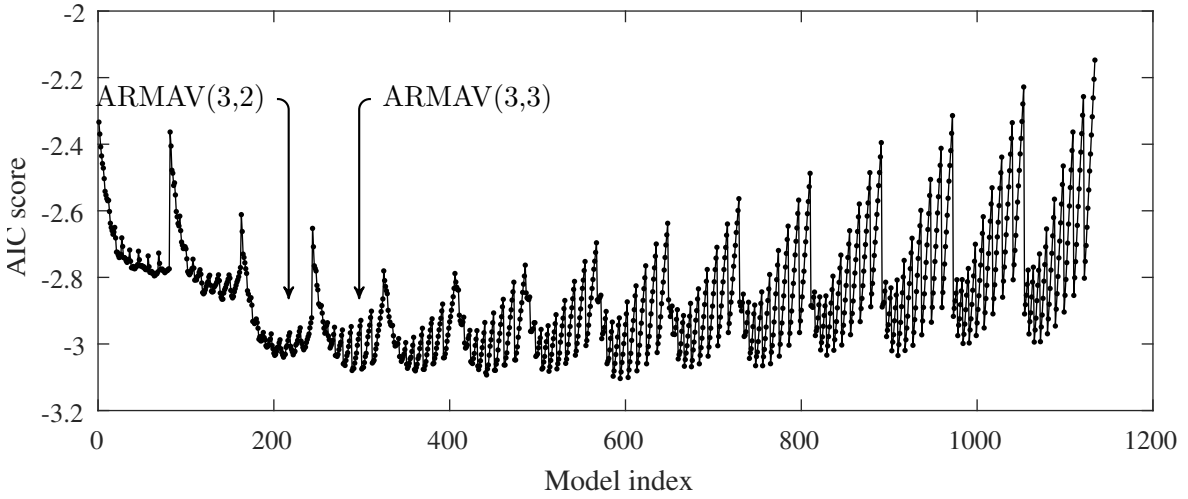

(b) AIC scores for the large batch of model candidates.

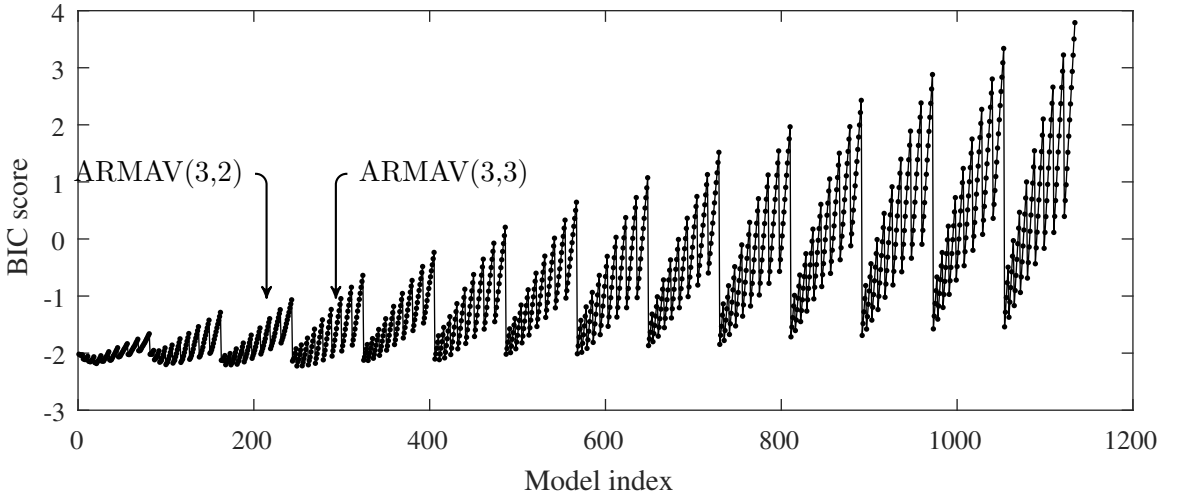

(c) BIC scores for the large batch of model candidates.

Figure 3.1: Good model structures candidates are selected based on the values of the FPE, AIC and BIC criterion. Chebyshev polynomials are used as basis functions.

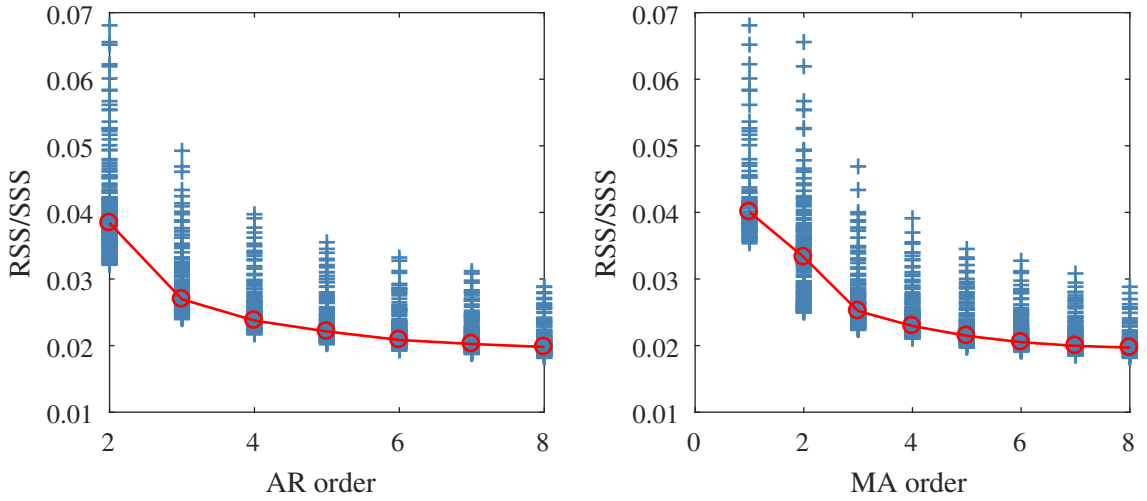

(a) RSS/SSS vs n_a.

(b) RSS/SSS vs n_b.

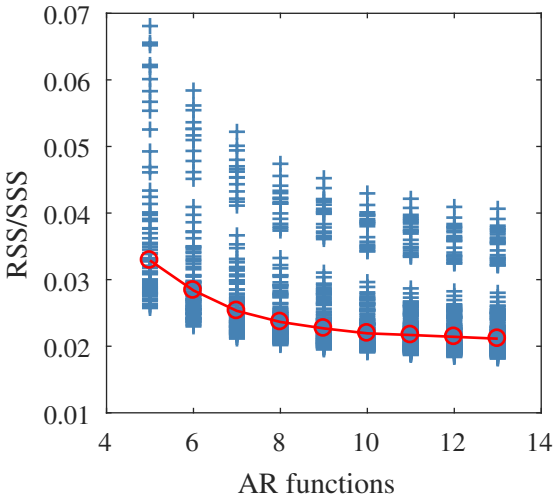

(c) RSS/SSS vs n_{f_a}.

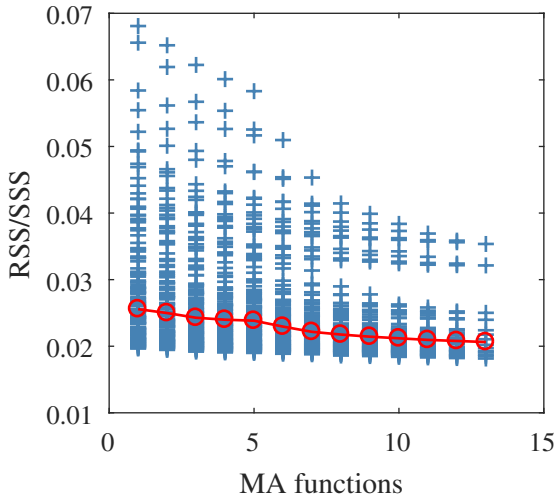

(d) RSS/SSS vs n_{f_b}.

Figure 3.2: RSS/SSS values with respect to each of the model structure parameter of the ARMAV model.

Model index	$d_{\mathcal{M}}$	n_a	n_b	n_{f_a}	n_{f_b}
38	1323	3	3	7	2
45	1470	3	3	8	2
52	1470	3	3	9	1
53	1617	3	3	9	2

Table 3.1: Refined set of possible model structures candidates.

all that results, models with minimum values in each criteria are listed in Table 3.1. The latter few candidates are then tested and the retained one for this identification is the ARMAV(3,3)[9,1] model. This choice is driven by the wish to restrain as much as possible the number of parameters but the ARMAV(3,3)[9,1] model describes a little bit better the lower frequency mode than the ARMAV(3,3)[7,2] and ARMAV(3,3)[8,2] models for similar values in the selection parameters.

3.2.3 Identified results

Discrimination between physical and spurious modes

Once the model orders are fixed, the difficulty is to deal with the number of calculated poles and mode shapes. Indeed, the multivariate ARMA model leads to a number of poles increasing linearly with both the model order n_a of the AR part and the number of measurements d (the dimension of the companion, or state trasition, matrix (3.17) is $n_a\, d \times n_a\, d$). The dimension of the companion matrix may grow rapidly and exceed the actual number of excited modes in the frequency range of interest. Because of that, a huge number of spurious poles are calculated besides the physical ones. A discrimination should then be performed in order to get clear results. The situation is similar as the one encountered with the scalar modeling in the previous chapter; the idea followed here is to retain a number M of modes that looks the more physical among all the modes. The subset selection of physical modes based on the radial distribution of the poles in the complex plane as in Section 2.3.3 may of course be applied. However, in this case we also have another information that can be exploited which is the time-varying mode shapes. The mode shapes may also serve for discrimination purposes between physical and spurious modes. Indeed, the physical modes of a real mechanical structure usually appear well aligned in the complex plane conversely to the spurious ones that exhibit a large dispersion. One way to quantify the aligned or scattered behavior of a mode is to compute its mean phase (MP) and its mean phase deviation (MPD) which can be seen as the variance of the phase from the mean phase. Obviously, the ideal value of the MPD for a physical mode is close to 0°. In the identification process, we will then retain only the M modes with the lowest time-averaged MPD. Note that if we do not know the actual number of physical modes, an automatic clustering process could be applied to distinguish the modes with a MPD close to zero from the others. Of course, both the radial distribution of the poles and the MPD may be used at once in the selection process. This kind of process is applied in [102]

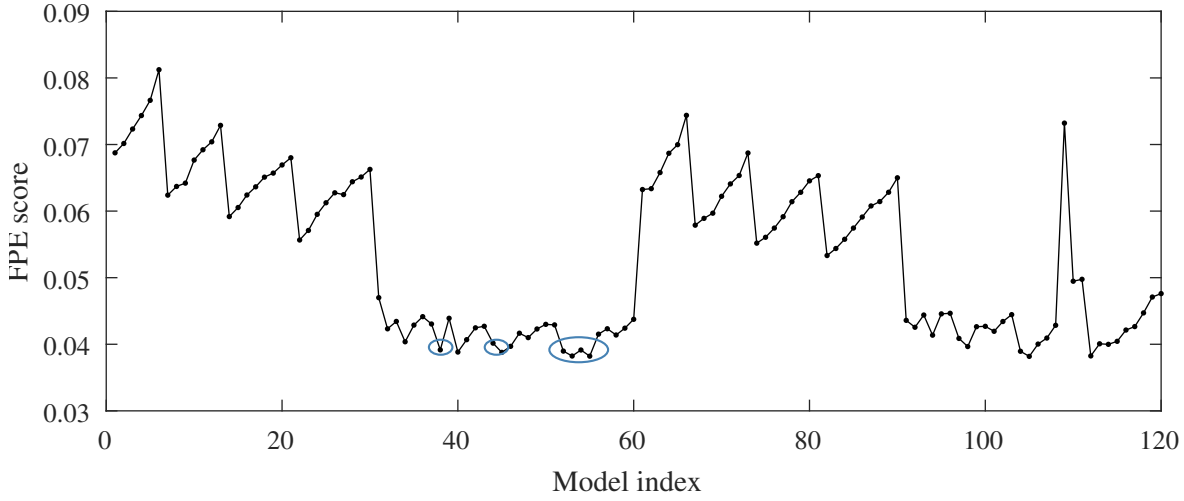

(a) FPE scores for the large batch of model candidates.

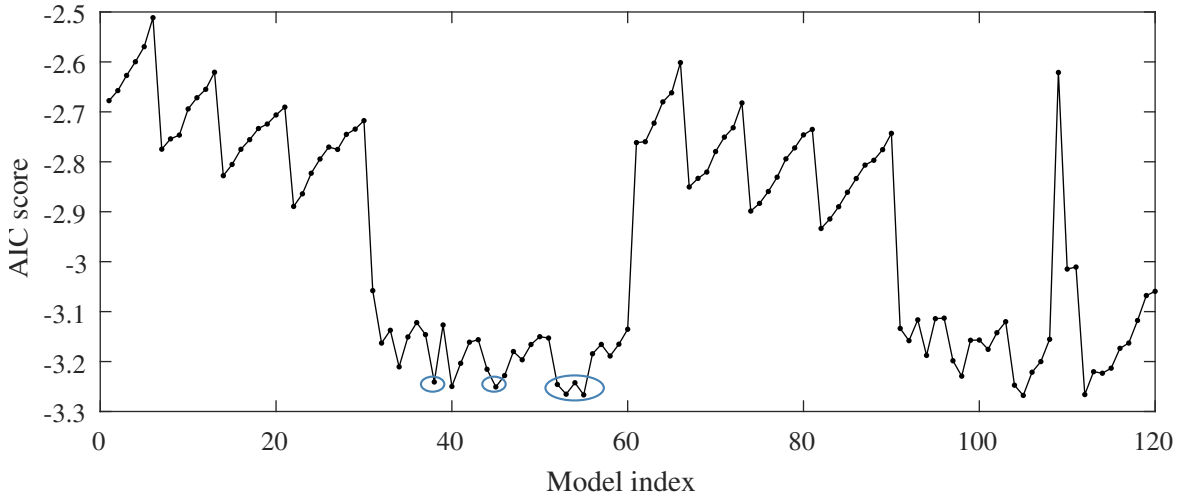

(b) AIC scores for the large batch of model candidates.

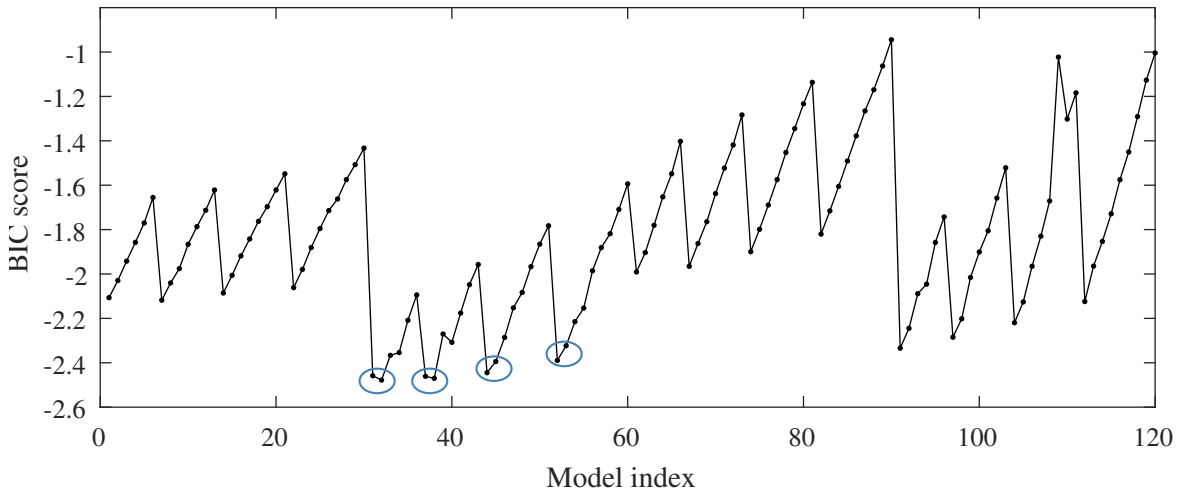

(c) BIC scores for the large batch of model candidates.

Figure 3.3: Good model structures candidates are selected based on the values of the FPE, AIC and BIC criterion. Chebyshev polynomials are used as basis functions. The blue ellipsoids indicate well suited candidates.

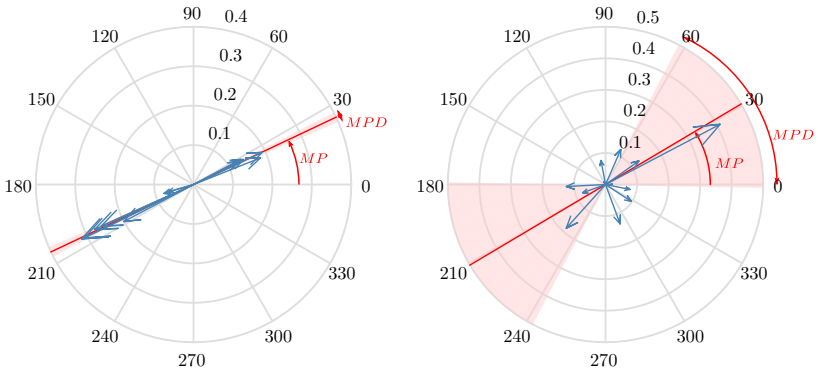

(a) Physical mode (low MPD) (b) Spurious mode (high MPD)

Figure 3.4: Illustrative example of the mode phase dispersion in the complex plane. (a) is a physical mode and (b) is classified as a spurious.

by Reynders *et al.* in an attempt to automatize the selection of the physical poles in modal analysis. In Figure 3.4, an example of a physical mode 3.4(a) and a spurious mode 3.4(b) is shown. The mean phase for each mode is drawn together with their mean phase deviation.

The identification model based on the selection process is then applied to provide an estimate of the time-varying poles and mode shapes. The obtained results are shown in Figure 3.5(a) in which the discrimination process between physical and spurious mode based on the MPD criterion is already applied. Note that the method employed in the previous chapter for the selection of the physical poles give the same physical and spurious sets of modes. As an illustration of the selection process, Figures 3.6 and 3.7 show the varying physical and spurious modes at a snapshot at $t = 10$ s.

The time-varying physical modes shown in Figure 3.6 represent somehow classical deflections for a doubly supported beam. The location of the moving mass may also be visually located because of the decrease in deflection of the mode shapes close to the second and third nodes with respect to their symmetric amplitude on the other side of the beam. The Argand plots showing the mode shapes in the complex plane describe well aligned complex deflections in phase or antiphase. It should also be noted that the damping ratio of the fifth physical mode is negative. This kind of value may be observed at some moments in time-varying systems without implying the instability of the whole system. Such negative damping was also observed on the bridge-like structure studied in [5]. This occurs at moments when the amplitude of vibration of the nonstationary responses show an increase in their amplitude.

Concerning the identified modes which are classified as spurious ones, two kinds of behaviors are shown in Figure 3.7. First, the first and the two last modes exhibit purely real deflections. This real-valued shapes are clues indicating they are not physical modes. The first one exhibits a damping ratio of 100% related to a real pole. The two last modes are related to complex poles, however, their respective values do not appear in complex-conjugated pairs which is also a useful information to eliminate them. Finally, it is easily seen that the MPD of the other modes is larger than the one

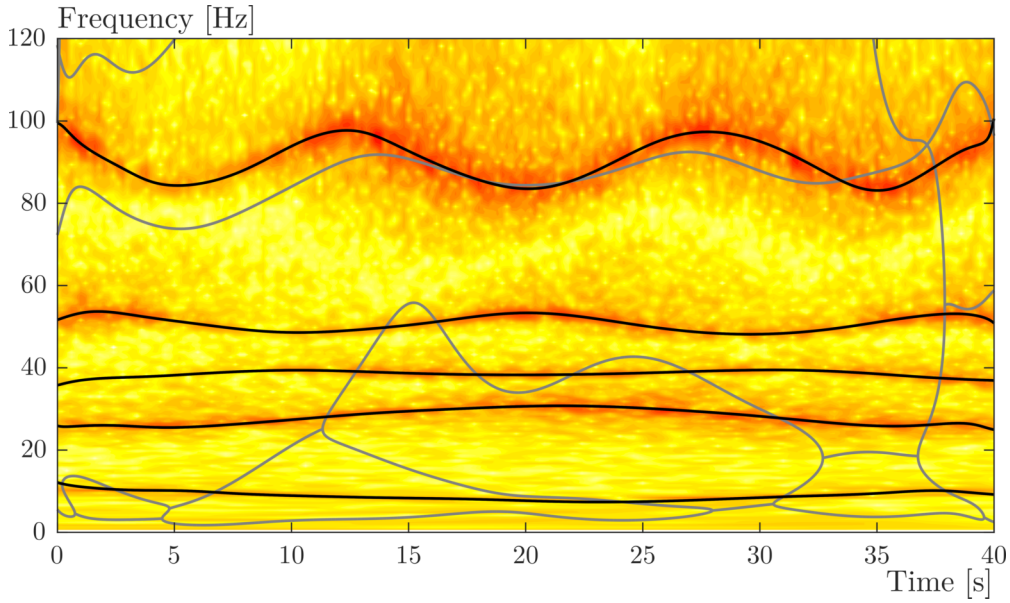

(a) Idendified time-varying modes.

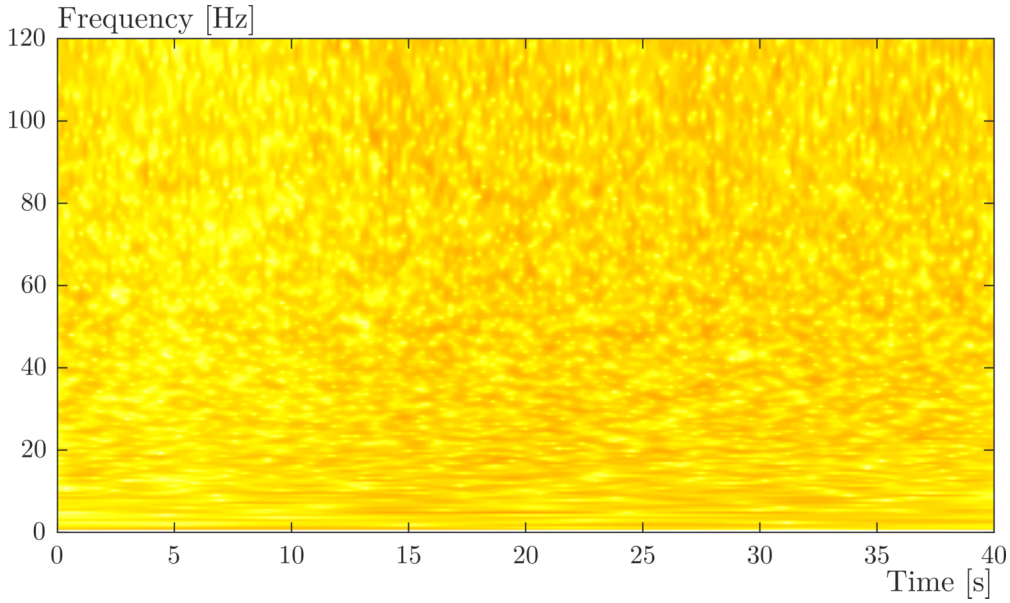

(b) Time-frequency representation of the residuals after the identification (channel 2).

Figure 3.5: Identified time-varying modes. The selection between physical (black) and spurious (gray) modes is performed using the MPD criterion.

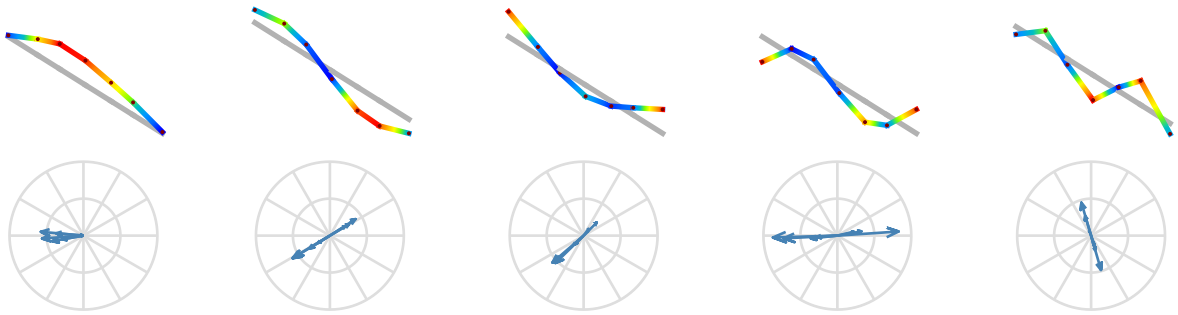

$f_1[10] = 8.95$ Hz	$f_2[10] = 27.39$ Hz	$f_3[10] = 39.42$ Hz	$f_4[10] = 48.60$ Hz	$f_5[10] = 93.87$ Hz
$\zeta_1[10] = 5.32$ %	$\zeta_2[10] = 1.35$ %	$\zeta_3[10] = 0.037$ %	$\zeta_4[10] = 2.25$ %	$\zeta_5[10] = -0.21$ %

Figure 3.6: Snapshots of the five physical modes at $t = 10$ s with their shape, Argand representation and frequency and damping ratio information.

for the modes selected as physical.

3.3 State-space model in the modal space

3.3.1 State-space modeling

Besides to the multivariate ARMA modeling, State-Space models are also investigated in this study for the application in the tracking of the time-varying modal properties of time-varying mechanical systems. The same assumptions as previously made are followed, i.e. the systems slowly vary with respect to their dynamics in order to cope with the frozen-time approach, and the parameters of the model may be properly described through a projection in a series of basis functions.

The particularity we follow here in the modeling is to recast the model equation in the modal domain. This way to model the system provides very attractive properties. First, concerning the parameters to identify, being in a modal description of the model directly brings a physical meaning of each parameters. Indeed, in that way, the poles and the components of the mode shapes appear directly in the structure of the model and eigenvalue decompositions for each time step are no more required as it is the case with the multivariate ARMA modeling. Second, the identification of the parameters in the optimization process may be facilitated because the values of the parameters may be more concentrated. The time-varying parameters describing the poles should be inside or closely outside the unit circle. This means that their real and imaginary parts lie inside or closely outside the $[-1; 1]$ interval. It is also true for the mode shapes if their initial guess is unit-normalized for example.

The state-space representation of a system is a very common representation used in many fields such as control or model identification for example. In the present case we will deal with only external measurements on the structure, the input force is recorded by the acquisition system, but not used as input of the method to show that it can be

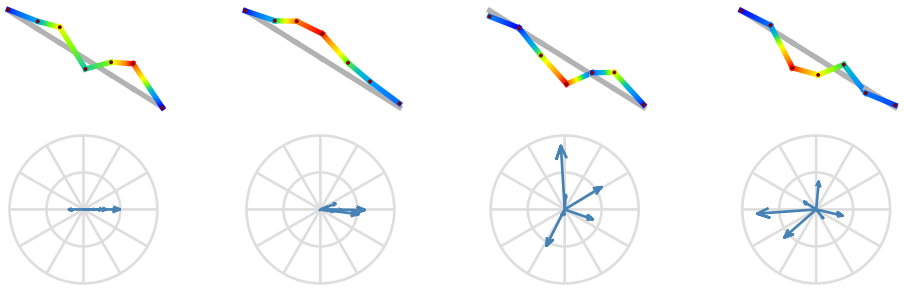

$f[10] = 2.87$ Hz $\quad f[10] = 21.10$ Hz $\quad f[10] = 84.05$ Hz $\quad f[10] = 142.12$ Hz
$\zeta[10] = 100$ % $\quad \zeta[10] = 97.83$ % $\quad \zeta[10] = 18.35$ % $\quad \zeta[10] = 42.55$ %

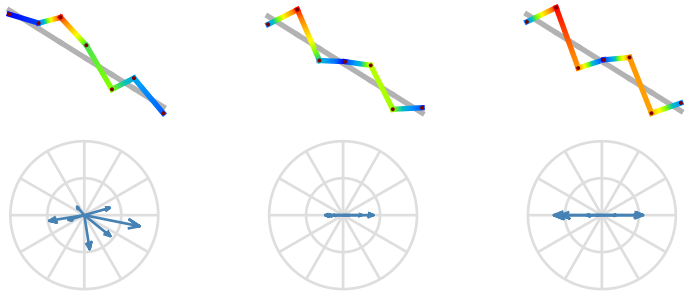

$f[10] = 146.54$ Hz $\quad f[10] = 160.01$ Hz $\quad f[10] = 160.35$ Hz
$\zeta[10] = 24.86$ % $\quad \zeta[10] = -0.94$ % $\quad \zeta[10] = 6.56$ %

Figure 3.7: Snapshots of seven spurious modes at $t = 10$ s with their shape, Argand representation and frequency and damping ratio information.

used in output only conditions. It is then not included in the state-space equations. In this case, the classical way to represent a system in a state-space form is composed of two equations, the *state equation* and the *output equation*:

$$\begin{cases} \boldsymbol{x}[t+1] &= \boldsymbol{F}[t]\,\boldsymbol{x}[t] + \boldsymbol{K}[t]\,\boldsymbol{e}[t] \\ \boldsymbol{y}[t] &= \boldsymbol{C}[t]\,\boldsymbol{x}[t] + \boldsymbol{e}[t] \end{cases} \tag{3.36}$$

in which

- $\boldsymbol{F}$ is the state-transition matrix,
- $\boldsymbol{x}$ is the state vector,
- $\boldsymbol{y}$ is the output vector (gathering the experimental measurements),
- $\boldsymbol{e}$ is the innovation vector, and
- $\boldsymbol{K}$ is the Kalman gain matrix.

It is also pointed out by Ljung in [58] that the modeling of time-varying systems may be performed by letting the matrices of the model vary with time.

Let us note that there are many ways to represent the same system in a state-space form. If all the matrices in (3.36) are fully populated, one speaks about a

fully parameterized form. The way to write the ARMAV model in (3.16) is one of the *canonical forms* of the state-space model. It has the advantage to be the more economical in parameters for equivalent models. Finally, the structure which interests us here is a *tridiagonal form*, in which the matrix $\boldsymbol{F}$ has non-zero components only on its three main diagonals. A short comparison between these different forms is given in [103] for example and summarized in Table 3.2 for a multivariate time-invariant case for illustrative purpose. The time-variant counterpart using the basis functions approach is simply obtained by multiplying each of the component by its number of projection coefficients of the functions which are considered in the model.

Parameterization	$\boldsymbol{F}$	$\boldsymbol{C}$	$\boldsymbol{K}$	$d_{\mathcal{M}}$
Full	n^2	dn	dn	$n^2 + 2dn$
Canonical	dn	0	dn	$2dn$
Tridiagonal	$3n - 2$	dn	dn	$3n + 2dn - 2$

Table 3.2: Model structure complexity of each form of parameterization of the state-space model. n the order of the state-space model, d the dimension of the response vector and $d_{\mathcal{M}}$ the model complexity.

The model shown in (3.36) is called an *innovation form* because of the presence in the model of the *innovation vector*, $\boldsymbol{e}$, that contains all the information that cannot be predicted by the model using the past data. It is similar to the moving-average part in the ARMA modeling that takes into account this innovation in the model. The use of the innovation is a convenient way to write the model instead of introducing process and measurement noises in the state-space equations. It should also be noted that there are also many ways to represent this system using similarity transformations.

Practically, a special case of similarity transformation is to transform any state-space form into a modal form which has the property to have a diagonal state-transition matrix. In order to perform this transformation an eigenvalues/eigenvectors decomposition of the state transition matrix $\boldsymbol{F}$ is required. The matrices of the system are then transformed by projections with the such obtained eigenvectors:

$$\boldsymbol{F}[t] = \boldsymbol{V}[t]\,\boldsymbol{A}[t]\,\boldsymbol{V}^{-1}[t]. \tag{3.37}$$

The model (3.36) can be transformed into the following one

$$\left\{\begin{array}{rcl} \boldsymbol{\eta}[t+1] & = & \boldsymbol{A}[t]\,\boldsymbol{\eta}[t] + \boldsymbol{\Psi}[t]\,\boldsymbol{e}[t] \\ \boldsymbol{y}[t] & = & \boldsymbol{\Phi}[t]\,\boldsymbol{\eta}[t] + \boldsymbol{e}[t] \end{array}\right. \tag{3.38}$$

with

$$\boldsymbol{\eta}[t] = \boldsymbol{V}^{-1}[t]\,\boldsymbol{x}[t], \tag{3.39}$$
$$\boldsymbol{A}[t] = \boldsymbol{V}^{-1}[t]\,\boldsymbol{F}[t]\,\boldsymbol{V}[t], \tag{3.40}$$
$$\boldsymbol{\Phi}[t] = \boldsymbol{C}[t]\,\boldsymbol{V}[t], \tag{3.41}$$
$$\boldsymbol{\Psi}[t] = \boldsymbol{V}^{-1}[t]\,\boldsymbol{K}[t]. \tag{3.42}$$

With that model, we get some physical interpretation of the new parameters which can be related to theoretical modal analysis. Indeed, the $\boldsymbol{A}$ matrix is now a diagonal one gathering the discrete poles of the system and the $\boldsymbol{\Phi}$ matrix its mode shapes. Both appear in complex conjugated pairs. The $\boldsymbol{\eta}$ vector corresponds to the modal coordinates and the output equation of (3.38) is no more than the modal expansion of the response of the system which is an important concept in linear modal analysis. This kind of modal representation of the system was already used by Brincker and Andersen in [104]. Their motivation to apply a series of ARMA to modal state-space model transformations is to reduce their number of optimization parameters in their algorithm. It can be surprising with respect to the observation done about the comparison of different kinds of parameterizations (Table 3.2), but in their method, they only focus on a reduced subset of modal parameters of interest in the optimization procedure.

In the following, we use a similar parameterization with a slight difference. The model (3.38) is made up with complex conjugated values for the poles and modes shapes. In order to avoid treating such complex values, separating the real and imaginary parts of each parameter offers the possibility to work with only real-valued parameters. This does not change anything to the modal decoupling of the model but slightly change the model matrices.

Matrix $\boldsymbol{A}$ is not purely diagonal anymore but is now a block-diagonal matrix (the tridiagonal form cited above):

$$\boldsymbol{A}[t] = \begin{bmatrix} \boldsymbol{A}_1[t] & & & \\ & \boldsymbol{A}_2[t] & & \\ & & \ddots & \\ & & & \boldsymbol{A}_n[t] \end{bmatrix} \tag{3.43}$$

in which each block is formed as follows

$$\boldsymbol{A}_i[t] = \begin{bmatrix} a_i[t] & b_i[t] \\ -b_i[t] & a_i[t] \end{bmatrix}. \tag{3.44}$$

The a_i and b_i represent the real and imaginary parts of the i^{th} pole, respectively. The left and right mode shapes in $\boldsymbol{\Phi}$ and $\boldsymbol{\Psi}$ are also constructed with couples of their real and imaginary parts of each mode instead of complex conjugated pairs. This kind of representation is explained in details in [105] for example.

3.3.2 Identification of the state-space model parameters

The identification of the model parameters is based on the same procedure as before, i.e. the minimization of the prediction error (PE). This prediction error is iteratively minimized by the same nonlinear optimization algorithm as used previously. If we denote by a hat ($\hat{}$) the estimates of the model (the output estimate $\hat{\boldsymbol{y}}[t]$ and the state estimate $\hat{\boldsymbol{\eta}}[t]$) we have

$$\left\{ \begin{array}{rcl} \hat{\boldsymbol{\eta}}[t+1,\boldsymbol{\theta}] & = & \boldsymbol{A}[t]\,\hat{\boldsymbol{\eta}}[t,\boldsymbol{\theta}] + \boldsymbol{\Psi}[t]\;(\boldsymbol{y}[t] - \hat{\boldsymbol{y}}[t,\boldsymbol{\theta}]) \\ \hat{\boldsymbol{y}}[t,\boldsymbol{\theta}] & = & \boldsymbol{\Phi}[t]\,\hat{\boldsymbol{\eta}}[t,\boldsymbol{\theta}] \end{array} \right. , \tag{3.45}$$

or equivalently

$$\left\{ \begin{array}{rcl} \hat{\boldsymbol{\eta}}[t+1,\boldsymbol{\theta}] & = & (\boldsymbol{A}[t] - \boldsymbol{\Psi}[t]\boldsymbol{\Phi}[t])\;\hat{\boldsymbol{\eta}}[t,\boldsymbol{\theta}] + \boldsymbol{\Psi}[t]\,\boldsymbol{y}[t] \\ \hat{\boldsymbol{y}}[t,\boldsymbol{\theta}] & = & \boldsymbol{\Phi}[t]\,\hat{\boldsymbol{\eta}}[t,\boldsymbol{\theta}] \end{array} \right. . \tag{3.46}$$

The error to be minimized is the difference between the measured and predicted output:

$$\boldsymbol{e}[t,\boldsymbol{\theta}] = \boldsymbol{y}[t] - \hat{\boldsymbol{y}}[t,\boldsymbol{\theta}] \tag{3.47}$$

and it is minimized in a least squares sense, using the following cost function

$$V(\boldsymbol{\theta}) = \frac{1}{2N}\sum_{t=1}^{N} \boldsymbol{e}[t,\boldsymbol{\theta}]^T \boldsymbol{e}[t,\boldsymbol{\theta}]. \tag{3.48}$$

The nonlinear optimization scheme described in Section 3.1 is still valid. The only difference in this case lies in the different parameterization of the state-space model. This only has an influence on the computation of the gradients of the cost function with respect to the model parameters. This computation implies the derivative of the prediction error with respect to the parameters and it is still given by

$$\frac{\mathrm{d}\,\boldsymbol{e}[t,\boldsymbol{\theta}]}{\mathrm{d}\theta_i} = -\frac{\mathrm{d}\,\hat{\boldsymbol{y}}[t,\boldsymbol{\theta}]}{\mathrm{d}\theta_i}. \tag{3.49}$$

The latter operation has to be performed for each of the parameters in the model in order to populate the Jacobian matrix of the optimization scheme. All the derivatives can be analytically computed as the realization of other state-space models. In fact, introducing first a new variable $\hat{\boldsymbol{z}}[t] = \frac{\partial \hat{\boldsymbol{\eta}}[t,\boldsymbol{\theta}]}{\partial \theta_i}$ and considering (3.46), we have the following cases

- If θ_i belongs to the $\boldsymbol{A}$ matrix :

$$\left\{ \begin{array}{rcl} \hat{\boldsymbol{z}}[t+1] & = & (\boldsymbol{A}[t] - \boldsymbol{\Psi}[t]\boldsymbol{\Phi}[t])\;\hat{\boldsymbol{z}}[t] + \boldsymbol{E}_{k,l}[t]\,\hat{\boldsymbol{\eta}}[t,\boldsymbol{\theta}] \\ \dfrac{\partial \hat{\boldsymbol{y}}[t,\boldsymbol{\theta}]}{\partial \theta_i} & = & \boldsymbol{\Phi}[t]\,\hat{\boldsymbol{z}}[t] \end{array} \right. , \tag{3.50}$$

- If θ_i belongs to the $\boldsymbol{\Phi}$ matrix :

$$\left\{ \begin{array}{rcl} \hat{\boldsymbol{z}}[t+1] & = & (\boldsymbol{A}[t] - \boldsymbol{\Psi}[t]\boldsymbol{\Phi}[t])\;\hat{\boldsymbol{z}}[t] - \boldsymbol{\Psi}[t]\boldsymbol{E}_{k,l}[t]\,\hat{\boldsymbol{\eta}}[t,\boldsymbol{\theta}] \\ \dfrac{\partial \hat{\boldsymbol{y}}[t,\boldsymbol{\theta}]}{\partial \theta_i} & = & \boldsymbol{\Phi}[t]\,\hat{\boldsymbol{z}}[t] + \boldsymbol{E}_{k,l}[t]\,\hat{\boldsymbol{\eta}}[t,\boldsymbol{\theta}] \end{array} \right. , \tag{3.51}$$

- If θ_i belongs to the $\boldsymbol{\Psi}$ matrix :

$$\left\{ \begin{array}{rcl} \hat{\boldsymbol{z}}[t+1] & = & (\boldsymbol{A}[t] - \boldsymbol{\Psi}[t]\boldsymbol{\Phi}[t])\;\hat{\boldsymbol{z}}[t] - \boldsymbol{E}_{k,l}[t]\boldsymbol{\Phi}[t]\,\hat{\boldsymbol{\eta}}[t,\boldsymbol{\theta}] + \boldsymbol{E}_{k,l}[t]\,\boldsymbol{y}[t] \\ \dfrac{\partial \hat{\boldsymbol{y}}[t,\boldsymbol{\theta}]}{\partial \theta_i} & = & \boldsymbol{\Phi}[t]\,\hat{\boldsymbol{z}}[t] \end{array} \right. , \tag{3.52}$$

where $\boldsymbol{E}_{k,l}[t]$ is a single entry matrix of appropriate dimension in which all components are null but one. This value represents the value of the basis function corresponding to the θ_i parameter evaluated at time t.

Direct advantage of the modal domain parameterization

One point we have to deal with in the optimization problem is its complexity i.e. the number of parameters involved in the identification process. It is well known in non-convex optimization with the Levenberg-Marquardt (and the Newton familly algorithms) that the greater the number of parameters, the greater is the risk to converge to a local minimum. To tackle this problem, a graduated optimization strategy may be investigated. It means that the initial (very-) complex problem is decomposed in a series of simpler optimization problems. An illustration of this way to solve the problem is shown in Figure 3.8. This method can be used in our case because of the chosen parameterization for the identification. Indeed, our parameterization corresponding to the modal decomposition, it is possible to identify one or few modes at a time and retrieve their contribution to the response before continuing with the identification of one or few other modes. Of course, it is better to begin by the modes having the greater influence in the response because the optimization algorithms tries to minimize the residual. This way to proceed may be advantageous on more complex structures.

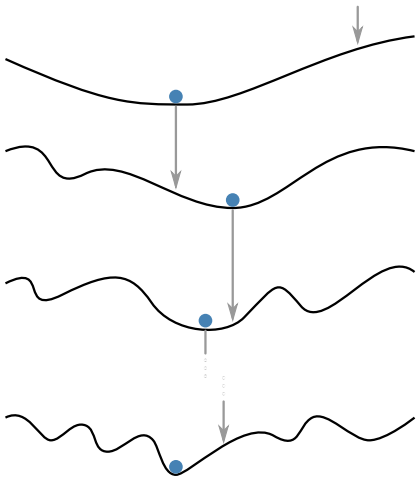

Figure 3.8: Illustration of the path to the solution by graduated optimization.

3.4 Experimental identification with the multivariate time-varying state-space model

3.4.1 Identification of a good model structure

In the present case, the identification of the time-varying structure is slightly different as previously done with the ARMA(V) models. Let us remind that in the preceding

sections and chapter, a first batch analysis using a fast 2SLS method was used to identify good possible model candidates. A more detailed analysis was then performed by nonlinear optimization on a reduced set of promising model candidates. The goal was to properly choose AR and MA orders and good bases dimensions. In the present case, no variation of the model order is performed, it is directly fixed to five because only five modes are identified in the frequency band of interest. Of course, fixing the order of the model in the ARMA models is also possible, but we saw that an overestimation of the order was required to get identified results of good quality. In the present state-space model, the order is fixed a priori and the only degrees-of-freedom in the model structure will be the number (and type) of the basis functions. It is chosen here to take the same number of functions for all the parameters in the model. A second difference is that, conversely to the ARMA models that could be initiated by other longer AR models, the state-space model requires an external initial guess to start properly. It is chosen here to start with the results of the LTI analysis performed without the moving mass (Section 1.5.1). If such results are not available, a simple analysis with any modal identification method applied on a short time window of the data may be suitable too. This starting guess is then placed in the vector of parameters at the place corresponding to the first function (generally a unit function). It will acts as the "mean value" of the vector of the model parameters. The other parameters are set to zero and will be updated in the subsequent optimization. Of course, if the first function is not a unitary one, for example if a basis of splines is chosen, the parameters have to be projected on the whole basis to form the average constant starting value.

A series of identification is then performed by iterating on the number of functions in the basis up to 15 functions. Chebyshev polynomials are again considered for consistency purpose between the results obtained with the other methods. Because only one parameter tunes the structure of the identification model, the plots of the FPE, AIC and BIC scores is far easily readable than in the previous cases. Each of these three scores is shown in Figure 3.9. Analyzing this figure indicates that nine polynomials in the basis of functions is the best choice for the identification. The identification is then performed using these basis functions and the results of the LTI analysis as starting point.

The result of the identification with the selected model structure is shown in Figure 3.10. It is also interesting to show the particular advantage brought by the modal modeling. Because the state-space model is written in a modal superposition way, it is possible to decompose the identification mode by mode. Indeed, the states of the model representing the modal coordinates, their product with their respective mode shape enables to study the influence of each mode on the total response separately. This is illustred in Figure 3.11 in which the modal response of each mode is plotted separately for the second measurement channel.

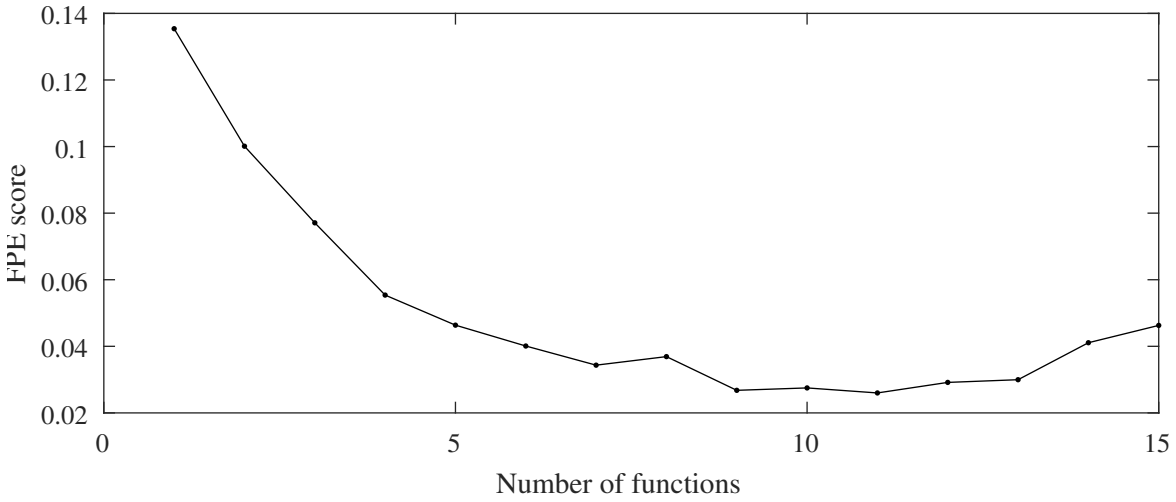

(a) FPE scores for the batch of model candidates.

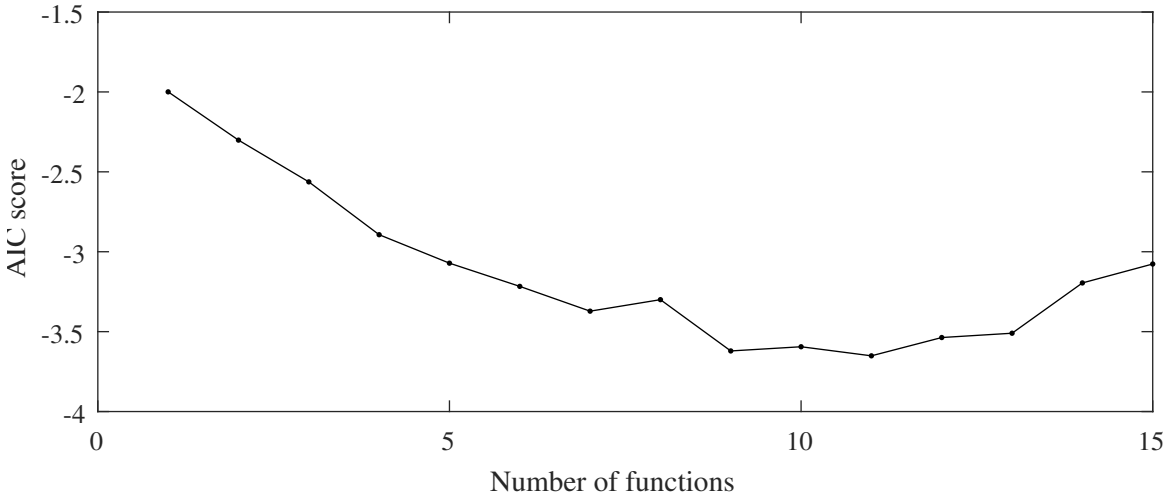

(b) AIC scores for the batch of model candidates.

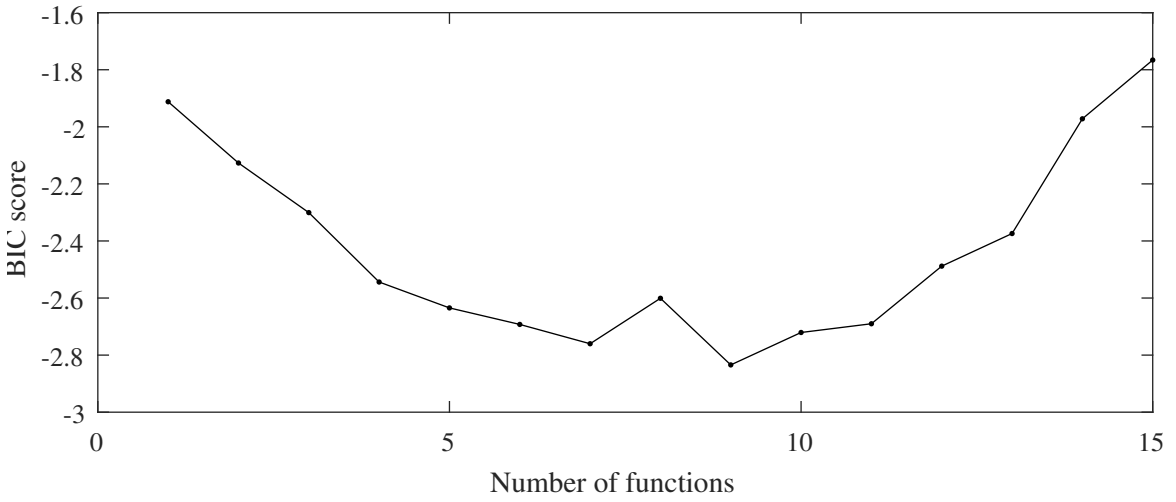

(c) BIC scores for the batch of model candidates.

Figure 3.9: FPE, AIC and BIC criteria with respect to the number of Chebyshev polynomials.

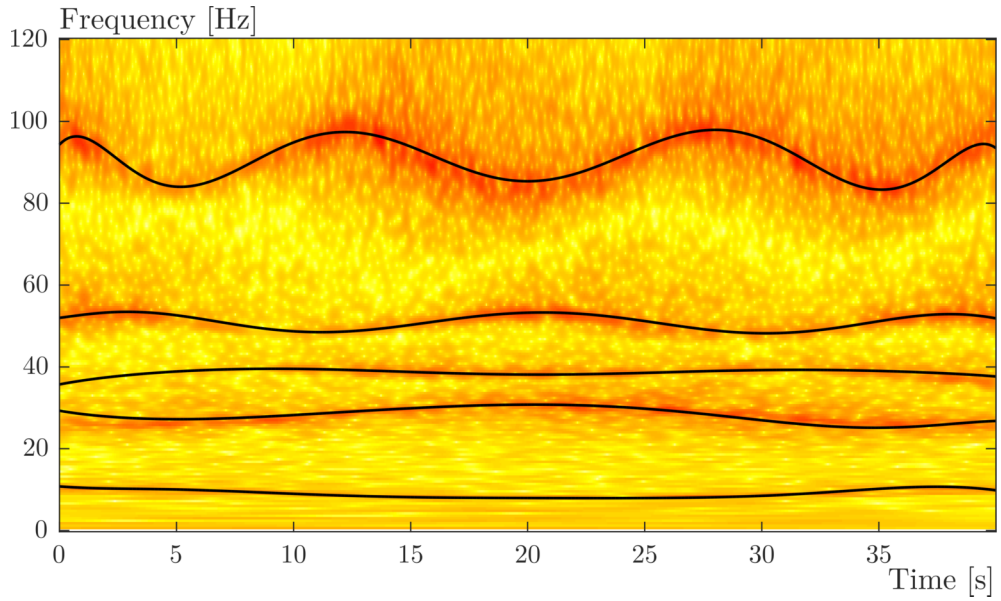

Figure 3.10: Identified results with 9 Chebyshev polynomials.

3.5 Comparison between both multivariate modelings

A fast comparison of the results may be drawn between both the time-varying ARMAV and state-space models. First, as it can be seen in Figure 3.12, the correspondence in frequencies between both the models is quite close. Further, they also lie close the the resonance frequencies that appear on the wavelet plot in the background. Then, concerning the identification of the mode shapes, Figures 3.13 and 3.14 compare the two sets of varying modes obtained by each method. The time-varying MAC being most of the time close to one, it can be concluded that the mode shapes extracted with each method correspond quite well.

A second comparison about the practical use of the methods may also be done. First, concerning the complexity of both identification model structures, the TV-ARMAV(3,3)[9,1] model contains 1323 parameters to identify against 1350 for the time-varying state-space model in the modal domain. These values are quite close. In theory, the theoretical ARMAV model orders should be [2,2] but as seen earlier, some overparameterization was required to properly identify the system. The over-parameterization of the model also brings an undesirable consequence by introducing spurious poles in the results. It seems that the state-space modeling is less impacted by the overparameterization issue because the true order, ten for the identification of the five modes, is used with success. The selection of a good model structure is also a challenge. Even if a strategy based on fast 2SLE identifications is applied with the ARMAV model, the fact that four parameters (the two model orders and the two sizes of the basis of functions) increases the complexity of this task. The model order of the state-space model being fixed a priori, only iterations about the number of basis functions are required. Concerning the starting of the identification process, the advantage goes to the ARMAV model because it can be initiated in a least square sense using a

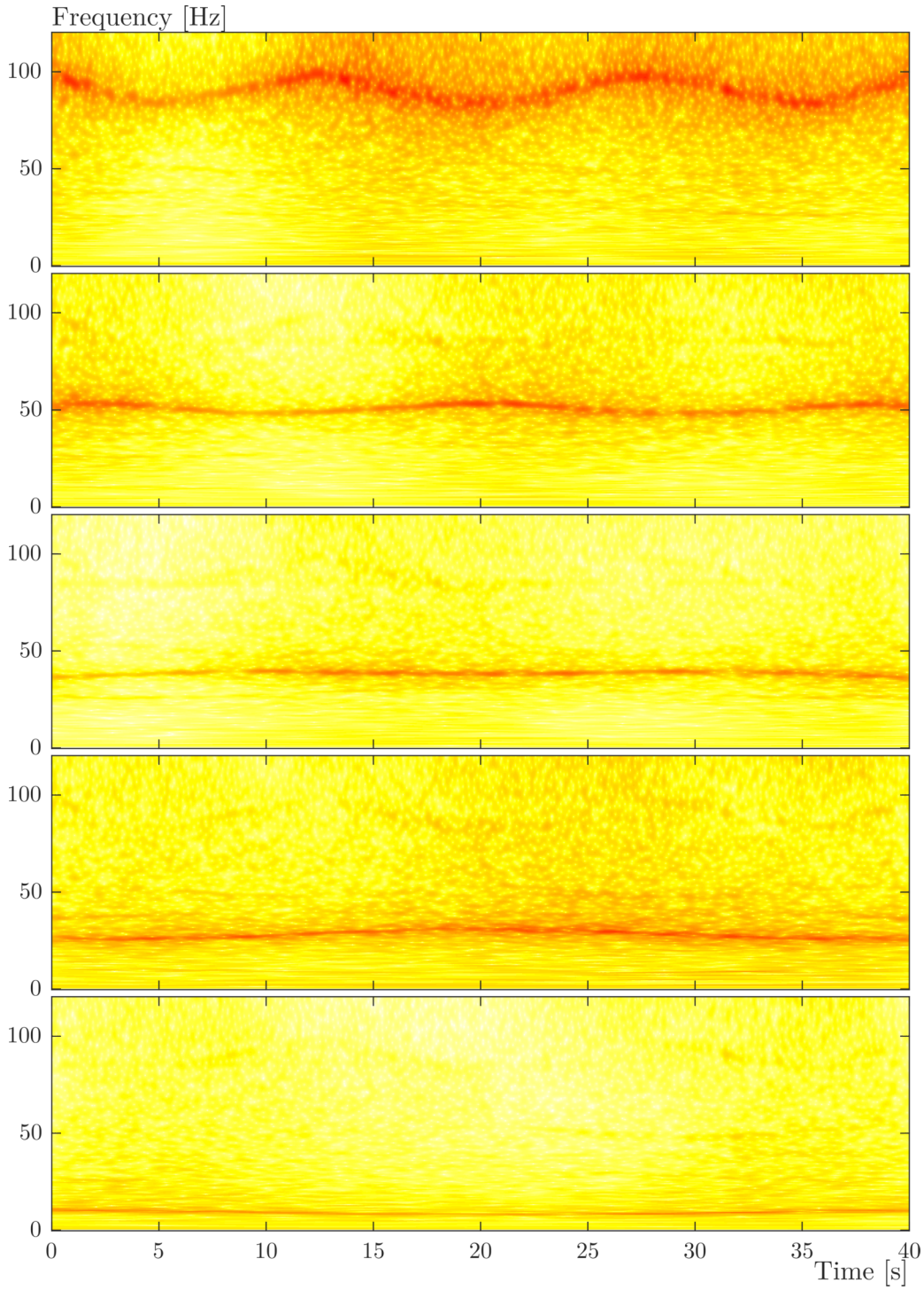

Figure 3.11: The modal contribution of each mode is a direct product of the modal domain state-space identification. Time-frequency representations of the five modal contributions of the second channel are shown.

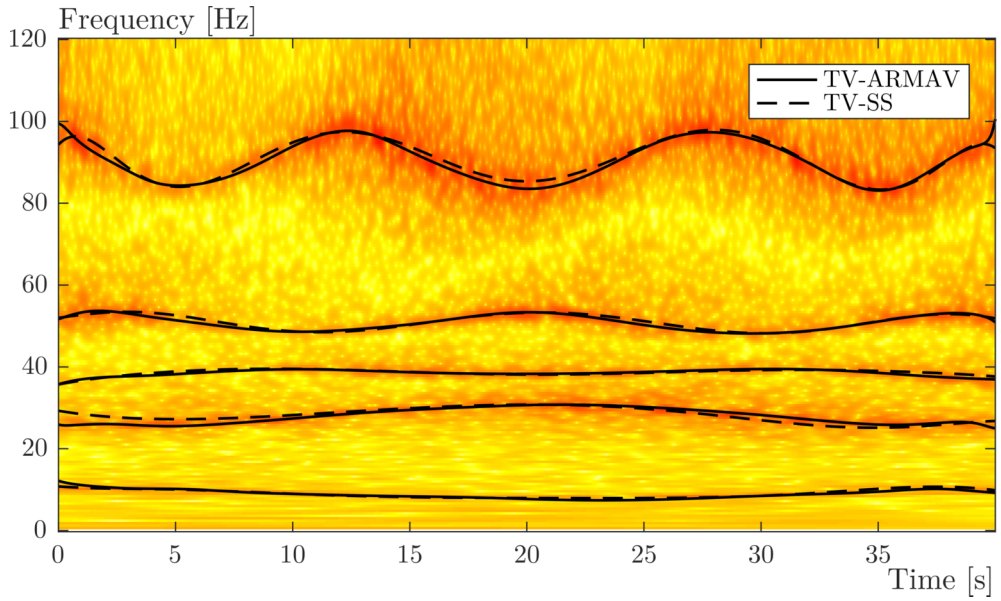

Figure 3.12: Comparison in frequency between the two kinds of models.

first AR model. The state-space model requires a good initial guess. If no information about the system is known, it can already be initiated through an approximate LTI identification on a more or less short time window.

3.6 Concluding remarks

In this chapter, two types of multivariate modelings are implemented for identification purposes in nonstationary conditions. The two methods are applied on the same data set as the one used in the two preceding chapters. It is shown here that the method of the basis functions can be applied on multivariate identification models in order to get a full set of time-varying parameters, the mode shapes included. The two methods considered here for the identification are able to correctly extract the varying modal parameters of the structure and the results with both methods show a good correlation. The challenges with each method are the model structure selection of the time-varying ARMAV model and the way to select the results corresponding to the physical modes from the spurious ones which are introduced by the overparameterization of the model. On the other hand, the structure of the time-varying modal state-space model is simpler to choose. However, conversely to the ARMAV model, it requires a good initial guess which has to be provided from another analysis.

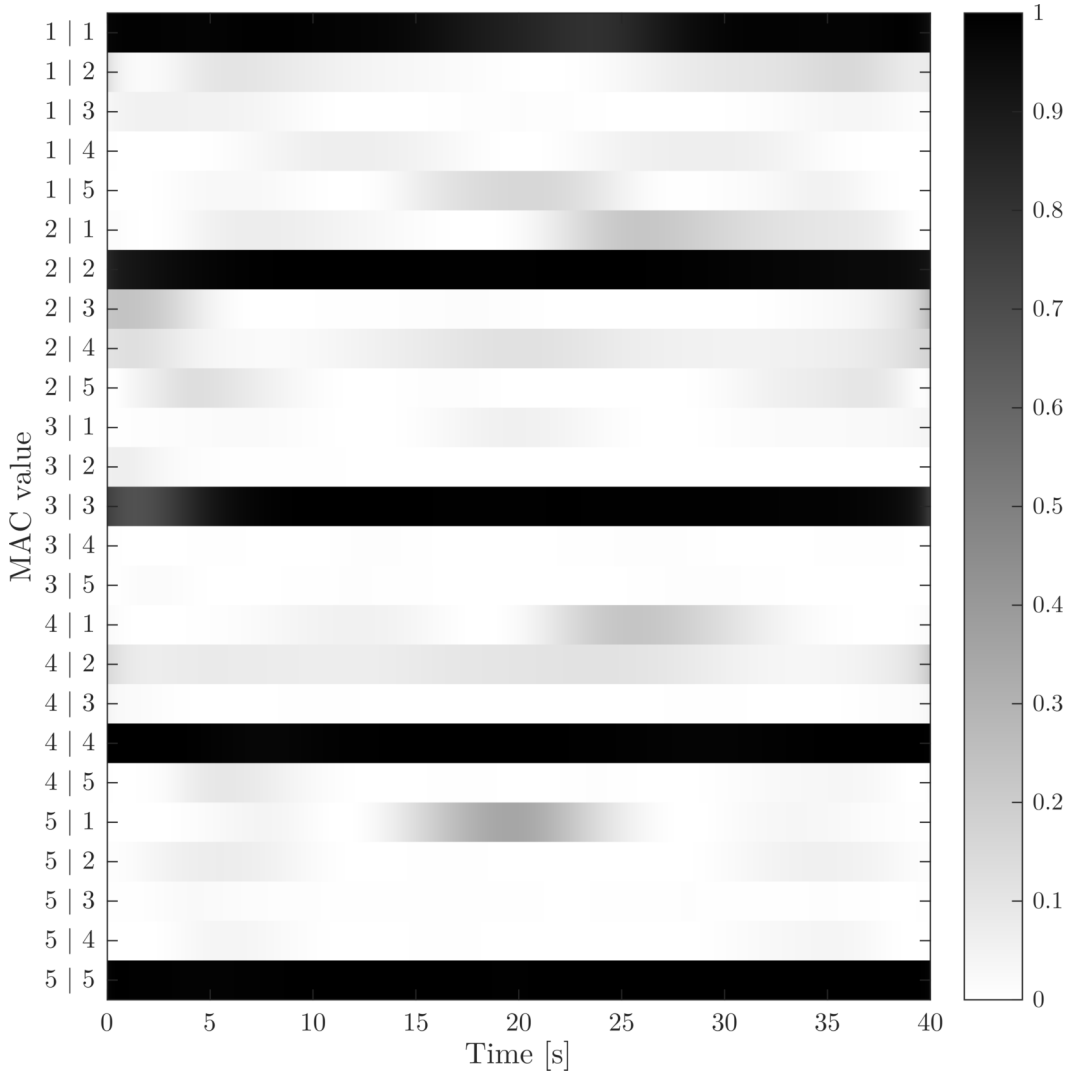

Figure 3.13: Comparison in mode shapes between the two kinds of models with the full TV MAC matrix.

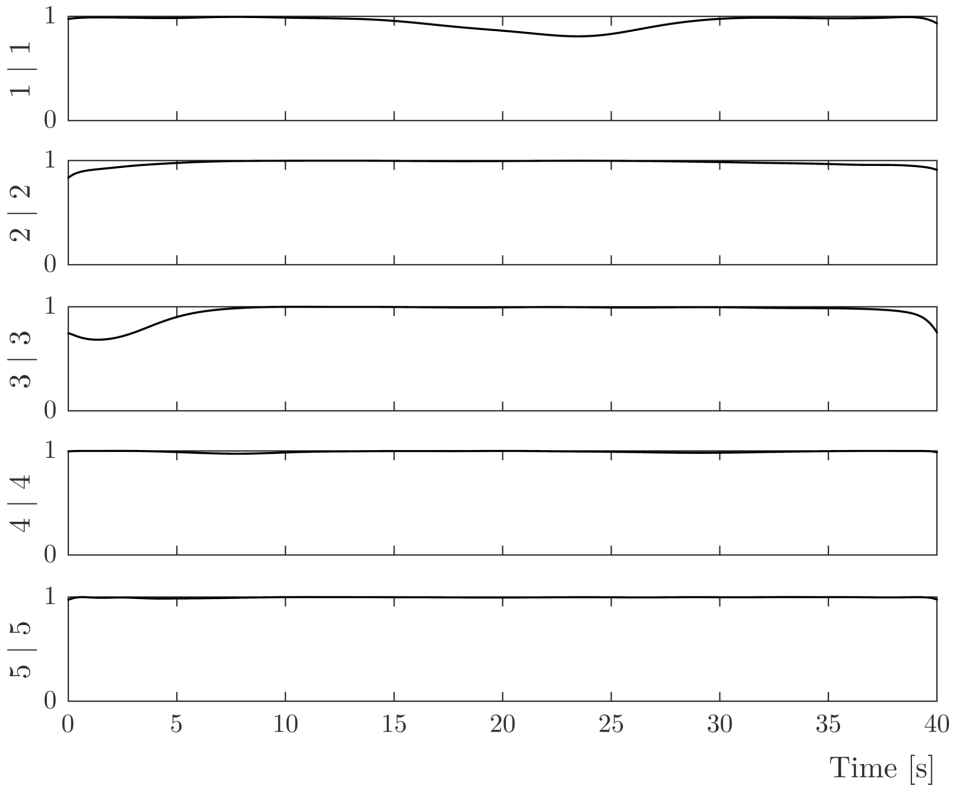

Figure 3.14: Comparison in mode shapes between only the paired modes.

4

Extended applications

In the preceding chapters, several methods able to perform the modal identification of structures which exhibit a time-dependency were introduced. The aim of this chapter is first to test the previous methods, especially the multivariate ones, when complexity is increased. Practically, the experimental setup is extended to twelve sensors placed at the edges of the beam and the considered frequency band is increased up to 200 Hz. The latter modifications render the problem more complex. Indeed, the extended frequency band and the new placement of the sensors brings new modes in the identification process. The upgrade to 200 Hz adds a new bending mode and the fact that the sensors are placed on the edges of the beam make the torsion and rotation modes to be visible.

A second point which is addressed is the knowledge of the varying parameter. In the present problem, another way to treat the problem could be to consider a parameterically-varying behavior. In our example it is the position of the moving mass which influence the dynamics of the primary structure even if this parameter is itself time-dependent. In the experiment, the position of the moving mass is monitored with a laser sensor and this information is used for monitoring purposes.

The chapter is divided as follows. First, a LTI identification is performed in order to understand the dynamics of the newly added modes. The identification is then performed in time-varying conditions to perform the same analysis as in the previous chapter. Next, because the methods developed here provide some information about the varying mode shapes of the structure, it is shown how they can be useful for monitoring purposes by trying to recover the time-varying position of the mass. Finally, another example of application with a direct use of the information of the position of the mass is presented.

4.1 LTI modal identification of the extended experimental setup

The same structure, the beam and its moving mass, is considered here but the frequency band is extended from 120 to 200 Hz and the number of sensors is increased from 7 to 12. Two sensors are placed at both ends in front of the springs and five pairs of sensors are located on each side of the beam in order to be able to detect bending as well as torsion modes. A schematic model of the measurement setup is shown in Figure 4.1. For all the tests, the system is randomly excited using a shaker at coordinate 3 (Figure 4.1(b)).

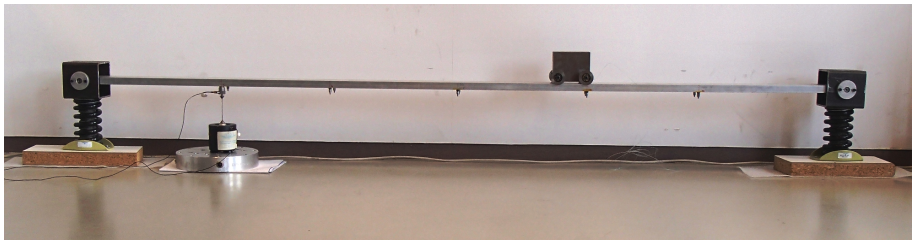

(a) Experimental beam.

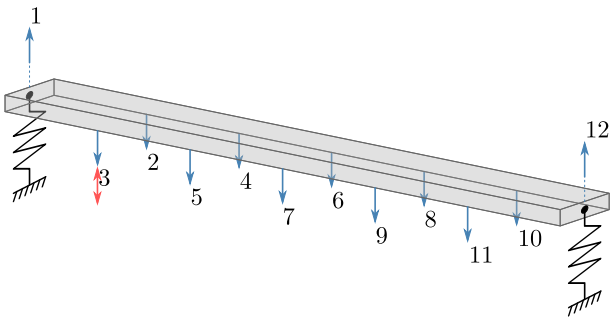

(b) Experimental measurement map.

Figure 4.1: Scheme of the excitation and recording coordinates.

The LTI analysis is performed in the same way as described in Chapter 1. The structure is randomly excited and modal analysis is performed using the frequency domain PolyMAX method. The obtained stabilization diagram is shown in Figure 4.2. The frequency, damping ratio and mode shape corresponding to each of the selected physical poles are listed and depicted in Table 4.1 and Figure 4.3, respectively. In these results, the bending modes identified previously are recovered. A new bending mode appears and two additional rotation and torsion modes are now also visible. It should be noted that a slight difference appears in the frequencies of the bending modes with respect to the previous results. It was observed that the setup is sensitive to small modifications at the supporting springs and they were moved between the two set of experiments. It should also be observed that the torsion modes have a larger damping ratio than the bending ones.

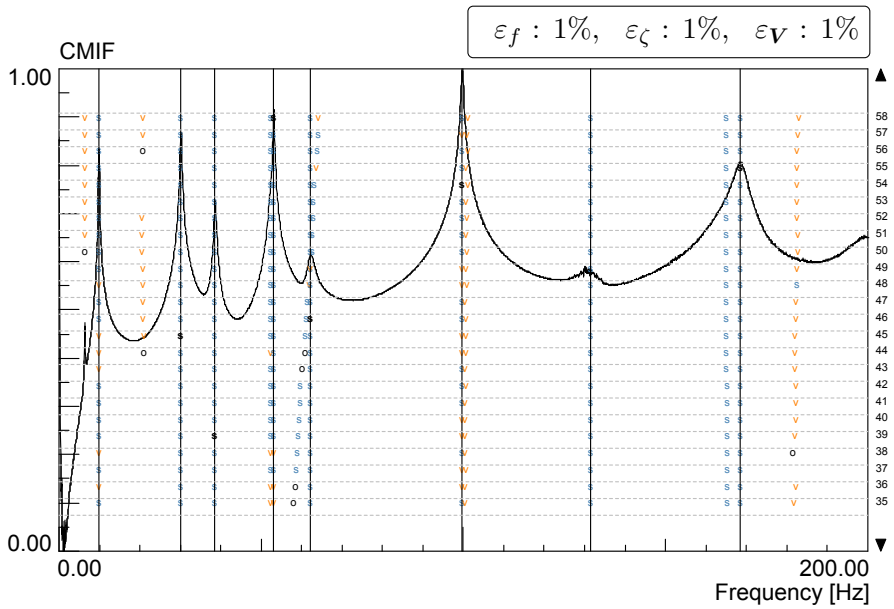

Figure 4.2: Stabilization diagram of the beam subsystem. The selected poles are appear as bold black **s**.

Mode #	f_r [Hz]	ζ_r [%]
1	9.86	0.32
2	30.12	0.52
3	38.6	0.65
4	53.14	0.28
5	62.17	1.57
6	99.70	0.28
7	131.57	2.039
8	168.60	0.99

Table 4.1: Frequencies and damping ratio's up to 200 Hz in the linear time invariant case.

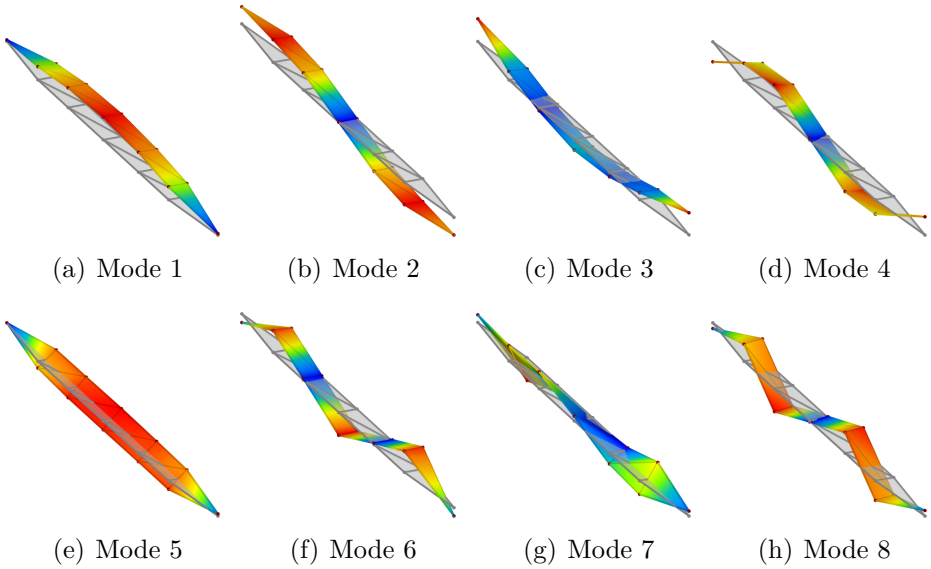

(a) Mode 1 (b) Mode 2 (c) Mode 3 (d) Mode 4

(e) Mode 5 (f) Mode 6 (g) Mode 7 (h) Mode 8

Figure 4.3: Complete set of mode shapes up to 200 Hz in the linear time invariant case.

4.2 Simple finite element model of the structure

In this section, a numerical model (a beam finite element model) is constructed and will serve later for monitoring purposes. The model consists in an assembly of Euler-Bernoulli beam elements. At both ends, the supports are modeled by stiffness elements and lumped masses. The updated finite element model has the following properties:

- Euler-Bernoulli beam finite elements:
  - Young's modulus: $E = 65$ GPa
  - Density: $\rho = 2695$ kg/m^3
  - Poisson's ratio: $\nu = 0.33$
- Stiffness elements
  - Stiffness in the vertical direction: $k_z = 1.68\,10^5$ N/m
  - Stiffness in the lateral direction: $k_y = 5.83\,10^4$ N/m
  - Stiffness in rotation about the beam axis: $k_{\theta_x} = 1555.79$ Nm/rad
  - Mass element in vertical translation : $m_z = 2.93$ kg
  - Mass element in vertical translation : $m_y = 2.72$ kg
  - Inertia element in rotation : $J_x = 7.5\,10^{-3}$ kg.m^2

The correlation between the experimental and the finite element results is illustrated in Figure 4.4 by a MAC matrix.

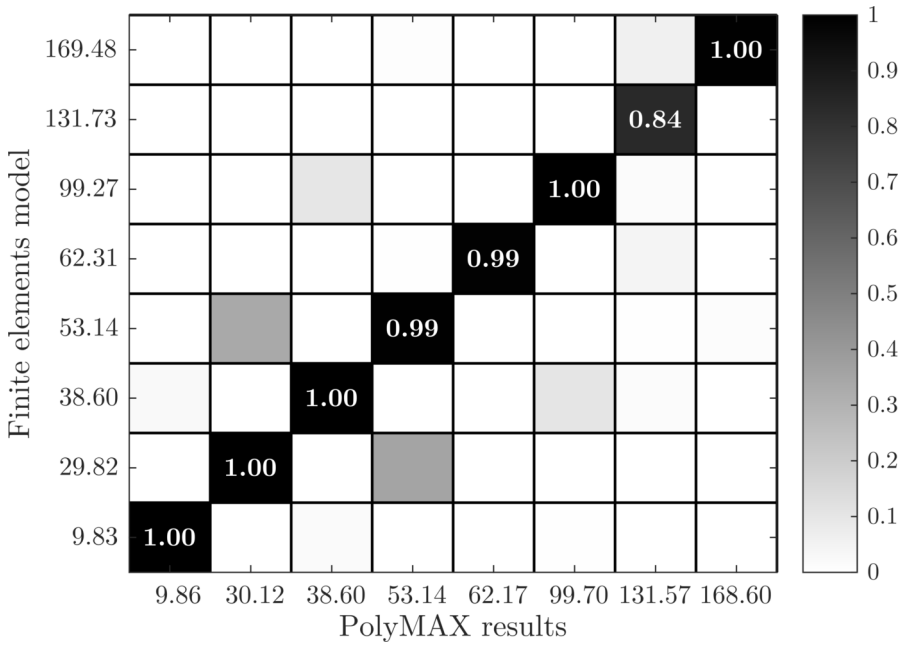

Figure 4.4: MAC matrix between the identified LTI structure and its basic finite element model.

4.3 Identification in time-varying conditions

For this test, the random excitation is turned on and the mass is pulled by hand using a simple wire while its current displacement is recorded by a laser position sensor. The acquisition time is around 50 seconds but only the time sequence when the mass is moving from the left to the right end of the beam is kept. The data is recorded for 42 seconds at a sampling rate of 400 Hz for each channel. The output of the laser sensor corresponds to a linearly increasing voltage from 0 V (when the mass is located at the left end of the beam) to 10 V (when the mass reaches the right end). For illustration, the displacement of the mass with respect to time during the experiment is plotted on top of Figure 4.5. The evolution of the frequencies of the system with respect to time (or with respect to the position of the mass) is also shown in this figure with the wavelet transform of the third channel as reference. The observation that can be drawn are similar to the case when sensors are placed only on the neutral axis of the beam. The time-varying resonance frequencies oscillate between upper and lower bounds and the upper ones are the frequencies of the beam without the moving mass.

4.3.1 Identification with the time-varying ARMAV model

The identification with the time-varying ARMAV model starts in the same way as what was done in the previous chapter. The process begins with a series of identifications using several models in order to identify good model candidates. This time, in order to save computation time, only equal AR and MA orders are considered in the loop. The FPE, AIC and BIC scores obtained by the 2SLS identifications of models with equal AR and MA orders going from 2 to 8 (and up to 13 functions) are plotted in Figure 4.6.

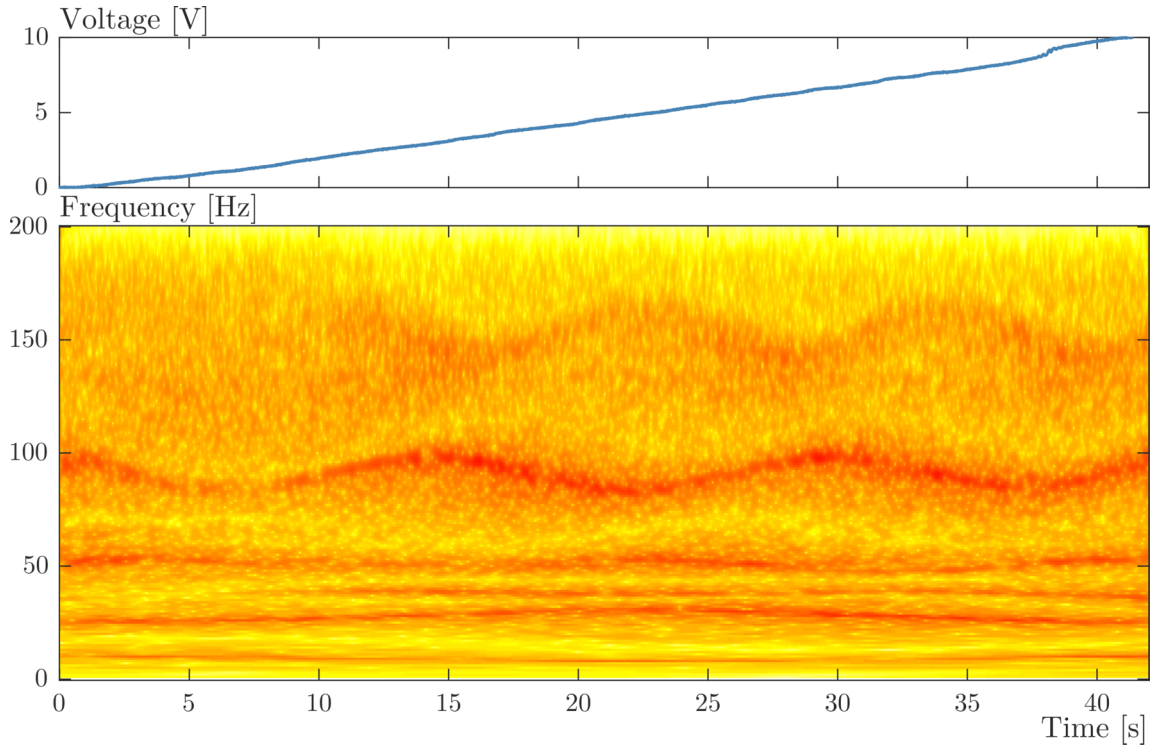

Figure 4.5: Time-frequency representation of the time-varying response in the third channel. The relative position of the center of the mass is plotted on the top.

Before going further, we can notice that the FPE criterion encounters negative values for some test cases. This is the illustration of one drawback of the multivariate ARMA modeling. Looking to the way the FPE criteria is computed, a negative value means that the number of coefficients to identify is greater than the number of data samples. In these configurations, the result of the identification should directly be rejected. It occurs here for the higher orders and sizes of the basis of functions. This huge increase in the number of parameters is also amplified by the higher dimensionality of the vector of measurements because each block in the model is proportional to the square of this dimension. As a rule of thumb, Niedźwiecki suggests that the number of parameters to identify should be less than 20% of the number of observations [61]. This high number of parameters should then be carefully analyzed when dealing with large problems.

As in the previous chapter, the selection of a good model candidate is not straightforward. As previously observed, the BIC criterion penalizes more the model complexity compared to the AIC one. In Figure 4.6, it can be observed that a good candidate may lie in the first block of identification scores related to the ARMAV(2,2) family but that few models in the second block of ARMAV(3,3) models may also be suitable. The AIC criteria in Figure 4.6(b) targets model in the (3,3) or (4,4) family, which are far more complex. The RSS/SSS criteria (Figure 4.7) does not give any additional clue on the best model candidate.

One of the best model candidates is the time-varying ARMAV(2,2)[8,1] model. The results of the identification performed with the latter model are shown in Figure 4.8(a). At first sight, most of the modes are identified by the identification model but some

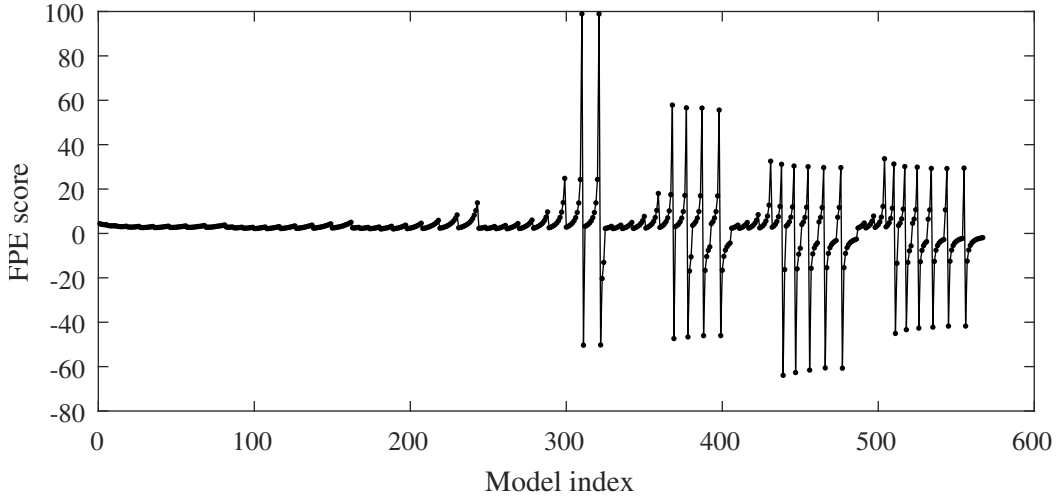

(a) FPE scores for the large batch of model candidates.

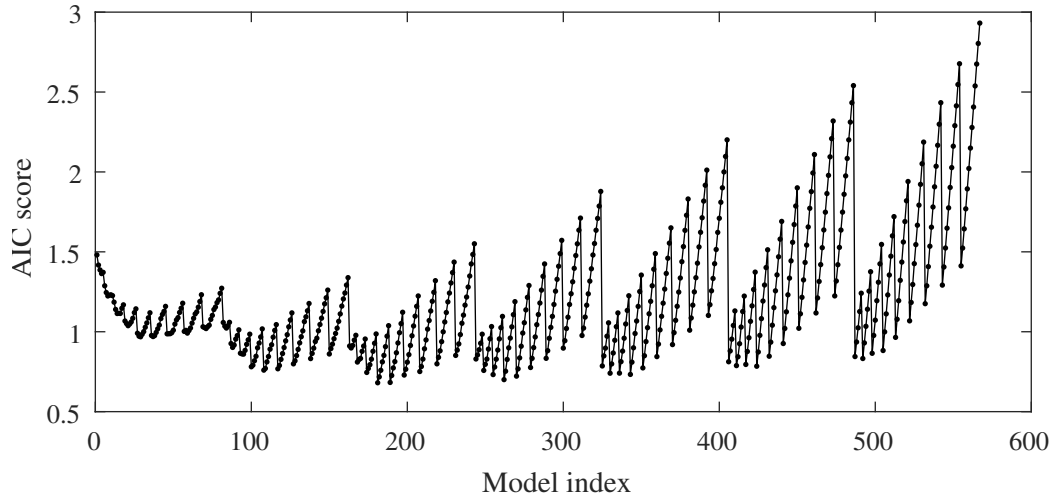

(b) AIC scores for the large batch of model candidates.

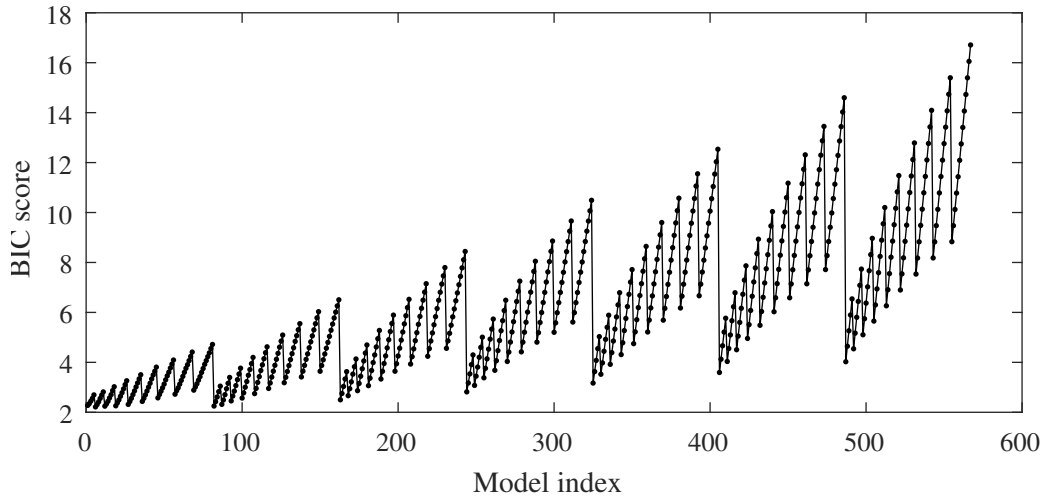

(c) BIC scores for the large batch of model candidates.

Figure 4.6: FPE, AIC and BIC criteria for the extended test setup. Chebyshev polynomials are used as basis functions.

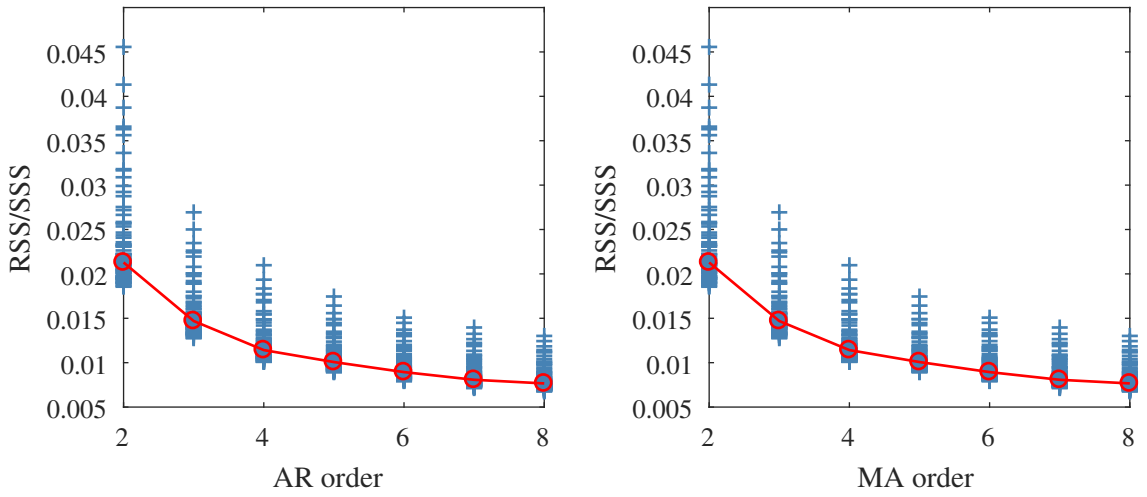

(a) RSS/SSS vs n_a.

(b) RSS/SSS vs n_b.

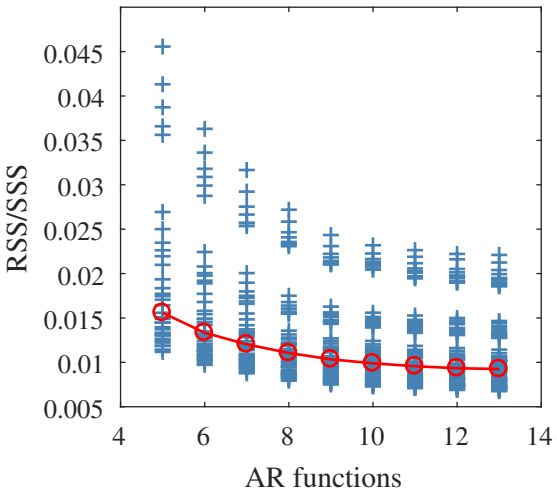

(c) RSS/SSS vs n_{f_a}.

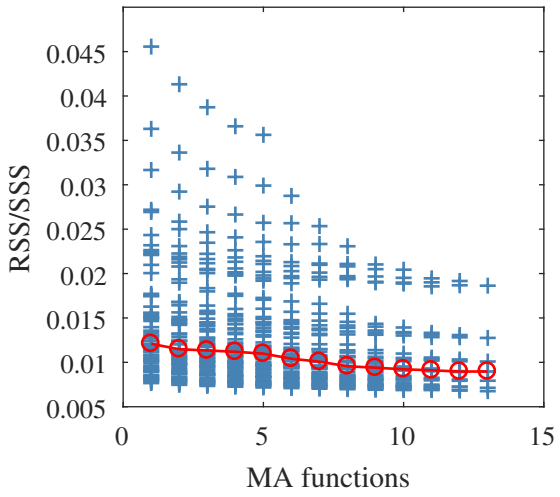

(d) RSS/SSS vs n_{f_b}.

Figure 4.7: RSS/SSS values with respect to each of the model structure parameter for the extended test setup.

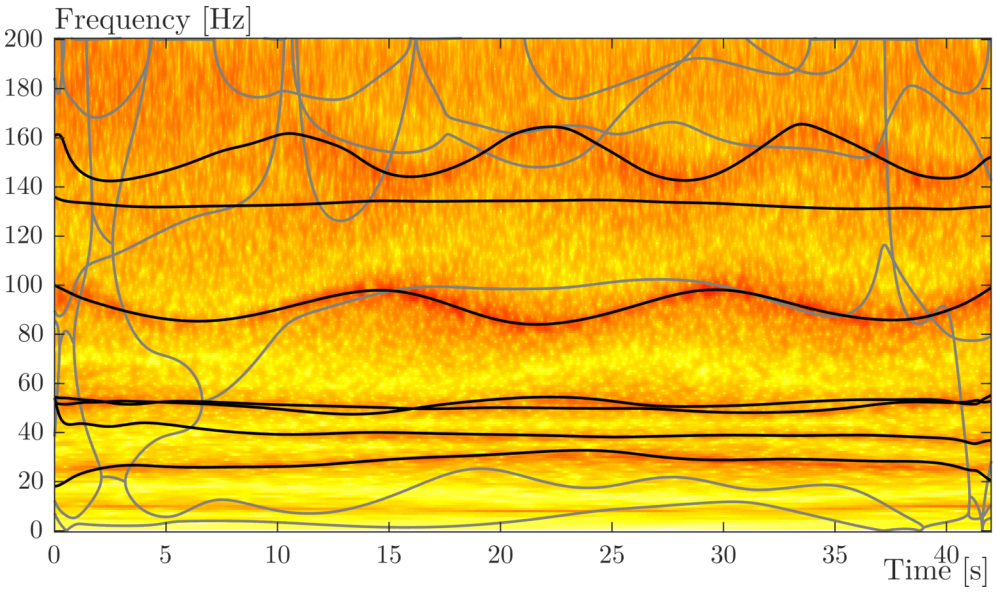

(a) First set of identified modes.

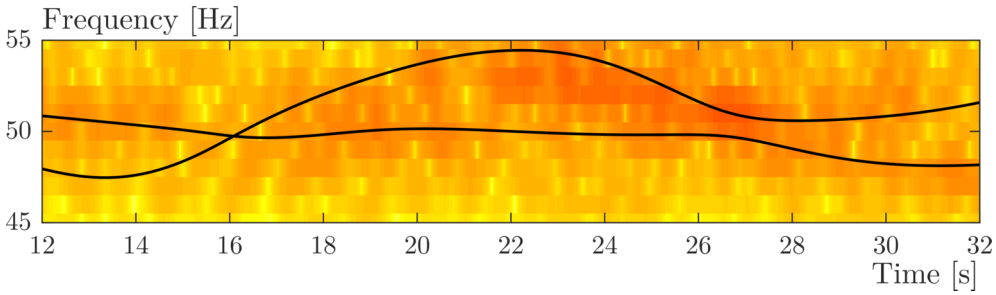

(b) Zoom around the crossing modes.

Figure 4.8: Identified results with the TV-ARMAV(2,2)[8,1]. Black physical modes, gray: spurious modes.

inaccuracies appear. The first one is that the mode at the lowest frequency is not identified by the model. As previously observed, some overparameterization will be required in order to get it. Second, the crossings between the fourth and fifth modes is not perfectly identified as illustrated in the zoom of Figure 4.8(b). The first crossing around 16 seconds is well caught but the second one, close to 27 seconds, not. It means that, even if the modes are identified all along the time axis, there is a switching in the middle of these two mode lines.

In all the set of possible good candidates, no one performs completely the identification of all the modes present in the frequency band. The strategy is then to combine the results of several model structures in order to get the best trajectory for each mode. Of course, in this way, we loose the uniqueness of the model, which makes impossible its direct use for simulation purposes for example. The combination of three model structures enables the identification of the full set of modes involved in the whole response. In Figure 4.9, the combination of ARMAV models (2,2)[8,1], (2,2)[11,2] and (6,6)[11,6] are able to represent the eight physical varying modes. The most difficult to catch is the first mode close to 10 Hz because it requires a drastic overparameterization of the model order up to six to be identified. With such a model, the number

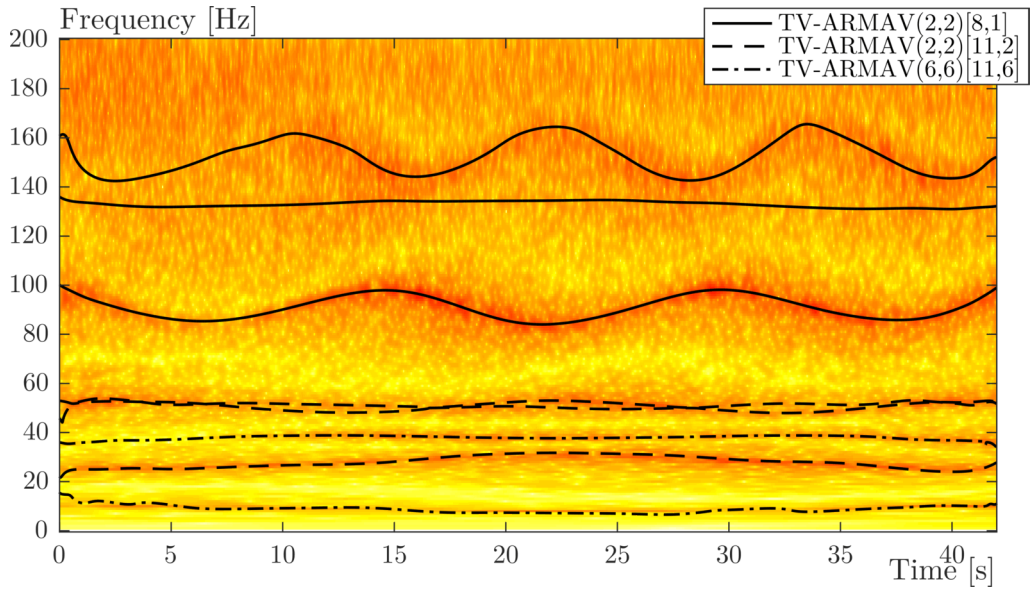

Figure 4.9: Combination of three model structures for the full identification.

of identified poles increases up to 72 and the number of parameters to identify is far more than the suggested 20 % of the number of data points. The drawback with such heavy models is that the identification with the nonlinear optimization process rapidly becomes impractical, even if the cutting procedure for the computation of the Jacobian matrix is used.

4.3.2 Identification with the time-varying state-space model

The same problem is now solved using the modal state-space identification model. As an initial guess, the method is started with the results of the LTI identification of the reference beam.

The problem is now more complex because of the increase of the number of parameters in the identification model. In order to make the work of the optimization scheme easier, the whole problem is cut in several pieces by considering few modes in the model. The vector of parameters is then upgraded with the other modes. The full convergence is not necessary, few iterations may be sufficient in order to have a better initial guess for the subsequent identifications. The identification is first started with modes 2, 4 and 6 which are the mainly excited bending modes. After few iterations, the vector of parameters is then upgraded with the initial guess of the first and third modes. In a final step, all the remaining modes are introduced in the identification scheme. The result is presented in Figure 4.10 which illustrates the different steps of the process. Twelve Chebyshev polynomials are used in this identification which gives the best results.

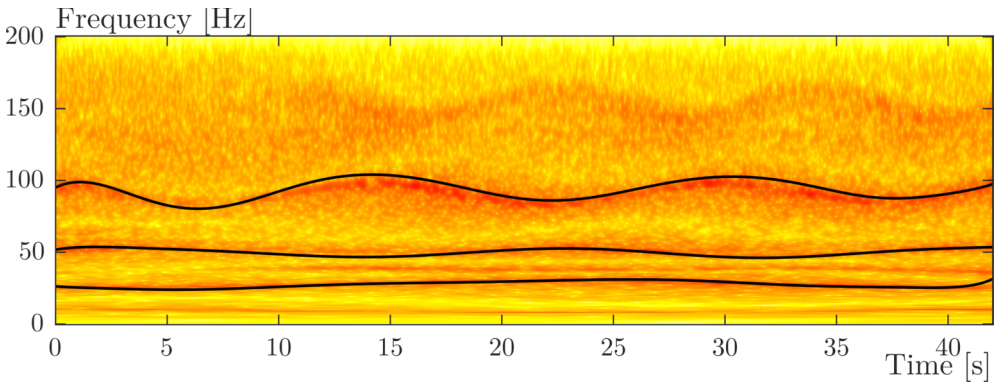

(a) Time-varying frequencies (modes 2, 4, 6).

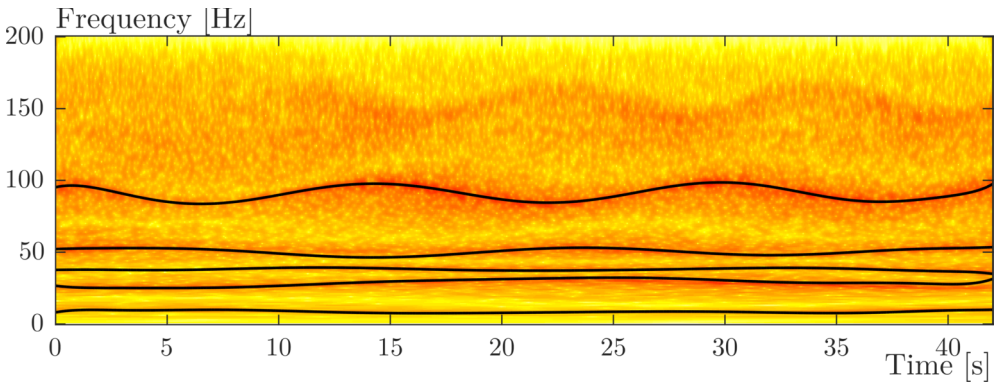

(b) Time-varying frequencies (modes 1, 2, 3, 4, 6).

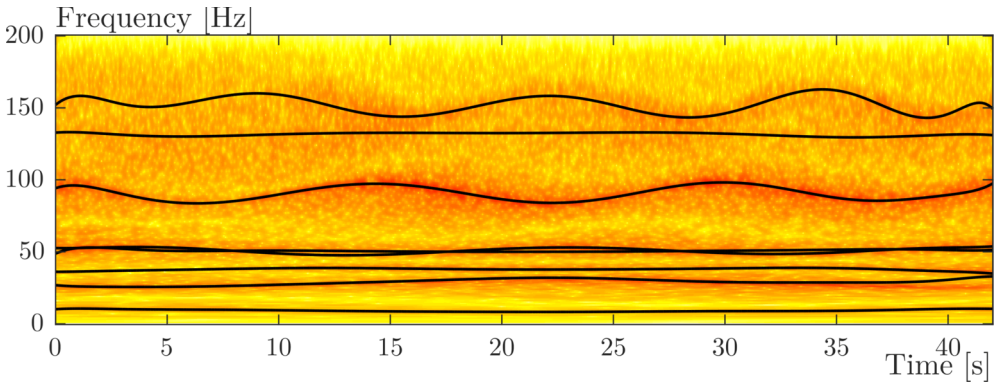

(c) Time-varying frequencies (all modes).

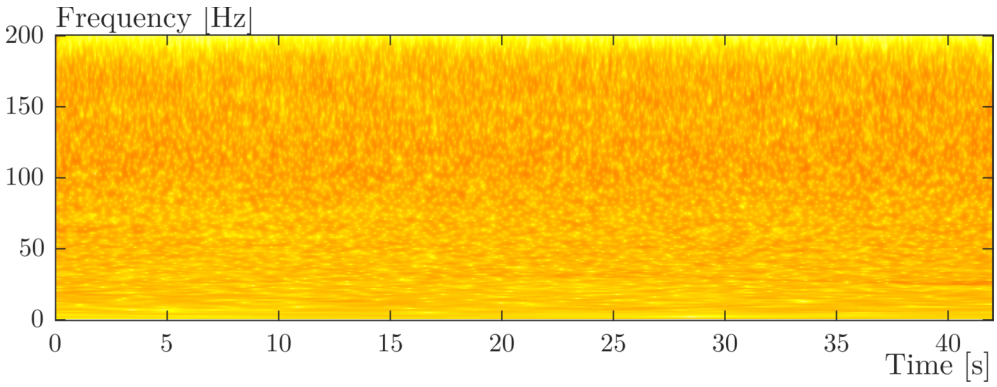

(d) Residual in the third channel.

Figure 4.10: Results of the time-varying identification of the extended setup with the state space model.

4.4 Application for monitoring purposes

In this section, it is shown how the identified time-varying mode shapes may be used for tracking of structural changes. To this end, tools initially developed for error localization can be used. Model updating methods can be used to detect and locate errors or damages between numerical and experimental data [106] but they usually require the knowledge of the structural matrices obtained from a finite element model of the structure. At first glance, it is however possible to use the Coordinate Modal Assurance Criterion (*COMAC*) [107, 48] or its enhanced version (*eCOMAC*) [108] which are tools able to correlate the coordinates between two sets of modes. In what follows, we compare the set of experimental data of the time invariant system (beam and supports only) presented in Section 4.1 and the results of the corresponding finite element model presented in Section 4.2.

4.4.1 Mass tracking using only experimental results

The *COMAC* criterion is a vector containing as many coefficients as the number of degrees-of-freedom contained in the mode shapes. It is computed as follows:

$$COMAC(i) = \frac{\sum_{j=1}^{N_m} |\boldsymbol{X}_j(i) - \boldsymbol{Z}_j(i)|^2}{\sum_{j=1}^{N_m} \boldsymbol{X}_j(i)^2 \sum_{j=1}^{N_m} \boldsymbol{Z}_j(i)^2} \tag{4.1}$$

in which $\boldsymbol{X}$ and $\boldsymbol{Z}$ are two matrices containing two sets of corresponding mode shapes (for example from numerical and experimental analyses) and N_m is the number of modes used for the correlation. In the same way, the *eCOMAC* equation is given as:

$$eCOMAC(i) = \frac{\sum_{j=1}^{N_m} |\boldsymbol{X}_j(i) - \boldsymbol{Z}_j(i)|}{2\, N_m} \tag{4.2}$$

Let us note that for the *eCOMAC* criterion, the two sets of modes have to be unit-normalized and the modes in each pair have to be in phase.

Having performed a linear time invariant modal analysis of the system before the introduction of the moving mass, these results can be used as a reference for the tracking of the structural modification due to the presence of the mass. In Figure 4.11 the sixth mode of the beam in its reference condition (Figure 4.11(a)), the same mode in the system containing the moving mass identified at $t = 10$ s, (Figure 4.11(b)) and the *COMAC* values distributed on the experimental mesh (Figure 4.11(c)). The sixth mode is used here because of the visual effect of the mass for that mode at that particular time instant but all the modes could be obviously retained for the criterion calculation.

The COMAC criterion is calculated at each time step and the scores for each couple of sensors are averaged to only retain seven values along the beam axis. Because of the rather rough experimental mesh, a cubic interpolation of the criterion is used between successive nodes along the beam in order to "smooth" the spatial resolution. The COMAC values (in reality 1-COMAC because we are looking for a decrease in

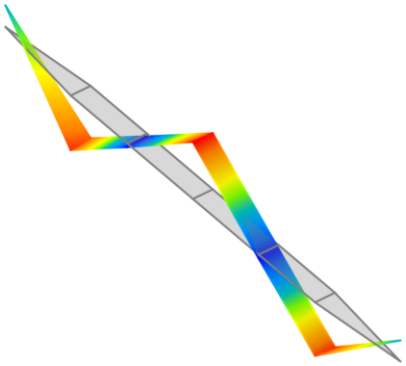

(a) Sixth LTI mode shape.

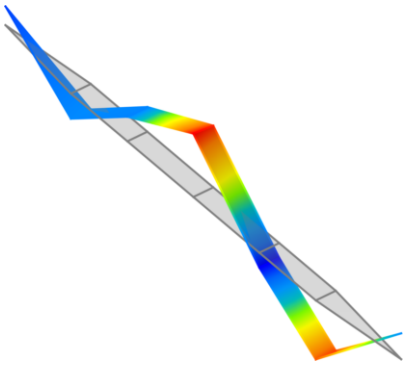

(b) Sixth TV mode shape at $t = 10$ s.

(c) COMAC distribution at $t = 10$ s.

Figure 4.11: Comparison between the reference experimental set of modes and the time-varying identified ones with the *COMAC* criterion. The gray rectangle represents the actual (recorded) position of the mass.

nodal correlation) are represented as a colormap in Figure 4.12. In this figure, the black trajectory represent the measured position of the center of the moving mass for comparison. We can see that the global motion is caught but the discrepancies between the measured and estimate positions may be large at some instants but let us recall the high simplicity of the method which does not need a lot of inputs while giving a good first approximation of position of the perturbing mass.

4.4.2 Mass tracking using experimental results and a reference numerical model

A second approach to track the modification of the system with time is to use our finite element model. As shown previously in Section 4.2, this model well represents the structure without the moving mass. The advantage of the results from that model compared to the results of the LTI modal analysis is that the model may be refined. The problem is how to compare our rough measurement mesh with the refined numerical one. To do so, expansion methods can be used to expand the measurements results to the refined numerical mesh. The *System Equivalent Reduction Expansion Process* (*SEREP*) [109] method is used here to expand our results. The aim of the method is to use a set of analytical modes to expand the experimental ones. First, let us separate the analytical degrees-of-freedom into two subsets, the m masters DoFs corresponding to the measured DoFs, and the s slaves DoFs. If $\boldsymbol{Z}$ represents the set of experimental mode shapes and

$$\boldsymbol{X} = \begin{bmatrix} \boldsymbol{X}_m \\ \hline \boldsymbol{X}_s \end{bmatrix}, \tag{4.3}$$

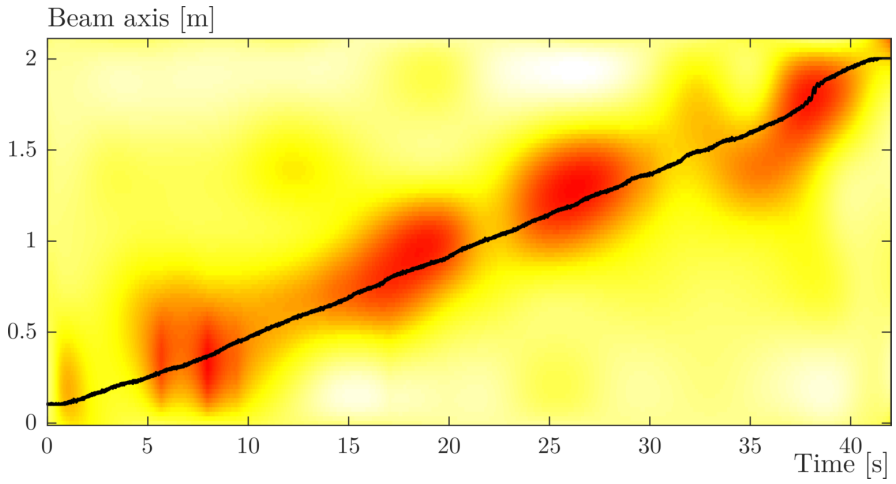

Figure 4.12: Estimated position of the mass by the COMAC criterion. The black line represents the measured position of the mass.

the (smoothed) expanded set of experimental modes is given by

$$\boldsymbol{Z}_{\text{expanded}} = \begin{bmatrix} \boldsymbol{Z}_m \\ \hline \boldsymbol{Z}_s \end{bmatrix} = \begin{bmatrix} \boldsymbol{X}_m \boldsymbol{T} \\ \hline \boldsymbol{X}_s \boldsymbol{T} \end{bmatrix}, \tag{4.4}$$

in which the transformation matrix $\boldsymbol{T}$ is computed with the experimental modes and the pseudoinverse (†) of the analytical modes at the master nodes:

$$\boldsymbol{T} = \boldsymbol{X}_m^\dagger \boldsymbol{Z}. \tag{4.5}$$

A remark should however be drawn here. The FE model is built using beam finite elements, meaning that the degrees-of-freedom of the model are nodal translation and rotations whereas in the experimental measurement process, only vertical displacements are recorded. An additional step is then required to make a good matching between both set of modes. The operation is to compute the displacements at the both sides of the beam using the rotation DoFs and the beam width or, conversely, estimating the rotation angle with both the displacements at each side.

Having our expanded experimental mode shapes, we may now use them in conjunction with the finite element model (analytical mode shapes and matrices). The method which is applied here is to analyze the discrepancies in energy for each element in the model. This method is quite simple and is described in [110]. With the elementary stiffness and mass matrices, it is possible to compute strain and kinematic energies with the finite element model. The difference in energies for the j^{th} element is computed as follows:

$$E_j^K = \sum_{i=1}^{N_m} \left(\boldsymbol{X}^{(j)} - \boldsymbol{Z}^{(j)}\right)^T \boldsymbol{K}^{(j)} \left(\boldsymbol{X}^{(j)} - \boldsymbol{Z}^{(j)}\right) \tag{4.6}$$

$$E_j^M = \sum_{i=1}^{N_m} \left(\boldsymbol{X}^{(j)} - \boldsymbol{Z}^{(j)}\right)^T \boldsymbol{M}^{(j)} \left(\boldsymbol{X}^{(j)} - \boldsymbol{Z}^{(j)}\right) \tag{4.7}$$

in which E_j^K and E_j^M are the strain and kinematic energy discrepancies, respectively and $\boldsymbol{X}^{(j)}$, $\boldsymbol{X}^{(j)}$, $\boldsymbol{K}^{(j)}$ and $\boldsymbol{M}^{(j)}$ are the numerical and experimental modes shapes and the system matrices, each one restricted to the degrees-of-freedom of the j^{th} element.

In the present application of a moving mass on the beam, it is natural to directly study the dispersion of the difference in kinematic energy on the structure. For illustration purposes, Figure 4.13 represents the sixth FE initial mode shape (Figure 4.13(a)), the sixth TV mode shape and its expansion at $t = 10$ s (Figures 4.13(b) and 4.13(c)). As in the previous example with the COMAC calculation, the effect of the mass is directly visible. The computation of the discrepancies in kinematic energy is represented in Figure 4.13(d) together with the actual position of the mass. A short gap is visible but it is explained in the following.

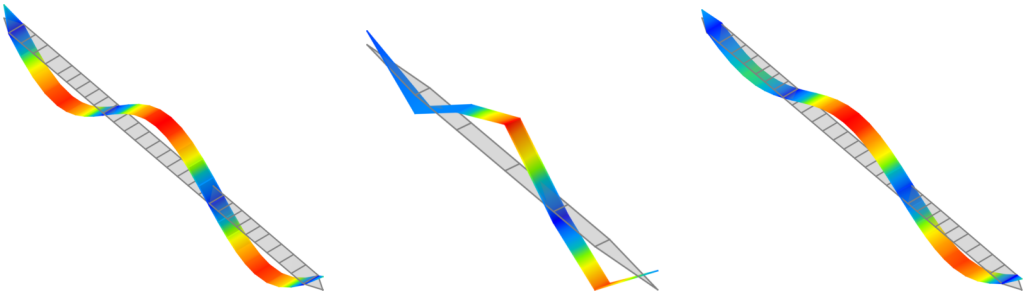

(a) Sixth FE mode shape.

(b) Sixth TV mode shape at $t = 10$ s.

(c) Expanded sixth TV mode shape at $t = 10$ s.

(d) Elementary kinematic energy discrepencies.

Figure 4.13: The expansion process of the experimental time-varying modes is illustrated to match the finite element mesh.

The moving mass in now tracked all along the time axis. Processing exactly in the same way as before, the results obtained using the refined mesh are closer to the actual position of the mass as shown in Figure 4.14. Regarding to this result, the use of the expansion method increases the tracking precision of the position but it requires an analytical or numerical (finite elements model) modal basis, which is not always available. One can also observe two horizontal lines with higher values of the energy differences. These two lines correspond to elements close to the springs and may be related to small errors between the numerical model and the experimental results. Further, the bottom one is also located at the location of the excitation shaker which is not represented in the model.

4.5 Application with additional information

In this section, we will make use of additional information about the structure under study. Let us assume that, in addition to the vibration response of the structure, some other quantities are recorded. This could be environmental conditions such as

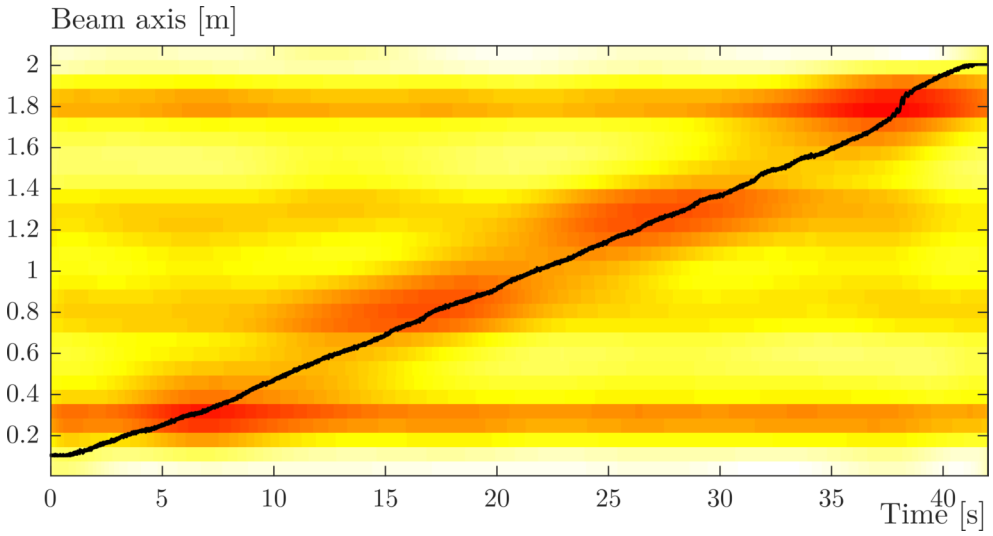

Figure 4.14: Estimation of the position of the mass by the deviation in elementary kinematic energies.

temperature, wind speed and direction and so on. Working conditions are also valuable information that may help the varying identification such as current configuration of the system or angular velocity in rotating machines for example. In our case, the position of the mass that impacts the dynamics of the system is known thanks to the laser sensor. It is shown hereafter how this additional information may help the identification process. Indeed, up to now, we considered the system as time-varying, meaning that the time was used as driving parameter in the basis functions. However, the actual parameter that impacts the dynamics of the supported beam is the moving mass which is itself traveling with time. Knowing its time-varying position, it is possible to build a new set of functions based on this parameter in order to improve the tracking ability of the identification algorithms.

As an example, let us consider the following problem with the mass moving as illustrated in Figure 4.15. Looking at the dynamic response of the system, it is obvious that the use of functions based on time would require a huge size of the basis in order to track this kind of dynamic evolution. This would results in a dramatically high number of parameters to identify and may easily lead to the failure of the identification. Conversely, linking the functions in the basis to the actual varying parameter is a better choice because in this way, the system matrices in the identification model are directly dependent on it, such as it would be the case in a mathematical model of the system.

The time-varying identification of this problem is performed with the time-varying state-space model in exactly the same way as above. Feeding a basis of twelve Chebyshev polynomials with the recorded instantaneous position of the mass leads to the results shown in Figure 4.16. The identified varying modes are also well identified and can be used for the same monitoring purposes. Applying the method described in Section 4.4.2, the position of the mass can be tracked using the discrepancies in the elementary kinetic energies of the mathematical model. The tracking ability of this method if shown in Figure 4.17 together with the recorded position of the mass. As in the previous case, it can be seen that the energy deviations element by element

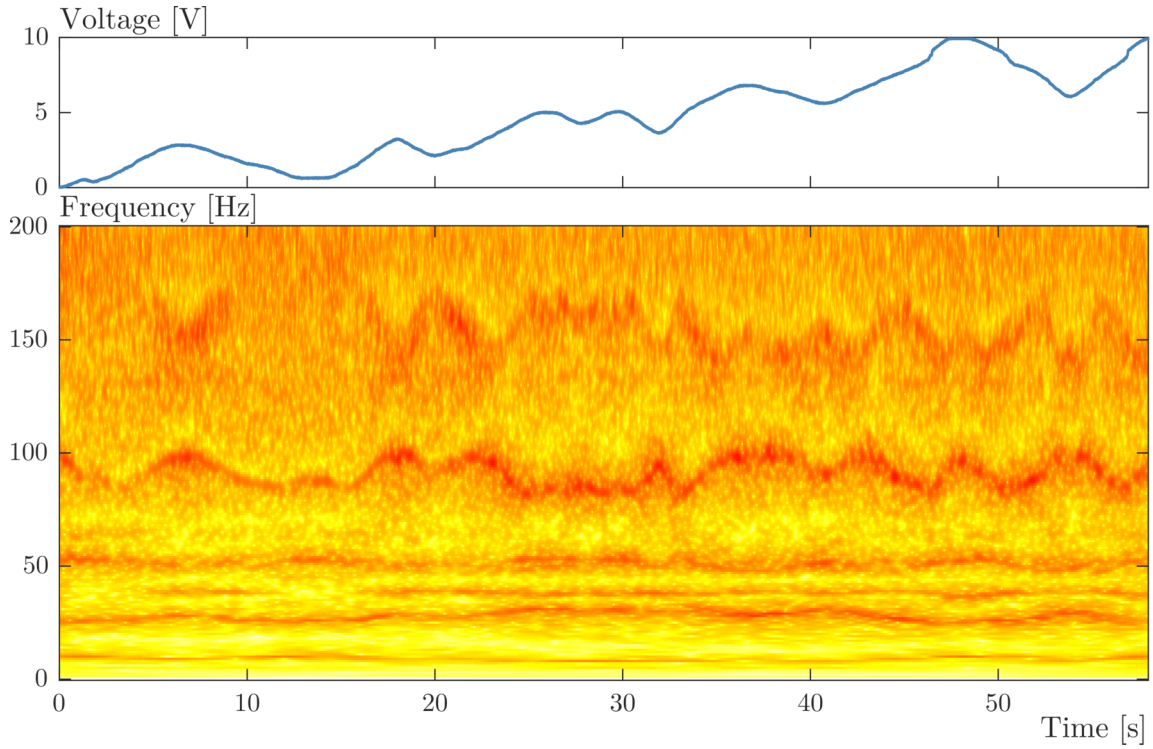

Figure 4.15: Experiment with a more complicated moving mass trajectory.

well match with the position of the mass, even in a case in which its motion is more complex.

Concluding remarks

The purpose of this chapter is to test the ability of the presented identification methods in more complex situations. In a first time, the time-varying ARMAV and state-space models were tested on an extended problem with both higher frequency range and spatial distribution. In these conditions, the task is harder to perform because of the increase of the number of parameters to be identified. Both the methods were applied with good identified results at the end. However, the identification with the ARMAV method was harder and it was not possible to get a single model able to fully identify the whole response of the system. The modal results obtained with this method were then selected from different sets of results. The weakness of this approach is that we do not have a full experimental model that can be used for other applications. The identification performed with the state-space model worked well, certainly due to the fact that it is less sensitive to the the need of overparameterization required by the ARMAV models when a too large frequency band is studied.

It was then shown that the results of the time-varying identification can be used for condition monitoring purposes. This was applied in two configurations, with and without the availability of a mathematical model. The method based on the COMAC and a reference experimental set of results gives coarse approximation of the location

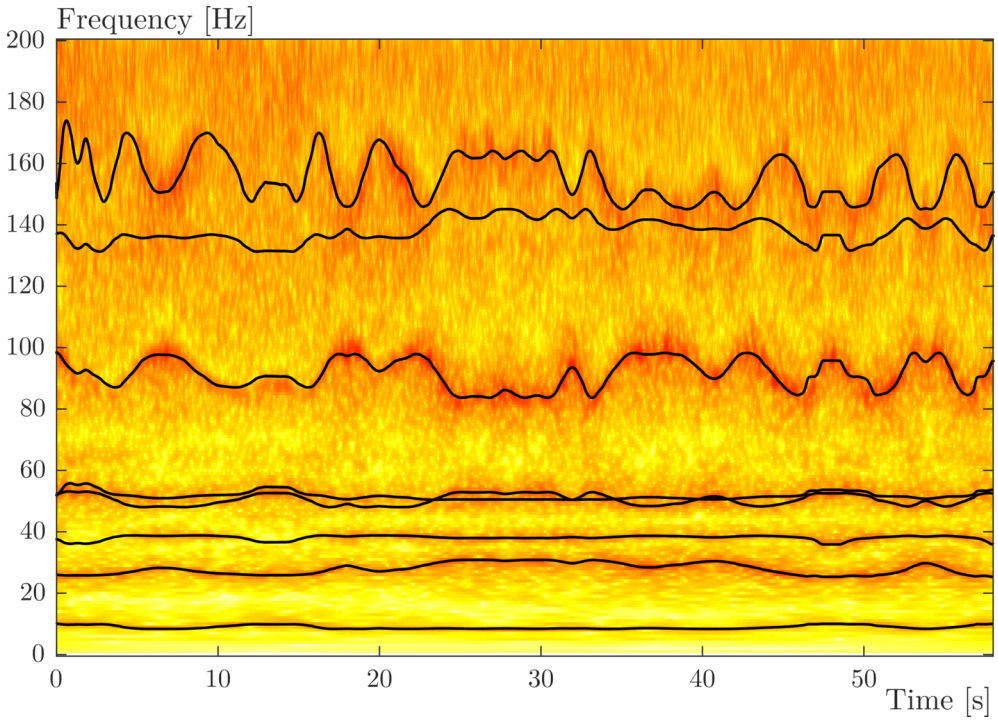

Figure 4.16: Time-varying frequencies identified with a basis of functions based on the position of the mass.

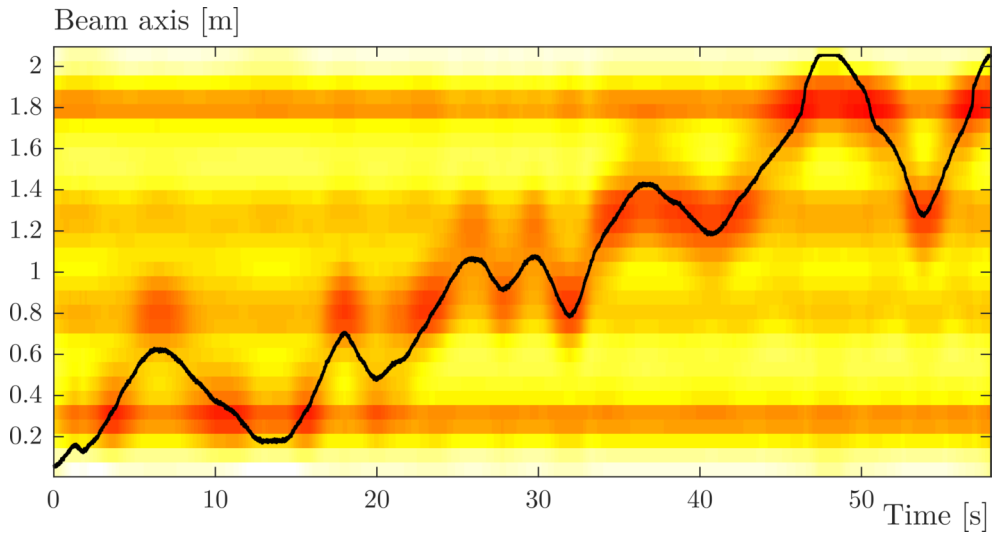

Figure 4.17: Tracking of the varying perturbation of the system in the more complex evolution.

of the moving mass. The method based on the kinematic energy discrepancies element by element on a mathematical model is shown to be more accurate. If such a model is available, it could be used for condition monitoring.

Finally, it was also shown that the time-varying identification may be drastically improved in complex cases if some additional information on the perturbing parameter is available. Using this information renders possible the identification of systems that could not be identified with bases of time functions because of the need of a too high increase in the basis size. It was also demonstrated that the tracking ability based on the elementary energies performed well in this condition.

Conclusion and perspectives

Concluding remarks

This thesis focuses on the development and improvement of current identification methods of time-varying mechanical systems. The methods can be classified in three categories: nonparametric, semi-parametric and parametric methods. Each of them was presented and successfully tested on an experimental time-varying laboratory structure. The main contribution of the thesis can be summarized as follows:

1. The nonparametric Hilbert Vibration Decomposition method has been extended to the field of multiple degrees-of-freedom problems using blind source decomposition techniques. The proposed method was proven to be efficient on small problems (few excited modes) with well separated natural frequencies. When tested on the laboratory structure, the method was able to identify the varying frequencies and mode shapes. A difficulty appeared however for the extraction of the first mode. This was assumed to be due to the weaker response of this mode with respect to the rest of the signal. The application of this method was presented at the 9th EURODYN conference [111].

2. The time-varying ARMA model based on the basis functions approach was introduced with a linking constraint added into the method in order to be able to treat the information from multiple measurement channels at once. The drawback of this method is that an overestimation of the AR and MA model orders is required. For this reason, a simple method to discriminate the physical poles from the spurious ones has been proposed. The good matching between the identified frequencies obtained from the nonparametric and the parametric approaches allows to validate the frozen-time approach on which the time-varying parametric modeling is based on. A simpler version of the method proposed in the present manuscript (an AR modeling was used) was presented at the ISMA conference in 2014 [112].

3. The scalar identification models were extended to their multivariate counterparts. In this way, it was possible to obtain the complete set of modal parameters in a parametric manner. Existing multivariate ARMA models were considered here with a specific focus on the identification of the mode shapes and the selection of the physical modes. This development was presented at the 34th IMAC conference [113] and published in the Mechanical Systems and Signal Processing (MSSP) journal [114].

4. An alternative modeling was developed in order to bring more physical meaning in the parameters to identify. The state-space model in the modal domain is closely related to the method of modal superposition which is very popular in the theory of vibration of linear systems. Even if this kind of model is theoretically less parsimonious, its use showed that it is less sensitive to the need of over parameterization. In this way, they are competitive with the ARMAV models in terms of number of parameters to identify. The method was presented at the 2016 edition of the ISMA conference [115].

5. The identification of the varying mode shapes was finally used for monitoring purposes. With few initial information, it was shown that the perturbing parameter (the position of the moving mass) could be estimated based only on the vibration measurements. This application was illustrated in [114] based on the varying mode shapes obtained with a time-varying ARMAV model.

Each of the proposed methods has its own advantages and drawbacks. If only the time-varying natural frequencies are of interest, the modified HVD method or the scalar ARMA method with multiple channels should be preferred in order to reduce the computational costs. They can also be used to get an approximate of the varying mode shapes. If the latter mode shapes are of high interest, their identification in a parametric way should be preferred using the time-varying ARMAV and state-space models. However, their increased computational complexity should be kept in mind for large problems. For this reason, for very large problems the multichannel scalar ARMA model could be the best compromise.

Perspectives

As shown in the last chapter, the use of time-varying identification methods may be used for monitoring purposes. It was shown that the knowledge of the varying mode shapes can be a valuable information in such applications, especially for damage location, which cannot be done by only analyzing the varying poles. The monitoring of time-varying structures with a locally perturbing element could then benefit from this knowledge.

Another field in which the proposed methods could be useful is the identification of parameterically excited problems and stability analyses [116, 117]. Instability monitoring in particular cases such as in periodically varying systems already exists using the

Floquet theory [116]. An extension to a more general type of time variation rather than periodic variation could be performed. As an example, flutter in aeroelastic problems by considering the effect of turbulence as a parametric excitation could be studied in this way.

The problem of the estimation of first-passage time may also benefit from methods able to deal with time-varying or parameter-varying identification in an experimental way. The first-passage estimation methods try to estimate in a system the time to reach a certain level of amplitude given some initial conditions. In civil engineering, this kind of problem may concern cranes left in auto rotation under some wind conditions for example [118].

A

Appendix

A.1 Details about common blind source separation techniques

This section describes the main properties of commonly used blind source separation methods. The first two methods, PCA and SOD, are very simple to implement.

Principal Component Analysis (PCA, POD, KLT): The PCA is a simple multivariate statistical tool based on the concept of decorrelation. The empirical covariance matrix is given as

$$\boldsymbol{R}_X = \frac{1}{N} \sum_{i=1}^{N} \boldsymbol{x}(i)\, \boldsymbol{x}^T(i). \tag{A.1}$$

Performing an eigenvalue decomposition (EVD) of the covariance matrix leads to the computation of the principal modes and variances:

$$\boldsymbol{R}_X\, \boldsymbol{V} = \boldsymbol{V}\, \boldsymbol{\Lambda} \tag{A.2}$$

in which the eigenvectors in $\boldsymbol{V}$ correspond to the principal modes and the $\boldsymbol{\Lambda}$ matrix gathers the variances of each principal component on its diagonal. Note that due to the real symmetric behavior of $\boldsymbol{R}_X$, one has the property $\boldsymbol{V}^T = \boldsymbol{V}^{-1}$. The principal components $\boldsymbol{s}_{PCA}$ are then extracted from the data by projection on the eigenvector basis

$$\boldsymbol{s}_{PCA}(t) = \boldsymbol{V}^{-1}\, \boldsymbol{x}(t) = \boldsymbol{V}^T\, \boldsymbol{x}(t) \tag{A.3}$$

With this procedure, it is easily shown that

$$\begin{aligned} \frac{1}{N} \sum_{i=1}^{N} \boldsymbol{s}_{PCA}(i)\, \boldsymbol{s}_{PCA}^T(i) &= \frac{1}{N} \sum_{i=1}^{N} \boldsymbol{V}^T \boldsymbol{x}(i)\, \boldsymbol{x}^T(i) \boldsymbol{V} && \text{(A.4)} \\ &= \boldsymbol{V}^T \boldsymbol{R}_X \boldsymbol{V} && \text{(A.5)} \\ &= \boldsymbol{\Lambda} && \text{(A.6)} \end{aligned}$$

So, the covariance matrix of the principal components data matrix is diagonal, which implies that the principal components are uncorrelated.

Another way to compute the principal components and modes is to rely on the definition of the singular value decomposition (SVD) and its relations with the eigenvalue decomposition. Let us stack the time data in a $n \times N$ matrix

$$\boldsymbol{X} = [\boldsymbol{x}(1), \boldsymbol{x}(2), \ldots, \boldsymbol{x}(N)]^T.$$

Applying the SVD to this matrix, one obtains

$$\boldsymbol{X} = \boldsymbol{U}\boldsymbol{\Sigma}\boldsymbol{V}^T \tag{A.7}$$

where $\boldsymbol{U}$ and $\boldsymbol{V}$ are the left and right singular vectors, respectively, and $\boldsymbol{\Sigma}$ contains the singular values on its main diagonal. The eigenvalue and singular value decompositions are closely related. First, the singular values of the data matrix $\boldsymbol{X}$ are equal to the eigenvalues of the square symmetric $\boldsymbol{X}^T\boldsymbol{X}$ matrix and are equal to the squared amplitudes of the eigenvalues in $\boldsymbol{\Lambda}$. The left and right singular mode are the eignevectors of the $\boldsymbol{X}\boldsymbol{X}^T$ and $\boldsymbol{X}^T\boldsymbol{X}$ matrices, respectively. By comparison, the principal components are located in the $\boldsymbol{U}$ matrix up to a scalar factor because both $\boldsymbol{U}$ and $\boldsymbol{V}$ are orthonormal matrices. It is well known that the vibration modes of a dynamical system are orthogonal in the metric of its structural mass and stiffness matrices, thus this enforced orthogonality between principal modes limits the use of this approach. Indeed, only systems which possess a mass matrix proportional to the identity fulfill this property. The other way to proceed to a correct analysis of the system with the PCA source separation is to a priori know the mass matrix of the system to correct the correlation matrix [119, 39].

Smooth Orthogonal Decomposition (SOD): The goal of the SOD method is to find a mapping of the data in a basis of modes that provides smooth orthogonal components (SOCs) with maximum variance but submitted to a smoothness constraint. Mathematically, lets assume that $\boldsymbol{v}$ is one of these modes, the problem of the SOD method is described as the following optimization [40]

$$\max_{\boldsymbol{v}} \|\boldsymbol{X}\boldsymbol{v}\|^2 \quad \text{subjected to} \quad \min_{\boldsymbol{v}} \|\boldsymbol{V}\boldsymbol{v}\|^2 \tag{A.8}$$

where $\boldsymbol{V}$ is an approximation of the derivative of $\boldsymbol{X}$ and can be computed as

$$\boldsymbol{V} = \boldsymbol{D}\,\boldsymbol{X}, \tag{A.9}$$

$\boldsymbol{D}$ being the $(N-1) \times N$ first-order numerical derivative operator

$$\boldsymbol{D} = \begin{bmatrix} -1 & 1 & 0 & \cdots & 0 \\ 0 & -1 & 1 & \cdots & 0 \\ \vdots & \ddots & \ddots & \ddots & \vdots \\ 0 & \cdots & 0 & -1 & 1 \end{bmatrix}. \tag{A.10}$$

Computing the square norms $\|\boldsymbol{X}\boldsymbol{v}\|^2$ and $\|\boldsymbol{V}\boldsymbol{v}\|^2$ as

$$\|\boldsymbol{X}\boldsymbol{v}\|^2 = \boldsymbol{v}^T\boldsymbol{X}^T\boldsymbol{X}\boldsymbol{v} = N\,\boldsymbol{v}^T\boldsymbol{R}_X\boldsymbol{v} \tag{A.11}$$

$$\|\boldsymbol{V}\boldsymbol{v}\|^2 = \boldsymbol{v}^T\boldsymbol{V}^T\boldsymbol{V}\boldsymbol{v} = (N-1)\,\boldsymbol{v}^T\boldsymbol{R}_V\boldsymbol{v} \tag{A.12}$$

with the covariance matrices of $\boldsymbol{X}$ and $\boldsymbol{V}$, respectively, the optimization problem (A.8) can be equivalently reformulated as follows

$$\max_{\boldsymbol{v}} \left(\lambda(\boldsymbol{v}) = \frac{\boldsymbol{v}^T \boldsymbol{R}_X \boldsymbol{v}}{\boldsymbol{v}^T \boldsymbol{R}_V \boldsymbol{v}} \right). \tag{A.13}$$

The solution of the decomposition is then obtained by solving the Rayleigh's quotient (A.13) which can be done by the generalized eigenvalue problem

$$\boldsymbol{R}_X \boldsymbol{v}_i = \lambda_i \boldsymbol{R}_V \boldsymbol{v}_i, \qquad i = 1, \ldots, n \tag{A.14}$$

in which n is the size of the covariance matrix. The smooth orthogonal components are finally obtained by the projection of the data on the smooth orthogonal modes.

The next two methods are based on the concept of independence between variables (the sources) to perform the separation. This property of independence between sources is a realistic assumption in many practical applications. The assumption of independence is stronger than simply uncorrelation. Independence implies uncorrelation, but the inverse is not true. Statistically speaking, the independence can be defined through probability density functions. Two variables are said independent if their joint probability density function can be obtained by the product of the marginal probability functions of each variable. The property of independence is better suited for modal analysis of mechanical systems than uncorrelation because the normal coordinates are themselves usually independent. The limit case for which the independence between normal coordinates is lost is when the ratio between two component frequencies is rational [42].

Independent Component Analysis (ICA): To perform the separation between sources, the ICA method tries to maximize the degree of independence between the sources. This can be done by several ways [42]. A first technique is based on the central limit theorem stating that the distribution of the sum of independent random variables converges to a normal law. The method of maximization of non-Gaussianity is based on that principle because a mixture of independent sources is more Gaussian than the sources themselves. The Gaussianity can be measured by higher-order cumulants such as the Kurtosis (fourth order) which is a very simple measure but which can be very sensitive to the outlier values in the data. This is the main drawback of the ICA method. The kurtosis is defined as:

$$\gamma(s|\,\mu,\,\sigma) = E\left[\left(\frac{s-\mu}{\sigma} \right)^4 \right] \tag{A.15}$$

where E denotes the expected value, and μ and σ the mean and standard deviation of s, respectively. The value of the kurtosis defined as in (A.15) equals 3 for Gaussian variable. Note also that another definition of the kurtosis exists, the excess kurtosis, in which 3 is retrieved in a way to get a null kurtosis for Gaussian distribution. One has to be careful about which definition is implemented when using an existing software. For example, Matlab uses the definition (A.15)

without the -3 normalization. The negentropy may also be used as a measure of non-Gaussianity [120]. In information theory, the entropy of a random signal can be related to the amount of information it contains. The higher the randomness of variable, the higher its entropy and for a same variance, a Gaussian variable has the highest entropy. Other methods based on minimization of mutual information, maximum likelihood or projection pursuit may also be implemented [120]. Finally, because the ICA method is based on non-Gaussianity, Gaussian sources may not be separated.

Second-Order Blind Identification: Similarly to the ICA, the SOBI method also performs a separation into independent sources. The advantage of SOBI over ICA is that the temporal structure of the signals is taken into account. Indeed, this method is based on time-lagged covariance matrices, hence the reference to second order. The use of second-order statistical measures renders the SOBI method also more robust than ICA based on higher-order statistics. We saw earlier that the PCA method is able to perform a decomposition leading to uncorrelated sources. In the case of independent sources, not only the covariance matrix is diagonal, but all the time-lagged covariance matrices are diagonal too. This latter property is the basis of the SOBI algorithm. The SOBI workflow is as follows (the whole implementation details may be found in References [121, 42, 122], among others):

1. Whitening the data: this preprocessing procedure transforms the data set to a unit variance uncorrelated one:

$$\boldsymbol{x}_w = \boldsymbol{W}\,\boldsymbol{x}(t) = \boldsymbol{W}\,\boldsymbol{A}\,\boldsymbol{s}(t) \tag{A.16}$$

   The whitening matrix $\boldsymbol{W}$ can be straightforwardly computed using the previously described PCA method (Equation (A.3)).

2. Computation of a series of p time-lagged covariance matrices of the whitened data:

$$\boldsymbol{R}_{x_w}(\tau) = \sum_{i=1}^{N} \boldsymbol{x}_w(t+\tau)\,\boldsymbol{x}_w(t)^T \qquad \forall \tau = \tau_1,\, \tau_2,\, \ldots,\, \tau_p \tag{A.17}$$

   By assuming that the sources are of unit variance (this is a simplifying constraint to remove the scaling indeterminacy), the latter equation becomes

$$\begin{aligned} \boldsymbol{R}_{x_w}(\tau) &= \sum_{i=1}^{N} \boldsymbol{x}_w(t+\tau)\,\boldsymbol{x}_w(t)^T && \text{(A.18)} \\ &= \boldsymbol{W}\boldsymbol{A} \sum_{i=1}^{N} \boldsymbol{s}(t+\tau)\,\boldsymbol{s}(t)^T \boldsymbol{A}^T \boldsymbol{W}^T && \text{(A.19)} \\ &= \boldsymbol{W}\boldsymbol{A}\,\boldsymbol{R}_s(\tau)\,\boldsymbol{A}^T \boldsymbol{W}^T && \text{(A.20)} \end{aligned}$$

   with $\boldsymbol{R}_s(\tau)$, the τ-lagged covariance matrix of the unknown sources.

3. Joint diagonalization of the p covariance matrices. This operation is the optimization part of the method to find a suitable $\boldsymbol{A}$ matrix that diagonalyzes

the p covariance matrices as much as possible [121]. The optimization operates on the elements of the $\boldsymbol{A}$ matrix in order to minimize a loss function such as

$$\min_{A} \sum_{\tau_k} \text{off}\left(\boldsymbol{R}_s(\tau_k)\right) \tag{A.21}$$

in which the "off" operator sums the square of all the off diagonal elements of a matrix:

$$\text{off}(\boldsymbol{M}) = \sum_{i \neq j} |M_{i,j}|^2. \tag{A.22}$$

4. Once the mixing matrix $\boldsymbol{A}$ in known, the corresponding independent sources may be computed by (1.39).

A.2 Practical computation of the gradients in the nonlinear optimization schemes.

In this section, we discuss an issue that may rapidly occur in case of large test campaigns, i.e. larger number of involved modes in the frequency band, a larger number of sensors on the structure or a higher complexity in the time evolution of the dynamics. A high number of excited modes requires the selection of high orders in the identification models. More sensors increase the amount of information about the dynamics but enlarge the size of the response vector. If the time-varying behavior of the dynamics of the system increases, a higher number of basis functions will be necessary. Each of these cases, and even worse, a combination of them, will increase the complexity of the problem by increasing the number of parameters to identify. In such cases, the calculation costs, especially in the nonlinear optimization process, may become prohibitive because of the huge requirements in computation and memory.

The critical point in the optimization is the computation of the Jacobian matrix of the residuals. As a reminder the cost function of the optimization process is given in a least squares sense:

$$V(\boldsymbol{\theta}) = \frac{1}{2N} \sum_{t=1}^{N} \boldsymbol{e}[t, \boldsymbol{\theta}]^T \boldsymbol{e}[t, \boldsymbol{\theta}]. \tag{A.23}$$

Stacking all the residual terms in a single vector $\boldsymbol{E}(\boldsymbol{\theta}) = \left[\boldsymbol{e}[1, \boldsymbol{\theta}]^T \, \boldsymbol{e}[2, \boldsymbol{\theta}]^T \, \cdots \, \boldsymbol{e}[N, \boldsymbol{\theta}]^T\right]^T$, the latter equation may be rewritten as

$$V(\boldsymbol{\theta}) = \frac{1}{2N} \boldsymbol{E}(\boldsymbol{\theta})^T \boldsymbol{E}(\boldsymbol{\theta}). \tag{A.24}$$

The updating of the vector of parameters in the Levenberg-Marquard optimization is iteratively processed as

$$\boldsymbol{\theta}^{(k+1)} = \boldsymbol{\theta}^{(k)} + \boldsymbol{d} \tag{A.25}$$

with the update ste $\boldsymbol{d}$ given by the solution of

$$\left(\boldsymbol{J}^T \boldsymbol{J} + \lambda \boldsymbol{I}\right) \boldsymbol{d} = \boldsymbol{J}^T \boldsymbol{E}. \tag{A.26}$$

The Jacobian matrix appearing in this equation being computed as the derivative of the residual vector

$$\boldsymbol{J} = \frac{\partial \boldsymbol{E}(\boldsymbol{\theta})}{\partial \boldsymbol{\theta}^T}, \tag{A.27}$$

its dimension is equal to $N \times \dim(\boldsymbol{\theta})$. Its computation may then represents a huge quantity of components in case of large number of samples and/or number of parameters and it may be critical for the computation. A solution however exists to tackle this problem and it relies on QR factorization and is explained in details in [123]. First, stacking the $\boldsymbol{J}$ matrix and the $\boldsymbol{E}$ vector together and performing their QR factorization, one gets

$$\begin{bmatrix} \boldsymbol{J} & \boldsymbol{E} \end{bmatrix} = \begin{bmatrix} \boldsymbol{Q}_1 & \boldsymbol{Q}_2 \end{bmatrix} \begin{bmatrix} \boldsymbol{R}_{11} & \boldsymbol{R}_{12} \\ \boldsymbol{0} & \boldsymbol{R}_{22} \end{bmatrix}. \tag{A.28}$$

Due the the orthogonal properties of the $\boldsymbol{Q}$ matrix, the following matrix product gives

$$\begin{bmatrix} \boldsymbol{J}^T \\ \boldsymbol{E}^T \end{bmatrix} \begin{bmatrix} \boldsymbol{J} & \boldsymbol{E} \end{bmatrix} = \begin{bmatrix} \boldsymbol{R}_{11}^T & \boldsymbol{0} \\ \boldsymbol{R}_{12}^T & \boldsymbol{R}_{22}^T \end{bmatrix} \begin{bmatrix} \boldsymbol{R}_{11} & \boldsymbol{R}_{12} \\ \boldsymbol{0} & \boldsymbol{R}_{22} \end{bmatrix}. \tag{A.29}$$

This makes appear that the (cumbersome) $\boldsymbol{Q}$ matrix is not required and only the $\boldsymbol{R}$ matrix is needed, which does not depends on the number of data samples N but only the number of parameters plus 1. The computations on $\boldsymbol{J}^T\boldsymbol{J}$ and $\boldsymbol{J}^T\boldsymbol{E}$ need only the $\boldsymbol{R}_{11}$ and $\boldsymbol{R}_{12}$ matrices.

In case of very long measurements, it may also be possible that the computation of the whole $\boldsymbol{J}$ matrix is not possible because of too many coefficients. In such a case, the latter properties combined with the fact that the Jacobian matrix is computed by state-space filtering offer the possibility to cut the whole calculation into several blocks. Let $\boldsymbol{J}^{(1)}$ be the Jacobian matrix computed for $N_1 < N$ data samples. Similarly, let $\boldsymbol{E}^1$ being the residual vector with the N_1 first error terms. A first QR decomposition is then performed as previously described in order to get rid of the number of data samples

$$\begin{bmatrix} \boldsymbol{J}^{(1)} & \boldsymbol{E}^{(1)} \end{bmatrix} = \begin{bmatrix} \boldsymbol{Q}_1^{(1)} & \boldsymbol{Q}_2^{(1)} \end{bmatrix} \begin{bmatrix} \boldsymbol{R}_{11}^{(1)} & \boldsymbol{R}_{12}^{(1)} \\ \boldsymbol{0} & \boldsymbol{R}_{22}^{(1)} \end{bmatrix}. \tag{A.30}$$

Based on the last state vectors at time N_1 in the derivative operations, the next part of the Jacobian may be computed for times $N_1 + 1$ to N_2. The QR decomposition is then iteratively updated by a series of computation of subblocks of the whole Jacobian matrix

$$\begin{bmatrix} \boldsymbol{R}_{11}^{(k)} & \boldsymbol{R}_{12}^{(k)} \\ \boldsymbol{J}^{(k+1)} & \boldsymbol{E}^{(k+1)} \end{bmatrix} = \begin{bmatrix} \boldsymbol{Q}_1^{(k+1)} & \boldsymbol{Q}_2^{(k+1)} \end{bmatrix} \begin{bmatrix} \boldsymbol{R}_{11}^{(k+1)} & \boldsymbol{R}_{12}^{(k+1)} \\ \boldsymbol{0} & \boldsymbol{R}_{22}^{(k+1)} \end{bmatrix}. \tag{A.31}$$

Bibliography

[1] G. Kerschen, K. Worden, A. F. Vakakis, and J.-C. Golinval. Past, present and future of nonlinear system identification in structural dynamics. *Mechanical Systems and Signal Processing*, 20(3):505–592, 2006.

[2] J.-P. Noël and G. Kerschen. Nonlinear system identification in structural dynamics: 10 more years of progress. *Mechanical Systems and Signal Processing*, 83:2–35, jan 2017.

[3] L. Garibaldi and S. Fassois. MSSP special issue on the identification of time varying structures and systems. *Mechanical Systems and Signal Processing*, 47(1-2):1–2, aug 2014.

[4] L. Garibaldi. Output-Only, Time-Variant And Non Linear Systems: Headache Or Challenge To System Identification? In R. SERRA, editor, *3ième Colloque « Analyse Vibratoire Expérimentale »*, Blois, 2012.

[5] S. Marchesiello, S. Bedaoui, L. Garibaldi, and P. Argoul. Time-dependent identification of a bridge-like structure with crossing loads. *Mechanical Systems and Signal Processing*, 23(6):2019–2028, aug 2009.

[6] D. Cantero, M. Ülker-Kaustell, and R. Karoumi. Time–frequency analysis of railway bridge response in forced vibration. *Mechanical Systems and Signal Processing*, 76-77:518–530, aug 2016.

[7] D. Tcherniak and M. S. Allen. Experimental Dynamic Characterization of Operating Wind Turbines with Anisotropic Rotor. volume 2 of *Conference Proceedings of the Society for Experimental Mechanics Series*, pages 131–143. Springer International Publishing, Cham, 2016.

[8] G. Coppotelli, C. Grappasonni, and C. D. Trapani. Dynamic Identification of a Solid Rocket Motor From Firing Test Using Operational Modal Analysis. In *52nd AIAA/ASME/ASCE/AHS/ASC Structures, Structural Dynamics and Materials Conference*, number April, Denver, 2011.

[9] S. Manzato, B. Peeters, T. Brault, and E. Fily. Tracking the evolution of modal properties of a solid propellant launcher during static firing test. *Conference Proceedings of the Society for Experimental Mechanics Series*, 5(February):559–570, 2012.

[10] A. M. Brown. Temperature-Dependent Modal Test/Analysis Correlation of X-34 FASTRAC Composite Rocket Nozzle. *Journal of Propulsion and Power*, 18(2):284–288, mar 2002.

[11] A. Haar. Zur Theorie der orthogonalen Funktionensysteme. *Mathematische Annalen*, 69(3):331–371, sep 1910.

[12] E. Wigner. On the quantum correction for thermodynamic equilibrium. *Physical Review*, 40(5):749–759, 1932.

[13] J. Ville. Théorie et Applications de la Notion de Signal Analytique. *Cables et Transmissions*, 2a(1):61–74, 1948.

[14] L. Cohen. Time-frequency distributions - a review. *Proceedings of the IEEE*, 77(7):941–981, jul 1989.

[15] D. Gabor. Theory of communication. *Journal of the Institution of Electrical Engineers - Part III: Radio and Communication Engineering*, 93(26):429–441, nov 1946.

[16] E. Bedrosian. A product theorem for Hilbert transforms. *Proceedings of the IEEE*, 51(5):868–869, 1963.

[17] N. E. Huang, Z. Shen, S. R. Long, M. C. Wu, H. H. Shih, Q. Zheng, N.-C. Yen, C. C. Tung, and H. H. Liu. The empirical mode decomposition and the Hilbert spectrum for nonlinear and non-stationary time series analysis. *Proceedings of the Royal Society A: Mathematical, Physical and Engineering Sciences*, 454(1971):903–995, mar 1998.

[18] J. Chen. Application of empirical mode decomposition in structural health monitoring: some experience. *Advances in Adaptive Data Analysis*, 01(04):601–621, oct 2009.

[19] C. Park. A tutorial on empirical mode decomposition in brain research. In *The 18th IEEE International Symposium on Consumer Electronics (ISCE 2014)*, volume 01, pages 1–2. IEEE, jun 2014.

[20] M. Feldman. Time-varying vibration decomposition and analysis based on the Hilbert transform. *Journal of Sound and Vibration*, 295(3-5):518–530, aug 2006.

[21] M. Feldman. *Hilbert Transform Applications in Mechanical Vibration*. John Wiley & Sons, Ltd, Chichester, UK, mar 2011.

[22] Z. Wu and N. E. Huang. Ensemble empirical mode decomposition: a noise-assisted data analysis method. *Advances in Adaptive Data Analysis*, 01(01):1–41, jan 2009.

[23] M. Feldman. Theoretical analysis and comparison of the Hilbert transform decomposition methods. *Mechanical Systems and Signal Processing*, 22(3):509–519, apr 2008.

[24] B. Boashash. Estimating and interpreting the instantaneous frequency of a signal. I. Fundamentals. *Proceedings of the IEEE*, 80(4):520–538, apr 1992.

[25] M. Feldman. Analytical basics of the EMD: Two harmonics decomposition. *Mechanical Systems and Signal Processing*, 23(7):2059–2071, oct 2009.

[26] D. Spina, C. Valente, and G. R. Tomlinson. A new procedure for detecting nonlinearity from transient data using the gabor transform. *Nonlinear Dynamics*, 11(3):235–254, nov 1996.

[27] W. Staszewski. Identification Of Non-Linear Systems Using Multi-Scale Ridges And Skeletons Of The Wavelet Transform. *Journal of Sound and Vibration*, 214(4):639–658, jul 1998.

[28] P. Argoul and T.-P. Le. Instantaneous indicators of structural behaviour based on the continuous cauchy wavelet analysis. *Mechanical Systems and Signal Processing*, 17(1):243–250, jan 2003.

[29] G. Kerschen, A. Vakakis, Y. Lee, D. McFarland, and L. Bergman. Toward a Fundamental Understanding of the Hilbert-Huang Transform in Nonlinear Structural Dynamics. *Journal of Vibration and Control*, 14(1-2):77–105, jan 2008.

[30] A. F. Vakakis, L. A. Bergman, D. M. McFarland, Y. S. Lee, and M. Kurt. Current efforts towards a non-linear system identification methodology of broad applicability. *Proceedings of the Institution of Mechanical Engineers, Part C: Journal of Mechanical Engineering Science*, 225(11):2497–2515, nov 2011.

[31] M. Feldman. Non-linear system vibration analysis using Hilbert transform–I. Free vibration analysis method 'Freevib'. *Mechanical Systems and Signal Processing*, 8(2):119–127, mar 1994.

[32] M. Feldman. Non-linear system vibration analysis using Hilbert transform–II. Forced vibration analysis method 'Forcevib'. *Mechanical Systems and Signal Processing*, 8(3):309–318, may 1994.

[33] M. Feldman and S. Braun. Identification of non-linear system parameters via the instantaneous frequency: application of the Hilbert transform and wigner-ville techniques. In *International Modal Analysis Conference (IMAC)*, pages 637–642, 1995.

[34] M. Feldman, I. Bucher, and J. Rotberg. Experimental Identification of Nonlinearities under Free and Forced Vibration using the Hilbert Transform. *Journal of Vibration and Control*, 15(10):1563–1579, oct 2009.

[35] W. J. Staszewski and J. Giacomin. Application of the wavelet based FRFs to the analysis of nonstationary vehicle data. *Proceedings of the International Modal Analysis Conference - IMAC*, 1:425–431, 1997.

[36] W. J. Staszewski and D. M. Wallace. Wavelet-based Frequency Response Function for time-variant systems—An exploratory study. *Mechanical Systems and Signal Processing*, 47(1-2):35–49, aug 2014.

[37] K. Dziedziech, W. Staszewski, and T. Uhl. Wavelet-based modal analysis for time-variant systems. *Mechanical Systems and Signal Processing*, 50-51:323–337, jan 2015.

[38] G. Kerschen and J. Golinval. Physical Interpretation of the Proper Orthogonal Modes Using the Singular Value Decomposition. *Journal of Sound and Vibration*, 249(5):849–865, jan 2002.

[39] S. Han and B. Feeny. Application of proper orthogonal decomposition to structural vibration analysis. *Mechanical Systems and Signal Processing*, 17(5):989–1001, sep 2003.

[40] D. Chelidze and W. Zhou. Smooth orthogonal decomposition-based vibration mode identification. *Journal of Sound and Vibration*, 292(3-5):461–473, may 2006.

[41] F. Poncelet, G. Kerschen, J.-C. Golinval, and D. Verhelst. Output-only modal analysis using blind source separation techniques. *Mechanical Systems and Signal Processing*, 21(6):2335–2358, aug 2007.

[42] F. Poncelet. *Experimental Modal Analysis using Blind Source Separation Techniques*. PhD thesis, 2010.

[43] R. J. Hodrick and E. C. Prescott. Postwar U . S . Business Cycles : An Empirical Investigation. *Journal of Money, Credit and Banking*, 29(1):1–16, 1997.

[44] D. Broomhead and G. P. King. Extracting qualitative dynamics from experimental data. *Physica D: Nonlinear Phenomena*, 20(2-3):217–236, jun 1986.

[45] H. Vold and J. Leuridan. High Resolution Order Tracking at Extreme Slew Rates, Using Kalman Tracking Filters. In *Shock and Vibration*, volume 2, pages 507–515, may 1993.

[46] C. Feldbauer and R. Höldrich. Realization of a Vold-Kalman Tracking Filter - A Least Squares Problem. In *Proceedings of the COST G-6 Conference on Digital Audio Effects (DAFX-00)*, number 8, pages 8–11, Verona, Italy, 2000.

[47] J. Tuma. Setting the passband width in the vold- kalman order tracking filter. In *Twelfth International Congress on Sound and Vibration*, Lisbon, 2005.

[48] D. Ewins. *Modal Testing: Theory, Practice and Application*. Research Studies Press LTD., 2000.

[49] M. H. Richardson. Is It a Mode Shape, or an Operating Deflection Shape? *Sound & Vibration Magazine*, (30th Anniversary Issue), 1997.

[50] A. Poulimenos and S. Fassois. Parametric time-domain methods for non-stationary random vibration modelling and analysis — A critical survey and comparison. *Mechanical Systems and Signal Processing*, 20(4):763–816, may 2006.

[51] LMS SCADAS Mobile. http://www.lmsintl.com/scadas-mobile.

[52] LMS Test.Lab. http://www.plm.automation.siemens.com/en_us/products/lms/testing/test-lab/index.shtml.

[53] B. Peeters, G. Lowet, V. der Auweraer, and J. Leuridan. A new procedure for modal parameter estimation. *Sound and Vibration*, 38(January):24–29, 2004.

[54] S. Fassois. Identification, Model-Based Methods. *Encyclopedia of Vibration*, pages 673–685, 2001.

[55] B. Peeters, H. V. D. Auweraer, P. Guillaume, and J. Leuridan. The PolyMAX frequency-domain method: a new standard for modal parameter estimation? *Shock and Vibration*, 11(3-4):395–409, 2004.

[56] B. Peeters and H. Van der Auweraer. PolyMAX: A revolution in operational modal analysis. In *1st International Operational Modal Analysis Conference*, Copenhagen, 2005.

[57] P. Van Overschee and B. De Moor. *Subspace Identification for Linear Systems*, volume 2008. Kluwer Academic Publishers, 1996.

[58] L. Ljung. *System identification: theory for the user*. Prentice Hall PTR, 2 edition, 1999.

[59] J. E. Dennis and R. B. Schnabel. *Numerical Methods for Unconstrained Optimization and Nonlinear Equations*. Society for Industrial and Applied Mathematics, jan 1996.

[60] L. Zadeh. Frequency Analysis of Variable Networks. *Proceedings of the IRE*, 38(3):291–299, mar 1950.

[61] M. Niedzwiecki. *Identification of Time-Varying Processes*. John Wiley & Sons, Inc., New York, NY, USA, 2000.

[62] L. A. Liporace. Linear estimation of nonstationary signals. *The Journal of the Acoustical Society of America*, 58(6):1288–1295, dec 1975.

[63] M. G. Hall, A. V. Oppenheim, and A. S. Willsky. Time-varying parametric modeling of speech. *Signal Processing*, 5(3):267–285, may 1983.

[64] Y. Grenier. Rational nonstationary spectra and their estimation, 1981.

[65] Y. Grenier. Time-Dependent ARMA Modeling of Nonstationary Signals. *IEEE Transactions on Acoustics, Speech, and Signal Processing*, 31(4):899–911, aug 1983.

[66] Y. Grenier. Modèles ARMA à coefficients dépendant du temps estimateurs et applications. *Traitement du signal*, 3:219–233, 1986.

[67] K. Petsounis and S. Fassois. Non-stationary functional series tarma vibration modelling and analysis in a planar manipulator. *Journal of Sound and Vibration*, 231(5):1355–1376, apr 2000.

[68] M. Spiridonakos, A. Poulimenos, and S. Fassois. Output-only identification and dynamic analysis of time-varying mechanical structures under random excitation: A comparative assessment of parametric methods. *Journal of Sound and Vibration*, 329(7):768–785, mar 2010.

[69] M. Spiridonakos and S. Fassois. Non-stationary random vibration modelling and analysis via functional series time-dependent ARMA (FS-TARMA) models – A critical survey. *Mechanical Systems and Signal Processing*, 47(1-2):175–224, aug 2014.

[70] S.-D. Zhou, W. Heylen, P. Sas, and L. Liu. Parametric modal identification of time-varying structures and the validation approach of modal parameters. *Mechanical Systems and Signal Processing*, 47(1-2):94–119, aug 2014.

[71] K. Levenberg. A method for the solution of certain non-linear problems in least squares. *Quarterly of Applied Mathematics*, 2:164–168, 1944.

[72] D. W. Marquardt. An Algorithm for Least-Squares Estimation of Nonlinear Parameters. *Journal of the Society for Industrial and Applied Mathematics*, 11(2):431–441, jun 1963.

[73] J. J. Moré and D. C. Sorensen. Computing a Trust Region Step. *SIAM Journal on Scientific and Statistical Computing*, 4(3):553–572, sep 1983.

[74] H. Akaike. Fitting autoregressive models for prediction. *Annals of the Institute of Statistical Mathematics*, 21:243–247, 1969.

[75] H. Akaike. Information theory and an extension of the maximum likelihood principle, 1973.

[76] J. Rissanen. Modeling by shortest data description. *Automatica*, 14(5):465–471, sep 1978.

[77] A. Beex and S. Peijun. A time-varying Prony method for instantaneous frequency estimation at low SNR. In *ISCAS'99. Proceedings of the 1999 IEEE International Symposium on Circuits and Systems VLSI (Cat. No.99CH36349)*, volume 3, pages 5–8. IEEE, 1999.

[78] E. Reynders, J. Houbrechts, and G. De Roeck. Fully automated (operational) modal analysis. *Mechanical Systems and Signal Processing*, 29:228–250, may 2012.

[79] P. Andersen, R. Brincker, and P. H. Kirkegaard. Theory of covariance equivalent ARMAV models of civil engineering structures. In *IMAC XIV - 14th International Modal Analysis Conference*, volume 71, pages –, 1995.

[80] M. Smail, M. Thomas, and A. Lakis. ARMA models for modal analysis: effect of model orders and sampling frequency. *Mechanical Systems and Signal Processing*, 13(6):925–941, nov 1999.

[81] M. Smail, M. Thomas, and A. Lakis. Assessment of optimal ARMA model orders for modal analysis. *Mechanical Systems and Signal Processing*, 13(5):803–819, sep 1999.

[82] Z.-S. Ma, L. Liu, S.-D. Zhou, and W. Yang. Modal parameter estimation of the coupled moving-mass and beam time-varying system. *Proceedings of the International Conference on Noise and Vibration Engineering and USD 2014*, pages 587–596, 2014.

[83] N. R. Draper and H. Smith. *Applied Regression Analysis*. John Wiley & Sons, Inc., Hoboken, NJ, USA, apr 1998.

[84] D. L. Brown, R. J. Allemang, R. Zimmerman, and M. Mergeay. Parameter Estimation Techniques for Modal Analysis. feb 1979.

[85] S. R. Ibrahim and E. C. Mikulcik. A method for the direct identification of vibration parameters from the free response. *Shock and Vibration Bulletin*, 4:183–198, 1977.

[86] P. Andersen. *Identification of civil engineering structures using vector ARMA models*. PhD thesis, 1997.

[87] J.-B. Bodeux and J.-C. Golinval. Application of ARMAV models to the identification and damage detection of mechanical and civil engineering structures. *Smart Materials and Structures*, 10(3):479–489, jun 2001.

[88] S. Fassois. MIMO LMS-ARMAX identification of vibrating structures - Part I: the method. *Mechanical Systems and Signal Processing*, 15(4):723–735, jul 2001.

[89] A. Florakis, S. Fassois, and F. Hemez. MIMO LMS-ARMAX identification of vibrating structures - Part II: a critical assessment. *Mechanical Systems and Signal Processing*, 15(4):737–758, jul 2001.

[90] J.-N. Juang and R. S. Papa. An Eigensystem Realization Algorithm for Modal Parameter Identification and Model Reduction. *Journal of Guidance and Dynamics*, 8(4):620–627, 1985.

[91] G. H. James, T. G. Carne, J. P. Lauffer, and A. R. Nord. Modal testing using natural excitation. *10th International Modal Analysis Conference*, (JANUARY), 1992.

[92] M. Goursat, M. Döhler, L. Mevel, and P. Andersen. Crystal Clear SSI for Operational Modal Analysis of Aerospace Vehicles. In *Proceedings of the IMAC-XXVIII*, pages 1421–1430. 2011.

[93] M. Goursat and L. Mevel. Algorithms for covariance subspace identification : a choice of effective implementations. In *Proceedings of the IMAC-XXVII*, 2009.

[94] M. D. Spiridonakos and S. D. Fassois. Parametric identification of a time-varying structure based on vector vibration response measurements. *Mechanical Systems and Signal Processing*, 23(6):2029–2048, 2009.

[95] K. Liu. Identification of Linear Time-Varying Systems. *Journal of Sound and Vibration*, 206(4):487–505, 1997.

[96] K. Liu. Extension of modal analysis to linear time-varying systems. *Journal of Sound and Vibration*, 226(1):149–167, 1999.

[97] K. Liu and L. Deng. Identification of pseudo-natural frequencies of an axially moving cantilever beam using a subspace-based algorithm. *Mechanical Systems and Signal Processing*, 20(1):94–113, 2006.

[98] F. Tasker, a. Bosse, and S. Fisher. Real-Time Modal Parameter Estimation Using Subspace Methods: Theory. *Mechanical Systems and Signal Processing*, 12:797–808, 1998.

[99] A. Bosse, F. Tasker, and S. Fisher. Real-Time Modal Parameter Estimation Using Subspace Methods: Applications. *Mechanical Systems and Signal Processing*, 12(6):809–823, nov 1998.

[100] B. Piombo, E. Giorcelli, L. Garibaldi, and A. Fasana. Structures Identification Using ARMAV Models. In Society for Experimental Mechanics, editor, *IMAC 11, International Modal Analysis Conference*, pages 588–592, Orlando, 1993.

[101] J.-B. Bodeux and J.-C. Golinval. Modal identification and damage detection using the data-driven stochastic subspace and ARMAV methods. *Mechanical Systems and Signal Processing*, 17(1):83–89, jan 2003.

[102] E. Reynders, J. Houbrechts, and G. De Roeck. Fully automated (operational) modal analysis. *Mechanical Systems and Signal Processing*, 29:228–250, may 2012.

[103] P. Carette and T. McKelvey. Model parameter gradients in predication identification of state-space systems. Technical report, Linköping University, Linköping, 1998.

[104] R. Brincker and P. Andersen. ARMA models in modal space. In *Proceedings of the 17th International Modal Analysis Conference (IMAC)*, volume 1, pages 330–334, Kissimmee, Florida, 1999.

[105] M. Patil. Decoupled second-order equations and modal analysis of a general nonconservative system. In *41st Structures, Structural Dynamics, and Materials Conference and Exhibition*, Reston, Virigina, apr 2000. American Institute of Aeronautics and Astronautics.

[106] M. Friswell and J. E. Mottershead. *Finite Element Model Updating in Structural Dynamics*. Springer, 1995.

[107] N. A. J. Lieven and D. J. Ewins. Spatial correlation of mode shapes: the coordinate modal assurance criterion (COMAC). In *Proceedings of the 6th International Modal Analysis Conference (IMAC)*, pages 690–695, 1988.

[108] D. L. Hunt. Application of an enhanced Coordinate Modal Assurance Criterion. In *10th International Modal Analysis Conference*, pages 66–71, San Diego, 1992.

[109] J. O'Callahan, P. Avitabile, and R. Riemer. System Equivalent Reduction Expansion Process (SEREP). In *Seventh International Modal Analysis Conference*, Las Vegas, 1989.

[110] M. Link. Updating of Analytical Models — Basic Procedures and Extensions. In J. M. M. Silva and N. M. M. Maia, editors, *Modal Analysis and Testing*, pages 281–304. Springer Netherlands, Dordrecht, 1999.

[111] M. Bertha and J.-C. Golinval. Experimental modal analysis of a beam travelled by a moving mass using Hilbert Vibration Decomposition. In *Proceedings of the 9th International Conference on Structural Dynamics, EURODYN 2014*, Porto, 2014.

[112] M. Bertha and J.-C. Golinval. Modal identification of time-varying systems using Hilbert transform and signal decomposition. In *Proceedings of the International Conference on Noise and Vibration Engineering, ISMA 2014*, pages 2409–2419, Leuven, 2014.

[113] M. Bertha and J. C. Golinval. Multivariate ARMA Based Modal Identification of a Time-varying Beam. In *Proceedings of the International Modal Analysis Conference (IMAC) XXXIV*, Orlando, 2016.

[114] M. Bertha and J.-C. Golinval. Identification of non-stationary dynamical systems using multivariate ARMA models. *Mechanical Systems and Signal Processing*, 88(5):166–179, may 2017.

[115] M. Bertha and J. Golinval. Time-varying modal parameters identification in the modal domain. In *Proceedings of ISMA 2016 - International Conference on Noise and Vibration Engineering*, Leuven, 2016.

[116] A. Jhinaoui, L. Mevel, and J. Morlier. Subspace Instability Monitoring for Linear Periodically Time-Varying Systems. *IFAC Proceedings Volumes*, 45(16):380–385, jul 2012.

[117] B. Zhou. On asymptotic stability of linear time-varying systems. *Automatica*, 68:266–276, jun 2016.

[118] H. Vanvinckenroye and V. Denoël. Average first-passage time of a quasi-Hamiltonian Mathieu oscillator with parametric and forcing excitations. *Journal of Sound and Vibration*, 406:328–345, oct 2017.

[119] B. Feeny and R. Kappagantu. On the physical interpretation of proper orthogonal modes in vibrations. *Journal of Sound and Vibration*, 211(4):607–616, apr 1998.

[120] A. Hyvärinen and E. Oja. Independent component analysis: algorithms and applications. *Neural networks : the official journal of the International Neural Network Society*, 13(4-5):411–30, 2000.

[121] A. Belouchrani, K. Abed-Meraim, J. Cardoso, and E. Moulines. A blind source separation technique using second-order statistics. *IEEE Transactions on Signal Processing*, 45(2):434–444, 1997.

[122] C. Rainieri and G. Fabbrocino. *Operational Modal Analysis of Civil Engineering Structures*. 2014.

[123] N. H. Bergboer, V. Verdult, and M. H. G. Verhaegen. An efficient implementation of maximum likelihood identification of LTI state-space models by local gradient search, 2002.